



Experimental Investigation of Project Orion Crew Exploration Vehicle Aeroheating in AEDC Tunnel 9

*Brian R. Hollis, Thomas J. Horvath, and Karen T. Berger
Langley Research Center, Hampton, Virginia*

*Randolph P. Lillard and Benjamin S. Kirk
Lyndon B. Johnson Space Center, Houston, Texas*

*Joseph J. Coblish and Joseph D. Norris
Arnold Engineering Development Center, White Oak, Maryland*

The NASA STI Program Office . . . in Profile

Since its founding, NASA has been dedicated to the advancement of aeronautics and space science. The NASA Scientific and Technical Information (STI) Program Office plays a key part in helping NASA maintain this important role.

The NASA STI Program Office is operated by Langley Research Center, the lead center for NASA's scientific and technical information. The NASA STI Program Office provides access to the NASA STI Database, the largest collection of aeronautical and space science STI in the world. The Program Office is also NASA's institutional mechanism for disseminating the results of its research and development activities. These results are published by NASA in the NASA STI Report Series, which includes the following report types:

- **TECHNICAL PUBLICATION.** Reports of completed research or a major significant phase of research that present the results of NASA programs and include extensive data or theoretical analysis. Includes compilations of significant scientific and technical data and information deemed to be of continuing reference value. NASA counterpart of peer-reviewed formal professional papers, but having less stringent limitations on manuscript length and extent of graphic presentations.
- **TECHNICAL MEMORANDUM.** Scientific and technical findings that are preliminary or of specialized interest, e.g., quick release reports, working papers, and bibliographies that contain minimal annotation. Does not contain extensive analysis.
- **CONTRACTOR REPORT.** Scientific and technical findings by NASA-sponsored contractors and grantees.

- **CONFERENCE PUBLICATION.** Collected papers from scientific and technical conferences, symposia, seminars, or other meetings sponsored or co-sponsored by NASA.
- **SPECIAL PUBLICATION.** Scientific, technical, or historical information from NASA programs, projects, and missions, often concerned with subjects having substantial public interest.
- **TECHNICAL TRANSLATION.** English-language translations of foreign scientific and technical material pertinent to NASA's mission.

Specialized services that complement the STI Program Office's diverse offerings include creating custom thesauri, building customized databases, organizing and publishing research results ... even providing videos.

For more information about the NASA STI Program Office, see the following:

- Access the NASA STI Program Home Page at <http://www.sti.nasa.gov>
- E-mail your question via the Internet to help@sti.nasa.gov
- Fax your question to the NASA STI Help Desk at (301) 621-0134
- Phone the NASA STI Help Desk at (301) 621-0390
- Write to:
NASA STI Help Desk
NASA Center for AeroSpace Information
7115 Standard Drive
Hanover, MD 21076-1320

NASA/TP-2008-215547



Experimental Investigation of Project Orion Crew Exploration Vehicle Aeroheating in AEDC Tunnel 9

*Brian R. Hollis, Thomas J. Horvath, and Karen T. Berger
Langley Research Center, Hampton, Virginia*

*Randolph P. Lillard and Benjamin S. Kirk
Lyndon B. Johnson Space Center, Houston, Texas*

*Joseph J. Coblish and Joseph D. Norris
Arnold Engineering Development Center, White Oak, Maryland*

National Aeronautics and
Space Administration

Langley Research Center
Hampton, Virginia 23681-2199

December 2008

Acknowledgments

The authors wish to thank the entire staff of Arnold Engineering Development Center Tunnel for their conduct of this test series.

Available from:

NASA Center for AeroSpace Information (CASI)
7115 Standard Drive
Hanover, MD 21076-1320
(301) 621-0390

National Technical Information Service (NTIS)
5285 Port Royal Road
Springfield, VA 22161-2171
(703) 605-6000

Table of Contents

List of Tables	iv
List of Figures	v
Abstract	1
Nomenclature	1
Symbols	1
Subscripts	2
Abbreviations	2
Background and Introduction	3
Experimental Method	3
Model Configuration and Instrumentation	3
Test Facility	4
Run Matrix	4
Data Reduction Method	5
Coordinate Systems for One-Dimensional Data Reduction	6
Wind Tunnel Model Material Thermal Properties	8
Experimental Uncertainty	11
Computational Methods and Results	11
Results, Analysis, and Comparisons	13
Reynolds Number Trends	13
Angle-of-Attack Trends	13
Off-Centerline Data	14
Boundary-Layer Trip Effects	14
Comparison of Forebody Experimental Data with Predictions	14
Mach 8 Comparisons	14
Mach 10 Comparisons	15
General observations on forebody comparisons	18
Comparison of Aftbody Experimental Data with Predictions	19
Wind Tunnel Data Repeatability	19
Transition Onset Correlations	20
Transitional/Turbulent Heating Augmentation	20
Summary and Conclusions	21
References	22

List of Tables

Table 1. Gage locations	24
Table 2. Tunnel 9 CEV Test Matrix	26
Table 4. Thermocouple calibration test data	27

List of Figures

Figure 1. NASA CEV (conceptual artwork).....	28
Figure 2. Wind tunnel model dimensions	28
Figure 3. CEV model installed in Tunnel 9 (test section opened for viewing)	29
Figure 4. CEV model inserts.....	29
Figure 5. CEV model heat shield during thermocouple installation process.....	30
Figure 6. Disassembled CEV model heat shield and aftbody.....	30
Figure 7. Thermocouple layout on CEV model.....	31
Figure 8. AEDC Hypervelocity Tunnel 9 (Mach 10 nozzle).....	32
Figure 9. Schematic of AEDC Hypervelocity Tunnel 9	32
Figure 10. Run 3057 free stream conditions	33
Figure 11. Run 3058 free stream conditions	34
Figure 12. Run 3059 free stream conditions	35
Figure 13. Run 3060 free stream conditions	36
Figure 14. Run 3061 free stream conditions	37
Figure 15. Run 3062 free stream conditions	38
Figure 16. Run 3063 free stream conditions	39
Figure 17. Run 3064 free stream conditions	40
Figure 18. Run 3065 free stream conditions	41
Figure 19. Run 3066 free stream conditions	42
Figure 20. Run 3067 free stream conditions	43
Figure 21. Run 3068 free stream conditions	44
Figure 22. Run 3069 free stream conditions	45
Figure 23. Run 3070 free stream conditions	46
Figure 24. Run 3071 free stream conditions	47
Figure 25. Run 3072 free stream conditions	48
Figure 26. Run 3073 free stream conditions	49
Figure 27. Run 3074 free stream conditions	50
Figure 28. Run 3075 free stream conditions	51
Figure 29. Run 3076 free stream conditions	52
Figure 30. Run 3077 free stream conditions	53
Figure 31. Run 3078 free stream conditions	54
Figure 32. Run 3079 free stream conditions	55
Figure 33. Run 3080 free stream conditions	56
Figure 34. Run 3081 free stream conditions	57
Figure 35. Run 3082 free stream conditions	58
Figure 36. Run 3083 free stream conditions	59
Figure 37. Run 3084 free stream conditions	60
Figure 38. Run 3085 free stream conditions	61
Figure 39. Run 3086 free stream conditions	62
Figure 40. Run 3087 free stream conditions	63
Figure 41. Sample time-histories of temperature, heat-flux and Stanton-number data from AEDC Tunnel 9 test of CEV model	64
Figure 42. Sample comparison of heating parameters along centerline vs. Reynolds number from AEDC Tunnel 9 test of CEV model	65
Figure 43. Heating distributions resulting from analyses in different one-dimensional coordinate systems	66
Figure 44. Chromel thermal properties	67
Figure 46. Stainless steel (17-4) thermal properties	67
Figure 47. Effects of material thermal properties on CEV experimental heating distribution in AEDC Tunnel 9	68
Figure 48. Effects of material thermal properties on MSL experimental heating distribution in AEDC Tunnel 9	68
Figure 49. Thermocouple Calibration Experiment Set-up	69
Figure 50. Effects of material thermal properties on CEV experimental heating distribution in LaRC 20-Inch Mach 6 Air Tunnel.....	70

Figure 51. Effects of material thermal properties on MSL experimental heating distribution in LaRC 20-Inch Mach 6 Air Tunnel.....	70
Figure 52. CEV grid (every 4 th point shown)	71
Figure 53. Predicted boundary-layer transition parameters at Mach 8	72
Figure 53. Predicted boundary-layer height parameters at Mach 8.....	73
Figure 54. Predicted surface heating and pressure at Mach 8.....	74
Figure 55. Predicted Stanton numbers at Mach 8.....	75
Figure 56. Laminar correlation parameter for predicted heating at Mach 8	76
Figure 58. Turbulent correlation parameter for predicted heating at Mach 8.....	77
Figure 59. Predicted boundary-layer transition parameters at Mach 10	78
Figure 59. Predicted boundary-layer height parameters at Mach 10.....	79
Figure 60. Predicted surface heating and pressure at Mach 10.....	80
Figure 61. Predicted Stanton numbers at Mach 10.....	81
Figure 62. Laminar correlation parameter for predicted heating at Mach 10	82
Figure 64. Turbulent correlation parameter for predicted heating at Mach 10.....	83
Figure 65. Reynolds numbers effects, Mach = 8, α = 24-deg	84
Figure 65. Reynolds numbers effects, Mach = 8, α = 28-deg	84
Figure 66. Reynolds numbers effects, Mach = 8, α = 32-deg	85
Figure 67. Reynolds numbers effects, Mach = 10, α = 0-deg	85
Figure 68. Reynolds numbers effects, Mach = 10, α = 8-deg	86
Figure 69. Reynolds numbers effects, Mach = 10, α = 12-deg	86
Figure 70. Reynolds numbers effects, Mach = 10, α = 16-deg	87
Figure 71. Reynolds numbers effects, Mach = 10, α = 20-deg	87
Figure 72. Reynolds numbers effects, Mach = 10, α = 24-deg	88
Figure 73. Reynolds numbers effects, Mach = 10, α = 28-deg	88
Figure 75. Reynolds numbers effects, Mach = 10, α = 32-deg	89
Figure 76. Turbulent heating correlation with Reynolds number, Mach = 8, α = 24-deg.....	90
Figure 76. Turbulent heating correlation with Reynolds number, Mach = 8, α = 28-deg.....	90
Figure 77. Turbulent heating correlation with Reynolds number, Mach = 8, α = 32-deg.....	90
Figure 78. Turbulent heating correlation with	91
Figure 79. Turbulent heating correlation with	91
Figure 80. Turbulent heating correlation with Reynolds number, Mach = 10, α = 28-deg.....	91
Figure 82. Turbulent heating correlation with Reynolds number, Mach = 10, α = 32-deg.....	91
Figure 83. Angle-of-attack effects, Run 3074, Mach = 8, $Re_\infty = 8 \times 10^6/\text{ft}$	92
Figure 83. Angle-of-attack effects, Run 3075, Mach = 8, $Re_\infty = 17 \times 10^6/\text{ft}$	92
Figure 84. Angle-of-attack effects, Run 3076, Mach = 8, $Re_\infty = 31 \times 10^6/\text{ft}$	93
Figure 85. Angle-of-attack effects, Run 3057, Mach = 10, $Re_\infty = 2 \times 10^6/\text{ft}$	93
Figure 86. Angle-of-attack effects, Run 3058, Mach = 10, $Re_\infty = 5 \times 10^6/\text{ft}$	94
Figure 87. Angle-of-attack effects, Run 3060, Mach = 10, $Re_\infty = 9 \times 10^6/\text{ft}$	94
Figure 88. Angle-of-attack effects, Run 3063, Mach = 10, $Re_\infty = 15 \times 10^6/\text{ft}$	95
Figure 89. Angle-of-attack effects, Run 3065, Mach = 10, $Re_\infty = 15 \times 10^6/\text{ft}$	95
Figure 90. Angle-of-attack effects, Run 3086, Mach = 10, $Re_\infty = 20 \times 10^6/\text{ft}$	96
Figure 91. Angle-of-attack effects, Run 3061, Mach = 10, $Re_\infty = 20 \times 10^6/\text{ft}$	96
Figure 92. Angle-of-attack effects, Run 3066, Mach = 10, $Re_\infty = 20 \times 10^6/\text{ft}$	97
Figure 94. Angle-of-attack effects, Run 3087, Mach = 10, $Re_\infty = 20 \times 10^6/\text{ft}$	97
Figure 94. Reynolds numbers effects, Mach = 8, α = 24-deg	98
Figure 95. Reynolds numbers effects, Mach = 8, α = 28-deg	99
Figure 96. Reynolds numbers effects, Mach = 8, α = 32-deg	100
Figure 97. Reynolds numbers effects, Mach = 10, α = 0-deg	101
Figure 98. Reynolds numbers effects, Mach = 10, α = 16-deg	102
Figure 99. Reynolds numbers effects, Mach = 10, α = 20-deg	103
Figure 100. Reynolds numbers effects, Mach = 10, α = 24-deg	104
Figure 101. Reynolds numbers effects, Mach = 10, α = 28-deg	105

[illegible]

Figure 154. Run 3086 data and comparison with predictions, Mach = 10, $Re_\infty = 14 \times 10^6/\text{ft}$, $\alpha = 16\text{-deg}$	135
Figure 155. Run 3086 data and comparison with predictions, Mach = 10, $Re_\infty = 14 \times 10^6/\text{ft}$, $\alpha = 20\text{-deg}$	135
Figure 156. Run 3086 data and comparison with predictions, Mach = 10, $Re_\infty = 14 \times 10^6/\text{ft}$, $\alpha = 24\text{-deg}$	135
Figure 157. Run 3086 data and comparison with predictions, Mach = 10, $Re_\infty = 14 \times 10^6/\text{ft}$, $\alpha = 28\text{-deg}$	135
Figure 158. Run 3061 data and comparison with predictions, Mach = 10, $Re_\infty = 20 \times 10^6/\text{ft}$, $\alpha = 20\text{-deg}$	136
Figure 159. Run 3061 data and comparison with predictions, Mach = 10, $Re_\infty = 20 \times 10^6/\text{ft}$, $\alpha = 24\text{-deg}$	136
Figure 160. Run 3061 data and comparison with predictions, Mach = 10, $Re_\infty = 20 \times 10^6/\text{ft}$, $\alpha = 28\text{-deg}$	136
Figure 161. Run 3061 data and comparison with predictions, Mach = 10, $Re_\infty = 20 \times 10^6/\text{ft}$, $\alpha = 32\text{-deg}$	136
Figure 162. Run 3062 data and comparison with predictions, Mach = 10, $Re_\infty = 20 \times 10^6/\text{ft}$, $\alpha = 28\text{-deg}$	137
Figure 163. Run 3066 data and comparison with predictions, Mach = 10, $Re_\infty = 21 \times 10^6/\text{ft}$, $\alpha = 20\text{-deg}$	138
Figure 164. Run 3066 data and comparison with predictions, Mach = 10, $Re_\infty = 21 \times 10^6/\text{ft}$, $\alpha = 24\text{-deg}$	138
Figure 165. Run 3066 data and comparison with predictions, Mach = 10, $Re_\infty = 21 \times 10^6/\text{ft}$, $\alpha = 28\text{-deg}$	138
Figure 166. Run 3066 data and comparison with predictions, Mach = 10, $Re_\infty = 21 \times 10^6/\text{ft}$, $\alpha = 32\text{-deg}$	138
Figure 167. Run 3067 data and comparison with predictions, Mach = 10, $Re_\infty = 21 \times 10^6/\text{ft}$, $\alpha = 28\text{-deg}$	139
Figure 168. Run 3087 data and comparison with predictions, Mach = 10, $Re_\infty = 20 \times 10^6/\text{ft}$, $\alpha = 16\text{-deg}$	140
Figure 169. Run 3087 data and comparison with predictions, Mach = 10, $Re_\infty = 20 \times 10^6/\text{ft}$, $\alpha = 20\text{-deg}$	140
Figure 170. Run 3087 data and comparison with predictions, Mach = 10, $Re_\infty = 20 \times 10^6/\text{ft}$, $\alpha = 24\text{-deg}$	140
Figure 171. Comparison of wake heating data with predictions, Mach = 8, $Re_\infty = 8 \times 10^6/\text{ft}$, $\alpha = 28\text{-deg}$	141
Figure 172. Comparison of wake heating data with predictions, Mach = 8, $Re_\infty = 17 \times 10^6/\text{ft}$, $\alpha = 28\text{-deg}$	141
Figure 173. Comparison of wake heating data with predictions, Mach = 8, $Re_\infty = 31 \times 10^6/\text{ft}$, $\alpha = 28\text{-deg}$	141
Figure 174. Comparison of wake heating data with predictions, Mach = 8, $Re_\infty = 48 \times 10^6/\text{ft}$, $\alpha = 28\text{-deg}$	141
Figure 175. Comparison of wake heating data with predictions, Mach = 10, $Re_\infty = 2 \times 10^6/\text{ft}$, $\alpha = 28\text{-deg}$	142
Figure 176. Comparison of wake heating data with predictions, Mach = 10, $Re_\infty = 5 \times 10^6/\text{ft}$, $\alpha = 28\text{-deg}$	142
Figure 177. Comparison of wake heating data with predictions, Mach = 10, $Re_\infty = 9 \times 10^6/\text{ft}$, $\alpha = 28\text{-deg}$	142
Figure 178. Comparison of wake heating data with predictions, Mach = 10, $Re_\infty = 15 \times 10^6/\text{ft}$, $\alpha = 28\text{-deg}$	142
Figure 179. Comparison of wake heating data with predictions, Mach = 10, $Re_\infty = 20 \times 10^6/\text{ft}$, $\alpha = 28\text{-deg}$	143
Figure 180. Data repeatability, $\alpha = 28\text{-deg}$, Mach = 8, $Re_\infty = 8 \times 10^6/\text{ft}$	144
Figure 181. Data repeatability, $\alpha = 28\text{-deg}$, Mach = 8, $Re_\infty = 17 \times 10^6/\text{ft}$	144
Figure 182. Data repeatability, $\alpha = 28\text{-deg}$, Mach = 8, $Re_\infty = 31 \times 10^6/\text{ft}$	145
Figure 183. Data repeatability, $\alpha = 0\text{-deg}$, Mach = 10, $Re_\infty = 5 \times 10^6/\text{ft}$	145
Figure 184. Data repeatability, $\alpha = 20\text{-deg}$, Mach = 10, $Re_\infty = 5 \times 10^6/\text{ft}$	146
Figure 185. Data repeatability, $\alpha = 28\text{-deg}$, Mach = 10, $Re_\infty = 5 \times 10^6/\text{ft}$	146
Figure 186. Data repeatability, $\alpha = 28\text{-deg}$, Mach = 10, $Re_\infty = 9 \times 10^6/\text{ft}$	147
Figure 187. Data repeatability, $\alpha = 20\text{-deg}$, Mach = 10, $Re_\infty = 15 \times 10^6/\text{ft}$	147
Figure 188. Data repeatability, $\alpha = 24\text{-deg}$, Mach = 10, $Re_\infty = 15 \times 10^6/\text{ft}$	148
Figure 189. Data repeatability, $\alpha = 28\text{-deg}$, Mach = 10, $Re_\infty = 15 \times 10^6/\text{ft}$	148
Figure 190. Data repeatability, $\alpha = 32\text{-deg}$, Mach = 10, $Re_\infty = 15 \times 10^6/\text{ft}$	149
Figure 191. Data repeatability, $\alpha = 20\text{-deg}$, Mach = 10, $Re_\infty = 20 \times 10^6/\text{ft}$	149
Figure 192. Data repeatability, $\alpha = 24\text{-deg}$, Mach = 10, $Re_\infty = 20 \times 10^6/\text{ft}$	150
Figure 193. Data repeatability, $\alpha = 28\text{-deg}$, Mach = 10, $Re_\infty = 20 \times 10^6/\text{ft}$	150
Figure 194. Data repeatability, $\alpha = 32\text{-deg}$, Mach = 10, $Re_\infty = 20 \times 10^6/\text{ft}$	151
Figure 195. Sample of plot for determination of transition onset location	152
Figure 196. Correlations for forebody leeward centerline transition onset location	153
Figure 197. Body points for heating correlations	154
Figure 198. Lee side shoulder heating augmentation ratio	155
Figure 199. Wind side shoulder heating augmentation ratio	155
Figure 200. Aftbody corner heating augmentation ratio	156
Figure 201. Lee side shoulder heating augmentation ratio with MSL data added	156
Figure 202. Wind side shoulder heating augmentation ratio with MSL data added	157

Abstract

An investigation of the aeroheating environment of the Project Orion Crew Entry Vehicle has been performed in the Arnold Engineering Development Center Tunnel 9. The goals of this test were to measure turbulent heating augmentation levels on the heat shield and to obtain high-fidelity heating data for assessment of computational fluid dynamics methods. Data were collected on a ~3.5% scale model (0.1778 m/7-inch diameter) of the vehicle using coaxial thermocouples in the Mach 8 and Mach 10 nozzles of Tunnel 9. Runs were performed at free stream Reynolds numbers of $1 \times 10^6/\text{ft}$ to $20 \times 10^6/\text{ft}$ in the Mach 10 nozzle and $8 \times 10^6/\text{ft}$ to $48 \times 10^6/\text{ft}$ in the Mach 8 nozzle. The test gas in Tunnel 9 is pure nitrogen, which at the tunnel operating conditions remains undissociated and may be modeled as a perfect gas. At these conditions, laminar, transitional, and turbulent flows were produced on the model at Mach 10, and transitional and turbulent flows were produced on the model at Mach 8. The majority of runs were made on a clean, smooth-surface model configuration and a limited number of runs were made in which inserts with varying boundary-layer trip configurations were used to force the onset of transition. Laminar and turbulent predictions were generated for all wind tunnel test conditions and comparisons were performed with the data for the purpose of helping to define uncertainty margins for the computational method. Data from both the wind tunnel test and the computational study are presented herein.

The experimental data showed that transition began on the lee side of the heat-shield at a free stream Reynolds number of $9 \times 10^6/\text{ft}$ in the Mach 10 nozzle and fully-developed turbulent flow was produced at $20 \times 10^6/\text{ft}$. In the Mach 8 nozzle, transition on the lee side of the heat-shield was observed for all test conditions, and fully-developed turbulent flow occurred at a free stream Reynolds number of $18 \times 10^6/\text{ft}$. On the aftbody of the vehicle no evidence of turbulence was detected at Mach 10 conditions, while at Mach 8 conditions, transition appeared to begin on the wind side of the aftbody at free stream Reynolds number of $18 \times 10^6/\text{ft}$ with fully-developed turbulent flow occurring only at the highest test condition of $48 \times 10^6/\text{ft}$. From the comparisons it was concluded that, for perfect-gas conditions, the computations for either fully-laminar or fully-turbulent cases matched the experimental data to within $\pm 10\%$. Correlations of transitional/turbulent heating augmentation over laminar levels were developed for several body-point locations from these data. These correlations can be employed to estimate heating augmentation at flight conditions, absent effects of ablation/blowing and chemistry.

Nomenclature

Symbols

c_p	material specific heat (J/kg-K)
D	vehicle maximum diameter (m or in.)

H_w	wall enthalpy (J/kg)
H_o	total enthalpy (J/kg)
H_∞	free stream enthalpy (J/kg)
k	roughness element height (m)
k_m	material thermal conductivity (W/m-K)
M_e	boundary layer edge Mach number
M_∞	free stream Mach number
n	penetration depth normal to right-cone surface (m)
p_w	pressure at model wall (Pa)
q_{300}	predicted heat transfer rate at 300 K wall temperature (W/m ²)
q	heat transfer rate (W/m ²)
T_w	wall temperature (K)
T_∞	free stream temperature (K)
t	time (sec)
R	vehicle maximum radius (m)
R_c	local radius of right-cone (m)
R_n	radius of vehicle nose (m)
R_s	radius of aftbody corner (m)
R_t	radius of heat-shield/aftbody tangency point (m)
Re_θ	Reynolds number based on boundary layer momentum thickness
Re_∞	free stream unit Reynolds number (1/m or 1/ft)
$Re_{\infty,D}$	free stream Reynolds number based on model diameter
St	Stanton number
$St \times (Re_{\infty,D})^{1/2}$	non-dimensional laminar heating correlation parameter
$St \times (Re_{\infty,D})^{1/5}$	non-dimensional turbulent heating correlation parameter
x, y, z	geometric coordinates (m)
$x/R, y/R, z/R$	normalized geometric coordinates
U_∞	free stream velocity (m/s)
α	angle of attack (deg)
δ	boundary layer thickness (m)
ΔH	difference between total and wall enthalpy (J/kg)
θ	boundary layer momentum thickness (m)
θ_c	half-angle of right-cone (deg)
ρ_m	material density (kg/m ³)
ρ_∞	free stream density (kg/m ³)

Subscripts

e	edge
m	material (of wind tunnel model)
w	wall
0	stagnation or total
∞	free stream

Abbreviations

AEDC	Arnold Engineering Development Center
AoA	angle of attack
CEV	Crew Exploration Vehicle

CFD	computational fluid dynamics
ISS	International Space Station
MSL	Mars Science Laboratory
NIST	National Institute of Standards and Technology
TPS	thermal protection system

Background and Introduction

The Project Orion Crew Exploration Vehicle (CEV) concept was defined by the NASA Exploration Systems Architecture Study (Ref. 1). This study was conducted in 2005 to define requirements for crew and cargo launch systems to support lunar and Mars exploration programs as well as access to the International Space Station (ISS). Several versions of the Orion CEV are planned that will provide transportation first to the ISS, then to the moon, and finally to Mars.

The Crew Module of the CEV (Figure 1) has a configuration that is externally similar to the Apollo Command Module - a spherical-segment heat shield joined by a small toroidal section to a truncated-cone shaped crew compartment. The Orion CEV however, will be considerably larger than Apollo with a maximum heat shield diameter of ~5 m (current configuration) vs. 3.912 m for Apollo. This larger size will allow transport of up to six crew members on International Space Station missions or up to 4 crew members on Lunar missions.

An investigation of the aeroheating environment of the CEV crew module has been performed in the Arnold Engineering Development Center (AEDC) Tunnel 9 facility. The primary goals of this study were to determine heating augmentation levels due to turbulent flow on the heat shield (which is the assumed environment for the design of the vehicle) and to obtain high-fidelity heat-transfer measurements on the heat shield in laminar and turbulent flow in order to assess the accuracy of computational fluid dynamics (CFD) predictions. Secondary goals were to assess the effects of boundary-layer trips on transition and turbulent heating augmentation and to obtain heating data on the aftbody crew module.

Experimental Method

Model Configuration and Instrumentation

A 0.03556-scale model (based on an assumed 5.00 m full-scale at the time of the model design) of the CEV crew module was used in this test. A drawing of the model is shown in Figure 2 (note that the current configuration has advanced beyond that shown in this figure) and the model is shown installed in Tunnel 9 in Figure 3. The model was fabricated from 15-5 precipitation-hardened stainless steel with an H1100 heat treatment. The model maximum diameter of 17.78 cm (7.00-in) was chosen for consistency with previous CEV tests (Refs. 2, 3) and to allow subsequent testing of this model in NASA Langley Research Center hypersonic wind tunnels. The model was designed to permit substitution of a removable insert piece on the lower half of the forebody heat-shield as shown in Figure 4. Inserts with varying forms of distributed and discrete roughness elements were fabricated to allow for investigation of roughness effects on transition and turbulent heating. In the current program, a very limited study of trip effects was conducted using inserts with discrete roughness elements of 0.007-in. nominal height and with distributed roughness elements of 0.001-in., 0.007-in., and 0.012-in. nominal heights.

The model was instrumented with 101 Type-E (chromel-constantan) coaxial thermocouples (installation shown in Figure 5 and Figure 6). The gages were press-fit through holes drilled into the model and then hand-worked to conform to the model surface and to form the required electrical junctions between the chromel and constantan elements of the thermocouple. Thermocouple instrumentation has long been used at Tunnel 9 as the primary

method for obtaining heat-transfer data (Ref. 4) The two dissimilar metals that comprise a thermocouple produce a small, but measurable, voltage when two junctions are formed between the materials. In the case of wind tunnel test instrumentation, one junction is at the surface of the model where it is exposed to heating, and the other is located externally and maintained at a controlled reference temperature. The voltage output of a thermocouple is related to temperature through a National Institute of Standards and Technology (NIST) calibration standard (Ref. 5). Temperature-time histories recorded using the thermocouples are processed through conduction analysis to determine heat-transfer rate time-histories.

A schematic of the thermocouple instrumentation layout is provided in Figure 7, and the gage locations are listed in Table 1. There were 82 gages located on the forebody heat-shield portion of the model and the remaining 19 gages were located on the aftbody crew compartment. Gages on the heat shield were arrayed vertically along the centerline (pitch-plane) of the model and horizontally across the lee side (top) of the model where the highest turbulent augmentation occurs. This gage layout was intended for a general assessment of heating distributions over the entire body, not for detailed investigation of specific areas. As such, the spatial resolution in the high-gradient regions of the heat-shield shoulder and on the aftbody immediately following the shoulder was considered to be insufficient for definitive comparisons with computational results.

Test Facility

The United States Air Force's Arnold Engineering Development Center Hypervelocity Tunnel 9 (Figure 8), located in Silver Spring, Maryland, is a hypersonic, nitrogen-gas, blow-down wind tunnel with interchangeable nozzles. These nozzles allow for testing at Mach numbers of 7, 8, 10, and 14 over a 0.054×10^6 to 48.4×10^6 per-ft (0.177×10^6 to 158.8×10^6 per-m) unit Reynolds number range. More detailed information on this facility can be found in Refs. 4 and 6 - 8.

A schematic of the facility is shown in Figure 9. The tunnel has a 5-ft (1.52 m)-diameter, 12-ft (3.66 m)-long test section that permits testing of large-scale model configurations. Tunnel 9 features a pitch system that can sweep models from -10 -deg to 50 -deg at pitch rates up to 80 deg/sec. With the tunnel's 0.2 sec to 15 sec run times, the dynamic pitch capability allows for a large volume of data to be captured over an entire range of pitch angles during a single run.

During a run, nitrogen in the vertical gas heater is compressed and heated to a desired pressure and temperature, where the maximum conditions are 27 kpsi (186 MPa) and 3040°F (1944 K). The nozzle and test cell are evacuated to a pressure of less than 0.02 psi (138 Pa) and are isolated from the high-pressure side by a pair of metal diaphragms upstream of the throat. When the desired conditions are reached in the heater, the diaphragms are burst and the high-pressure/high-temperature nitrogen expands through the nozzle into the test cell. During the run, the driver vessels use cold gaseous nitrogen to replace the hot gas in the heater to maintain constant supply conditions.

Run Matrix

A total of 31 runs were performed in this test series. These runs are listed in the test matrix in Table 2 in which nominal conditions for each run are given. The actual free stream conditions, which varied slightly over the length of a run, are listed in Figure 10 - Figure 40. In these figures, flow properties are both plotted and tabulated; the tabulated values represent either ~ 2 -deg increments for pitch-sweep runs or constant-time increments for static AoA runs. The majority of runs (23) were performed in the Mach 10 nozzle at nominal free stream Reynolds numbers of $2, 5, 9, 15$ and $20 \times 10^6/\text{ft}$, while the rest of the runs were performed in the Mach 8 nozzle at nominal free stream Reynolds numbers of $8, 17, 31$, and $48 \times 10^6/\text{ft}$. During the planning stages of this test, the nominal trim angle-of-attack of the CEV was expected to be 28 -deg (152 -deg in the formal CEV coordinate system, which is rotated 180 -

deg from that of the wind tunnel model coordinate system). To allow for deviations during flight or design changes that affect the nominal pitch attitude, pitch sweep runs of 20-deg to 32-deg and static 28-deg runs were performed in the Mach 10 nozzle and pitch sweep runs of 24-deg to 32-deg were made in the Mach 8 nozzle (the smaller increments were due to shorter test times). A few runs were also performed at 0-deg angle-of-attack as a symmetry check and with pitch sweeps of 16-deg to 30-deg to obtain lower AoA data after the possibility of flight at a lower trim angle began to be considered by the Orion program. During several of the fixed $\alpha = 28$ -deg runs, interchangeable insert pieces with discrete and distributed roughness elements of various sizes were employed to promote boundary layer transition.

Data Reduction Method

The coaxial thermocouples with which the CEV model were instrumented produced voltage-time history data that were converted to temperature-time history data via gage calibration standards. These data were acquired at a frequency of 500 Hz and analog-filtered at 30 Hz to eliminate 60 Hz analog noise. From these data, a conduction analysis of the temperature distribution within the substrate of the model was then performed to determine the time-history of the external, convective heating experienced by the wind tunnel model.

The conduction analysis may be performed through either an analytical technique in which the temperature data is numerically integrated with the assumption of conduction into a semi-infinite slab, or through a finite-volume technique in which the heat-conduction equation is solved numerically with the thermocouple temperature data as a boundary condition. In both cases, a one-dimensional conduction (in-depth only) assumption is made; multi-dimensional numerical solutions of the heat conduction problem are possible but are usually not practical for wind tunnel problems. Both methods have been documented extensively (e.g. Refs. 9-11). For this test program, the finite-volume reduction method was employed through two codes: QCALC (Ref. 10) and 1DHEAT (Ref. 11).

Both of these techniques produce a time-history of the dimensional heat transfer rate to each gage on the model. However, because the free stream conditions in Tunnel 9 vary over the course of the run, and because the rise in model surface temperature can be non-negligible with respect to the stagnation temperature (which drives the convective heating), the heat transfer rates were not constant and thus heat transfer was not the best parameter with which to report the test data. These data can better be represented in terms of the Stanton number, which is defined for this study as:

$$St = \frac{q}{\rho_{\infty} U_{\infty} \Delta H} \quad (1)$$

where

$$\Delta H = (H_0 - H_w) = \left(c_p T_{\infty} + \frac{U_{\infty}^2}{2} \right) - c_p T_w \quad (2)$$

This non-dimensional quantity is very nearly a constant over the course of the run (if the angle of attack is held fixed) as the ΔH and q terms both decrease with increasing wall temperature. The use of the non-dimensional Stanton number instead of a dimensional heating rate removes the need to specify a complete temperature distribution boundary condition when performing computations for the wind tunnel conditions – instead a uniform temperature representative of that on the model at a given time during the run can be specified. A sample comparison between the Stanton number and the dimensional heat-flux is given in Figure 41. It should be noted that the Stanton number is sometimes defined using edge conditions instead of free stream conditions for the density and velocity and/or the adiabatic wall enthalpy instead of the total enthalpy.

In order to correlate the data over the wide range of test conditions, two additional heating parameters, $St \times (Re_{\infty,D})^{1/2}$ and $St \times (Re_{\infty,D})^{1/5}$ were also computed. The test data will be presented in this report in terms of these parameters. The first quantity, $St \times (Re_{\infty,D})^{1/2}$ is a laminar heating correlation parameter defined by:

$$St \times (Re_{\infty,D})^{(1/2)} = \frac{q}{\rho_{\infty} U_{\infty} \Delta H} \times \left(\frac{\rho_{\infty} U_{\infty} D}{\mu_{\infty}} \right)^{(1/2)} \quad (3)$$

It can be shown from compressible, flat-plate boundary-layer theory (e.g. Ref. 12) that this parameter is a weakly varying function of M_{∞} and the temperature ratio T_w/T_e for laminar flow. Even for a non-similar flow such as that over the CEV model, this parameter remains nearly constant at given location on the body for constant Mach number and angle-of-attack as the free stream Reynolds number is varied. Thus, it can serve as a check on the quality of laminar data over a wide range of test conditions. Additionally, by plotting data from different test conditions together in terms of this parameter, non-laminar behavior, i.e. transition onset and turbulent growth, can be identified from for each Mach- α condition. A sample comparison of CEV centerline data plotted in terms of St and $St \times (Re_{\infty,D})^{1/2}$ is given in Figure 42.

For turbulent flow, an analogous parameter is $St \times (Re_{\infty,D})^{1/5}$ which remains nearly constant at a given body point with varying Reynolds number. This parameter is defined as

$$St \times (Re_{\infty,D})^{(1/5)} = \frac{q}{\rho_{\infty} U_{\infty} \Delta H} \times \left(\frac{\rho_{\infty} U_{\infty} D}{\mu_{\infty}} \right)^{(1/5)} \quad (4)$$

By plotting data from different test conditions in terms of this parameter, the point at which the boundary-layer becomes fully-turbulent can be estimated.

The data reduction process produced a complete time-history of the heat-flux and dimensionless heating parameters (as defined in Eqs. 1, 3 and 4) over the duration of each run. For static AoA cases, these data were then time-averaged over the high flow quality test-time period of each run. For runs in which the model was pitched through an AoA range, the data were time-averaged over periods corresponding to ± 0.5 -deg from each integer value of α (e.g. 28-deg ± 0.5 -deg).

Coordinate Systems for One-Dimensional Data Reduction

The one-dimensional finite-volume data reduction methodology employed in the QCALC and 1DHEAT codes is typically expressed in a Cartesian coordinate system in which the governing equation for heat conduction is given by:

$$(\rho c_p)_m \frac{\partial T}{\partial t} = \frac{\partial}{\partial x} \left(k_m \frac{\partial T}{\partial x} \right) \quad (5)$$

However, the heat conduction equation can also be formulated and solved in other coordinate systems, such as cylindrical, spherical, or right-cone. With respect to the CEV geometry, it is more physically appropriate to express the problem at the heat-shield shoulder in cylindrical coordinates (because of the small radial thickness of the wall with respect to the radius) as:

$$(\rho c_p)_m \frac{\partial T}{\partial t} = \frac{\partial}{\partial r} \left(r k_m \frac{\partial T}{\partial r} \right) = \frac{\partial}{\partial r} \left(k_m \frac{\partial T}{\partial r} \right) + \frac{k_m}{r} \frac{\partial T}{\partial r} \quad (6)$$

Similarly, the heat conduction problem over the spherical cap of the heat shield can be expressed more accurately in terms of spherical coordinates as:

$$\left(\rho c_p\right)_m \frac{\partial T}{\partial t} = \frac{1}{r^2 \sin \theta} \frac{\partial}{\partial r} \left(r^2 \sin \theta k_m \frac{\partial T}{\partial r} \right) = \frac{\partial}{\partial r} \left(k_m \frac{\partial T}{\partial r} \right) + \frac{2k_m}{r} \frac{\partial T}{\partial r} \quad (7)$$

And finally, the aftbody crew module is represented by a right-cone coordinate system (where θ_c and R_c are the cone half-angle and the local radius):

$$\left(\rho c_p\right)_m \frac{\partial T}{\partial t} = \frac{1}{R_c - n \cos \theta_c} \frac{\partial}{\partial r} \left[(R_c - n \cos \theta_c) k_m \frac{\partial T}{\partial r} \right] = \frac{\partial}{\partial r} \left(k_m \frac{\partial T}{\partial r} \right) + k_m \left(\frac{\cos \theta_c}{R_c - n \cos \theta_c} \right) \frac{\partial T}{\partial r} \quad (8)$$

These different coordinate systems are all subsets of the generalized one-dimensional formulation for orthogonal coordinates given by:

$$\left(\rho c_p\right)_m \frac{\partial T}{\partial t} = \left(\frac{1}{h_1} \right)^2 \left[\frac{\partial}{\partial x^1} \left(k_m \frac{\partial T}{\partial x^1} \right) + k_m \left(-\frac{1}{h_1} \frac{\partial h_1}{\partial x^1} + \frac{1}{h_2} \frac{\partial h_2}{\partial x^1} + \frac{1}{h_3} \frac{\partial h_3}{\partial x^1} \right) \frac{\partial T}{\partial x^1} \right] = \left(\frac{1}{h_1} \right)^2 \left[\frac{\partial}{\partial x^1} \left(k_m \frac{\partial T}{\partial x^1} \right) + k_m \beta \frac{\partial T}{\partial x^1} \right] \quad (9)$$

where :

	Cartesian	Cylindrical	Spherical	Right - Cone
x^1	x	r	r	n
h_1	1	1	1	1
h_2	1	r	r	$R_c - n \cdot \cos(\theta_c)$
h_3	1	1	$r \cdot \sin(\phi)$	1
$\frac{\partial h_1}{\partial x^1}$	0	0	0	0
$\frac{\partial h_2}{\partial x^1}$	0	1	1	$-\cos(\theta_c)$
$\frac{\partial h_3}{\partial x^1}$	0	0	$\sin(\phi)$	0
$\beta = -\frac{1}{h_1} \frac{\partial h_1}{\partial x^1} + \frac{1}{h_2} \frac{\partial h_2}{\partial x^1} + \frac{1}{h_3} \frac{\partial h_3}{\partial x^1}$	0	$\frac{1}{r}$	$\frac{2}{r}$	$\frac{-\cos(\theta_c)}{R_c - n \cdot \cos(\theta_c)}$

The option to reduce data in any of these coordinate systems is detailed in the QCALC manual (Ref. 10), while the 1DHEAT code has been upgraded to utilize any of these coordinate systems.

An example of the differences in computed heating distributions obtained by using the geometrically-correct coordinate systems as compared to using a Cartesian system is shown in Figure 43 for the heat shield of the CEV model. Over most of the heat shield, the spherical coordinate system analysis resulted in levels no more than 1% lower than those of the Cartesian system. This difference was small because the thickness of the model wall (and thus the change in computational element size through that thickness) is very small with respect to the heat shield

radius (~7% of the radius) and therefore the effect of the coordinate system was almost negligible. In contrast, the thickness of the model wall at the heat shield shoulder is ~70% of the shoulder radius, and thus the curvature in the coordinate system resulted in the cylindrical analysis producing heating rates ~10% lower than those of the Cartesian system. It could thus be concluded that from a purely geometric perspective, the cylindrical coordinate system was most appropriate for those gages located on the shoulder of the heat shield. However, there is another factor to consider at the shoulder – the assumption of one-dimensional heat conduction through the model surface is not correct. There was a very large difference between the external convective heating distributions on the heat-shield and aftbody of the CEV which produced a strong heating gradient around the shoulder of the vehicle and multi-dimensional conduction within the model. Based on an analysis presented in Ref. 10 for multi-dimensional conduction effects, it was estimated that the one-dimensional conduction analysis produced heating rates that were approximately 10% higher than the correct values.

It is somewhat coincidental that the two errors present in the one-dimensional, Cartesian analysis for the shoulder gages were of approximately the same magnitude, but of opposing signs, and so produced a more accurate result than a one-dimensional cylindrical analysis. However, it was found to be more convenient from the data reduction perspective to take advantage of these offsetting errors and reduce the shoulder gage data in the Cartesian coordinate system rather than to use a cylindrical coordinate. Results elsewhere on the heat shield are based on the geometrically-appropriate coordinate system (spherical on the heat shield and conical on the crew module), although, as noted, the differences from the Cartesian system were very small.

With respect to these shoulder gages, it should also be noted that the instrumentation spacing near the shoulder was very sparse (a single gage at each shoulder in the pitch plane), and therefore was not sufficient to accurately measure the very sharp heating gradient that occurred in this region. Therefore, the data presented in this report should not be taken as definitive with respect to the shoulder heating environment. The sparseness of sensors in this region is also the reason that a multi-dimensional conduction analysis, which is theoretically fairly simple, was not performed for the shoulder gages. Without a better resolution of the external temperature/heating gradient at the shoulder, such an analysis would likely have a high level of uncertainty.

Wind Tunnel Model Material Thermal Properties

The data reduction methods discussed in the previous sections require specification of the thermal properties of the wind tunnel model in order to determine heat transfer rates from the temperature-time history. Thermal property data can be obtained from several sources (e.g. as cited in Refs. 10-11), however the accuracy of these data is hard to assess.

Prior to this test, the standard set of properties employed at AEDC Tunnel 9 in the QCALC code for thermocouple data reduction were based on curve fits for chromel, as given by Eqs. 10-12. These curve fits differ slightly from those used in the 1DHEAT code for chromel, as given by Eqs.13-15. The thermal conductivity and specific heat fits from each equation set are plotted in Figure 44.

QCALC Chromel properties:

$$(\rho)_m = 8719.2 \left(\frac{kg}{m^3} \right) \quad (10)$$

$$(c_p)_m = 369.87 + 0.25653 \times T \left(\frac{J}{kg - K} \right) \quad (11)$$

$$(k)_m = 14.27 + 1.0985 \times 10^{-2} T + 6.4196 \times 10^{-6} T^2 \left(\frac{W}{m - K} \right) \quad (12)$$

1DHEAT Chromel properties:

$$(\rho)_m = 8714 \left(\frac{kg}{m^3} \right) \quad (13)$$

$$(c_p)_m = 386.25 + 0.2398 \times T \left(\frac{J}{kg-K} \right) \quad (14)$$

$$(k)_m = 11.845 + 1.9132 \times 10^{-2} T \left(\frac{W}{m-K} \right) \quad (15)$$

The default use of chromel properties at AEDC Tunnel 9 was based on the assumptions that since Type-E thermocouples are composed primarily of this material, chromel thermal properties should dictate the conduction process and that differences in material properties between a thermocouple and the surrounding model material (15-4 stainless steel in this case) could be neglected. However, opportunities for validation of these properties have been limited, and the current test program highlighted significant differences in comparisons of CFD predictions to the tunnel data.

Preliminary comparisons of the data obtained in this test program with CFD results revealed that the predictions were consistently lower than the data, sometimes by up to 20%. Such results were clearly outside the expected bounds of CFD reliability (a comparison to within $\pm 10\%$ for a steady, attached, laminar, perfect-gas flow is a reasonable expectation), which cast doubt on the experimental results.

After thorough investigation and elimination of many possible sources of bias and uncertainty (both experimental and computational) it was noted that the use of different material property data in the conduction analysis had a first-order effect on the resultant heat transfer rates, and furthermore, that the available material property data were not well documented and often differed between sources. To investigate the effects of material properties on the data reduction process, the test data were reduced using the property data for chromel and constantan (the two materials that comprise the thermocouple) and for both 15-5 stainless steel (from which the model was fabricated) and 17-4 stainless steel (which is very similar to 15-5 stainless steel). The best match between predictions and the experimental data was found when 17-4 stainless steel thermal properties were employed. Curve fits for 17-4 stainless steel used by in QCALC are given in Eqs. 16-18 and curve fits used in 1DHEAT are given in Eqs. 19-21 and are plotted in Figure 45.

QCALC 17-4 stainless steel properties:

$$(\rho)_m = 7805.7 \left(\frac{kg}{m^3} \right) \quad (16)$$

$$(c_p)_m = 409.76 - 5.3809 \times 10^{-2} T + 6.0366 \times 10^{-4} \left(\frac{J}{kg-K} \right) \quad (17)$$

$$(k)_m = 11.665 + 1.52078 \times 10^{-2} T \left(\frac{W}{m-K} \right) \quad (18)$$

1DHEAT 17-4 stainless steel properties:

$$(\rho)_m = 7800 \left(\frac{kg}{m^3} \right) \quad (19)$$

$$(c_p)_m = 460 \left(\frac{J}{kg-K} \right) \quad (20)$$

$$(k)_m = 11.63 + 1.4816 \times 10^{-2} T \left(\frac{W}{m-K} \right) \quad (21)$$

An example of the difference in heating distributions computed when chromel or 17-4 stainless steel properties were used is shown in Figure 46. Although the material thermal property curves vary considerably (and non-linearly) with respect to each other across the range of temperatures shown, for the current test program the range of temperatures was relatively small (300 K – 400 K), and the resulting spread in the predicted heating rates using the various material property curves was on the order of 10%

Comparisons of the heating rates based on the different thermal property curve fits with predictions were made for all tunnel conditions. As shown in Figure 46, it was found that the AEDC 17-4 stainless steel fits produced the most consistent match - generally within 10% or less – with predicted heating distributions (consistent results were obtained for all test conditions, as will be shown subsequently). This finding was supported by additional test data from a similar test program. Immediately prior to this CEV test in AEDC Tunnel 9, a test (Ref. 13) of a similarly-constructed, thermocouple-instrumented model of the Mars Science Laboratory (MSL) entry vehicle was conducted over the same range test conditions in Tunnel 9. As shown in Figure 47, the different thermal property curve fits used in the data reduction process again produced a spread of about 10% in the heating rates, and use of the 17-4 stainless steel properties produced the best match with the predictions. This result provided some confidence that there was not a problem unique to the model configuration or fabrications process with this CEV test.

These two independent wind tunnel tests provided supportive, if not conclusive, evidence that the observed results were neither configuration-dependent (MSL vs. CEV geometries) nor due to any flaw in the construction and/or instrumentation of the wind tunnel models. And in both tests, the best agreement was found when the AEDC-QCALC thermal properties for 17-4 stainless steel were used in the data reduction. However, the purpose of these studies was to obtain experimental data to validate computational methods, not the opposite. Therefore this agreement alone was not sufficient justification to employ these thermal properties curve fits. In order to provide independent experimental validation, two additional tests were conducted.

First, thermocouples were installed into plugs fabricated from 15-5 stainless steel (the material from which the CEV model was constructed) and chromel (the primary material of a Type-E thermocouple) that were set into a calibration plate adjacent to NIST-traceable heat-flux calorimeters and then bench-tested (Ref. 14) under a calibrated radiant lamp bank (as shown in Figure 48). The assembly was painted flat black (to maximize radiative heat absorption) and exposed to heating levels from 1 W/cm² to 13 W/cm² – for comparison, the maximum laminar heating levels produced in the wind tunnel test were in the 10 to 20 W/cm² range. The thermocouple data were then reduced using the QCALC procedure with thermal property data for both chromel, 15-5 stainless steel, and 17-4 stainless steel. The reduced data provided the closest agreement with the calibrated source when the AEDC-QCALC 17-4 stainless steel properties were used: as shown by the values in Table 3, the reduced data were ~15% higher than the standard when chromel properties were used; ~10% higher when 15-5 properties were used; and ~3% higher when 17-4 properties were used. This result suggests several possible hypotheses:

1) That the response of the thermocouple cannot be treated independently from the material surrounding it, but rather conduction between the two materials equilibrates their behavior to that of the larger surrounding thermal

mass. Note that such behavior could be much different when testing in a micro- or millisecond impulse facility in which such equilibration may not have time to occur. Since the bulk of the wind tunnel model is stainless steel, its properties dominate the conduction process. Although in this case, it would be expected that the agreement would be better when 15-5 properties were used than when 17-4 properties were used.

2) That the thermal properties data available for the chromel in the thermocouple are simply wrong, and that the correct thermal properties for the gages are coincidentally closer to those of the AEDC-QCALC 17-4 stainless steel properties.

3) That some unknown influence in the installation of the thermocouples into the wind tunnel model is affecting their performance, e.g. formation of the thermocouple junction, electrical interference, conduction losses to the lead wires, etc.

The second independent check was to test both the CEV and MSL wind tunnel models (which were designed for AEDC Tunnel 9) in the LaRC 20-Inch Mach 6 Air Tunnel (Ref. 15) in order to eliminate any possible concerns about facility-specific problems such as flow quality, blockage, data reduction methods, instrumentation installation and calibration, etc. As shown in Figure 49 - Figure 50 for two sample cases, the experimental data and predictions again matched best when 17-4 stainless steel thermal properties were used in the data reduction process.

At this point, the issue of material properties is not closed, but for the purposes of this test, it will be assumed that the use of the AEDC-QCALC 17-4 stainless steel properties represent the best practice for reduction of the thermocouple data. However, AEDC has initiated a more detailed investigation into the question of material thermal properties, as discussed in Ref. 14, but this work has not yet been completed. The use of 17-4 thermal properties is supported by the bench calibration testing and by comparisons with computational predictions for two different models (CEV and MSL) in two different wind tunnels (AEDC Tunnel 9 and LaRC 20-Inch Mach 6 Air Tunnel). Therefore all data reported hereafter are based on these properties. Furthermore, because the bench-test evaluation of thermocouple performance against calibrated standards showed a consistent bias of ~3% over the standards, the CEV data presented in this report have been post-processed to remove that bias; i.e. all data were multiplied by a factor of $1.00/1.03 = 0.971$.

Experimental Uncertainty

Given the unresolved issue of the material thermal properties effects on the conduction analyses used to determine heat transfer rates, it was not possible to perform a rigorous error analysis at this time. AEDC quotes heating uncertainties of $\pm 6\%$ based on their own internal studies; however, those values were generated before the current issues with material thermal properties were discovered, and thus are likely to be too low. Given the large differences in heating rates that were generated using different thermal properties in the conduction analysis, it is recommended that the quoted AEDC uncertainty value be increased to $\pm 10\%$ until more definitive material properties analyses can be conducted. Additionally, because of the sparseness of gages in the shoulder region and because of the recognized deficiencies in using a one-dimensional methodology there, it is recommended that the uncertainty at and near the shoulder be doubled to $\pm 20\%$.

Computational Methods and Results

Flow field computations at the wind tunnel test conditions were performed using LAURA (Refs. 16 - 17). The LAURA (Langley Aerothermodynamic Upwind Relaxation Algorithm) code is a three-dimensional, finite-volume solver that includes perfect-gas, equilibrium, and non-equilibrium chemistry models. The code can be used to solve the inviscid, viscous thin-layer Navier-Stokes, or full Navier-Stokes equations; in the current study the thin-layer model was employed. Time integration to steady-state in LAURA is accomplished through a combination of line-

relaxation and point-relaxation schemes. Roe-averaging (Ref. 18) with Harten's entropy fix (Ref. 19) and Yee's Symmetric Total Variation Diminishing limiter (Ref. 20) is used for inviscid fluxes, and a second-order scheme is employed for viscous fluxes. In this study, a perfect-gas model was used with the appropriate gas parameters for nitrogen. Application of the LAURA code to the test conditions generally follows that detailed in Ref. 21. However, only the perfect-gas simulation option was necessary for AEDC Tunnel 9 conditions, and for forebody-only computations, the thin-layer equation set was employed instead of the full Navier-Stokes equations.

A structured, finite-volume, multiple-block grid (Figure 51) with a singularity-free nose was employed for the computations. The grid was comprised of 3.8 million points divided into 10 forebody heat-shield blocks and 28 aftbody/sting/wake blocks. Grid adaptation was performed (as per the method detailed in Ref. 17) to align the grid with the bow shock and to produce nominal wall cell Reynolds numbers on the order of 1. This grid was originally developed for CEV flight cases as per Ref. 21 and was then scaled to the correct wind tunnel model size.

Computations were performed for selected tunnel cases. Free stream conditions were taken from the tunnel data for one run at each of the nominal Reynolds number conditions in the Mach 8 ($Re_\infty = 8, 17, 31, \text{ and } 48 \times 10^6/\text{ft}$) and Mach 10 ($Re_\infty = 2, 5, 9, 15, \text{ and } 20 \times 10^6/\text{ft}$) nozzles, with the assumption that run-to-run variations would have minimal effects on the computed non-dimensional heating levels. For static AoA runs, the conditions were selected from the middle of the test period, and for pitch-sweep runs, conditions were selected at 4-deg intervals. In both cases, a uniform surface temperature over the body equal to that recorded at the nose at the specified time during the run was used. For some cases, especially at higher Reynolds numbers where much of the forebody became turbulent and higher heating rates were experienced, the surface temperature distribution was very non-uniform and the constant wall temperature boundary condition did not produce accurate results for dimensional heating rates. For this reason, comparisons with Tunnel 9 data should always be made in terms of the non-dimensional heating parameters as given in Eqs. 1, 3, or 4.

Because of the sparseness of gages on the aftbody of the model and the higher computational overhead for full-body computations, solutions with the wake and sting were performed only for a small subset of the tunnel conditions (all $\alpha = 28$ -deg cases), while forebody-only computations were performed for all of the cases. Laminar computations were performed for all Mach 8 and Mach 10 conditions and for the Mach 10 conditions. Turbulent computations were also performed for Mach 10 cases with Reynolds numbers of $9 \times 10^6/\text{ft}$ and higher, while turbulent computations were performed for all Mach 8 cases. The turbulent computations were performed using the algebraic Cebeci-Smith turbulence model (the algebraic Baldwin-Lomax model was also used for a few selected cases and was found to produce only slightly different results for these perfect-gas conditions). While it is recognized that more complex turbulent models exist, different models can produce very different results (e.g. Ref. 22) and the validation status of any and all turbulence models for hypersonic flow is both debatable and configuration-specific. Algebraic models were employed in this study because they are computationally fast and stable, and as will be shown subsequently, the accuracy of algebraic model turbulent predictions on the forebody was generally as good as that of the laminar predictions at least for the conditions under consideration.

Results from the computations are shown in Figure 52 - Figure 57 for the Mach 8 cases and Figure 58 - Figure 63 for the Mach 10 cases. In these figures, forebody centerline values are plotted for the boundary-layer quantities Re_θ , Re_θ/M_e , δ , θ , the dimensional pressure, p , the dimensional heating at a uniform 300 K wall temperature, q_{300} , the non-dimensional Stanton number, St , and the non-dimensional heating correlation parameters $St \times (Re_{\infty,D})^{1/2}$ and $St \times (Re_{\infty,D})^{1/5}$ for laminar and turbulent flow, respectively. In subsequent sections, these values will be used in correlations of the heating data and in comparisons with experimental values

Results, Analysis, and Comparisons

Reynolds Number Trends

Reynolds number effects on centerline heating distributions are presented in terms of the laminar non-dimensional parameter $St \times (Re_{\infty D})^{1/2}$ in Figure 64 - Figure 74. Forebody (heat-shield) and aftbody (crew compartment) data are presented on separate plots since the aftbody heating levels were approximately an order of magnitude lower than those on the forebody. These data are organized by Mach number and angle-of-attack and, where available, repeat-run data for a given condition are shown.

For the Mach 8 cases the forebody lee side flow appeared to be transitional (at $Re_{\infty} = 8 \times 10^6/\text{ft}$) or turbulent (for $Re_{\infty} \geq 17 \times 10^6/\text{ft}$) for all angles of attack; laminar around the forebody stagnation region for most Mach 8 conditions; and transitional/turbulent on the forebody wind side between the stagnation point and the shoulder for most cases. At Mach 10, forebody lee side transition was first noticeable at $Re_{\infty} = 9 \times 10^6/\text{ft}$, and the forebody lee side boundary layer became fully-turbulent by $Re_{\infty} = 20 \times 10^6/\text{ft}$. The forebody wind side appeared to remain laminar up until $Re_{\infty} = 20 \times 10^6/\text{ft}$ at the shoulder, but, because of the sparseness of gages and the difficulties in accurately measuring heating at this location, it was not possible to reach a definitive conclusion. Another point to note in these plots is a small region of elevated heating in the stagnation region which appeared to increase with Reynolds number. This phenomena will be discussed in more depth in later sections.

With respect to the aftbody heating environment, conclusions were more difficult to make because of the small number of gages and the very low heating rates that were measured. However, based on these figures, it would appear that, at least for the Mach 10 conditions, both the lee side and wind side of the aftbody remained laminar at all Reynolds numbers and angles-of-attack. For the Mach 8 conditions, the non-dimensional heating levels on the wind side of the aftbody increased with Reynolds number for $Re_{\infty} \geq 31 \times 10^6/\text{ft}$, which was an indication of transitional/turbulent behavior.

For turbulent flow, an analogous parameter to the laminar parameter $St \times (Re_{\infty D})^{1/2}$ is $St \times (Re_{\infty D})^{1/5}$, which remains nearly constant at a given body point with varying Reynolds number. The forebody data were re-computed in terms of this parameter and these distribution are plotted in Figure 75 - Figure 81. From these plots, it can be seen that significant regions of fully-developed turbulent flow were generated on the forebody lee side (and in some cases wind side) for $Re_{\infty} \geq 17 \times 10^6/\text{ft}$ at Mach 8 and for $Re_{\infty} \geq 15 \times 10^6/\text{ft}$ at Mach 10.

Angle-of-Attack Trends

Angle-of-attack effects on the centerline heating distribution are shown in Figure 82 - Figure 93. Forebody and aftbody data are again presented on separate plots since the aftbody heating levels were approximately an order of magnitude lower than those on the forebody. These data were obtained during the continuous pitch sweep runs with included angle-of-attack ranges of 8-deg to 32-deg depending on the run duration for each condition. Two phenomena are noteworthy in the figures. The first is an upstream movement (toward the stagnation point) of the forebody lee side transition onset location with increasing angle of attack (most noticeable in Figure 91 or Figure 93). The second is the off-setting effects of increasing angle-of-attack on the forebody lee side heating levels. Increasing angles-of-attack caused a decrease in laminar heating levels, but also acted to promote transition earlier which then caused a heating increase. As an example, contrast the monotonically decreasing forebody lee side heating distributions at the laminar Mach 10, $Re_{\infty} = 5 \times 10^6/\text{ft}$ condition (Run 3058 in Figure 86) with the nearly constant levels at the transitional/turbulent Mach 10, $Re_{\infty} = 20 \times 10^6/\text{ft}$ condition (Run 3061 in Figure 92).

Off-Centerline Data

In this report, the off-centerline data will not be discussed in depth because the highest heating levels were generated along the centerline when the vehicle was at zero-deg of yaw which was the only condition tested. However, these data are presented in a graphical format in Figure 94 - Figure 102. In each figure, a view of the forebody is presented with a colored symbol that represents the heating level at each gage location. These figures are organized by Mach number and angle-of-attack in order to show the effects of increasing free stream Reynolds number over the whole forebody. At the higher Reynolds numbers, the images can be examined to estimate the spread of transitional/turbulent flow over the forebody of the CEV model.

Boundary-Layer Trip Effects

As noted previously, the wind tunnel model was designed with a removable section between the nose and stagnation point location (for a 28-deg angle-of-attack) into which inserts with various patterns of discrete or distributed roughness could be placed (see Figure 4). Several Mach 10, $\alpha = 28$ -deg runs were performed with these roughness elements in place (see the test matrix in Table 2) as a preliminary study on the effects of these trips on the heating levels. However, this brief study was not in any way intended to provide definitive data on transition onset criteria or heating augmentation in the presence of roughness.

The data from these runs are presented in Figure 103 - Figure 105. At each of the three Reynolds numbers in which trips were employed, turbulent flow was produced – either by forced transition due to the trips at the two lower Reynolds numbers, or naturally at the highest Reynolds number of $Re_\infty = 20 \times 10^6/\text{ft}$. At least in this small data set, it appeared that the turbulent heating levels produced on the forebody downstream from the transition point by the trips reached the same levels regardless of the trip height or configuration and that these levels were the same as those produced by naturally-developing turbulent flow. Furthermore, the aftbody heating levels appeared to be unaffected by the presence of forebody trips, which indicated that even though these trips did produce turbulent forebody flow, the boundary-layer re-laminarized as it was accelerated around the heat-shield shoulder onto the aftbody of the model.

Comparison of Forebody Experimental Data with Predictions

Comparisons of the experimental data with computational predictions for the forebody of the CEV model are shown in Figure 106 - Figure 170. These data are organized by run number, with runs ordered in terms of increasing Reynolds numbers, first for the Mach 8 cases, then for the Mach 10 cases. For continuous pitch-sweep runs, comparisons are shown for 4-deg α -increments. In each figure, a $\pm 10\%$ error-bar based on the previously discussed approximate uncertainty analysis is shown.

Comments will be made first on the individual run comparisons, to be followed by general observations on the comparisons:

Mach 8 Comparisons

Run 3070, $\alpha = 28$ deg, $Re_\infty = 8 \times 10^6/\text{ft}$ (Figure 106): data on the lee side of the stagnation point were transitional and approached fully-turbulent level at the shoulder; data on the wind side of the stagnation point appeared to be laminar; laminar predictions were $\sim 15\%$ lower than the laminar data; turbulent predictions were $\sim 5\%$ higher than the data.

Run 3074, $\alpha = 24$ -28 deg, $Re_\infty = 8 \times 10^6/\text{ft}$ (Figure 107 - Figure 109): data on the lee side of the stagnation point were transitional but did not appear to reach fully-turbulent levels; data on the wind side of the stagnation point

appeared to be laminar; laminar predictions were ~12% lower than the laminar data; turbulent predictions exceeded the measured transitional lee side data.

Run 3071, $\alpha = 28$ deg, $Re_\infty = 17 \times 10^6/\text{ft}$ (Figure 110): transition occurred on the lee side shortly downstream of the stagnation point and the data reached fully-turbulent levels further downstream; data windward of the stagnation point appeared to be laminar/transitional; laminar predictions were ~15% lower than the stagnation region data; turbulent predictions were ~2.5% higher than the lee side data.

Run 3075, $\alpha = 24\text{-}32$ deg, $Re_\infty = 17 \times 10^6/\text{ft}$ (Figure 111 - Figure 113): transition occurred immediately to the lee side of the stagnation point and the data reached fully-turbulent levels further downstream near the nose; data windward of the stagnation point appeared to be laminar/transitional; laminar predictions were ~15%-20% lower than the stagnation region data; turbulent predictions were ~2.5% higher than the lee side data. Also of note was a region of elevated heating in the experimental data around the stagnation point for $\alpha = 24\text{-deg}$ as well as smaller regions at $\alpha = 28\text{-deg}$ and 32-deg .

Run 3077, $\alpha = 28$ deg, $Re_\infty = 18 \times 10^6/\text{ft}$ (Figure 114): transition occurred immediately to the lee side of the stagnation point and the data reached fully-turbulent levels further downstream near the nose; data windward of the stagnation point appeared to be laminar/transitional; laminar predictions were ~15%-20% lower than the stagnation region data; turbulent predictions were ~2.5% higher than the lee side data. Elevated heating levels were observed in the experimental data at the stagnation point.

Run 3072, $\alpha = 28$ deg, $Re_\infty = 31 \times 10^6/\text{ft}$ (Figure 115): transition occurred immediately to the lee side of the stagnation point and reached fully-turbulent levels before the nose; the wind side data appeared to be transitional or perhaps fully turbulent approaching the wind side shoulder; laminar predictions were within ~10% at the stagnation point; turbulent predictions were ~5% higher than the lee side turbulent data and ~10%-15% higher than the wind side turbulent data.

Run 3076, $\alpha = 24\text{-}32$ deg, $Re_\infty = 31 \times 10^6/\text{ft}$ (Figure 116 - Figure 118): transition occurred immediately downstream of the stagnation point in both leeward and windward directions and quickly reached fully-turbulent levels; laminar predictions were within ~10% at the stagnation point; turbulent predictions were ~5% higher than the lee side turbulent data and ~10%-20% higher than the wind side turbulent data.

Run 3073, $\alpha = 28$ deg, $Re_\infty = 48 \times 10^6/\text{ft}$ (Figure 119): experimental data appeared to be fully turbulent over the entire forebody; turbulent predictions were ~5% lower than the data leeward of the stagnation point and ~10% lower than the data windward of the stagnation point.

Mach 10 Comparisons

Run 3057, $\alpha = 16\text{-}32$ deg, $Re_\infty = 2 \times 10^6/\text{ft}$ (Figure 120 - Figure 124): the data appeared to be laminar for all angles-of-attack; laminar predictions were ~12% lower than the data from the start of the run ($\alpha=16$ deg) but only ~5% lower than the data at the end of the run ($\alpha=32\text{-deg}$) which suggest the possibility that the earliest data were not taken during a high flow quality portion of the run.

Run 3058, $\alpha = 16\text{-}32$ deg, $Re_\infty = 5 \times 10^6/\text{ft}$ (Figure 125 - Figure 130): the data appeared to be laminar for all angles-of-attack; laminar predictions were ~2% to 7% lower than the data and the agreement became better over the course of the run, which may again indicate changing flow quality; runs subsequent to 3058 employed smaller angle-of-attack sweeps beginning later into the run to ensure that flow quality was not a problem.

Run 3064, $\alpha = 28$ deg, $Re_\infty = 5 \times 10^6/\text{ft}$ (Figure 131): the data appeared to be laminar; the laminar predictions

were ~5% lower than the data.

Run 3079, $\alpha = 0$ deg, $Re_\infty = 5 \times 10^6/\text{ft}$ (Figure 132): the data appeared to be laminar except at the stagnation point where the levels were slightly elevated; laminar predictions were ~5% lower than the data except at the stagnation point.

Run 3083, $\alpha = 20$ deg, $Re_\infty = 10 \times 10^6/\text{ft}$ (Figure 133): the data appeared to be laminar except at the stagnation point where the levels were elevated; laminar predictions were ~2%-5% lower than the data except at the stagnation point.

Run 3060, $\alpha = 20\text{-}32$ deg, $Re_\infty = 9 \times 10^6/\text{ft}$ (Figure 134 - Figure 137): transition was observed in the data on the lee side of the stagnation point for all angles-of-attack, a region of elevated heating was noted in the data at the stagnation point that appeared to decrease in size with increasing α ; in the laminar regions, the predictions were ~2% to 5% lower than the experimental data.

Run 3069, $\alpha = 28$ deg, $Re_\infty = 9 \times 10^6/\text{ft}$, 0.007-in. discrete roughness (Figure 138): the discrete trip produced a rapid transition to turbulent flow leeward of the stagnation point; wind side data remained laminar; laminar predictions were ~5%-7% lower than the wind side laminar data; turbulent predictions were ~10% higher than the lee side turbulent data.

Run 3080, $\alpha = 28$ deg, $Re_\infty = 9 \times 10^6/\text{ft}$, 0.001-in. distributed roughness (Figure 139): the distributed roughness produced gradual boundary-layer transition leeward of the stagnation point with levels approaching fully-developed turbulent flow near the lee side shoulder; the wind side data were laminar; laminar predictions were ~7%-10% lower than the wind side laminar data; turbulent predictions were well in excess of the lee side transitional data except near the lee side shoulder.

Run 3081, $\alpha = 28$ deg, $Re_\infty = 9 \times 10^6/\text{ft}$, 0.007-in. distributed roughness (Figure 140): the distributed roughness produced a rapid transition to turbulent flow leeward of the stagnation point; wind side data remained laminar; laminar predictions were ~5%-7% lower than the laminar wind side data; turbulent predictions were ~10% higher than the lee side turbulent data.

Run 3082, $\alpha = 28$ deg, $Re_\infty = 9 \times 10^6/\text{ft}$, 0.012-in. distributed roughness (Figure 141): the distributed roughness produced a rapid transition to turbulent flow leeward of the stagnation point; wind side data remained laminar; laminar predictions were ~5%-7% lower than the wind side laminar data; turbulent predictions were ~10% higher than the lee side turbulent data.

Run 3085, $\alpha = 28$ deg, $Re_\infty = 9 \times 10^6/\text{ft}$ (Figure 142): the data windward of the stagnation point remained laminar; data lee side of the stagnation point indicated gradual transition; laminar predictions were ~7% lower than the data except near the transitional lee side shoulder.

Run 3063, $\alpha = 20\text{-}32$ deg, $Re_\infty = 15 \times 10^6/\text{ft}$ (Figure 143 - Figure 146): the data indicated natural transition leeward of the stagnation point at or around the nose; elevated heating levels were observed in the data in the stagnation region with the magnitude of the augmentation decreasing with angle-of-attack; data windward of the stagnation point appear to remain laminar except perhaps near the wind side shoulder; laminar predictions were ~7%-12% lower than the laminar data, with the agreement becoming better at higher angles-of-attack; turbulent predictions were within 5% of the lee side data for the two highest angles-of-attack where it appeared that the data were fully turbulent.

Run 3065, $\alpha = 20\text{-}32$ deg, $Re_\infty = 15 \times 10^6/\text{ft}$ (Figure 147 - Figure 150): the data indicated natural transition

leeward of the stagnation point at or around the nose; elevated heating levels were observed in the data in the stagnation region with the magnitude of the augmentation decreasing with angle-of-attack; data windward of the stagnation point appear to remain laminar except perhaps near the wind side shoulder; laminar predictions were ~7%-12% lower than the laminar data, with the agreement becoming better at higher angles-of-attack; turbulent predictions were within 5% of the lee side data for the two highest angles-of-attack where it appeared that the data were fully turbulent.

Run 3068, $\alpha = 28$ deg, $Re_\infty = 14 \times 10^6/\text{ft}$, discrete roughness (Figure 151): the discrete trip produced a rapid rise to fully-turbulent flow on the lee side of the stagnation point; the wind side remained laminar; laminar predictions were ~10-12% lower than the laminar wind side data, turbulent predictions were ~2% higher than the turbulent lee side data.

Run 3078, $\alpha = 0$ deg, $Re_\infty = 14 \times 10^6/\text{ft}$ (Figure 152): a significant region of elevated heating was noted in the data near the nose; away from the nose, the data indicated transition approaching the shoulders; laminar predictions were ~15%-20% lower than the data at the nose and ~10%-15% lower elsewhere.

Run 3084, $\alpha = 28$ deg, $Re_\infty = 14 \times 10^6/\text{ft}$ (Figure 153): data on the wind side of the stagnation point remained laminar except near the shoulder; transition was observed on the lee side data near the nose, but the flow did not appear to reach fully-developed turbulent levels; laminar predictions were ~7%-15% lower than the data

Run 3086, $\alpha = 16$ -28 deg, $Re_\infty = 14 \times 10^6/\text{ft}$ (Figure 154 - Figure 157): the data indicated natural transition leeward of the stagnation point at or around the nose; elevated heating levels were observed in the data in the stagnation region with the magnitude of the augmentation decreasing with angle-of-attack; data windward of the stagnation point appear to remain laminar except perhaps near the wind side shoulder; laminar predictions were ~7%-12% lower than the laminar data, with the agreement becoming better at higher angles-of-attack; turbulent predictions were within 5% of the lee side data for the two highest angles-of-attack where it appeared that the data were fully turbulent.

Run 3061, $\alpha = 20$ -32 deg, $Re_\infty = 20 \times 10^6/\text{ft}$ (Figure 158 - Figure 161): data on the wind side of the stagnation point were transitional and may have been turbulent near the wind side shoulder at the higher angles-of-attack; heating augmentation was noted in the stagnation region data for the lower angles-of-attack; transition occurred on the lee side of the stagnation point near the nose for all angles-of-attack; laminar predictions were ~5%-15% lower than the wind side data with the best agreement at the lowest α ; turbulent predictions were within $\sim \pm 5\%$ of the lee side turbulent data.

Run 3062, $\alpha = 28$ deg, $Re_\infty = 20 \times 10^6/\text{ft}$ (Figure 162): the wind side data appeared to remain laminar expect near the wind side shoulder; flow leeward of the stagnation point became transitional before the nose and reached fully-turbulent levels well before the shoulder; laminar predictions were ~5% lower than the wind side laminar data; turbulent predictions were ~5% higher than the lee side turbulent data

Run 3066, $\alpha = 20$ -32 deg, $Re_\infty = 21 \times 10^6/\text{ft}$ (Figure 163 - Figure 166): data on the wind side of the stagnation point were transitional and may have been turbulent near the wind side shoulder at the higher angles-of-attack; heating augmentation was noted in the stagnation region data for the lower angles-of-attack; transition occurred on the lee side of the stagnation point near the nose for all angles-of-attack; laminar predictions were ~5%-15% lower than the wind side data with the best agreement at the higher angles-of-attack; turbulent predictions varied from ~5% lower to ~5% higher than the data depending on angle-of-attack.

Run 3067, $\alpha = 28$ deg, $Re_\infty = 21 \times 10^6/\text{ft}$, discrete roughness (Figure 167): although a trip was present and likely caused transition sooner than would have occurred naturally, the lee side turbulent heating data were consistent with

earlier, non-tripped cases; wind side data remained laminar; laminar predictions were ~7% lower than the wind side data; turbulent predictions were ~2% higher than the lee side turbulent data.

Run 3087, $\alpha = 16\text{-}24$ deg, $Re_\infty = 20 \times 10^6/\text{ft}$ (Figure 168 - Figure 170): large regions of elevated heating were noted in the data around the stagnation point expect at the highest α ; fully-turbulent conditions were reached on the lee side for all conditions; laminar predictions were ~10%-20% lower than the wind side data depending on angle of attack; turbulent lee side predictions were from ~5% lower than the data to ~8% higher than the data on the lee side.

General observations on forebody comparisons

In addition to the specific comparisons shown for each run and the discussion in the previous sections, some general observations can be made that pertain to the whole data set.

Laminar conditions: at definitively laminar conditions (such as those produced over the whole forebody for the Mach 10, $Re_\infty = 2.5 \times 10^6/\text{ft}$ and $5 \times 10^6/\text{ft}$ cases or over the wind side and the part of the lee side at $Re_\infty = 9 \times 10^6/\text{ft}$) laminar predictions were ~5% lower than the data at most conditions and were not more than 10% lower than the data. The only exceptions were data from the beginning of some of the runs, where the flow quality may not have been fully established and, as will be noted later, in the stagnation region.

With respect to the Mach 8 data, it should be noted that the lowest Mach 8 Reynolds numbers test point of $Re_\infty = 8 \times 10^6/\text{ft}$ produced data that *may* have been laminar over portions of the body, but without a lower Reynolds number test condition for comparison, this assumption cannot be verified. For these Mach 8 cases, laminar predictions were ~10-15% lower than the data as compared to the ~5-10% for the Mach 10 laminar conditions. The reason for the poorer comparisons at Mach 8 cannot be determined without further testing and facility diagnostics. However, as the same computational methods were used for both cases, it would not appear likely that the larger differences were due to the computations. Two possible reasons for these differences are: 1) The Mach 8, $Re_\infty = 8 \times 10^6/\text{ft}$ case was marginally transitional over the entire forebody, and thus the measured heating levels were higher than the laminar predictions; 2) The temporal or spatial flow quality of this condition was not as good as that of the Mach 10 conditions and the flow quality affected the heating measurements.

Turbulent conditions: at definitively turbulent conditions (such as on the forebody to the lee side of the nose at Mach 10, $Re_\infty = 20 \times 10^6/\text{ft}$ or for Mach 8, $Re_\infty \geq 17 \times 10^6/\text{ft}$) the algebraic Cebeci-Smith turbulence model predictions were between ~2% lower to ~5% higher than the experimental data. For the higher Reynolds number Mach 8 cases ($Re_\infty \geq 31 \times 10^6/\text{ft}$) the data appeared to be turbulent on the wind side also – that is, the flow was turbulent over the entire forebody. For these cases, the turbulent wind side predictions fell within $\pm 10\%$ of the wind side data except at the shoulder, where the data were sparse and the data uncertainty higher due to conduction effects. In general, the turbulent comparisons appear to be better than the laminar comparisons. However, an argument could be made that the turbulent predictions should be biased to compensate for the observed differences between the laminar data and laminar predictions. If such a step was taken to account for the under-prediction in the laminar cases (assuming an average difference of 10% from the laminar comparisons), then turbulent predictions would be ~7.5% to 15% lower than the data for Mach 10 cases and up to ~20% lower for Mach 8 cases.

Stagnation region: in the stagnation region of the CEV model, the experimental data from several of the runs revealed a small, localized heating disturbance that was not predicted by either laminar or turbulent computational methods. This augmentation was most apparent at lower angles-of-attack (e.g. Figure 111, Figure 155, Figure 163). With respect to Reynolds number, this phenomenon was negligible at low Reynolds numbers, more distinct at moderate Reynolds numbers, and appeared to be swallowed into the larger heating increase due to natural transition at higher Reynolds numbers. This phenomenon has previously been noted in the stagnation region of blunt, large-angle cones such as the MSL in several previous studies (Refs. 23 - 25). Because the post-shock flow field

produced by such configurations is mostly subsonic, it is possible that disturbances elsewhere in the flow – due perhaps to fluctuations at the shock or transitional/turbulent eddies in the boundary-layer – are propagating all across the forebody and may be coalescing in the stagnation region causing a destabilization there that produces augmented heating. However, more in-depth flow field diagnostics would be required to determine the exact mechanisms at work in this region. For the purpose of the CEV development program, this phenomenon does not appear to be a cause for concern as the augmentation was considerably less than that produced elsewhere on the vehicle due to natural transition to turbulent flow.

Comparison of Aftbody Experimental Data with Predictions

Laminar and turbulent computations were also performed for the entire vehicle flow field (forebody, aftbody and wake) for a limited number of cases ($\alpha = 28$ deg at each Reynolds number). Comparisons between the aftbody predictions and experimental data are shown in Figure 171 - Figure 179. When evaluating these comparisons, it should be remembered that there were only a very limited number of gages on the aftbody and so any conclusions should be considered as tentative until a more detailed set of measurements are made.

The steady-state solution residuals in the computational blocks on the lee side of the aftbody ($z/R > 0$) did not converge, which indicated that this region of the flow was separated and unsteady. Therefore comparisons on the lee side of the aftbody to the laminar, steady-state solutions were not valid. However, on the wind side of the aftbody, the flow remained attached and steady up until close to the base of the vehicle and therefore comparisons were appropriate.

The Mach 8 aftbody wind side data (Figure 171 - Figure 174) showed a large increase (a factor of 4-6) in heating with increasing Reynolds number that indicated transition to turbulence. This increase began near the base of the model at $Re_\infty = 17 \times 10^6/\text{ft}$ and moved upstream to encompass the entire wind side aftbody at $Re_\infty = 48 \times 10^6/\text{ft}$. In contrast, for the Mach 10 conditions (Figure 175 - Figure 179), the data did not vary with Reynolds numbers which indicated that the aftbody remained laminar. At Mach 10, the laminar, aftbody wind side predictions were ~5%-10% lower than the experimental data. At the lower Reynolds number Mach 8 conditions, the laminar predictions were again ~5-10% lower than the data, while at the higher Mach 8 Reynolds numbers the turbulent predictions were within 10% of the data.

Although trajectories for the actual flight vehicle are still under development, it seems unlikely that Reynolds numbers as high as those required in this test for aftbody turbulence to develop would be achieved in flight. This result would suggest that the aftbody need not be designed to turbulent conditions; however these test data do not include effects of chemistry, TPS ablation and blowing, or the presence of features (such as windows and ports) on the aftbody that could promote transition.

Wind Tunnel Data Repeatability

Several angle-of-attack/Reynolds number conditions were repeated during this test series. These repeat runs included both static and continuous pitch-sweep runs. The repeat cases are plotted in Figure 180 - Figure 194. The greatest differences in the repeat runs were seen for those cases where the flow on the lee side of the stagnation point was transitional (e.g. Figure 190). Over the course of this test series, the wind tunnel model sustained particulate damage during each run. This damage was usually minor, and the model surface was refinished after each run; however, smooth body transition onset location is a very sensitive parameter, and thus this damage caused some movement in the onset location from run to run. Aside from this transitional data, the fully-laminar and fully-turbulent data were very repeatable; the only case where the data varied by more than 10% was at the Mach 8, $Re_\infty = 8 \times 10^6/\text{ft}$ condition (Figure 180).

Transition Onset Correlations

The wind tunnel data were examined in order to determine the transition onset location along the centerline of the forebody leeward of the stagnation point. The transition location was determined by comparing the experimental heating data with laminar predictions for each test point (as shown for a sample case in Figure 195). Boundary layer parameters at that location were then extracted from the CFD solution for that case for use in correlating these results. Because the onset location can be difficult to precisely determine, an average value was taken across a distance spanned by several gages. In addition to these data from AEDC Tunnel 9, transition onset locations were also determined from testing of this CEV model conducted in the LaRC 20-Inch Mach 6 Air Tunnel. A description of this test is provided in Ref. 26.

The transition onset data are plotted against several different commonly-used boundary layer parameters in Figure 196. In these plots, the parameters Re_θ and $Re_{\theta,mod}$ are defined as:

$$Re_\theta = \frac{\rho_e U_e \theta}{\mu_e} \quad (22)$$

$$Re_{\theta,mod} = \frac{\rho_e U_e \theta}{\mu_w} = Re_\theta \left(\frac{\mu_e}{\mu_w} \right) \quad (23)$$

As shown in these plots, the parameters Re_θ/M_e or $Re_{\theta,mod}/M_e$ provide the best correlations with the free stream Reynolds number, whereas $Re_{\theta,mod}$ is the worst parameter for correlating these data.

These correlations are provided only for informational value and are not intended to be used for vehicle design purposes. Numerous studies have shown that transition data obtained from ground testing is highly dependent on tunnel noise and model surface quality. The onset location can also be difficult to specify precisely because of sparse instrumentation coverage, noise in the data, or varying definitions for the onset location itself (e.g. by increasing noise in the measured time-history data; by a specified percentage increase over a theoretical or predicted heating level; by comparison with lower Reynolds number data; etc). Additionally, the data presented herein are from testing on a smooth-surface wind tunnel model, whereas transition on an actual flight vehicle's TPS could be influenced by ablation roughness, material blowing, and/or tile steps and gaps. Furthermore, the transition onset location is, by itself, of more academic than practical usefulness. The onset location merely specifies when/where transition begins, but does not provide any information on heating (and shear) augmentation downstream of transition due to the growth of the turbulent boundary layer.

Transitional/Turbulent Heating Augmentation

Although correlations of the transition onset location data may be of questionable value, it was found that more useful correlations of heating data at various locations on the model could be formulated with the boundary layer parameter Re_θ across the range of laminar, transitional and turbulent test conditions. Three locations were considered (Figure 197): the tangency points between the spherical section and the shoulder on the leeward and windward sides of the heat shield, and a point on the windward side of the aftbody just prior to the base of the model. Data at these three points from testing of the CEV model in both AEDC Tunnel 9 and the LaRC 20-Inch Mach 6 Air Tunnel are shown in Figure 198 - Figure 200. In the plots, the ratio (in terms of $St \times (Re_{\infty,D})^{1/2}$) between the measured heating at each point, whether laminar, transitional, or turbulent, to the predicted, laminar heating is plotted vs. the laminar value of Re_θ . These plots provide useful information about heating augmentation at each point, although it must be noted that this information is for perfect-gas, non-reacting, non-ablating/blowing flow over a smooth model surface. Flight conditions will be considerably different and these correlations may not be valid.

From Figure 198, it can be seen the lee side shoulder is laminar for Re_θ values below ~ 200 , transitional between 200 and 400, and fully-turbulent for values over ~ 400 . The heating augmentation ratio obtained from the data approaches a value of 6 and the max value does not appear to be bounded by the data, however, the Re_θ values obtained from the testing likely do bound those that would be obtained in flight. In Figure 199 for the wind side shoulder heat-shield values, it can be seen this point appears to remain laminar throughout the test range, in which max Re_θ values of ~ 150 were obtained. Finally, from the aftbody wind side point data plotted in Figure 200, it would appear that the aftbody remains laminar for Re_θ values of up to ~ 400 , is transitional between ~ 400 to 600, and is turbulent for higher values. This data set is, however, very sparse – not due to a lack of experimental data, but rather due to the small number of aftbody flow-field predictions performed because of the length of time required to complete such simulations.

For comparison to the CEV data, data from the previously mentioned MSL testing in both AEDC Tunnel 9 and the NASA LaRC 20-Inch Mach 6 Air Tunnel have been added to the plots for the forebody lee side and wind side shoulder (Figure 201 - Figure 202). The MSL data compare well to the CEV data for both body points; additionally, the MSL wind side shoulder data encompasses higher Re_θ values than the CEV data and provides some information on when transitional effects begin at this point.

Summary and Conclusions

A convective aeroheating test of a CEV model has been conducted in the AEDC Tunnel 9. Computational simulations were also performed at the tunnel test conditions for comparison purposes and for use in correlating the experimental data. The goals of this test were to obtain turbulent heating augmentation data on the forebody of the vehicle and to obtain high-fidelity heating measurements to help assess the accuracy of CFD tools employed in the CEV program.

Testing was performed across a range of free stream Reynolds numbers from $2 \times 10^6/\text{ft}$ to $20 \times 10^6/\text{ft}$ at Mach 10 and $8 \times 10^6/\text{ft}$ to $48 \times 10^6/\text{ft}$ at Mach 8 for angles of attack of 16-32 deg at Mach 10 and 24-32 deg at Mach 8. Heating data were obtained from thermocouple measurements on the forebody heat-shield and aftbody of the model.

Laminar, transitional or turbulent flow was produced in this test, depending on the free stream conditions. The forebody lee side flow was laminar at Mach 10 for Reynolds numbers of $\sim 5 \times 10^6/\text{ft}$ or below, transitional at the $9 \times 10^6/\text{ft}$ and $15 \times 10^6/\text{ft}$ operating conditions, and turbulent at the $20 \times 10^6/\text{ft}$ condition. At Mach 8, the forebody lee side data were transitional at the $8 \times 10^6/\text{ft}$ condition and turbulent for higher Reynolds numbers; additionally the forebody wind side data were also turbulent at the highest Mach Reynolds number conditions. This test produced the first data set with natural transition to fully-developed turbulent flow over the entire heat shield available to the CEV program.

Comparisons between the data and laminar or turbulent (as appropriate) predictions were performed for the forebody heat shield for all test conditions and for a small subset ($\alpha = 28$ deg) of the aftbody crew compartment data. At the Mach 10 conditions, laminar predictions were between 5% to 10% lower than laminar test data and turbulent predictions were within $\pm 10\%$ of turbulent test data. At the Mach 8 conditions, laminar predictions were 10% to 20% lower than data which were assumed to be laminar (at the $8 \times 10^6/\text{ft}$ free stream Reynolds number case), but it was unclear whether these data were truly laminar or were possibly transitional since there was no lower Reynolds number test case at Mach 8. Mach 8, turbulent predictions were within $\pm 10\%$ of the test data for Reynolds numbers greater than $8 \times 10^6/\text{ft}$, at which conditions the flow was assumed to be turbulent.

Transitional onset correlation of the centerline data were generated and it was found that the best correlation could be generated in terms of Re_θ/M_e or $Re_{\theta,mod}/M_e$. However, because of many factors which affect transition onset (such as noise, roughness, etc), it is not recommended that these correlations be employed for design purposes.

Heating augmentation ratios between the experimental data and laminar predictions were generated for three body points – the wind side and lee side forebody shoulder points and a point on the aftbody wind side. These ratios were plotted against Re_θ and the data from various Mach and Reynolds number as well as angles-of-attack were found to correlate well in these terms. From analysis of these plots, it was found that the forebody lee side shoulder was laminar for $Re_\theta < 200$ and fully-turbulent for $Re_\theta > 400$; the wind side shoulder was laminar up to the maximum test condition value of $Re_\theta \sim 160$; and the aftbody wind side shoulder was laminar for $Re_\theta < 400$ and fully-turbulent for $Re_\theta > 600$. Based on these smooth-body, non-ablating/blowing correlations, it is likely that the conditions for the actual CEV flight vehicle could reach the levels required for forebody turbulence but not for aftbody turbulence.

References

1. “NASA’s Exploration Systems Architecture Study, Final Report,” NASA TM-2005-214062, November, 2005.
2. Liechty, D. S., “Aerothermodynamic Testing of Protuberances and Penetrations on the NASA Crew Exploration Vehicle Heat Shield”, AIAA Paper 2008-1240, 46th AIAA Aerospace Sciences Meeting and Exhibit, January 7-10, 2008, Reno, NV.
3. Berger, K. T., “Aerothermodynamic Testing of the Crew Exploration Vehicle in the LaRC 20-Inch Mach 6 and 31-Inch Mach 10 Tunnels,” AIAA Paper 2008-1225, 46th AIAA Aerospace Sciences Meeting and Exhibit, January 7-10, 2008, Reno, NV.
4. Coblish, J. J., and Davenport, A. H., “Recent Efforts at AEDC’s Von Karman Facility and Hypervelocity Wind Tunnel 9 to Enhance Facility Compatibility”, AIAA Paper 2002-2787, 22nd AIAA Aerodynamic Measurement Technology and Ground Testing Conference, June 24-26, 2002.
5. Burns, G. W., Scroger, M. G., Strouse, G. F., Croarkin, M. C., and Guthrie, W. F., “Temperature-Electromotive Force Reference Functions and Tables for the Letter-Designated Thermocouple Types Based on ITS-90,” NIST Monograph 175, 1993.
6. Ragsdale, W. C., and Boyd, C. F., “Hypervelocity Wind Tunnel 9 Facility Handbook, Third Edition,” Technical Report NAVSWC TR 91-616, Naval Surface Warfare Center, Silver Spring, MD, July 1993.
7. Marren, D., and Lafferty, J., “The AEDC Hypervelocity Wind Tunnel 9,” Advanced Hypersonic Test Facilities, Progress in Aeronautics and Astronautics, Vol. 198, American Institute of Aeronautics and Astronautics, Reston, VA, 2002, pp. 467-477. “NASA’s Exploration Systems Architecture Study, Final Report,” NASA TM-2005-214062, November, 2005.
8. Norris, J. D., Lafferty, J. F., Smith, M. S., Collier, A. S., and Hand, T., “Design and Aerodynamic Calibration of the New AEDC Hypervelocity Wind Tunnel No. 9 Mach 8 Nozzle,” AIAA Paper 2005-4278, 41st AIAA/ASME/SAE/ASEE Joint Propulsions Conference and Exhibit, Tuscon, AZ, June 10-13, 2005.
9. Hedlund, E. R., Hill, J. A. F., Ragsdale, W. C., and Voisiniet, R. L. P., “Heat Transfer Testing in the NSWC Hypervelocity Wind Tunnel Utilizing Co-Axial Surface Thermocouples,” Naval Surface Weapons Center - NSWC-MP 80-151, March 1980.
10. Boyd, C. F., and Howell, A., “Numerical Investigation of One-Dimensional Heat-Flux Calculations,” Naval Surface Warfare Center NSWCDD/TR-94/114, October 1994.
11. Hollis, B. R., “User’s Manual for the One-Dimensional Hypersonic Aero-Thermodynamic (1DHEAT) Data Reduction Code,” NASA CR-4691, August 1995

12. Anderson, J. D. Jr., *Hypersonic and High-Temperature Gas Dynamics*, McGraw-Hill Book Company, New York, 1989.
13. Hollis, B. R. and Collier, A. S., "Turbulent Aeroheating Testing of Mars Science Laboratory Entry Vehicle in Perfect-Gas Nitrogen," AIAA Paper 2007-1208, 45th AIAA Aerospace Sciences Meeting and Exhibit, Reno, NV, Jan. 8-11, 2007.
14. Coblisch, J. J., Coulter, S. M., Norris, J. D., "Aerothermal Measurement Improvements Using Coaxial Thermocouples at AEDC Hypervelocity Wind Tunnel No. 9," AIAA Paper 2007-1467, 45th AIAA Aerospace Sciences Meeting and Exhibit, Reno, NV, Jan. 8-11, 2007.
15. Micol, J. R. "Langley Aerothermodynamic Facilities Complex: Enhancements and Testing Capabilities," AIAA Paper 98-0147, 36th AIAA Aerospace Sciences Meeting and Exhibit, Reno, NV, Jan. 12-15, 1998.
16. Gnoffo, P. A., "An Upwind-Biased, Point-Implicit Algorithm for Viscous, Compressible Perfect-Gas Flows," NASA TP-2953, February 1990.
17. Cheatwood, F. M., and Gnoffo, P. A., "User's Manual for the Langley Aerothermodynamic Upwind Relaxation Algorithm (LAURA)," NASA TM 4674, April, 1996.
18. Roe, P. L., "Approximate Riemann Solvers, Parameter Vectors and Difference Schemes," Journal of Computational Physics, Vol. 43, No. 2, 1981, pp. 357-372.
19. Harten, A., "High Resolution Schemes for Hyperbolic Conservation Laws," Journal of Computational Physics, Vol. 49, No. 3, 1983, pp. 357-393.
20. Yee, H. C., "On Symmetric and Upwind TVD Schemes," NASA TM 88325, 1990.
21. "Guidelines for Application of the LAURA Code for CEV," NASA EG-CEV-07-153, June 2007.
22. Brown, J. L., "Turbulence Model Validation for Hypersonic Flows," AIAA Paper 2002-3308, 8th AIAA/ASME Joint Thermophysics and Heat Transfer Conference, St. Louis, MO. June 24-26, 2002.
23. Hollis, B. R., Liechty, D. S., Wright, M. J., Holden, M. S., Wadhams, T. P., and MacLean, M., "Transition Onset and Turbulent Heating Measurements for the Mars Science Laboratory Entry Vehicle," AIAA Paper 2005-1437, 43rd Aerospace Sciences Meeting and Exhibit, Reno, NV, January 10-13, 2007.
24. Shimshi, J. P. and Walberg, G. D., "An Investigation of Aerodynamic Heating to Spherically Blunted Cones at Angle of Attack," AIAA Paper 1993-2764, 28th AIAA Thermophysics Conference, Orlando, FL, January 6-9, 1993.
25. Petersen, F. Server, D., and Carroll, H. "Heat Transfer and Pressure Distributions at M = 8 on 0.029 Scale Models of the Viking Entry Vehicle," NASA CR-132413, July 1972.
26. Hollis, B. R., Berger, K. T., and Horvath, T. J., Coblisch, J. J., Norris, J. D., Lillard, R. P., and Kirk, B. S., "Aeroheating Testing and Predictions for Project Orion CEV at Turbulent Conditions," AIAA Paper 2008-1226, 46th AIAA Aerospace Sciences Meeting and Exhibit, January 7-10, 2008, Reno, NV.

Table 1. Gage locations

Gage	x(m)	y(m)	z(m)	x/R	y/R	z/R	Local thickness (m)	Local radius (m)	Location
1	0.0175	0.0845	0.0000	0.1971	0.9500	0.0000	0.0062	0.0089	Heat Shield
2	0.0164	0.0622	0.0533	0.1841	0.7000	0.6000	0.0067	0.2134	Heat Shield
3	0.0105	0.0622	0.0222	0.1180	0.7000	0.2500	0.0095	0.2134	Heat Shield
4	0.0138	0.0356	0.0667	0.1556	0.4000	0.7500	0.0093	0.2134	Heat Shield
5	0.0030	0.0356	0.0000	0.0336	0.4000	0.0000	0.0095	0.2134	Heat Shield
6	0.0056	0.0356	0.0333	0.0635	0.4000	0.3750	0.0095	0.2134	Heat Shield
7	0.0138	0.0356	0.0667	0.1556	0.4000	0.7500	0.0093	0.2134	Heat Shield
8	0.0175	0.0133	0.0834	0.1971	0.1500	0.9379	0.0062	0.0089	Heat Shield
9	0.0051	0.0133	0.0445	0.0575	0.1500	0.5000	0.0095	0.2134	Heat Shield
10	0.0016	0.0133	0.0222	0.0178	0.1500	0.2500	0.0095	0.2134	Heat Shield
11	0.0051	0.0133	0.0445	0.0575	0.1500	0.5000	0.0095	0.2134	Heat Shield
12	0.0111	0.0133	0.0667	0.1251	0.1500	0.7500	0.0095	0.2134	Heat Shield
13	0.0175	0.0000	0.0845	0.1971	0.0000	0.9500	0.0062	0.0089	Centerline Heat Shield
14	0.0156	0.0000	0.0800	0.1751	0.0000	0.9000	0.0075	0.2134	Centerline Heat Shield
15	0.0138	0.0000	0.0756	0.1556	0.0000	0.8500	0.0093	0.2134	Centerline Heat Shield
16	0.0122	0.0000	0.0711	0.1373	0.0000	0.8000	0.0095	0.2134	Centerline Heat Shield
17	0.0107	0.0000	0.0667	0.1202	0.0000	0.7500	0.0095	0.2134	Centerline Heat Shield
18	0.0093	0.0000	0.0622	0.1043	0.0000	0.7000	0.0095	0.2134	Centerline Heat Shield
19	0.0080	0.0000	0.0578	0.0897	0.0000	0.6500	0.0095	0.2134	Centerline Heat Shield
20	0.0068	0.0000	0.0533	0.0762	0.0000	0.6000	0.0095	0.2134	Centerline Heat Shield
21	0.0057	0.0000	0.0489	0.0639	0.0000	0.5500	0.0095	0.2134	Centerline Heat Shield
22	0.0047	0.0000	0.0445	0.0527	0.0000	0.5000	0.0095	0.2134	Centerline Heat Shield
23	0.0038	0.0000	0.0400	0.0426	0.0000	0.4500	0.0095	0.2134	Centerline Heat Shield
24	0.0030	0.0000	0.0356	0.0336	0.0000	0.4000	0.0095	0.2134	Centerline Heat Shield
25	0.0023	0.0000	0.0311	0.0257	0.0000	0.3500	0.0095	0.2134	Centerline Heat Shield
26	0.0017	0.0000	0.0267	0.0188	0.0000	0.3000	0.0095	0.2134	Centerline Heat Shield
27	0.0012	0.0000	0.0222	0.0131	0.0000	0.2500	0.0095	0.2134	Centerline Heat Shield
28	0.0003	0.0000	0.0111	0.0033	0.0000	0.1251	0.0100	0.2134	Centerline Heat Shield
29	0.0000	0.0000	0.0000	0.0000	0.0000	0.0000	0.0150	0.2134	Centerline Heat Shield
30	0.0000	0.0000	0.0044	0.0005	0.0000	0.0500	0.0095	0.2134	Centerline Heat Shield
31	0.0002	0.0000	0.0089	0.0021	0.0000	0.1000	0.0095	0.2134	Centerline Heat Shield
32	0.0004	0.0000	0.0133	0.0047	0.0000	0.1500	0.0095	0.2134	Centerline Heat Shield
33	0.0007	0.0000	0.0178	0.0083	0.0000	0.2000	0.0095	0.2134	Centerline Heat Shield
34	0.0012	0.0000	0.0222	0.0131	0.0000	0.2500	0.0095	0.2134	Centerline Heat Shield
35	0.0017	0.0000	0.0267	0.0188	0.0000	0.3000	0.0095	0.2134	Centerline Heat Shield
36	0.0023	0.0000	0.0311	0.0257	0.0000	0.3500	0.0095	0.2134	Centerline Heat Shield
37	0.0030	0.0000	0.0356	0.0336	0.0000	0.4000	0.0095	0.2134	Centerline Heat Shield
38	0.0038	0.0000	0.0400	0.0426	0.0000	0.4500	0.0095	0.2134	Centerline Heat Shield
39	0.0047	0.0000	0.0445	0.0527	0.0000	0.5000	0.0095	0.2134	Centerline Heat Shield
40	0.0057	0.0000	0.0489	0.0639	0.0000	0.5500	0.0095	0.2134	Centerline Heat Shield
41	0.0068	0.0000	0.0533	0.0762	0.0000	0.6000	0.0095	0.2134	Centerline Heat Shield
42	0.0080	0.0000	0.0578	0.0897	0.0000	0.6500	0.0095	0.2134	Centerline Heat Shield
43	0.0093	0.0000	0.0622	0.1043	0.0000	0.7000	0.0095	0.2134	Centerline Heat Shield
44	0.0107	0.0000	0.0667	0.1202	0.0000	0.7500	0.0095	0.2134	Centerline Heat Shield
45	0.0122	0.0000	0.0711	0.1373	0.0000	0.8000	0.0095	0.2134	Centerline Heat Shield
46	0.0138	0.0000	0.0756	0.1556	0.0000	0.8500	0.0093	0.2134	Centerline Heat Shield
47	0.0156	0.0000	0.0800	0.1751	0.0000	0.9000	0.0075	0.2134	Centerline Heat Shield
48	0.0175	0.0000	0.0845	0.1971	0.0000	0.9500	0.0062	0.0089	Centerline Heat Shield
49	0.0175	0.0133	0.0834	0.1971	0.1500	0.9379	0.0062	0.0089	Heat Shield
50	0.0111	0.0133	0.0667	0.1251	0.1500	0.7500	0.0095	0.2134	Heat Shield
51	0.0051	0.0133	0.0445	0.0575	0.1500	0.5000	0.0095	0.2134	Heat Shield
52	0.0004	0.0133	0.0000	0.0047	0.1500	0.0000	0.0112	0.2134	Heat Shield

Gage	x(m)	y(m)	z(m)	x/R	y/R	z/R	Local thickness (m)	Local radius (m)	Location
53	0.0016	0.0133	0.0222	0.0178	0.1500	0.2500	0.0095	0.2134	Heat Shield
54	0.0030	0.0133	0.0333	0.0342	0.1500	0.3750	0.0095	0.2134	Heat Shield
55	0.0051	0.0133	0.0445	0.0575	0.1500	0.5000	0.0095	0.2134	Heat Shield
56	0.0078	0.0133	0.0556	0.0882	0.1500	0.6250	0.0095	0.2134	Heat Shield
57	0.0111	0.0133	0.0667	0.1251	0.1500	0.7500	0.0095	0.2134	Heat Shield
58	0.0143	0.0133	0.0756	0.1606	0.1500	0.8500	0.0088	0.2134	Heat Shield
59	0.0175	0.0133	0.0834	0.1971	0.1500	0.9379	0.0062	0.0089	Heat Shield
60	0.0014	0.0244	0.0000	0.0158	0.2750	0.0000	0.0095	0.2134	Heat Shield
61	0.0026	0.0244	0.0222	0.0289	0.2750	0.2500	0.0095	0.2134	Heat Shield
62	0.0040	0.0244	0.0333	0.0455	0.2750	0.3750	0.0095	0.2134	Heat Shield
63	0.0061	0.0244	0.0445	0.0688	0.2750	0.5000	0.0095	0.2134	Heat Shield
64	0.0088	0.0244	0.0556	0.0992	0.2750	0.6250	0.0095	0.2134	Heat Shield
65	0.0122	0.0244	0.0667	0.1369	0.2750	0.7500	0.0095	0.2134	Heat Shield
66	0.0153	0.0244	0.0756	0.1725	0.2750	0.8500	0.0077	0.2134	Heat Shield
67	0.0138	0.0356	0.0667	0.1556	0.4000	0.7500	0.0093	0.2134	Heat Shield
68	0.0056	0.0356	0.0333	0.0635	0.4000	0.3750	0.0096	0.2134	Heat Shield
69	0.0032	0.0356	0.0089	0.0357	0.4000	0.1000	0.0112	0.2134	Heat Shield
70	0.0030	0.0356	0.0000	0.0336	0.4000	0.0000	0.0095	0.2134	Heat Shield
71	0.0042	0.0356	0.0222	0.0468	0.4000	0.2500	0.0095	0.2134	Heat Shield
72	0.0056	0.0356	0.0333	0.0635	0.4000	0.3750	0.0095	0.2134	Heat Shield
73	0.0077	0.0356	0.0445	0.0870	0.4000	0.5000	0.0095	0.2134	Heat Shield
74	0.0105	0.0356	0.0556	0.1176	0.4000	0.6250	0.0095	0.2134	Heat Shield
75	0.0138	0.0356	0.0667	0.1556	0.4000	0.7500	0.0093	0.2134	Heat Shield
76	0.0069	0.0489	0.0222	0.0773	0.5500	0.2500	0.0095	0.2134	Heat Shield
77	0.0105	0.0489	0.0445	0.1180	0.5500	0.5000	0.0095	0.2134	Heat Shield
78	0.0164	0.0622	0.0533	0.1841	0.7000	0.6000	0.0067	0.2134	Heat Shield
79	0.0093	0.0622	0.0000	0.1043	0.7000	0.0000	0.0095	0.2134	Heat Shield
80	0.0105	0.0622	0.0222	0.1180	0.7000	0.2500	0.0095	0.2134	Heat Shield
81	0.0164	0.0622	0.0533	0.1841	0.7000	0.6000	0.0067	0.2134	Heat Shield
82	0.0175	0.0845	0.0000	0.1971	0.9500	0.0000	0.0062	0.0089	Heat Shield
83	0.0508	0.0445	0.0595	0.5711	0.5000	0.6688	0.0158	0.0743	Aft body, wind side
84	0.0508	0.0222	0.0708	0.5711	0.2500	0.7967	0.0158	0.0743	Aft body, wind side
85	0.0508	0.0000	0.0742	0.5711	0.0000	0.8351	0.0158	0.0743	Aft body, wind side
86	0.0508	0.0222	0.0708	0.5711	0.2500	0.7967	0.0158	0.0743	Aft body, wind side
87	0.0508	0.0445	0.0595	0.5711	0.5000	0.6688	0.0158	0.0743	Aft body, wind side
88	0.0698	0.0445	0.0435	0.7849	0.5000	0.4890	0.0095	0.0622	Aft body, wind side
89	0.0698	0.0222	0.0581	0.7849	0.2500	0.6530	0.0095	0.0622	Aft body, wind side
90	0.0698	0.0000	0.0622	0.7849	0.0000	0.6992	0.0095	0.0622	Aft body, wind side
91	0.0698	0.0222	0.0581	0.7849	0.2500	0.6530	0.0095	0.0622	Aft body, wind side
92	0.0698	0.0445	0.0435	0.7849	0.5000	0.4889	0.0095	0.0622	Aft body, wind side
93	0.0975	0.0000	0.0445	1.0969	0.0000	0.5002	0.0095	0.0487	Aft body, wind side
94	0.0508	0.0222	0.0708	0.5711	0.2500	0.7967	0.0158	0.0743	Aft body, lee side
95	0.0508	0.0000	0.0742	0.5711	0.0000	0.8351	0.0158	0.0743	Aft body, lee side
96	0.0508	0.0222	0.0708	0.5711	0.2500	0.7967	0.0158	0.0743	Aft body, lee side
97	0.0698	0.0222	0.0581	0.7849	0.2500	0.6530	0.0095	0.0622	Aft body, lee side
98	0.0698	0.0000	0.0622	0.7849	0.0000	0.7000	0.0095	0.0622	Aft body, lee side
99	0.0698	0.0222	0.0581	0.7849	0.2500	0.6530	0.0095	0.0622	Aft body, lee side
100	0.0975	0.0000	0.0445	1.0969	0.0000	0.5000	0.0095	0.0487	Aft body, lee side
101	0.1087	0.0000	0.0373	1.2233	0.0000	0.4200	0.0182	0.0422	Aft body, lee side

Table 2. Tunnel 9 CEV Test Matrix

Run	α (deg)	Re_∞ (1/ft)	Re_∞ (1/m)	Mach	P_∞ (Pa)	T_∞ (K)	ρ_∞ (kg/m ³)	U_∞ (m/s)	H_0-H_{300K} (J/kg)	Trips
3057	0 - 34	1.953E+06	6.407E+06	9.64	2.601E+02	52.97	1.654E-02	1431.8	7.675E+05	Clean
3058	0 - 34	4.750E+06	1.558E+07	9.87	6.167E+02	52.91	3.927E-02	1464.9	8.153E+05	Clean
3059	34-0	4.778E+06	1.567E+07	9.85	6.135E+02	52.44	3.942E-02	1455.0	8.004E+05	Clean (bad run)
3060	20-34	8.890E+06	2.917E+07	10.10	1.115E+03	52.46	7.161E-02	1491.6	8.542E+05	Clean
3061	20-34	1.962E+07	6.438E+07	10.40	2.085E+03	47.84	1.468E-01	1466.8	8.131E+05	Clean
3062	28	2.026E+07	6.648E+07	10.39	2.213E+03	48.68	1.532E-01	1477.5	8.295E+05	Clean
3063	20-34	1.457E+07	4.781E+07	10.32	1.600E+03	48.67	1.108E-01	1468.6	8.162E+05	Clean
3064	28	4.469E+06	1.466E+07	9.85	5.862E+02	53.20	3.713E-02	1465.2	8.161E+05	Clean
3065	34-20	1.494E+07	4.901E+07	10.33	1.613E+03	48.19	1.129E-01	1461.6	8.058E+05	Clean
3066	34-20	2.059E+07	6.754E+07	10.42	2.166E+03	47.75	1.531E-01	1466.9	8.136E+05	Clean
3067	28	2.050E+07	6.726E+07	10.32	2.251E+03	48.64	1.559E-01	1467.1	8.142E+05	0.007” discrete
3068	28	1.411E+07	4.629E+07	10.27	1.596E+03	49.50	1.086E-01	1473.7	8.247E+05	0.007” discrete
3069	28	8.825E+06	2.895E+07	10.03	1.091E+03	51.72	7.107E-02	1470.6	8.225E+05	0.007” discrete
3070	28	8.620E+06	2.828E+07	7.44	2.417E+03	73.49	1.108E-01	1299.6	6.084E+05	Clean
3071	28	1.715E+07	5.627E+07	7.58	5.471E+03	81.27	2.270E-01	1392.3	7.413E+05	Clean
3072	28	3.070E+07	1.007E+08	7.80	8.351E+03	74.40	3.790E-01	1370.0	7.031E+05	Clean
3073	28	4.794E+07	1.573E+08	7.96	1.182E+04	70.59	5.662E-01	1360.4	6.860E+05	Clean
3074	24-32	8.202E+06	2.691E+07	7.45	2.278E+03	73.10	1.050E-01	1298.1	6.060E+05	Clean
3075	24-32	1.684E+07	5.526E+07	7.57	5.554E+03	83.04	2.255E-01	1407.0	7.633E+05	Clean
3076	24-32	3.060E+07	1.004E+08	7.80	8.318E+03	74.35	3.777E-01	1369.2	7.019E+05	Clean
3077	28	1.764E+07	5.788E+07	7.58	5.470E+03	79.72	2.314E-01	1379.6	7.219E+05	Clean
3078	0	1.375E+07	4.513E+07	10.32	1.481E+03	48.02	1.039E-01	1458.3	8.006E+05	Clean
3079	0	4.736E+06	1.554E+07	9.91	5.975E+02	52.02	3.869E-02	1457.8	8.039E+05	Clean
3080	28	8.635E+06	2.833E+07	10.13	1.052E+03	51.56	6.876E-02	1482.9	8.404E+05	0.001” distributed
3081	28	8.973E+06	2.944E+07	10.12	1.093E+03	51.50	7.149E-02	1480.6	8.369E+05	0.007” distributed
3082	28	8.753E+06	2.872E+07	10.11	1.073E+03	51.71	6.994E-02	1482.2	8.395E+05	0.012” distributed
3083	20	4.677E+06	1.534E+07	9.89	5.938E+02	52.15	3.835E-02	1456.8	8.026E+05	Clean
3084	28	1.357E+07	4.453E+07	10.35	1.551E+03	50.05	1.044E-01	1492.5	8.529E+05	Clean
3085	28	8.961E+06	2.940E+07	10.10	1.093E+03	51.48	7.151E-02	1477.4	8.321E+05	Clean
3086	16-30	1.390E+07	4.562E+07	10.32	1.582E+03	49.84	1.070E-01	1485.1	8.418E+05	Clean
3087	16-30	2.030E+07	6.662E+07	10.32	2.294E+03	49.60	1.558E-01	1482.1	8.373E+05	Clean

Table 3. Thermocouple calibration test data

Calibrated flux (W/cm ²)	Measured-flux/Calibrated-flux		
	Using chromel thermal properties	Using 15-4 thermal properties	Using 17-4 thermal properties
0.937	1.159	1.099	1.038
0.954	1.153	1.094	1.033
4.383	1.155	1.096	1.035
4.407	1.164	1.105	1.044
8.751	1.151	1.093	1.032
8.840	1.159	1.101	1.040
12.974	1.145	1.087	1.027
13.064	1.143	1.086	1.026
Average	1.154	1.095	1.034

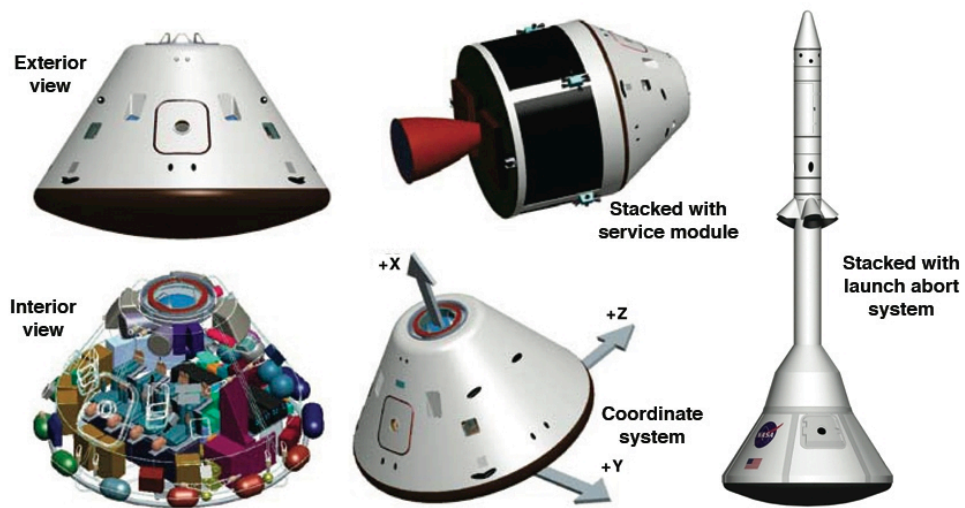


Figure 1. NASA CEV (conceptual artwork)

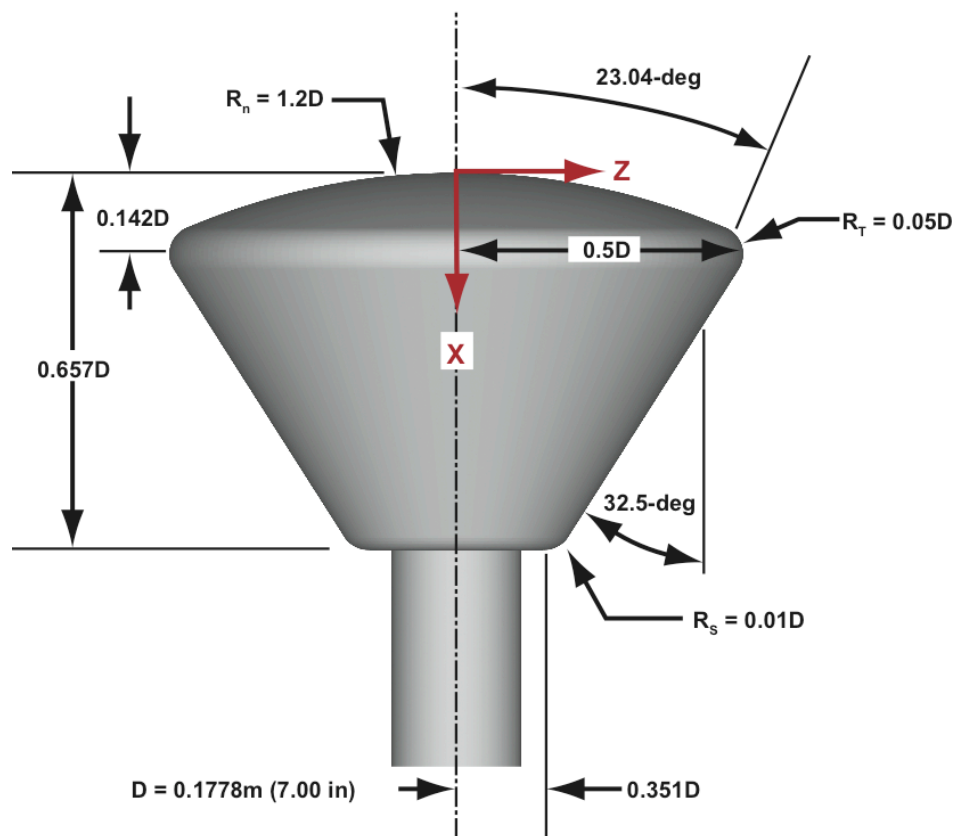


Figure 2. Wind tunnel model dimensions

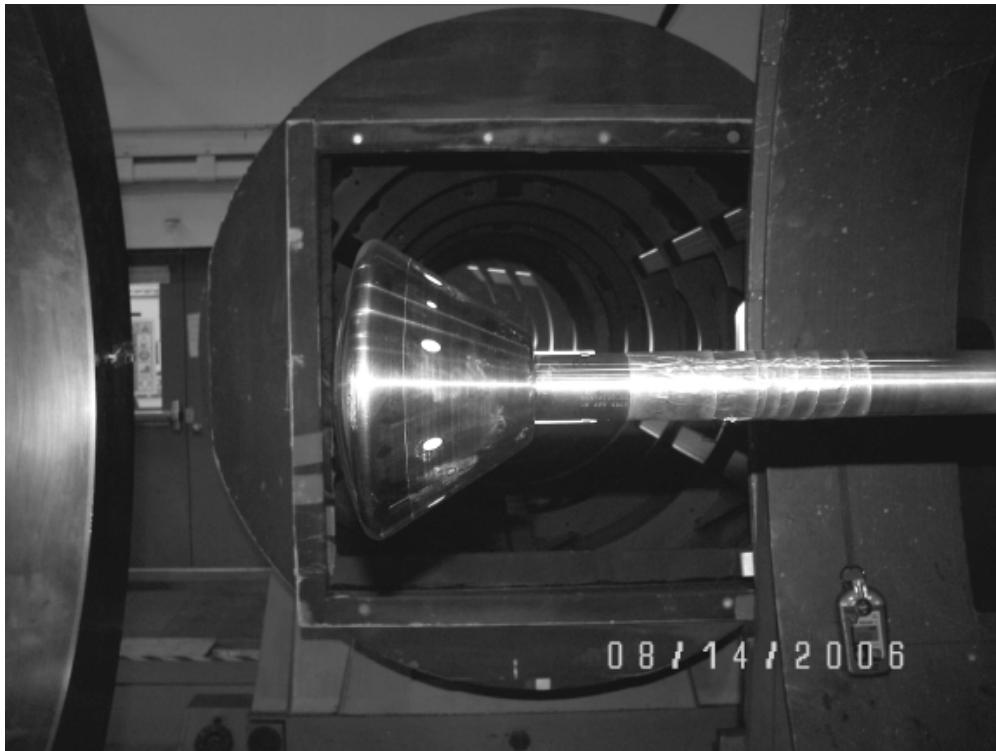


Figure 3. CEV model installed in Tunnel 9 (test section opened for viewing)

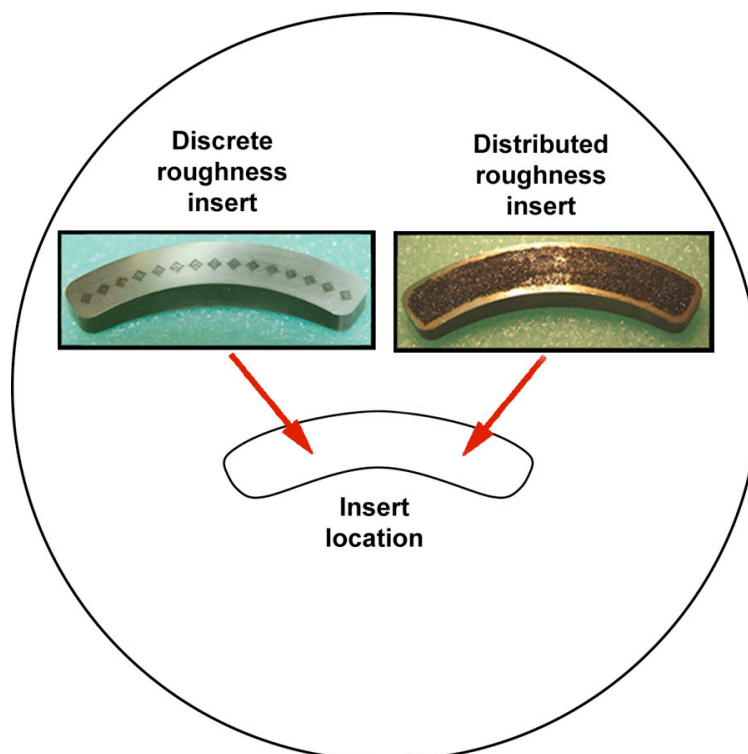


Figure 4. CEV model inserts



Figure 5. CEV model heat shield during thermocouple installation process



Figure 6. Disassembled CEV model heat shield and aftbody

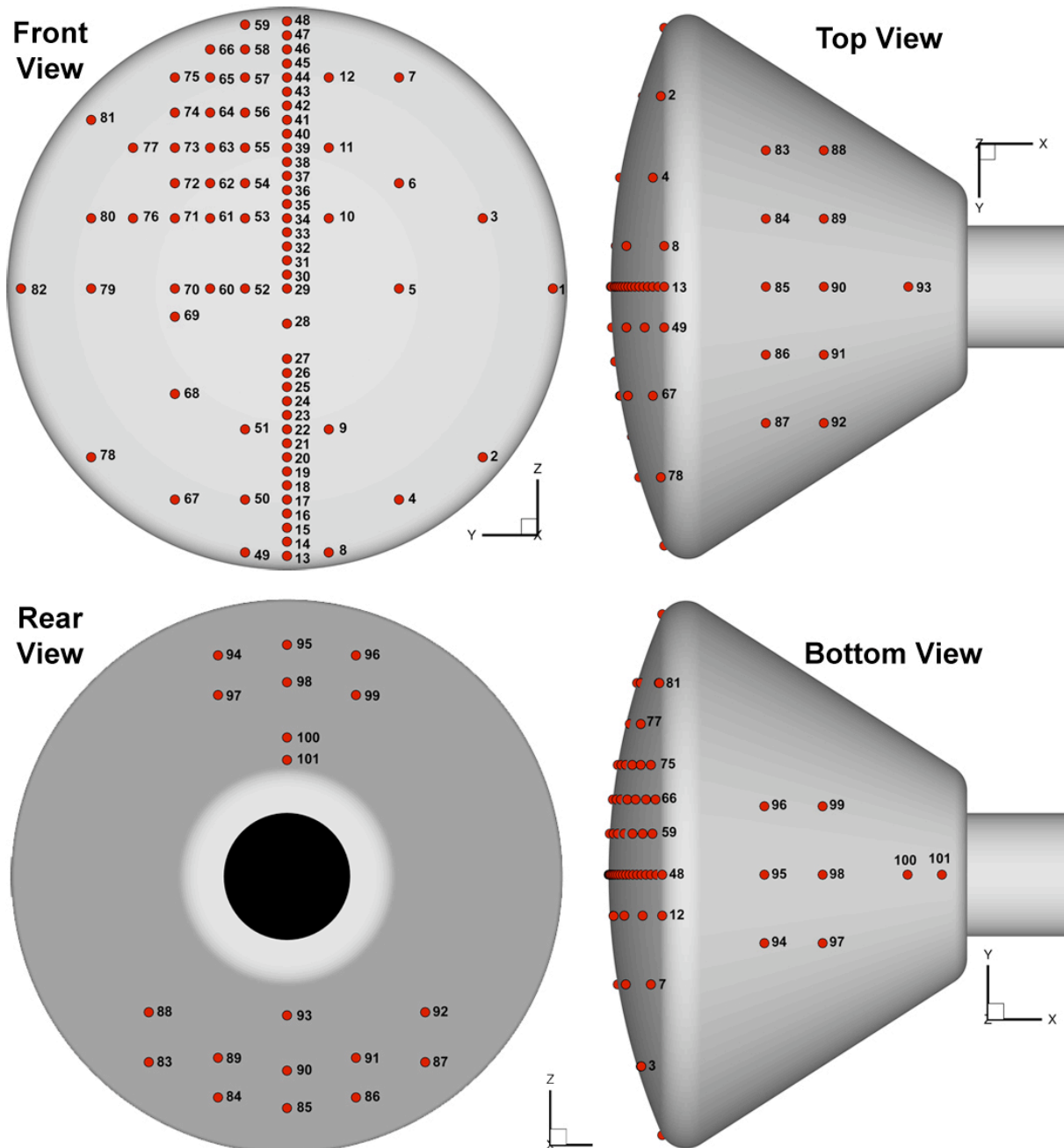


Figure 7. Thermocouple layout on CEV model



Figure 8. AEDC Hypervelocity Tunnel 9 (Mach 10 nozzle)

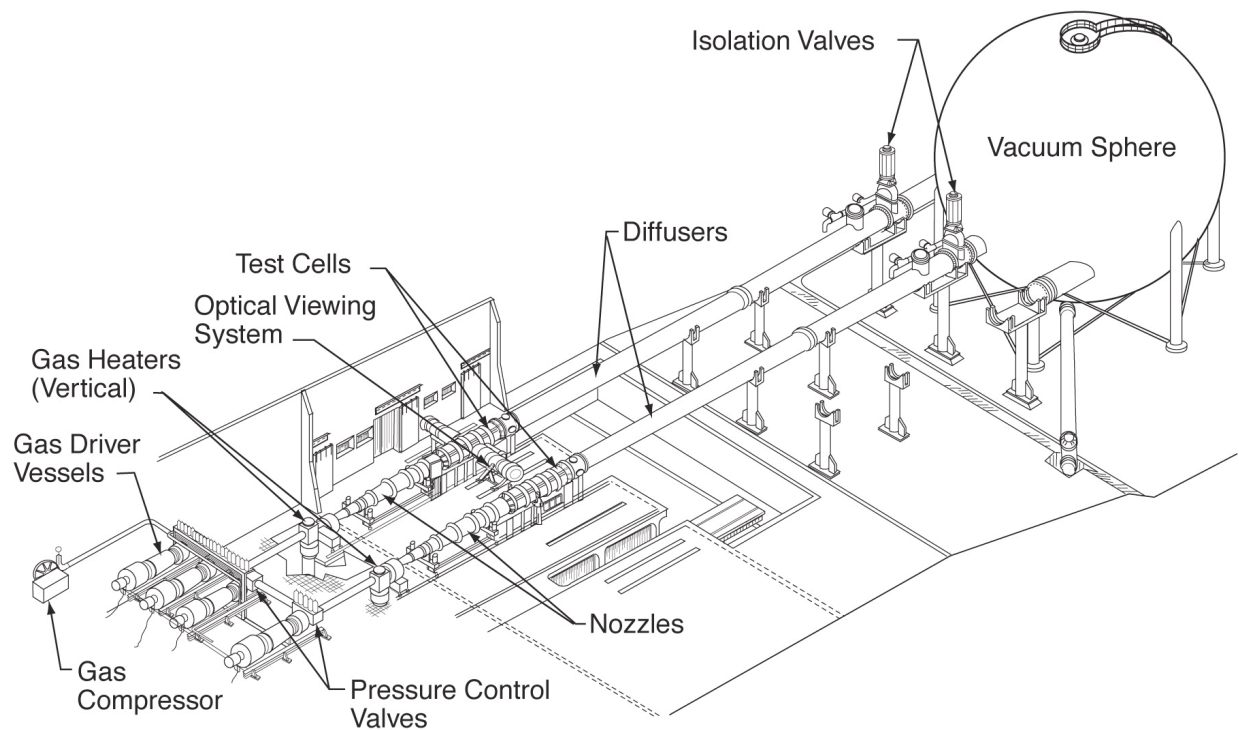
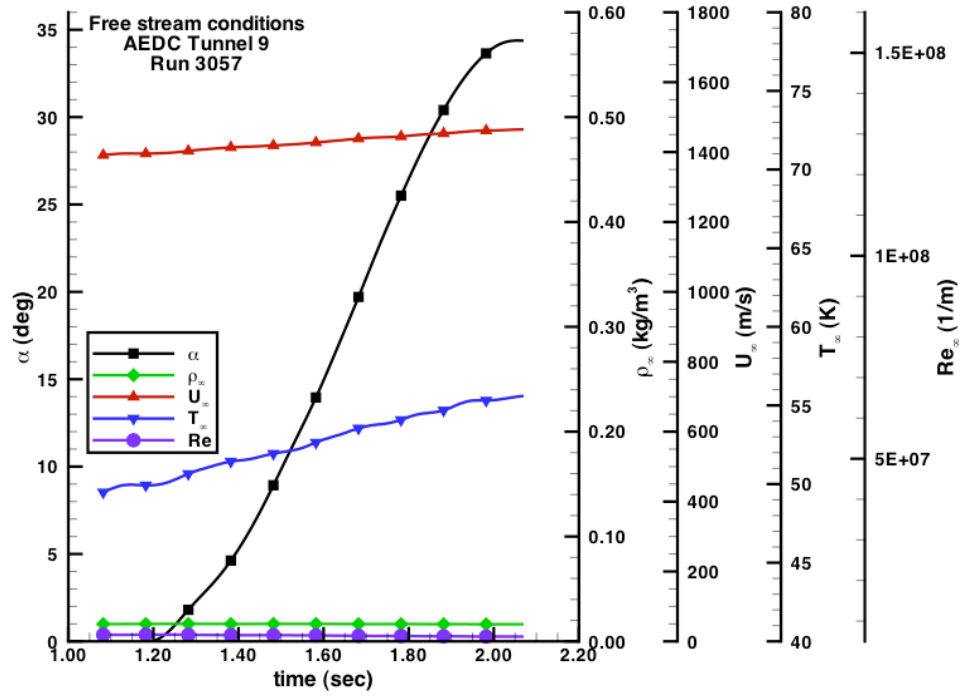
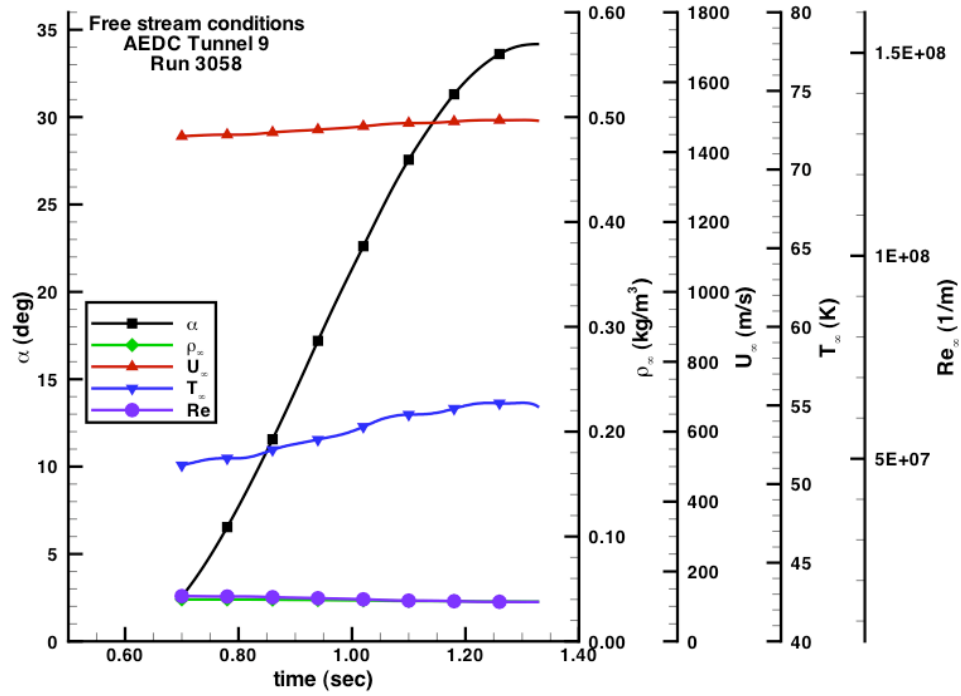


Figure 9. Schematic of AEDC Hypervelocity Tunnel 9



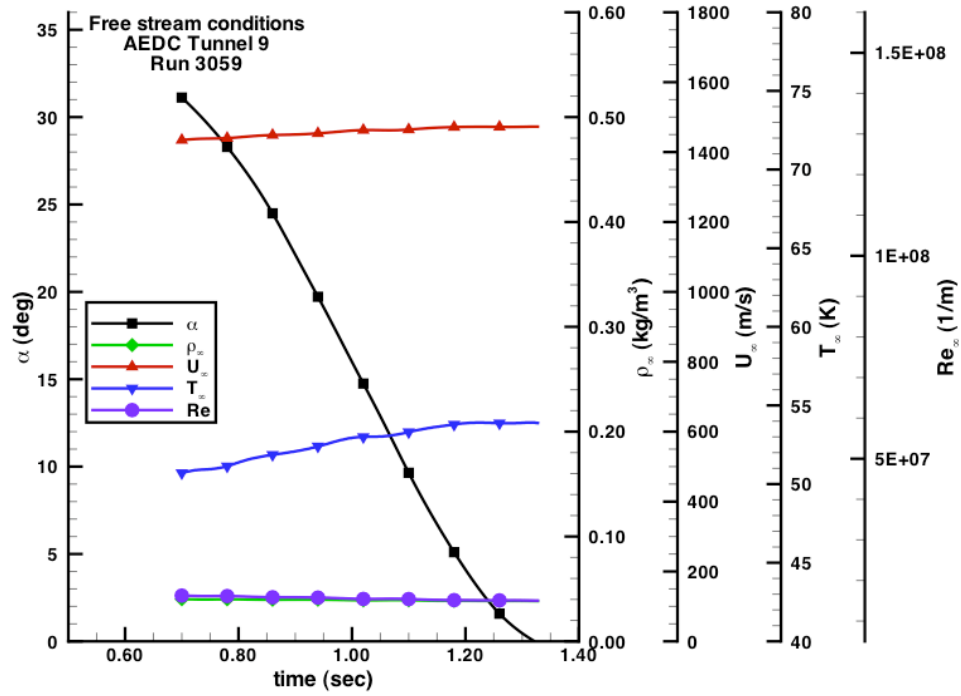
Time (sec)	α (deg)	Re_{∞} (1/ft)	Re_{∞} (1/m)	Mach	P_{∞} (Pa)	T_{∞} (K)	ρ_{∞} (kg/m ³)	U_{∞} (m/s)	H_0-H_{300K} (J/kg)
1.20	0.03	2.026E+06	6.648E+06	9.68	2.464E+02	49.93	1.662E-02	1396.1	7.137E+05
1.29	2.02	2.013E+06	6.606E+06	9.66	2.513E+02	50.74	1.668E-02	1404.2	7.259E+05
1.36	4.03	1.994E+06	6.541E+06	9.66	2.532E+02	51.33	1.661E-02	1411.8	7.372E+05
1.42	5.99	1.985E+06	6.514E+06	9.66	2.537E+02	51.55	1.657E-02	1415.3	7.423E+05
1.46	7.95	1.988E+06	6.521E+06	9.65	2.562E+02	51.82	1.665E-02	1417.5	7.457E+05
1.50	10.04	1.983E+06	6.507E+06	9.65	2.573E+02	52.04	1.665E-02	1420.3	7.499E+05
1.54	12.02	1.976E+06	6.481E+06	9.65	2.578E+02	52.25	1.661E-02	1423.3	7.545E+05
1.58	13.96	1.969E+06	6.459E+06	9.64	2.600E+02	52.64	1.663E-02	1427.3	7.605E+05
1.62	15.97	1.958E+06	6.424E+06	9.64	2.612E+02	52.98	1.660E-02	1431.3	7.666E+05
1.65	17.94	1.947E+06	6.388E+06	9.64	2.618E+02	53.26	1.655E-02	1435.1	7.723E+05
1.69	19.95	1.934E+06	6.347E+06	9.64	2.624E+02	53.57	1.649E-02	1438.9	7.780E+05
1.72	22.00	1.927E+06	6.322E+06	9.64	2.627E+02	53.76	1.645E-02	1441.5	7.820E+05
1.75	23.97	1.928E+06	6.327E+06	9.64	2.639E+02	53.88	1.649E-02	1442.7	7.840E+05
1.79	26.04	1.927E+06	6.321E+06	9.63	2.660E+02	54.18	1.653E-02	1445.6	7.885E+05
1.83	28.02	1.912E+06	6.272E+06	9.63	2.660E+02	54.48	1.644E-02	1449.9	7.950E+05
1.87	29.98	1.905E+06	6.252E+06	9.64	2.660E+02	54.62	1.640E-02	1452.7	7.991E+05
1.92	31.96	1.898E+06	6.227E+06	9.62	2.690E+02	55.13	1.643E-02	1457.2	8.062E+05
2.00	33.95	1.882E+06	6.174E+06	9.63	2.679E+02	55.34	1.630E-02	1461.9	8.132E+05
Average		1.953E+06	6.407E+06	9.64	2.601E+02	52.97	1.654E-02	1431.8	7.675E+05

Figure 10. Run 3057 free stream conditions



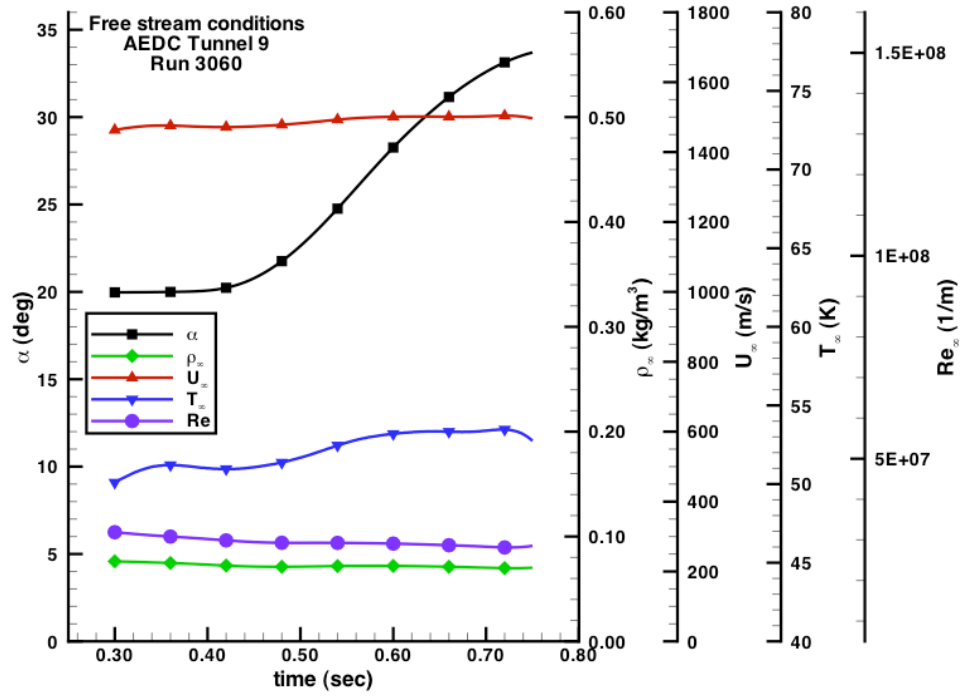
Time (sec)	α (deg)	Re_{∞} (1/ft)	Re_{∞} (1/m)	Mach	P_{∞} (Pa)	T_{∞} (K)	ρ_{∞} (kg/m ³)	U_{∞} (m/s)	H_0-H_{300K} (J/kg)
0.61	0.06	5.014E+06	1.645E+07	9.92	6.016E+02	50.27	4.030E-02	1434.2	7.680E+05
0.69	2.03	4.929E+06	1.617E+07	9.90	6.070E+02	51.12	3.999E-02	1444.0	7.829E+05
0.73	3.98	4.909E+06	1.610E+07	9.89	6.111E+02	51.46	3.999E-02	1447.7	7.886E+05
0.77	5.97	4.893E+06	1.605E+07	9.89	6.125E+02	51.64	3.994E-02	1449.5	7.914E+05
0.80	7.96	4.895E+06	1.606E+07	9.89	6.128E+02	51.64	3.996E-02	1449.7	7.917E+05
0.84	9.98	4.874E+06	1.599E+07	9.89	6.145E+02	51.88	3.989E-02	1452.3	7.957E+05
0.87	11.97	4.830E+06	1.585E+07	9.88	6.156E+02	52.25	3.968E-02	1456.9	8.027E+05
0.90	14.05	4.801E+06	1.575E+07	9.88	6.168E+02	52.52	3.955E-02	1460.2	8.078E+05
0.92	16.05	4.780E+06	1.568E+07	9.88	6.177E+02	52.71	3.946E-02	1462.5	8.114E+05
0.95	17.91	4.752E+06	1.559E+07	9.87	6.175E+02	52.91	3.930E-02	1465.2	8.155E+05
0.98	19.98	4.722E+06	1.549E+07	9.87	6.174E+02	53.14	3.913E-02	1468.2	8.202E+05
1.01	21.96	4.693E+06	1.540E+07	9.87	6.203E+02	53.49	3.905E-02	1471.9	8.260E+05
1.04	24.06	4.646E+06	1.524E+07	9.86	6.231E+02	53.98	3.887E-02	1477.1	8.342E+05
1.07	25.96	4.604E+06	1.510E+07	9.85	6.230E+02	54.31	3.863E-02	1481.2	8.406E+05
1.11	27.98	4.581E+06	1.503E+07	9.85	6.220E+02	54.43	3.849E-02	1482.8	8.431E+05
1.15	30.02	4.570E+06	1.499E+07	9.85	6.223E+02	54.53	3.843E-02	1484.2	8.453E+05
1.20	31.98	4.521E+06	1.483E+07	9.85	6.236E+02	54.98	3.820E-02	1489.2	8.531E+05
1.28	33.97	4.490E+06	1.473E+07	9.85	6.220E+02	55.14	3.799E-02	1491.3	8.565E+05
Average		4.750E+06	1.558E+07	9.87	6.167E+02	52.91	3.927E-02	1464.9	8.153E+05

Figure 11. Run 3058 free stream conditions



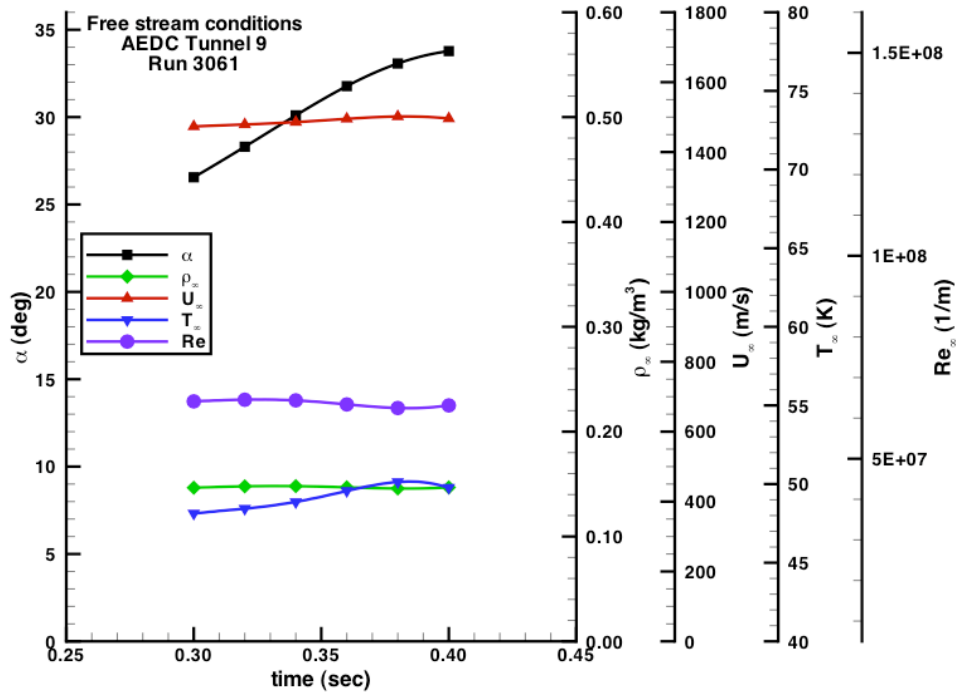
Time (sec)	α (deg)	Re_{∞} (1/ft)	Re_{∞} (1/m)	Mach	P_{∞} (Pa)	T_{∞} (K)	ρ_{∞} (kg/m ³)	U_{∞} (m/s)	H_0-H_{300K} (J/kg)
0.53	33.96	5.087E+06	1.669E+07	9.90	5.966E+02	49.45	4.062E-02	1420.4	7.474E+05
0.67	31.96	4.991E+06	1.637E+07	9.88	6.028E+02	50.38	4.030E-02	1430.3	7.624E+05
0.73	30.02	4.924E+06	1.616E+07	9.88	6.043E+02	50.92	3.996E-02	1438.1	7.742E+05
0.79	28.05	4.923E+06	1.615E+07	9.87	6.098E+02	51.20	4.011E-02	1440.5	7.779E+05
0.83	25.98	4.861E+06	1.595E+07	9.86	6.107E+02	51.68	3.979E-02	1446.4	7.870E+05
0.87	24.04	4.834E+06	1.586E+07	9.86	6.116E+02	51.91	3.968E-02	1448.9	7.908E+05
0.90	22.00	4.832E+06	1.585E+07	9.85	6.150E+02	52.09	3.976E-02	1450.3	7.930E+05
0.94	19.96	4.813E+06	1.579E+07	9.85	6.177E+02	52.36	3.973E-02	1453.1	7.974E+05
0.97	18.00	4.775E+06	1.567E+07	9.84	6.187E+02	52.68	3.954E-02	1457.1	8.035E+05
1.00	15.99	4.727E+06	1.551E+07	9.85	6.165E+02	52.94	3.921E-02	1461.4	8.101E+05
1.03	14.01	4.708E+06	1.545E+07	9.85	6.149E+02	53.01	3.906E-02	1463.0	8.125E+05
1.06	11.98	4.720E+06	1.549E+07	9.84	6.182E+02	53.07	3.923E-02	1462.4	8.117E+05
1.09	10.03	4.709E+06	1.545E+07	9.83	6.205E+02	53.26	3.924E-02	1463.8	8.138E+05
1.13	8.06	4.660E+06	1.529E+07	9.84	6.181E+02	53.50	3.891E-02	1467.5	8.195E+05
1.16	6.04	4.626E+06	1.518E+07	9.84	6.167E+02	53.70	3.867E-02	1470.6	8.243E+05
1.20	4.01	4.616E+06	1.514E+07	9.83	6.188E+02	53.88	3.868E-02	1472.0	8.266E+05
1.25	2.01	4.603E+06	1.510E+07	9.83	6.172E+02	53.89	3.857E-02	1472.1	8.268E+05
1.32	0.08	4.590E+06	1.506E+07	9.83	6.157E+02	53.91	3.846E-02	1472.7	8.276E+05
Average		4.778E+06	1.567E+07	9.85	6.135E+02	52.44	3.942E-02	1455.0	8.004E+05

Figure 12. Run 3059 free stream conditions



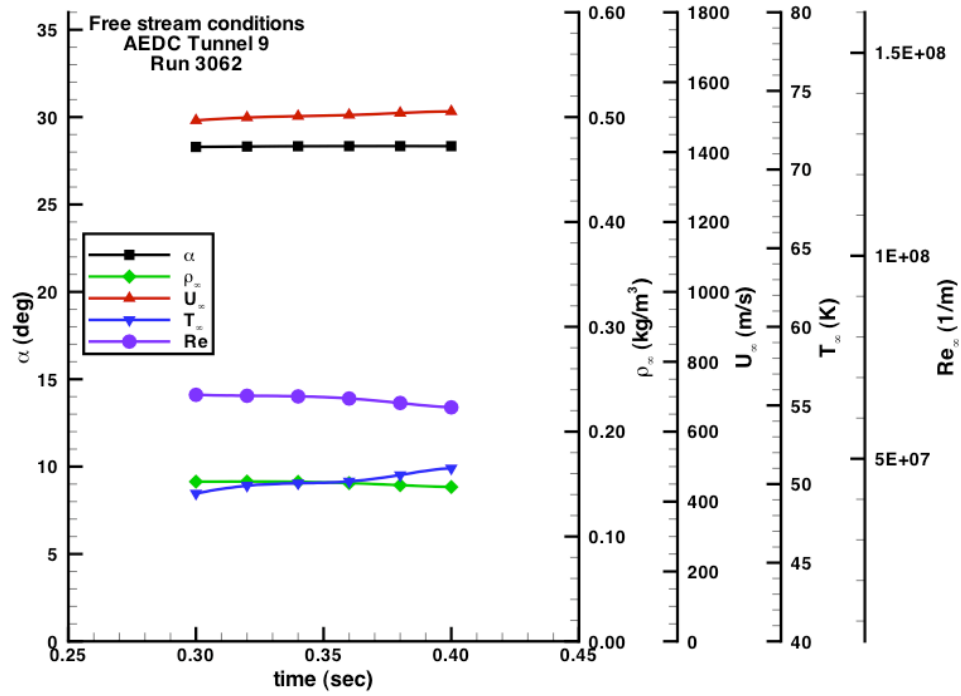
Time (sec)	α (deg)	Re_{∞} (1/ft)	Re_{∞} (1/m)	Mach	P_{∞} (Pa)	T_{∞} (K)	ρ_{∞} (kg/m ³)	U_{∞} (m/s)	H_0-H_{300K} (J/kg)
0.40	20.06	9.226E+06	3.027E+07	10.11	1.111E+03	51.04	7.330E-02	1472.3	8.240E+05
0.49	22.00	8.923E+06	2.928E+07	10.11	1.087E+03	51.46	7.113E-02	1479.3	8.348E+05
0.53	23.97	8.926E+06	2.929E+07	10.11	1.110E+03	52.17	7.165E-02	1489.0	8.499E+05
0.56	25.94	8.908E+06	2.923E+07	10.10	1.128E+03	52.80	7.195E-02	1497.0	8.625E+05
0.60	28.04	8.870E+06	2.910E+07	10.09	1.136E+03	53.16	7.196E-02	1500.7	8.684E+05
0.63	30.00	8.801E+06	2.887E+07	10.08	1.134E+03	53.34	7.159E-02	1501.5	8.698E+05
0.68	32.00	8.690E+06	2.851E+07	10.08	1.119E+03	53.32	7.068E-02	1501.1	8.692E+05
0.76	33.77	8.772E+06	2.878E+07	10.11	1.098E+03	52.41	7.058E-02	1492.2	8.550E+05
Average		8.890E+06	2.917E+07	10.10	1.115E+03	52.46	7.161E-02	1491.6	8.542E+05

Figure 13. Run 3060 free stream conditions



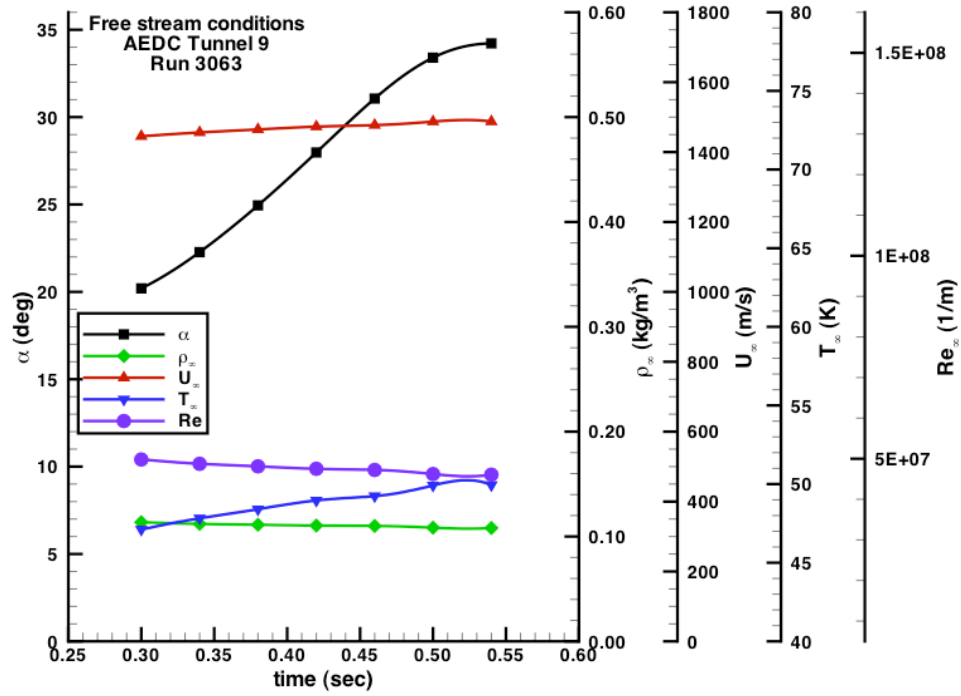
Time (sec)	α (deg)	Re_{x_0} (1/ft)	Re_{x_0} (1/m)	Mach	P_{∞} (Pa)	T_{∞} (K)	ρ_{∞} (kg/m ³)	U_{∞} (m/s)	H_0-H_{300K} (J/kg)
0.17	20.04	2.043E+07	6.704E+07	1.037E+01	1.970E+03	4.467E+01	1.484E-01	1.413E+03	7.325E+05
0.24	21.94	1.963E+07	6.441E+07	1.037E+01	1.999E+03	4.637E+01	1.452E-01	1.440E+03	7.723E+05
0.27	24.01	1.942E+07	6.370E+07	1.040E+01	2.031E+03	4.731E+01	1.446E-01	1.458E+03	7.999E+05
0.29	26.05	1.951E+07	6.399E+07	1.041E+01	2.082E+03	4.801E+01	1.461E-01	1.471E+03	8.193E+05
0.32	28.13	1.967E+07	6.453E+07	1.042E+01	2.124E+03	4.841E+01	1.478E-01	1.478E+03	8.303E+05
0.34	30.10	1.962E+07	6.438E+07	1.042E+01	2.147E+03	4.886E+01	1.480E-01	1.486E+03	8.416E+05
0.36	32.07	1.925E+07	6.316E+07	1.041E+01	2.164E+03	4.971E+01	1.466E-01	1.497E+03	8.591E+05
0.41	33.87	1.946E+07	6.383E+07	1.040E+01	2.166E+03	4.937E+01	1.478E-01	1.491E+03	8.495E+05
Average		1.962E+07	6.438E+07	1.040E+01	2.085E+03	4.784E+01	1.468E-01	1.467E+03	8.131E+05

Figure 14. Run 3061 free stream conditions



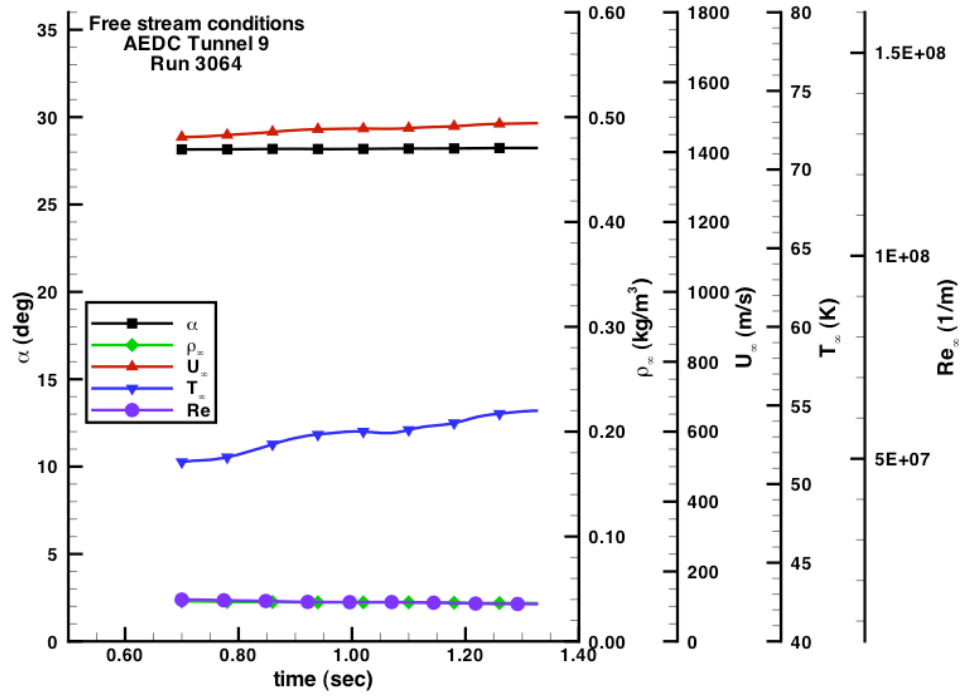
Time (sec)	α (deg)	Re_{∞} (1/ft)	Re_{∞} (1/m)	Mach	P_{∞} (Pa)	T_{∞} (K)	ρ_{∞} (kg/m ³)	U_{∞} (m/s)	H_0-H_{300K} (J/kg)
0.220	28.25	2.072E+07	6.798E+07	10.35	2.168E+03	47.17	1.548E-01	1449.5	7.869E+05
0.240	28.26	2.059E+07	6.755E+07	10.36	2.182E+03	47.61	1.544E-01	1457.4	7.988E+05
0.260	28.26	2.040E+07	6.692E+07	10.38	2.186E+03	48.03	1.533E-01	1466.7	8.128E+05
0.280	28.27	2.019E+07	6.624E+07	10.40	2.203E+03	48.67	1.525E-01	1478.6	8.310E+05
0.300	28.29	2.003E+07	6.573E+07	10.40	2.234E+03	49.41	1.523E-01	1490.5	8.494E+05
0.320	28.32	1.997E+07	6.551E+07	10.41	2.258E+03	49.90	1.524E-01	1498.7	8.621E+05
0.330	28.33	1.996E+07	6.547E+07	10.41	2.262E+03	50.00	1.524E-01	1501.1	8.657E+05
Average		2.026E+07	6.648E+07	10.39	2.213E+03	48.68	1.532E-01	1477.5	8.295E+05

Figure 15. Run 3062 free stream conditions



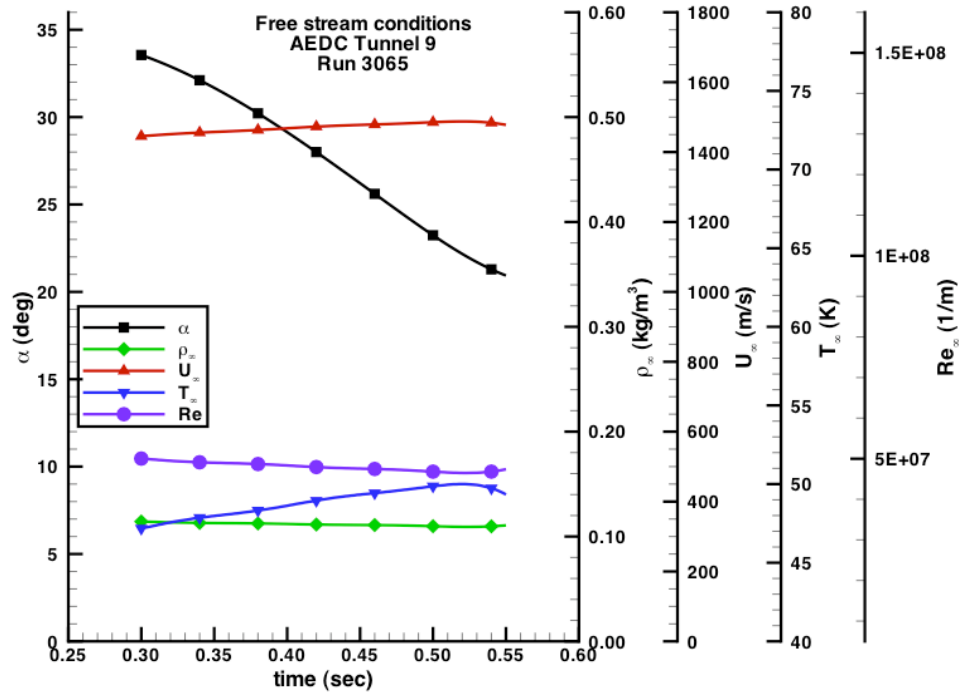
Time (sec)	α (deg)	Re_{∞} (1/ft)	Re_{∞} (1/m)	Mach	P_{∞} (Pa)	T_{∞} (K)	ρ_{∞} (kg/m ³)	U_{∞} (m/s)	H_0-H_{300K} (J/kg)
0.30	20.12	1.520E+07	4.986E+07	10.33	1.589E+03	47.07	1.137E-01	1444.6	7.796E+05
0.34	22.03	1.489E+07	4.884E+07	10.32	1.590E+03	47.76	1.121E-01	1455.1	7.956E+05
0.37	23.96	1.473E+07	4.832E+07	10.33	1.595E+03	48.20	1.114E-01	1461.8	8.057E+05
0.39	25.98	1.459E+07	4.788E+07	10.32	1.601E+03	48.62	1.109E-01	1467.8	8.150E+05
0.42	27.98	1.448E+07	4.751E+07	10.32	1.605E+03	48.96	1.104E-01	1472.7	8.225E+05
0.45	30.02	1.443E+07	4.734E+07	10.32	1.608E+03	49.14	1.102E-01	1475.5	8.269E+05
0.47	32.02	1.433E+07	4.703E+07	10.32	1.610E+03	49.40	1.098E-01	1479.5	8.331E+05
0.52	33.97	1.393E+07	4.571E+07	10.32	1.604E+03	50.23	1.076E-01	1491.5	8.516E+05
Average		1.457E+07	4.781E+07	10.32	1.600E+03	48.67	1.108E-01	1468.6	8.162E+05

Figure 16. Run 3063 free stream conditions



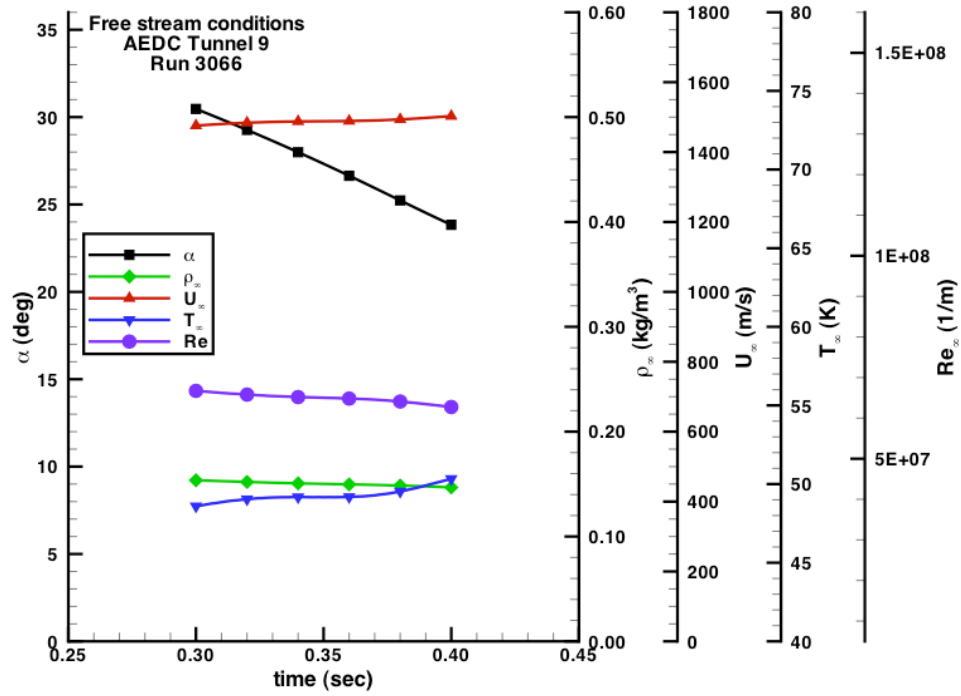
Time (sec)	α (deg)	Re_{∞} (1/ft)	Re_{∞} (1/m)	Mach	P_{∞} (Pa)	T_{∞} (K)	ρ_{∞} (kg/m ³)	U_{∞} (m/s)	H_0-H_{300K} (J/kg)
0.53	28.14	4.786E+06	1.570E+07	9.90	5.683E+02	49.85	3.839E-02	1425.0	7.544E+05
0.60	28.15	4.759E+06	1.561E+07	9.89	5.708E+02	50.17	3.831E-02	1429.1	7.605E+05
0.70	28.15	4.661E+06	1.529E+07	9.87	5.809E+02	51.40	3.806E-02	1442.8	7.815E+05
0.80	28.16	4.587E+06	1.505E+07	9.87	5.790E+02	51.88	3.759E-02	1450.7	7.934E+05
0.90	28.18	4.497E+06	1.475E+07	9.86	5.857E+02	52.93	3.727E-02	1462.5	8.117E+05
1.00	28.18	4.469E+06	1.466E+07	9.85	5.894E+02	53.34	3.721E-02	1466.9	8.186E+05
1.10	28.20	4.458E+06	1.463E+07	9.85	5.897E+02	53.45	3.716E-02	1468.4	8.208E+05
1.20	28.21	4.383E+06	1.438E+07	9.84	5.902E+02	54.07	3.676E-02	1475.7	8.322E+05
1.30	28.23	4.329E+06	1.420E+07	9.83	5.923E+02	54.62	3.652E-02	1481.9	8.419E+05
1.30	28.23	4.329E+06	1.420E+07	9.83	5.923E+02	54.62	3.652E-02	1481.9	8.420E+05
1.30	28.23	4.327E+06	1.420E+07	9.83	5.922E+02	54.63	3.651E-02	1482.0	8.420E+05
1.31	28.23	4.326E+06	1.419E+07	9.83	5.922E+02	54.63	3.650E-02	1482.0	8.421E+05
1.31	28.23	4.326E+06	1.419E+07	9.83	5.921E+02	54.63	3.650E-02	1482.1	8.422E+05
1.31	28.23	4.326E+06	1.419E+07	9.83	5.922E+02	54.64	3.650E-02	1482.1	8.423E+05
Average		4.469E+06	1.466E+07	9.85	5.862E+02	53.20	3.713E-02	1465.2	8.161E+05

Figure 17. Run 3064 free stream conditions



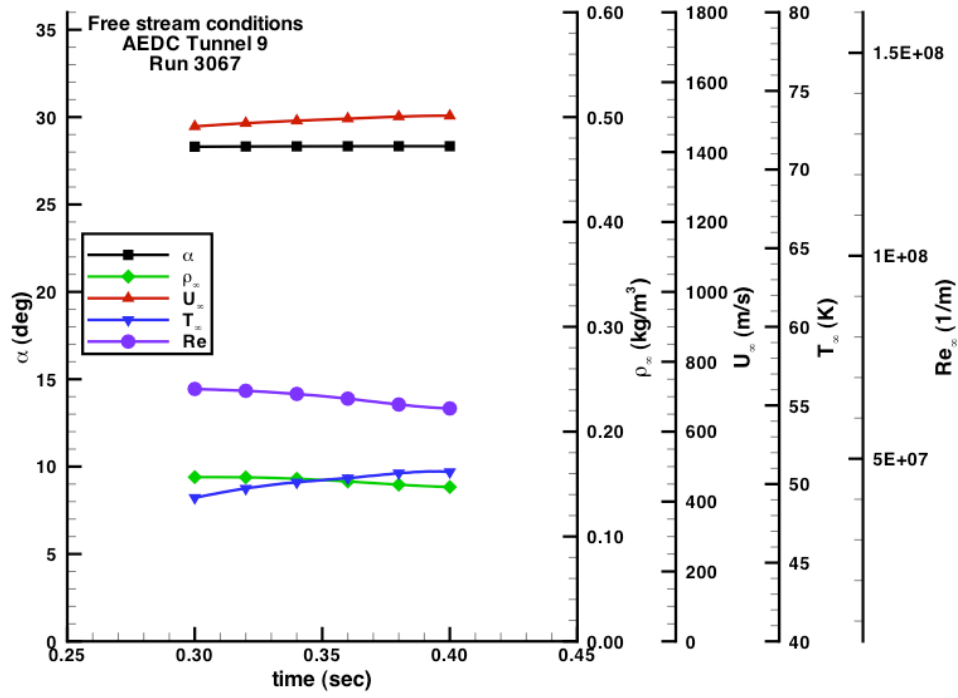
Time (sec)	α (deg)	Re_{∞} (1/ft)	Re_{∞} (1/m)	Mach	P_{∞} (Pa)	T_{∞} (K)	ρ_{∞} (kg/m ³)	U_{∞} (m/s)	H_0-H_{300K} (J/kg)
0.28	34.04	1.538E+07	5.045E+07	10.32	1.596E+03	46.83	1.148E-01	1440.3	7.732E+05
0.34	32.03	1.496E+07	4.909E+07	10.32	1.606E+03	47.89	1.129E-01	1456.1	7.971E+05
0.38	30.01	1.482E+07	4.862E+07	10.32	1.614E+03	48.38	1.124E-01	1464.1	8.093E+05
0.42	28.00	1.462E+07	4.795E+07	10.32	1.619E+03	48.95	1.114E-01	1472.7	8.225E+05
0.45	25.97	1.448E+07	4.752E+07	10.32	1.626E+03	49.37	1.110E-01	1478.2	8.310E+05
0.49	24.05	1.435E+07	4.710E+07	10.32	1.628E+03	49.70	1.103E-01	1482.9	8.383E+05
0.52	21.98	1.417E+07	4.650E+07	10.32	1.621E+03	49.99	1.092E-01	1487.5	8.455E+05
0.59	20.14	1.672E+07	5.484E+07	10.38	1.598E+03	44.45	1.210E-01	1411.2	7.293E+05
Average		1.494E+07	4.901E+07	10.33	1.613E+03	48.19	1.129E-01	1461.6	8.058E+05

Figure 18. Run 3065 free stream conditions



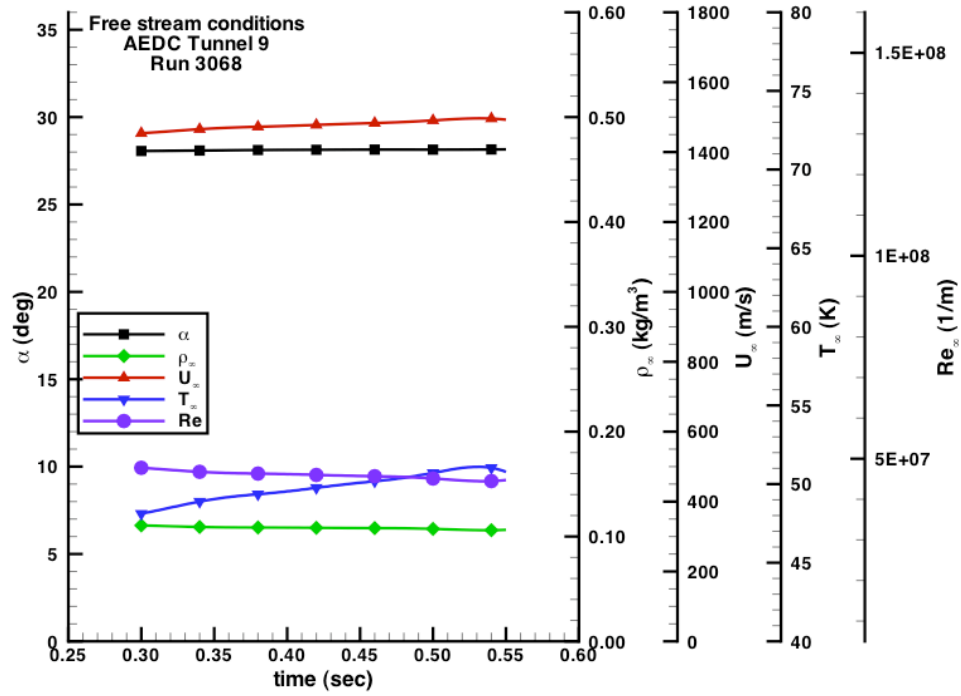
Time (sec)	α (deg)	Re_{x_0} (1/ft)	Re_{x_0} (1/m)	Mach	P_{∞} (Pa)	T_{∞} (K)	ρ_{∞} (kg/m ³)	U_{∞} (m/s)	H_0-H_{300K} (J/kg)
0.22	34.02	2.108E+07	6.915E+07	10.36	2.177E+03	46.79	1.567E-01	1445.32	7.804E+05
0.27	32.01	2.067E+07	6.782E+07	10.37	2.207E+03	47.89	1.552E-01	1463.61	8.081E+05
0.31	30.00	2.022E+07	6.634E+07	10.39	2.216E+03	48.80	1.530E-01	1479.40	8.323E+05
0.34	27.99	1.987E+07	6.519E+07	10.41	2.199E+03	49.18	1.507E-01	1487.59	8.448E+05
0.37	26.08	1.970E+07	6.462E+07	10.41	2.184E+03	49.25	1.493E-01	1490.01	8.485E+05
0.40	23.97	1.917E+07	6.288E+07	10.39	2.193E+03	50.25	1.470E-01	1501.86	8.672E+05
0.43	22.00	1.912E+07	6.272E+07	10.40	2.165E+03	49.92	1.461E-01	1498.13	8.613E+05
0.48	21.28	2.488E+07	8.162E+07	10.62	1.983E+03	39.92	1.671E-01	1369.09	6.662E+05
Average		2.059E+07	6.754E+07	10.42	2.166E+03	47.75	1.531E-01	1466.88	8.136E+05

Figure 19. Run 3066 free stream conditions



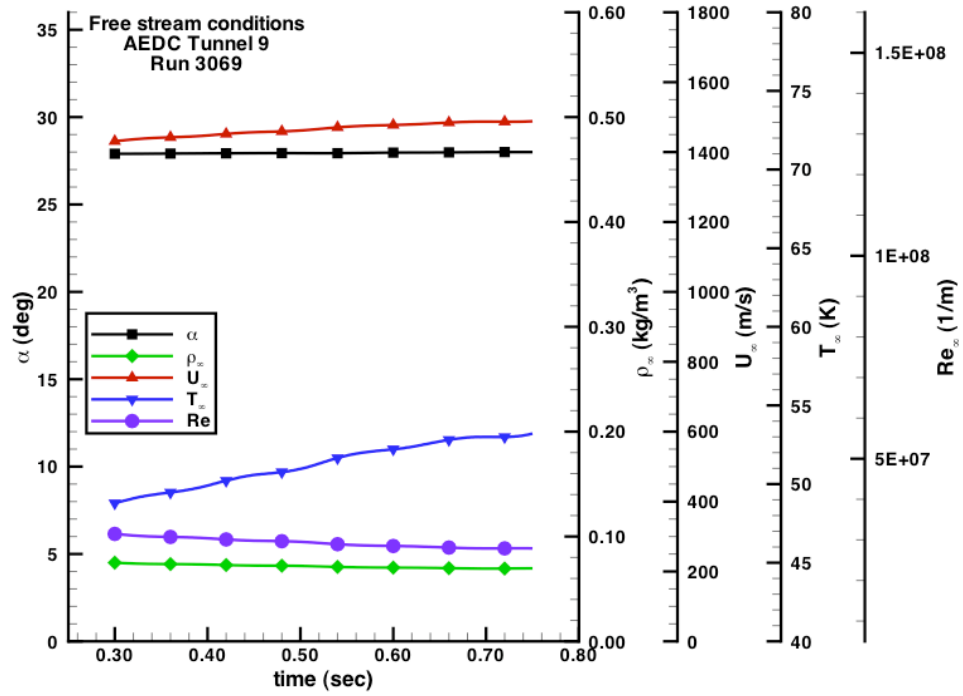
Time (sec)	α (deg)	Re_{∞} (1/ft)	Re_{∞} (1/m)	Mach	P_{∞} (Pa)	T_{∞} (K)	ρ_{∞} (kg/m ³)	U_{∞} (m/s)	H_0-H_{300K} (J/kg)
0.22	28.25	2.109E+07	6.918E+07	10.34	2.153E+03	46.34	1.564E-01	1434.5	7.643E+05
0.24	28.28	2.082E+07	6.831E+07	10.32	2.192E+03	47.26	1.562E-01	1446.0	7.819E+05
0.26	28.30	2.066E+07	6.778E+07	10.31	2.219E+03	47.89	1.561E-01	1454.8	7.952E+05
0.28	28.30	2.057E+07	6.748E+07	10.31	2.249E+03	48.47	1.563E-01	1463.6	8.086E+05
0.30	28.31	2.047E+07	6.717E+07	10.31	2.284E+03	49.13	1.566E-01	1473.3	8.236E+05
0.32	28.32	2.034E+07	6.673E+07	10.31	2.308E+03	49.72	1.564E-01	1482.5	8.378E+05
0.34	28.33	2.010E+07	6.596E+07	10.32	2.306E+03	50.11	1.551E-01	1489.7	8.488E+05
0.35	28.33	1.994E+07	6.543E+07	10.33	2.296E+03	50.25	1.539E-01	1492.6	8.534E+05
Average		2.050E+07	6.726E+07	10.32	2.251E+03	48.64	1.559E-01	1467.1	8.142E+05

Figure 20. Run 3067 free stream conditions



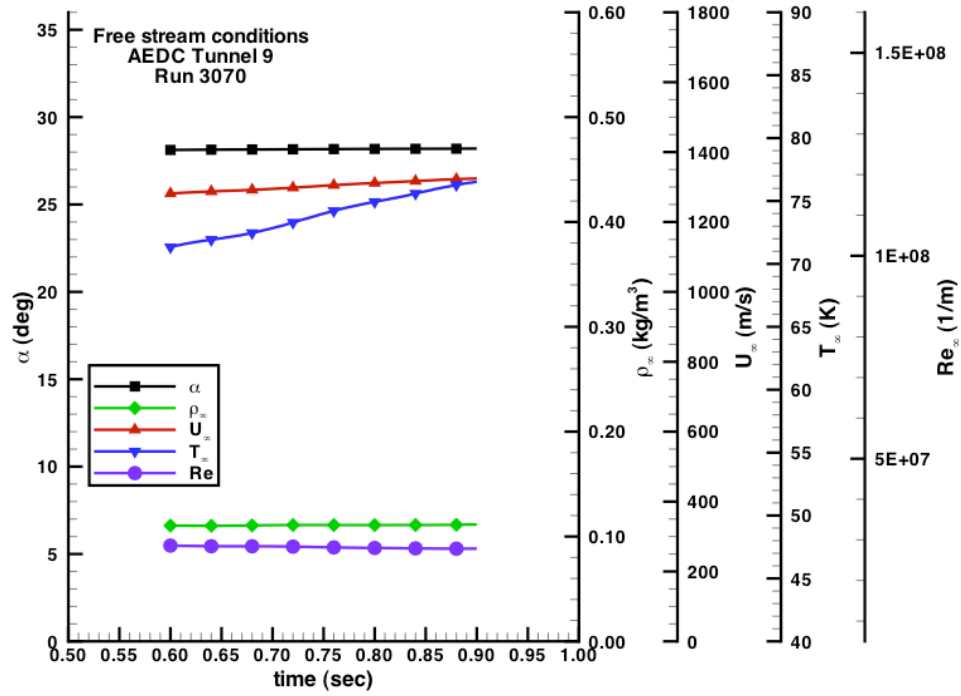
Time (sec)	α (deg)	Re_{∞} (1/ft)	Re_{∞} (1/m)	Mach	P_{∞} (Pa)	T_{∞} (K)	ρ_{∞} (kg/m ³)	U_{∞} (m/s)	H_0-H_{300K} (J/kg)
0.30	28.06	1.456E+07	4.777E+07	10.28	1.579E+03	48.11	1.106E-01	1453.9	7.942E+05
0.32	28.07	1.440E+07	4.724E+07	10.28	1.581E+03	48.51	1.098E-01	1459.6	8.029E+05
0.34	28.09	1.426E+07	4.678E+07	10.28	1.584E+03	48.89	1.091E-01	1465.4	8.118E+05
0.36	28.10	1.417E+07	4.648E+07	10.28	1.587E+03	49.17	1.087E-01	1469.7	8.183E+05
0.38	28.12	1.412E+07	4.634E+07	10.28	1.591E+03	49.35	1.086E-01	1472.4	8.224E+05
0.40	28.12	1.408E+07	4.620E+07	10.28	1.595E+03	49.54	1.085E-01	1474.8	8.262E+05
0.42	28.13	1.402E+07	4.601E+07	10.27	1.600E+03	49.76	1.083E-01	1477.7	8.306E+05
0.44	28.14	1.397E+07	4.582E+07	10.27	1.605E+03	49.99	1.081E-01	1480.5	8.351E+05
0.46	28.14	1.393E+07	4.569E+07	10.27	1.609E+03	50.18	1.080E-01	1483.0	8.390E+05
0.48	28.14	1.387E+07	4.550E+07	10.27	1.613E+03	50.40	1.078E-01	1486.0	8.437E+05
0.49	28.14	1.381E+07	4.532E+07	10.27	1.614E+03	50.55	1.076E-01	1488.1	8.470E+05
Average		1.411E+07	4.629E+07	10.27	1.596E+03	49.50	1.086E-01	1473.7	8.247E+05

Figure 21. Run 3068 free stream conditions



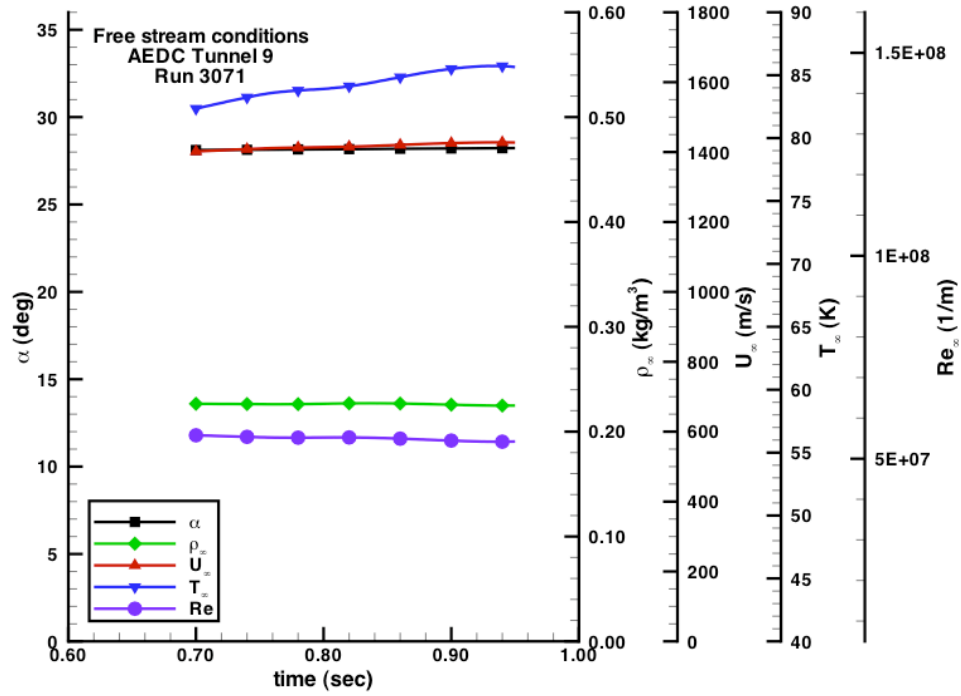
Time (sec)	α (deg)	Re_{x_0} (1/ft)	Re_{x_0} (1/m)	Mach	P_{∞} (Pa)	T_{∞} (K)	ρ_{∞} (kg/m ³)	U_{∞} (m/s)	H_0-H_{300K} (J/kg)
0.36	27.91	9.366E+06	3.073E+07	10.06	1.082E+03	49.47	7.368E-02	1442.20	7.786E+05
0.40	27.92	9.263E+06	3.039E+07	10.05	1.085E+03	49.90	7.323E-02	1447.52	7.867E+05
0.45	27.94	9.082E+06	2.980E+07	10.04	1.086E+03	50.58	7.229E-02	1456.75	8.008E+05
0.50	27.94	9.000E+06	2.953E+07	10.04	1.088E+03	50.96	7.192E-02	1461.68	8.084E+05
0.55	27.94	8.779E+06	2.880E+07	10.03	1.089E+03	51.81	7.077E-02	1472.54	8.252E+05
0.60	27.97	8.686E+06	2.850E+07	10.03	1.090E+03	52.22	7.033E-02	1477.37	8.327E+05
0.65	27.98	8.590E+06	2.818E+07	10.02	1.095E+03	52.71	6.993E-02	1483.00	8.416E+05
0.70	27.99	8.501E+06	2.789E+07	10.02	1.092E+03	53.00	6.938E-02	1487.12	8.480E+05
0.75	28.00	8.503E+06	2.790E+07	10.00	1.100E+03	53.21	6.961E-02	1488.22	8.498E+05
0.76	28.00	8.479E+06	2.782E+07	10.00	1.103E+03	53.38	6.956E-02	1489.99	8.527E+05
Average		8.825E+06	2.895E+07	10.03	1.091E+03	51.72	7.107E-02	1470.64	8.225E+05

Figure 22. Run 3069 free stream conditions



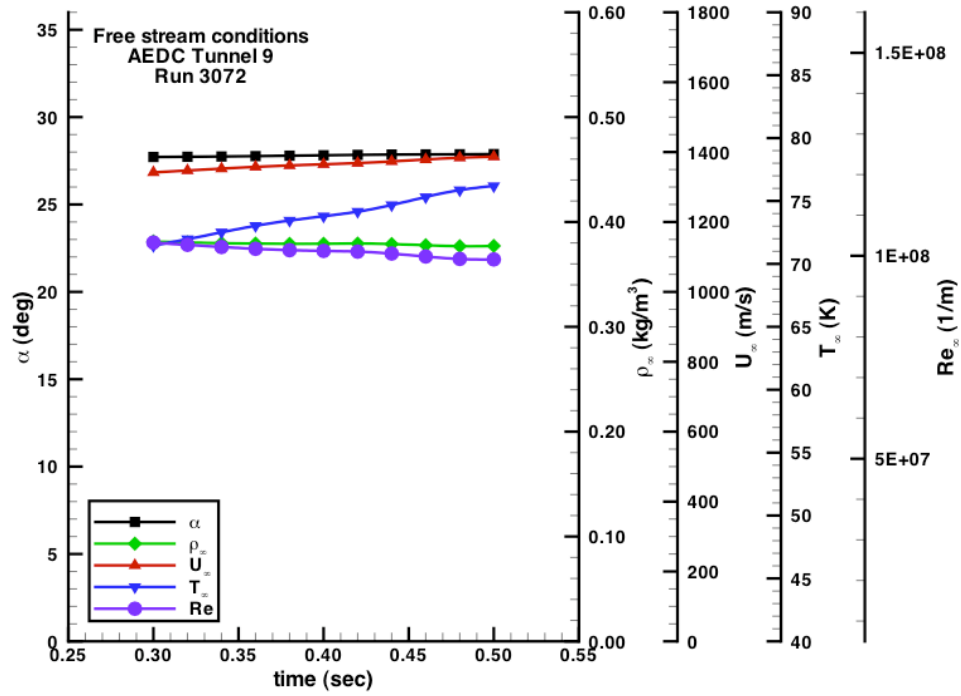
Time (sec)	α (deg)	Re_{∞} (1/ft)	Re_{∞} (1/m)	Mach	P_{∞} (Pa)	T_{∞} (K)	ρ_{∞} (kg/m ³)	U_{∞} (m/s)	H_0-H_{300K} (J/kg)
0.53	28.11	8.805E+06	2.889E+07	7.45	2.291E+03	69.92	1.104E-01	1269.5	5.659E+05
0.55	28.11	8.782E+06	2.881E+07	7.45	2.302E+03	70.27	1.104E-01	1272.7	5.702E+05
0.60	28.12	8.719E+06	2.860E+07	7.44	2.338E+03	71.33	1.105E-01	1281.4	5.825E+05
0.65	28.14	8.667E+06	2.843E+07	7.44	2.357E+03	72.04	1.103E-01	1288.5	5.923E+05
0.70	28.15	8.658E+06	2.841E+07	7.44	2.396E+03	72.85	1.108E-01	1294.7	6.011E+05
0.75	28.17	8.594E+06	2.819E+07	7.43	2.436E+03	74.00	1.109E-01	1303.6	6.139E+05
0.80	28.18	8.537E+06	2.801E+07	7.43	2.466E+03	74.93	1.109E-01	1311.4	6.251E+05
0.85	28.19	8.495E+06	2.787E+07	7.43	2.496E+03	75.78	1.110E-01	1318.6	6.354E+05
0.90	28.20	8.486E+06	2.784E+07	7.42	2.531E+03	76.53	1.114E-01	1324.4	6.439E+05
0.95	28.21	8.454E+06	2.774E+07	7.42	2.560E+03	77.30	1.116E-01	1330.9	6.532E+05
Average		8.620E+06	2.828E+07	7.44	2.417E+03	73.49	1.108E-01	1299.6	6.084E+05

Figure 23. Run 3070 free stream conditions



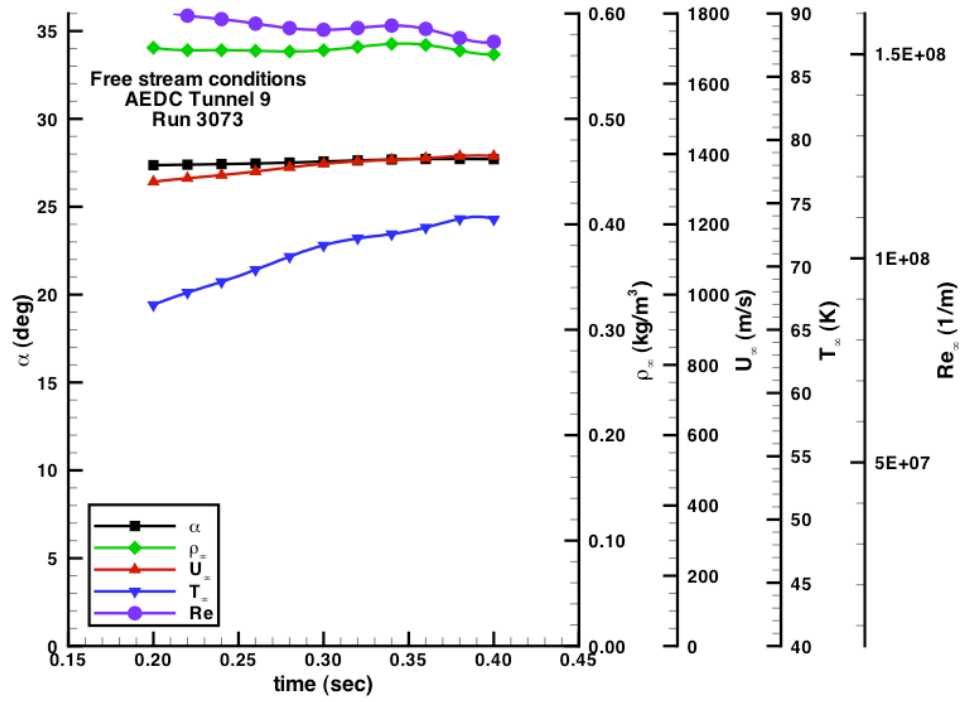
Time (sec)	α (deg)	Re_{∞} (1/ft)	Re_{∞} (1/m)	Mach	P_{∞} (Pa)	T_{∞} (K)	ρ_{∞} (kg/m ³)	U_{∞} (m/s)	H_0-H_{300K} (J/kg)
0.42	27.97	1.787E+07	5.863E+07	7.59	5.118E+03	75.62	2.282E-01	1346.1	6.719E+05
0.45	27.99	1.780E+07	5.841E+07	7.59	5.163E+03	76.26	2.283E-01	1351.6	6.799E+05
0.50	28.01	1.764E+07	5.789E+07	7.59	5.261E+03	77.67	2.284E-01	1362.9	6.967E+05
0.55	28.04	1.740E+07	5.708E+07	7.58	5.333E+03	79.11	2.273E-01	1375.0	7.147E+05
0.60	28.06	1.736E+07	5.695E+07	7.59	5.391E+03	79.83	2.277E-01	1381.7	7.247E+05
0.65	28.09	1.717E+07	5.632E+07	7.58	5.474E+03	81.23	2.272E-01	1392.7	7.414E+05
0.70	28.12	1.700E+07	5.576E+07	7.58	5.534E+03	82.36	2.266E-01	1401.7	7.552E+05
0.75	28.14	1.685E+07	5.529E+07	7.57	5.598E+03	83.44	2.262E-01	1410.0	7.679E+05
0.80	28.16	1.684E+07	5.523E+07	7.57	5.639E+03	83.91	2.266E-01	1414.0	7.740E+05
0.85	28.18	1.678E+07	5.505E+07	7.57	5.698E+03	84.64	2.270E-01	1419.1	7.820E+05
0.90	28.21	1.660E+07	5.447E+07	7.56	5.724E+03	85.50	2.257E-01	1425.6	7.921E+05
0.93	28.22	1.652E+07	5.420E+07	7.56	5.719E+03	85.73	2.249E-01	1427.6	7.953E+05
Average		1.715E+07	5.627E+07	7.58	5.471E+03	81.27	2.270E-01	1392.3	7.413E+05

Figure 24. Run 3071 free stream conditions



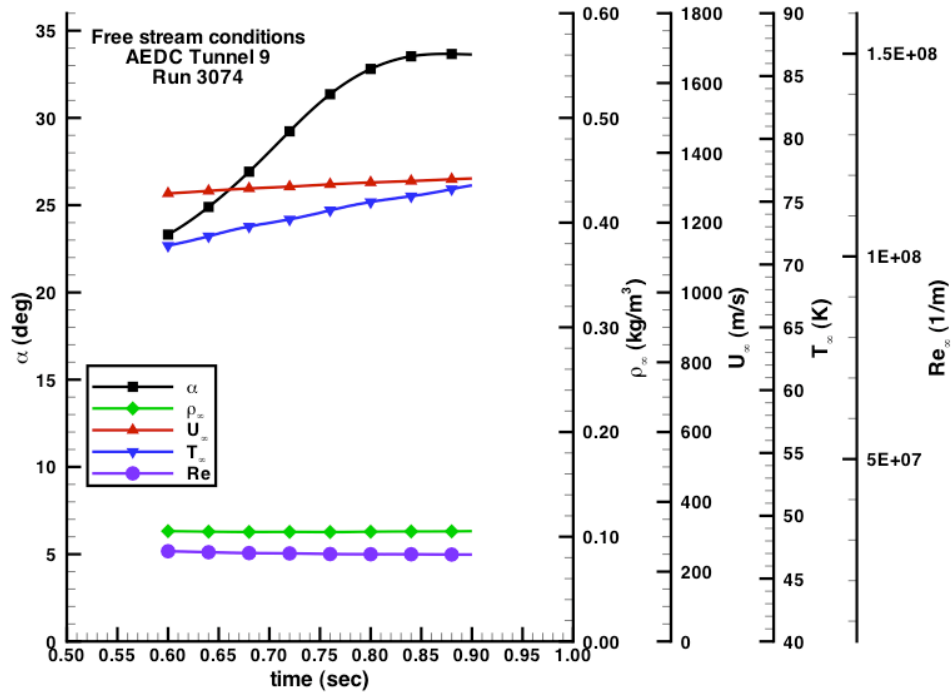
Time (sec)	α (deg)	Re_{∞} (1/ft)	Re_{∞} (1/m)	Mach	P_{∞} (Pa)	T_{∞} (K)	ρ_{∞} (kg/m ³)	U_{∞} (m/s)	H_0-H_{300K} (J/kg)
0.31	27.72	3.138E+07	1.030E+08	7.79	8.092E+03	71.71	3.809E-01	1344.5	6.656E+05
0.35	27.76	3.107E+07	1.019E+08	7.80	8.183E+03	72.77	3.796E-01	1355.2	6.811E+05
0.40	27.82	3.084E+07	1.012E+08	7.80	8.288E+03	73.79	3.792E-01	1365.0	6.955E+05
0.45	27.86	3.054E+07	1.002E+08	7.80	8.405E+03	74.99	3.784E-01	1376.0	7.118E+05
0.50	27.88	3.021E+07	9.910E+07	7.80	8.513E+03	76.19	3.772E-01	1386.7	7.279E+05
0.54	27.92	3.015E+07	9.892E+07	7.80	8.626E+03	76.94	3.785E-01	1392.6	7.368E+05
Average		3.070E+07	1.007E+08	7.80	8.351E+03	74.40	3.790E-01	1370.0	7.031E+05

Figure 25. Run 3072 free stream conditions



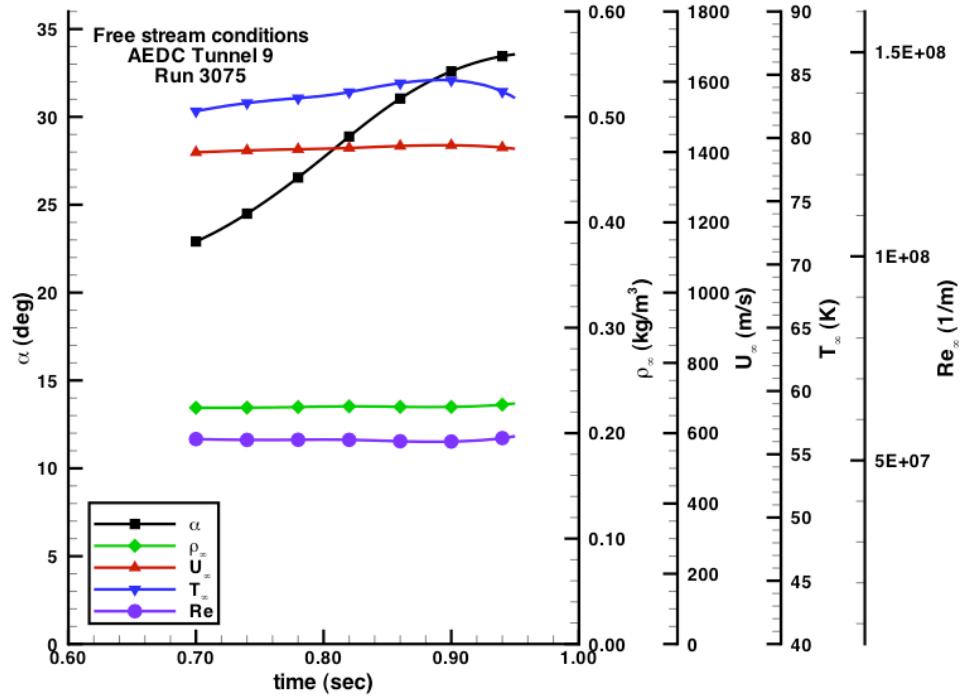
Time (sec)	α (deg)	Re_{∞} (1/ft)	Re_{∞} (1/m)	Mach	P_{∞} (Pa)	T_{∞} (K)	ρ_{∞} (kg/m ³)	U_{∞} (m/s)	H_0-H_{300K} (J/kg)
0.23	27.41	4.847E+07	1.590E+08	7.94	1.143E+04	68.37	5.652E-01	1335.6	6.502E+05
0.24	27.43	4.834E+07	1.586E+08	7.94	1.150E+04	68.79	5.652E-01	1340.0	6.566E+05
0.26	27.46	4.801E+07	1.575E+08	7.94	1.165E+04	69.75	5.646E-01	1350.3	6.714E+05
0.28	27.51	4.768E+07	1.564E+08	7.95	1.181E+04	70.78	5.640E-01	1361.9	6.881E+05
0.30	27.57	4.755E+07	1.560E+08	7.96	1.198E+04	71.67	5.651E-01	1372.2	7.032E+05
0.32	27.64	4.768E+07	1.564E+08	7.97	1.214E+04	72.23	5.682E-01	1379.2	7.133E+05
0.34	27.69	4.786E+07	1.570E+08	7.98	1.226E+04	72.56	5.711E-01	1383.5	7.195E+05
Average		4.794E+07	1.573E+08	7.96	1.182E+04	70.59	5.662E-01	1360.4	6.860E+05

Figure 26. Run 3073 free stream conditions



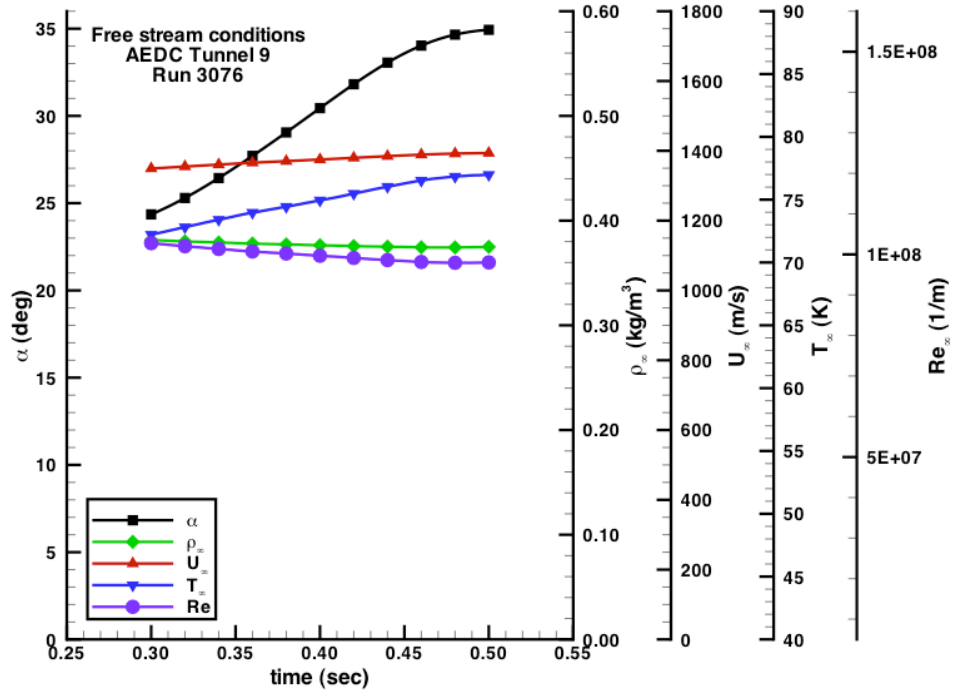
Time (sec)	α (deg)	Re_{∞} (1/ft)	Re_{∞} (1/m)	Mach	P_{∞} (Pa)	T_{∞} (K)	ρ_{∞} (kg/m ³)	U_{∞} (m/s)	H_0-H_{300K} (J/kg)
0.51	22.15	8.510E+06	2.792E+07	7.43	2.208E+03	69.71	1.067E-01	1265.6	5.607E+05
0.62	24.04	8.271E+06	2.714E+07	7.45	2.241E+03	71.85	1.051E-01	1287.0	5.903E+05
0.66	25.96	8.190E+06	2.687E+07	7.45	2.258E+03	72.71	1.046E-01	1295.0	6.014E+05
0.70	28.06	8.157E+06	2.676E+07	7.45	2.276E+03	73.31	1.046E-01	1300.4	6.091E+05
0.73	30.03	8.129E+06	2.667E+07	7.45	2.291E+03	73.83	1.046E-01	1305.3	6.159E+05
0.78	32.03	8.086E+06	2.653E+07	7.45	2.315E+03	74.61	1.046E-01	1312.0	6.255E+05
0.86	33.65	8.069E+06	2.647E+07	7.45	2.360E+03	75.69	1.050E-01	1321.5	6.392E+05
Average		8.202E+06	2.691E+07	7.45	2.278E+03	73.10	1.050E-01	1298.1	6.060E+05

Figure 27. Run 3074 free stream conditions



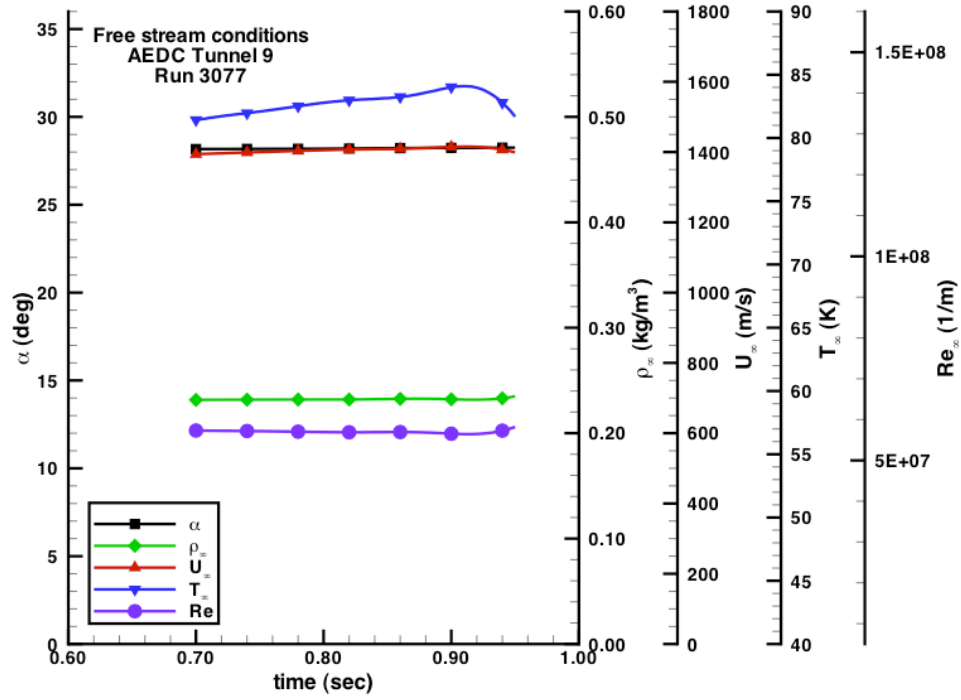
Time (sec)	α (deg)	Re_{∞} (1/ft)	Re_{∞} (1/m)	Mach	P_{∞} (Pa)	T_{∞} (K)	ρ_{∞} (kg/m ³)	U_{∞} (m/s)	H_0-H_{300K} (J/kg)
0.66	22.1	1.69E+07	5.54E+07	7.57	5.41E+03	81.40	2.24E-01	1392.8	7.42E+05
0.73	24.0	1.68E+07	5.51E+07	7.57	5.49E+03	82.62	2.24E-01	1403.3	7.58E+05
0.77	26.0	1.68E+07	5.50E+07	7.57	5.53E+03	83.07	2.25E-01	1407.2	7.64E+05
0.81	28.1	1.68E+07	5.51E+07	7.57	5.57E+03	83.40	2.25E-01	1410.0	7.68E+05
0.84	30.0	1.67E+07	5.49E+07	7.57	5.61E+03	84.01	2.25E-01	1414.4	7.75E+05
0.88	32.0	1.66E+07	5.46E+07	7.57	5.64E+03	84.56	2.25E-01	1419.0	7.82E+05
0.96	33.7	1.73E+07	5.68E+07	7.59	5.62E+03	82.24	2.30E-01	1402.5	7.56E+05
Average		1.68E+07	5.53E+07	7.57	5.55E+03	83.04	2.26E-01	1407.0	7.63E+05

Figure 28. Run 3075 free stream conditions



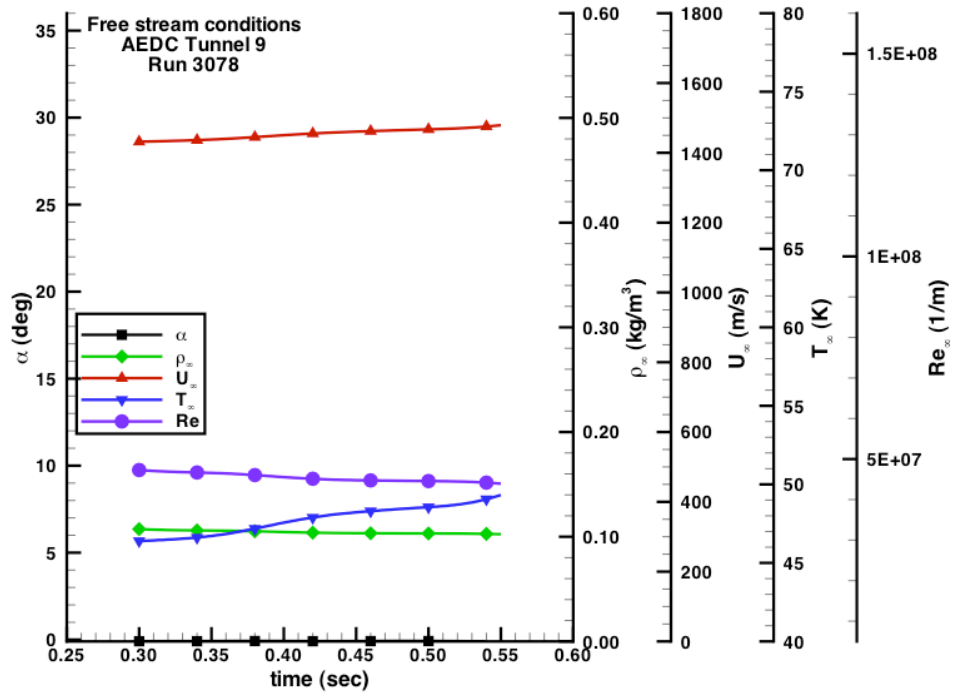
Time (sec)	α (deg)	Re_{∞} (1/ft)	Re_{∞} (1/m)	Mach	P_{∞} (Pa)	T_{∞} (K)	ρ_{∞} (kg/m ³)	U_{∞} (m/s)	H_0-H_{300K} (J/kg)
0.29	23.99	3.143E+07	1.031E+08	7.79	8.152E+03	71.99	3.823E-01	1346.9	6.691E+05
0.33	25.96	3.097E+07	1.016E+08	7.79	8.227E+03	73.18	3.795E-01	1358.3	6.857E+05
0.36	27.97	3.066E+07	1.006E+08	7.80	8.291E+03	74.07	3.778E-01	1366.8	6.983E+05
0.39	30.03	3.042E+07	9.982E+07	7.80	8.344E+03	74.79	3.766E-01	1373.7	7.084E+05
0.42	31.95	3.019E+07	9.905E+07	7.80	8.403E+03	75.54	3.755E-01	1380.4	7.184E+05
0.46	34.03	2.991E+07	9.815E+07	7.79	8.491E+03	76.53	3.745E-01	1389.0	7.314E+05
Average		3.060E+07	1.004E+08	7.80	8.318E+03	74.35	3.777E-01	1369.2	7.019E+05

Figure 29. Run 3076 free stream conditions



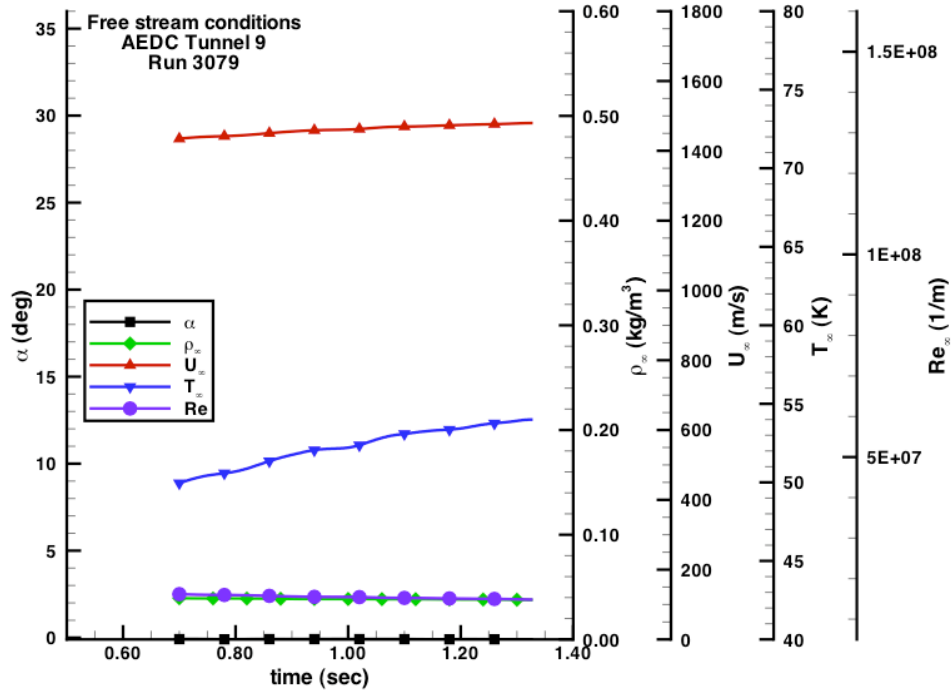
Time (sec)	α (deg)	Re_{∞} (1/ft)	Re_{∞} (1/m)	Mach	P_{∞} (Pa)	T_{∞} (K)	ρ_{∞} (kg/m ³)	U_{∞} (m/s)	H_0-H_{300K} (J/kg)
0.45	28.01	1.804E+07	5.919E+07	7.59	5.206E+03	75.96	2.311E-01	1347.6	6.742E+05
0.50	28.04	1.788E+07	5.865E+07	7.58	5.301E+03	77.34	2.311E-01	1359.3	6.914E+05
0.55	28.06	1.774E+07	5.820E+07	7.58	5.374E+03	78.47	2.309E-01	1369.1	7.060E+05
0.60	28.10	1.767E+07	5.796E+07	7.58	5.446E+03	79.41	2.313E-01	1377.3	7.182E+05
0.65	28.13	1.753E+07	5.751E+07	7.58	5.520E+03	80.54	2.311E-01	1386.7	7.324E+05
0.70	28.17	1.747E+07	5.732E+07	7.58	5.594E+03	81.42	2.316E-01	1393.9	7.433E+05
0.75	28.18	1.742E+07	5.716E+07	7.58	5.644E+03	82.09	2.318E-01	1399.9	7.524E+05
0.78	28.19	1.738E+07	5.703E+07	7.58	5.675E+03	82.51	2.319E-01	1403.4	7.576E+05
Average		1.764E+07	5.788E+07	7.58	5.470E+03	79.72	2.314E-01	1379.6	7.219E+05

Figure 30. Run 3077 free stream conditions



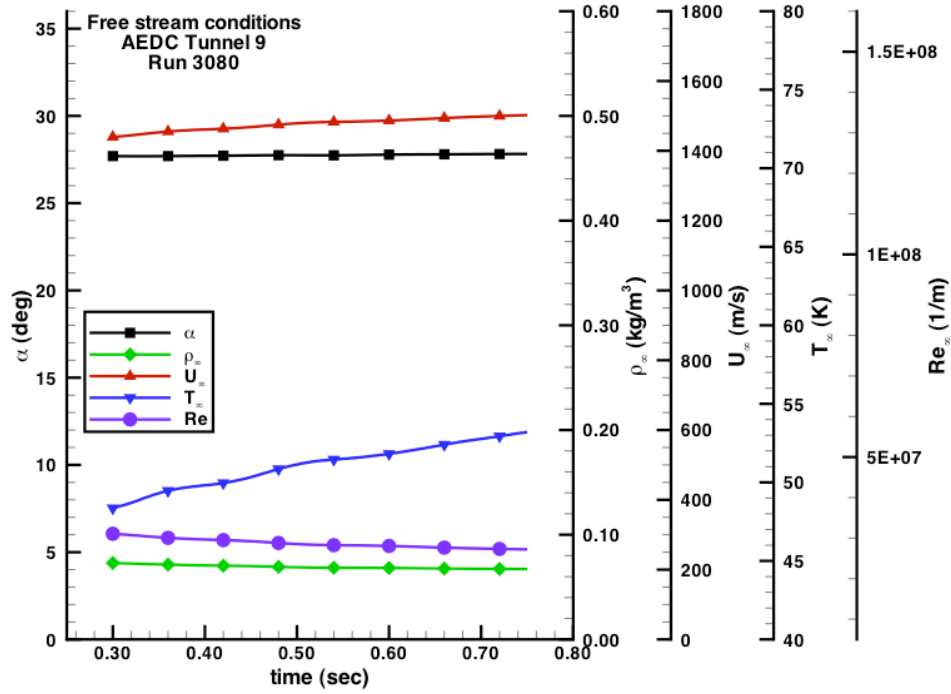
Time (sec)	α (deg)	Re_{∞} (1/ft)	Re_{∞} (1/m)	Mach	P_{∞} (Pa)	T_{∞} (K)	ρ_{∞} (kg/m ³)	U_{∞} (m/s)	H_0-H_{300K} (J/kg)
0.35	-0.08	1.420E+07	4.658E+07	10.32	1.469E+03	46.71	1.059E-01	1438.1	7.698E+05
0.40	-0.08	1.388E+07	4.555E+07	10.31	1.476E+03	47.56	1.045E-01	1450.5	7.886E+05
0.45	-0.08	1.365E+07	4.477E+07	10.32	1.480E+03	48.22	1.034E-01	1460.7	8.041E+05
0.50	-0.08	1.358E+07	4.456E+07	10.33	1.487E+03	48.55	1.031E-01	1467.2	8.140E+05
0.54	-0.10	1.346E+07	4.418E+07	10.33	1.496E+03	49.06	1.027E-01	1475.4	8.265E+05
Average		1.375E+07	4.513E+07	10.32	1.481E+03	48.02	1.039E-01	1458.3	8.006E+05

Figure 31. Run 3078 free stream conditions



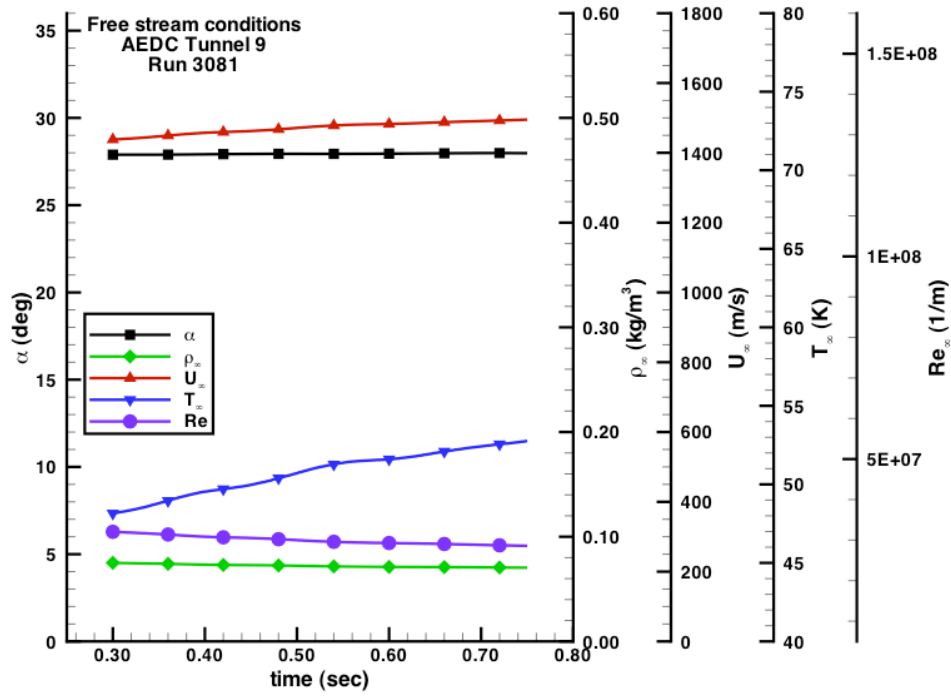
Time (sec)	α (deg)	Re_∞ (1/ft)	Re_∞ (1/m)	Mach	P_∞ (Pa)	T_∞ (K)	ρ_∞ (kg/m ³)	U_∞ (m/s)	H_0-H_{300K} (J/kg)
0.68	-0.08	4.968E+06	1.630E+07	9.95	5.837E+02	49.69	3.955E-02	1431.2	7.630E+05
0.70	-0.08	4.932E+06	1.618E+07	9.95	5.840E+02	49.95	3.937E-02	1434.6	7.682E+05
0.75	-0.08	4.877E+06	1.600E+07	9.94	5.864E+02	50.44	3.915E-02	1440.5	7.772E+05
0.80	-0.09	4.858E+06	1.594E+07	9.94	5.888E+02	50.69	3.911E-02	1443.3	7.815E+05
0.85	-0.08	4.811E+06	1.578E+07	9.93	5.930E+02	51.23	3.898E-02	1449.1	7.904E+05
0.90	-0.08	4.756E+06	1.560E+07	9.92	5.955E+02	51.75	3.875E-02	1455.4	8.001E+05
0.95	-0.08	4.723E+06	1.550E+07	9.91	5.978E+02	52.10	3.864E-02	1459.3	8.061E+05
1.00	-0.08	4.719E+06	1.548E+07	9.91	5.990E+02	52.21	3.863E-02	1460.8	8.084E+05
1.05	-0.08	4.674E+06	1.534E+07	9.90	6.030E+02	52.73	3.851E-02	1466.1	8.167E+05
1.10	-0.08	4.646E+06	1.524E+07	9.89	6.059E+02	53.09	3.844E-02	1469.4	8.219E+05
1.15	-0.09	4.622E+06	1.516E+07	9.88	6.067E+02	53.29	3.833E-02	1471.4	8.250E+05
1.20	-0.09	4.596E+06	1.508E+07	9.89	6.052E+02	53.43	3.815E-02	1474.0	8.290E+05
1.25	-0.09	4.572E+06	1.500E+07	9.87	6.079E+02	53.73	3.810E-02	1476.1	8.324E+05
1.29	-0.09	4.550E+06	1.493E+07	9.87	6.074E+02	53.87	3.797E-02	1477.9	8.352E+05
Average		4.736E+06	1.554E+07	9.91	5.975E+02	52.02	3.869E-02	1457.8	8.039E+05

Figure 32. Run 3079 free stream conditions



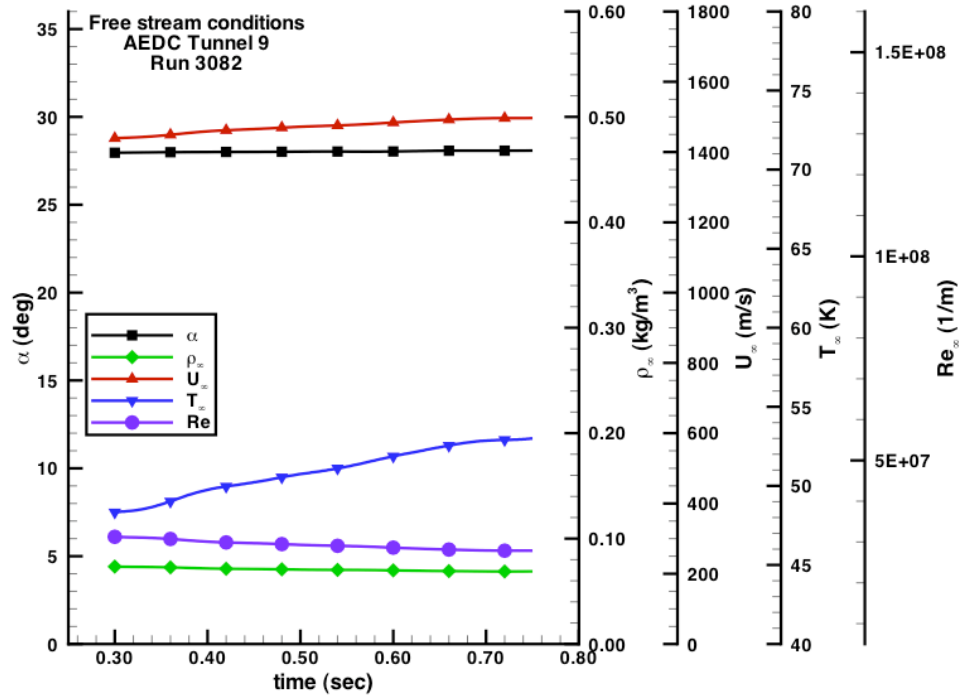
Time (sec)	α (deg)	Re_{∞} (1/ft)	Re_{∞} (1/m)	Mach	P_{∞} (Pa)	T_{∞} (K)	ρ_{∞} (kg/m ³)	U_{∞} (m/s)	H_0-H_{300K} (J/kg)
0.36	27.70	9.167E+06	3.008E+07	10.14	1.050E+03	49.47	7.147E-02	1455.2	7.974E+05
0.40	27.71	9.037E+06	2.965E+07	10.15	1.045E+03	49.82	7.066E-02	1461.1	8.063E+05
0.45	27.74	8.910E+06	2.923E+07	10.15	1.047E+03	50.33	7.003E-02	1468.2	8.173E+05
0.50	27.75	8.698E+06	2.854E+07	10.14	1.046E+03	51.13	6.892E-02	1478.9	8.339E+05
0.55	27.75	8.607E+06	2.824E+07	10.14	1.047E+03	51.50	6.847E-02	1483.3	8.408E+05
0.60	27.78	8.550E+06	2.805E+07	10.13	1.050E+03	51.82	6.828E-02	1486.7	8.462E+05
0.65	27.80	8.447E+06	2.771E+07	10.12	1.053E+03	52.30	6.780E-02	1492.5	8.553E+05
0.70	27.81	8.359E+06	2.742E+07	10.11	1.056E+03	52.77	6.743E-02	1498.2	8.642E+05
0.75	27.82	8.293E+06	2.721E+07	10.10	1.063E+03	53.21	6.727E-02	1502.3	8.709E+05
0.76	27.82	8.286E+06	2.718E+07	10.10	1.063E+03	53.26	6.724E-02	1502.9	8.718E+05
Average		8.635E+06	2.833E+07	10.13	1.052E+03	51.56	6.876E-02	1482.9	8.404E+05

Figure 33. Run 3080 free stream conditions



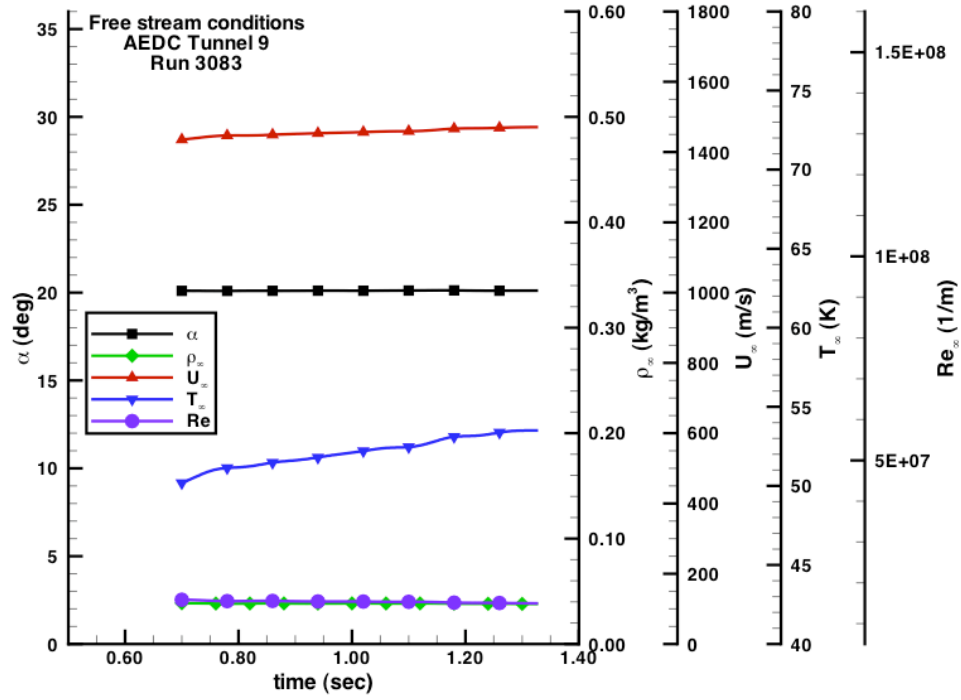
Time (sec)	α (deg)	Re_{∞} (1/ft)	Re_{∞} (1/m)	Mach	P_{∞} (Pa)	T_{∞} (K)	ρ_{∞} (kg/m^3)	U_{∞} (m/s)	H_0-H_{300K} (J/kg)
0.43	27.93	9.336E+06	3.063E+07	10.15	1.079E+03	49.78	7.297E-02	1460.4	8.053E+05
0.45	27.94	9.300E+06	3.051E+07	10.15	1.081E+03	49.97	7.286E-02	1462.5	8.086E+05
0.50	27.94	9.143E+06	3.000E+07	10.13	1.088E+03	50.71	7.223E-02	1471.3	8.223E+05
0.55	27.94	8.992E+06	2.950E+07	10.12	1.091E+03	51.37	7.155E-02	1479.5	8.351E+05
0.60	27.95	8.924E+06	2.928E+07	10.12	1.090E+03	51.60	7.117E-02	1482.6	8.399E+05
0.65	27.97	8.867E+06	2.909E+07	10.11	1.097E+03	51.99	7.104E-02	1486.8	8.465E+05
0.70	27.98	8.786E+06	2.883E+07	10.10	1.101E+03	52.42	7.075E-02	1491.0	8.532E+05
0.75	27.98	8.712E+06	2.858E+07	10.09	1.103E+03	52.77	7.043E-02	1495.2	8.598E+05
0.76	27.98	8.699E+06	2.854E+07	10.09	1.105E+03	52.86	7.038E-02	1496.3	8.616E+05
Average		8.973E+06	2.944E+07	10.12	1.093E+03	51.50	7.149E-02	1480.6	8.369E+05

Figure 34. Run 3081 free stream conditions



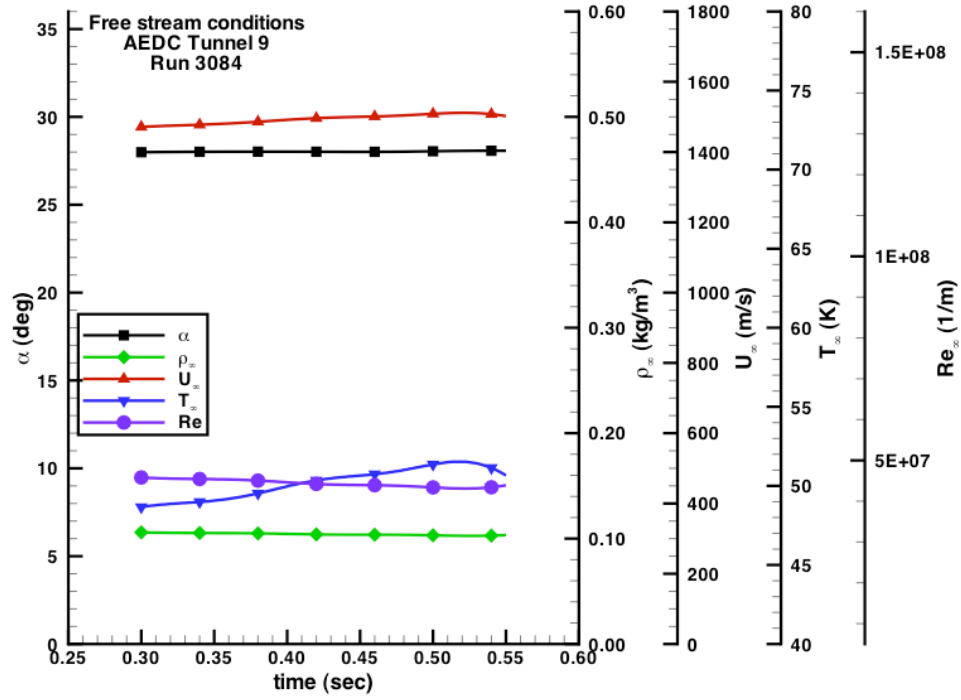
Time (sec)	α (deg)	Re_{∞} (1/ft)	Re_{∞} (1/m)	Mach	P_{∞} (Pa)	T_{∞} (K)	ρ_{∞} (kg/m ³)	U_{∞} (m/s)	H_0-H_{300K} (J/kg)
0.40	28.00	9.170E+06	3.008E+07	10.14	1.059E+03	49.75	7.170E-02	1458.9	8.031E+05
0.45	28.01	9.053E+06	2.970E+07	10.14	1.061E+03	50.23	7.115E-02	1465.3	8.130E+05
0.50	28.02	8.930E+06	2.930E+07	10.13	1.064E+03	50.75	7.058E-02	1471.9	8.232E+05
0.55	28.03	8.843E+06	2.901E+07	10.12	1.069E+03	51.22	7.029E-02	1476.7	8.307E+05
0.60	28.03	8.723E+06	2.862E+07	10.10	1.076E+03	51.87	6.985E-02	1483.9	8.420E+05
0.65	28.07	8.597E+06	2.821E+07	10.10	1.079E+03	52.44	6.927E-02	1491.0	8.532E+05
0.70	28.08	8.514E+06	2.793E+07	10.09	1.081E+03	52.85	6.889E-02	1495.9	8.610E+05
0.75	28.08	8.497E+06	2.788E+07	10.08	1.084E+03	53.00	6.890E-02	1496.8	8.623E+05
0.78	28.10	8.451E+06	2.773E+07	10.07	1.089E+03	53.31	6.879E-02	1499.6	8.669E+05
Average		8.753E+06	2.872E+07	10.11	1.073E+03	51.71	6.994E-02	1482.2	8.395E+05

Figure 35. Run 3082 free stream conditions



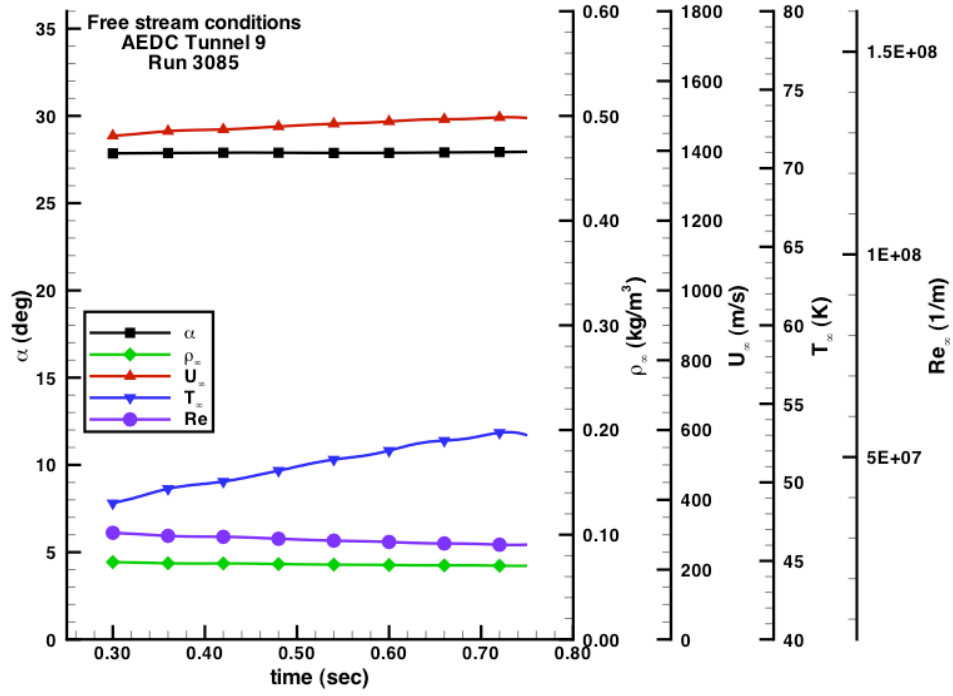
Time (sec)	α (deg)	Re_{∞} (1/ft)	Re_{∞} (1/m)	Mach	P_{∞} (Pa)	T_{∞} (K)	ρ_{∞} (kg/m ³)	U_{∞} (m/s)	H_0-H_{300K} (J/kg)
0.78	20.10	4.728E+06	1.551E+07	9.92	5.814E+02	51.13	3.829E-02	1447.0	7.872E+05
0.80	20.10	4.728E+06	1.551E+07	9.92	5.823E+02	51.17	3.831E-02	1447.3	7.877E+05
0.90	20.10	4.717E+06	1.548E+07	9.90	5.890E+02	51.61	3.843E-02	1451.6	7.944E+05
1.00	20.11	4.699E+06	1.542E+07	9.89	5.962E+02	52.11	3.853E-02	1455.9	8.011E+05
1.10	20.12	4.676E+06	1.534E+07	9.88	5.998E+02	52.46	3.850E-02	1459.3	8.065E+05
1.20	20.12	4.603E+06	1.510E+07	9.87	6.026E+02	53.15	3.818E-02	1467.4	8.190E+05
1.27	20.11	4.585E+06	1.504E+07	9.86	6.056E+02	53.43	3.817E-02	1469.6	8.225E+05
Average		4.677E+06	1.534E+07	9.89	5.938E+02	52.15	3.835E-02	1456.8	8.026E+05

Figure 36. Run 3083 free stream conditions



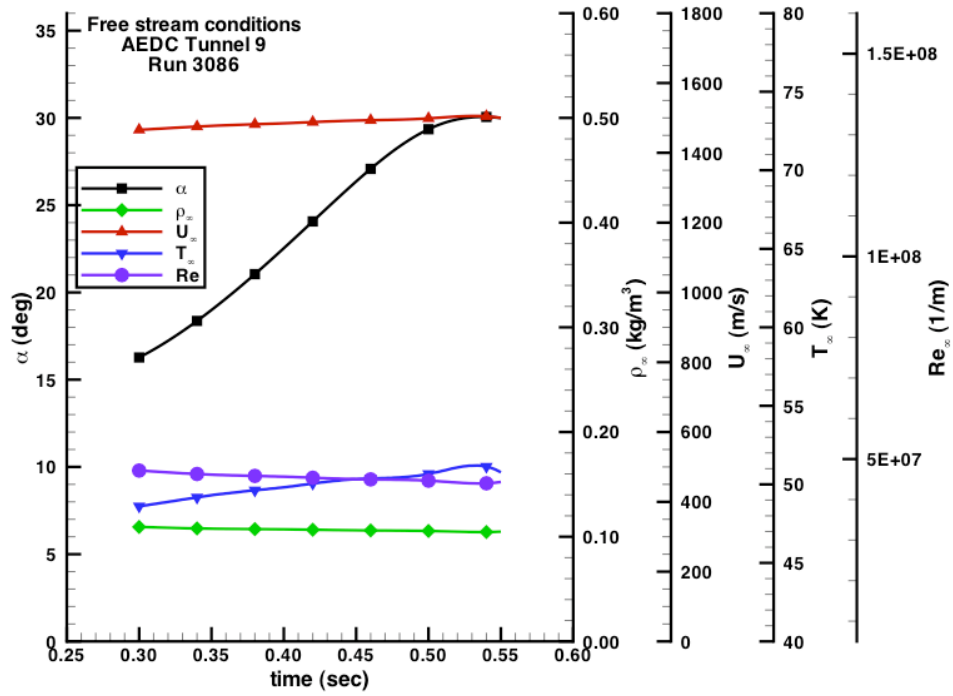
Time (sec)	α (deg)	Re_{∞} (1/ft)	Re_{∞} (1/m)	Mach	P_{∞} (Pa)	T_{∞} (K)	ρ_{∞} (kg/m ³)	U_{∞} (m/s)	H_0-H_{300K} (J/kg)
0.35	28.02	1.383E+07	4.539E+07	10.36	1.534E+03	49.07	1.053E-01	1479.4	8.326E+05
0.36	28.02	1.382E+07	4.533E+07	10.36	1.536E+03	49.18	1.052E-01	1481.3	8.355E+05
0.38	28.02	1.373E+07	4.506E+07	10.36	1.543E+03	49.52	1.049E-01	1486.2	8.431E+05
0.40	28.02	1.360E+07	4.462E+07	10.35	1.550E+03	49.97	1.045E-01	1491.7	8.517E+05
0.42	28.02	1.348E+07	4.422E+07	10.34	1.554E+03	50.34	1.040E-01	1496.3	8.590E+05
0.44	28.01	1.342E+07	4.401E+07	10.34	1.557E+03	50.57	1.037E-01	1499.2	8.635E+05
0.46	28.01	1.339E+07	4.392E+07	10.34	1.562E+03	50.74	1.037E-01	1501.2	8.667E+05
0.48	28.02	1.333E+07	4.372E+07	10.33	1.568E+03	51.01	1.036E-01	1504.2	8.715E+05
Average		1.357E+07	4.453E+07	10.35	1.551E+03	50.05	1.044E-01	1492.5	8.529E+05

Figure 37. Run 3084 free stream conditions



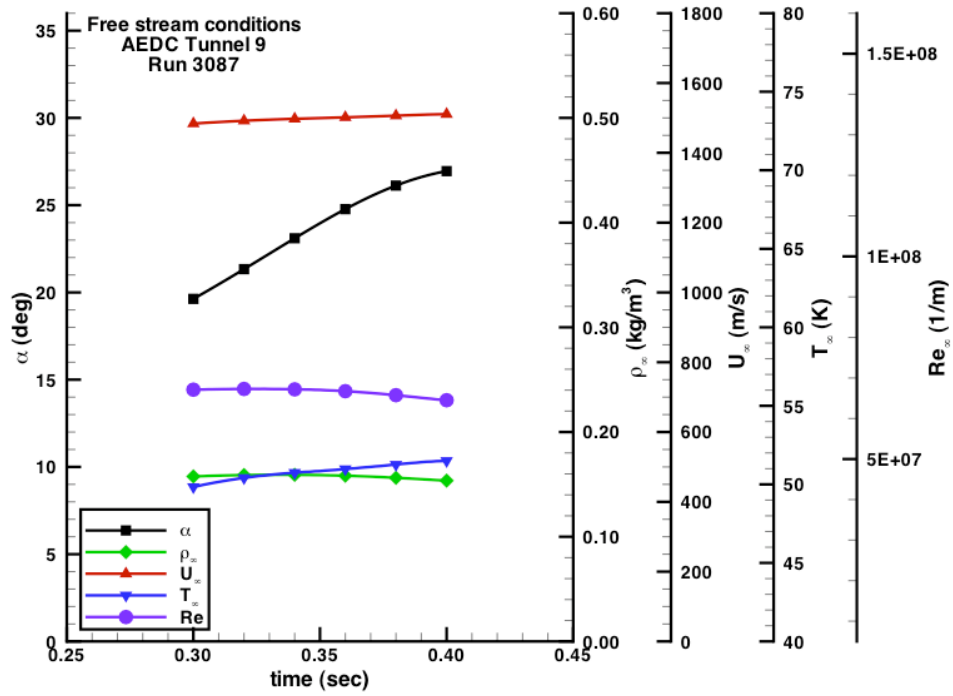
Time (sec)	α (deg)	Re_∞ (1/ft)	Re_∞ (1/m)	Mach	P_∞ (Pa)	T_∞ (K)	ρ_∞ (kg/m ³)	U_∞ (m/s)	H_0-H_{300K} (J/kg)
0.38	27.88	9.267E+06	3.040E+07	10.14	1.072E+03	49.79	7.252E-02	1458.9	8.031E+05
0.40	27.89	9.252E+06	3.036E+07	10.13	1.075E+03	49.91	7.252E-02	1460.0	8.049E+05
0.45	27.90	9.185E+06	3.013E+07	10.12	1.083E+03	50.37	7.240E-02	1464.9	8.125E+05
0.50	27.89	9.040E+06	2.966E+07	10.11	1.087E+03	51.00	7.177E-02	1472.6	8.244E+05
0.55	27.88	8.934E+06	2.931E+07	10.10	1.092E+03	51.53	7.137E-02	1478.3	8.334E+05
0.60	27.88	8.853E+06	2.905E+07	10.09	1.098E+03	52.02	7.110E-02	1484.0	8.424E+05
0.65	27.90	8.744E+06	2.869E+07	10.07	1.105E+03	52.63	7.073E-02	1490.2	8.522E+05
0.70	27.92	8.696E+06	2.853E+07	10.06	1.111E+03	52.96	7.063E-02	1493.2	8.571E+05
0.71	27.92	8.673E+06	2.846E+07	10.06	1.111E+03	53.07	7.052E-02	1494.6	8.592E+05
Average		8.961E+06	2.940E+07	10.10	1.093E+03	51.48	7.151E-02	1477.4	8.321E+05

Figure 38. Run 3085 free stream conditions



Time (sec)	α (deg)	Re_{∞} (1/ft)	Re_{∞} (1/m)	Mach	P_{∞} (Pa)	T_{∞} (K)	ρ_{∞} (kg/m ³)	U_{∞} (m/s)	H_0-H_{300K} (J/kg)
0.29	15.95	1.442E+07	4.732E+07	10.31	1.577E+03	48.48	1.096E-01	1464.2	8.095E+05
0.33	18.01	1.415E+07	4.642E+07	10.32	1.575E+03	49.09	1.081E-01	1473.9	8.243E+05
0.37	20.06	1.401E+07	4.597E+07	10.32	1.579E+03	49.48	1.074E-01	1479.8	8.336E+05
0.39	22.08	1.393E+07	4.572E+07	10.32	1.583E+03	49.75	1.071E-01	1483.7	8.396E+05
0.42	24.07	1.383E+07	4.538E+07	10.31	1.586E+03	50.06	1.067E-01	1488.1	8.464E+05
0.45	26.06	1.374E+07	4.506E+07	10.32	1.586E+03	50.31	1.062E-01	1492.0	8.525E+05
0.47	28.01	1.370E+07	4.493E+07	10.32	1.585E+03	50.41	1.059E-01	1494.5	8.563E+05
0.52	29.95	1.346E+07	4.415E+07	10.32	1.590E+03	51.11	1.048E-01	1504.5	8.721E+05
Average		1.390E+07	4.562E+07	10.32	1.582E+03	49.84	1.070E-01	1485.1	8.418E+05

Figure 39. Run 3086 free stream conditions



Time (sec)	α (deg)	Re_{∞} (1/ft)	Re_{∞} (1/m)	Mach	P_{∞} (Pa)	T_{∞} (K)	ρ_{∞} (kg/m ³)	U_{∞} (m/s)	H_0-H_{300K} (J/kg)
0.21	13.95	2.095E+07	6.873E+07	10.31	2.181E+03	46.89	1.566E-01	1440.0	7.729E+05
0.25	15.93	2.032E+07	6.665E+07	10.34	2.178E+03	47.93	1.531E-01	1460.0	8.028E+05
0.28	18.07	2.035E+07	6.678E+07	10.33	2.261E+03	49.04	1.553E-01	1474.0	8.245E+05
0.30	19.96	2.047E+07	6.715E+07	10.31	2.342E+03	49.98	1.579E-01	1485.6	8.427E+05
0.35	23.96	2.044E+07	6.706E+07	10.32	2.397E+03	50.84	1.589E-01	1499.5	8.643E+05
0.38	26.01	2.007E+07	6.585E+07	10.32	2.380E+03	51.24	1.565E-01	1506.0	8.744E+05
0.42	27.18	1.954E+07	6.409E+07	10.34	2.316E+03	51.29	1.521E-01	1509.4	8.796E+05
Average		2.030E+07	6.662E+07	10.32	2.294E+03	49.60	1.558E-01	1482.1	8.373E+05

Figure 40. Run 3087 free stream conditions

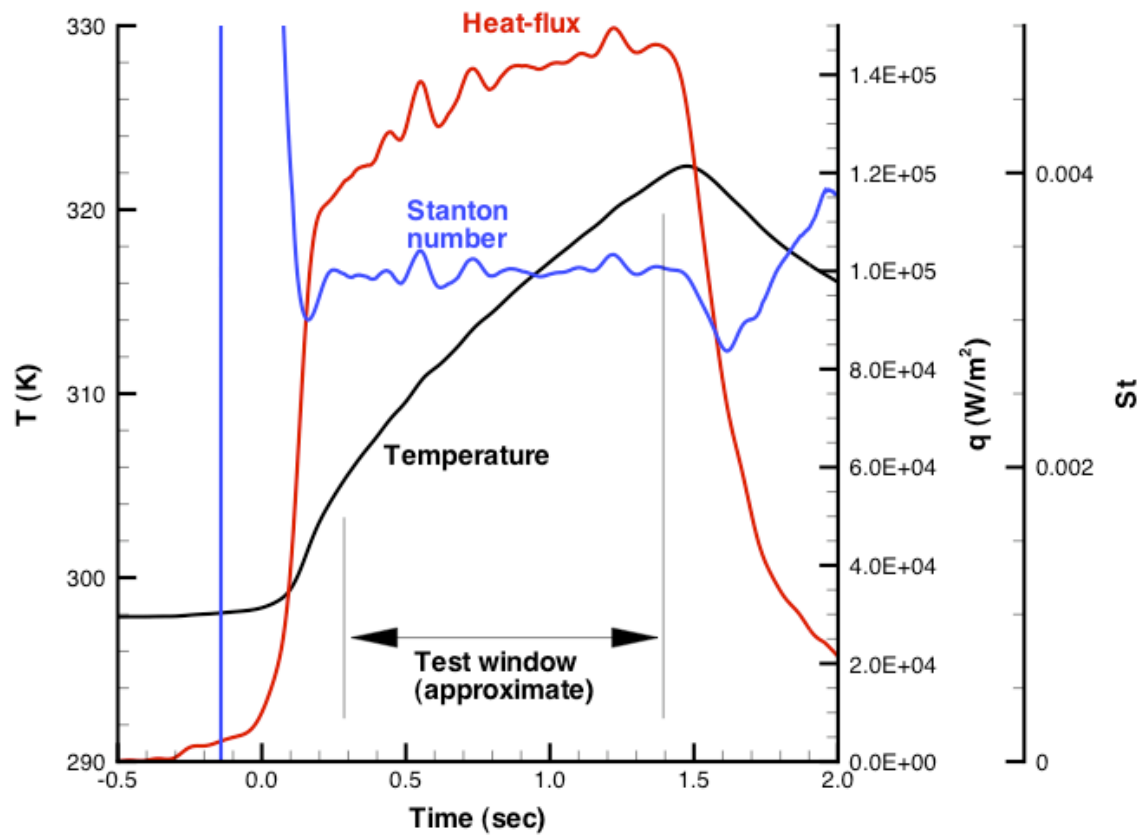


Figure 41. Sample time-histories of temperature, heat-flux and Stanton-number data from AEDC Tunnel 9 test of CEV model

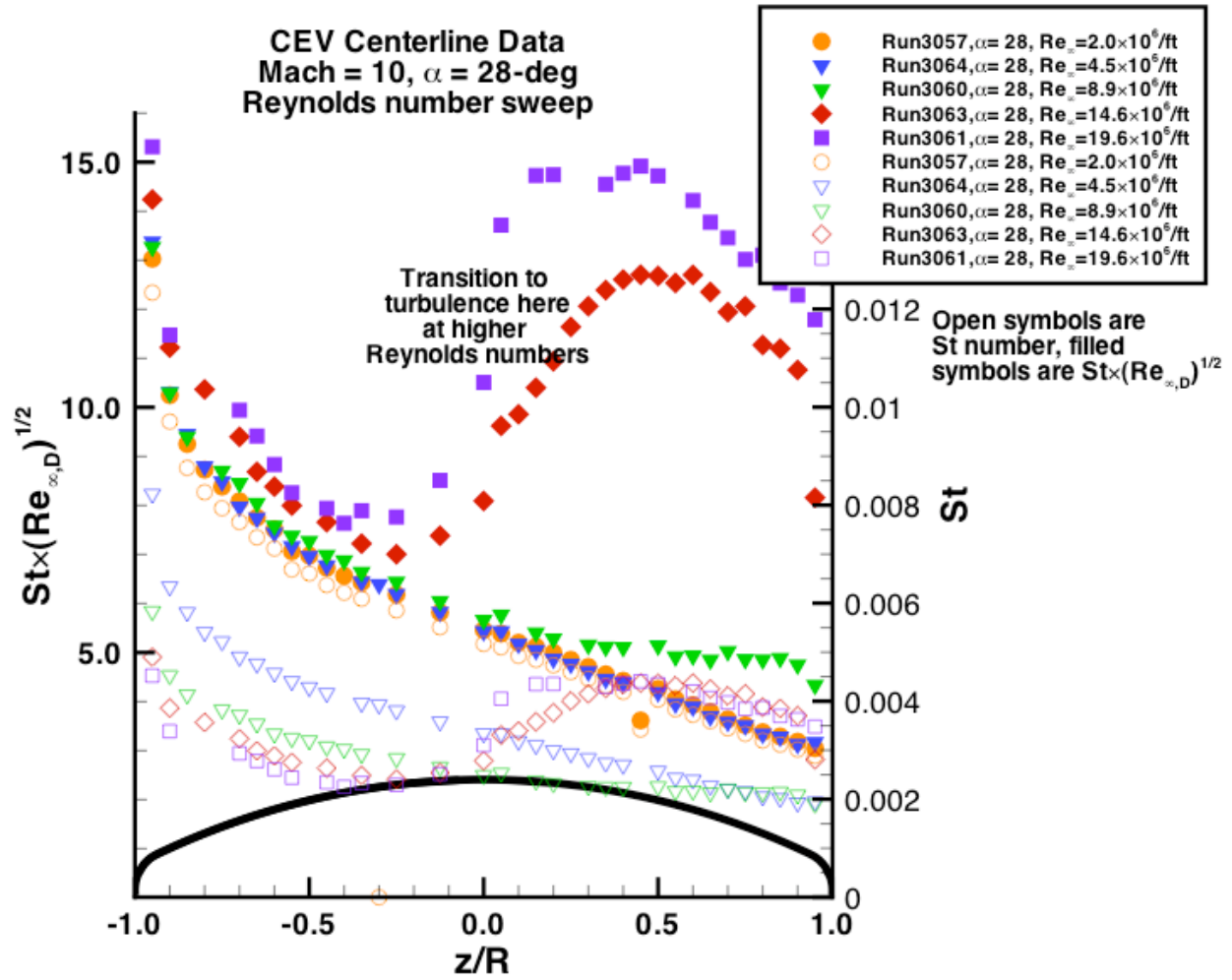


Figure 42. Sample comparison of heating parameters along centerline vs. Reynolds number from AEDC Tunnel 9 test of CEV model

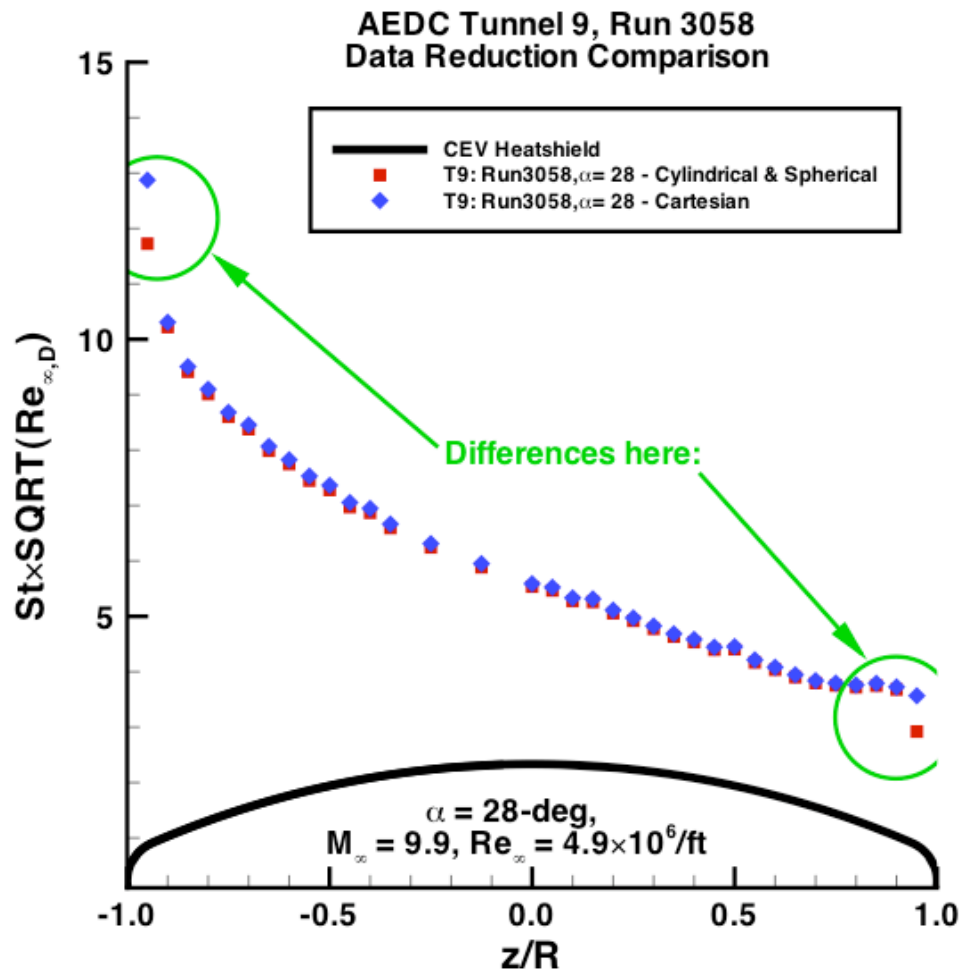


Figure 43. Heating distributions resulting from analyses in different one-dimensional coordinate systems

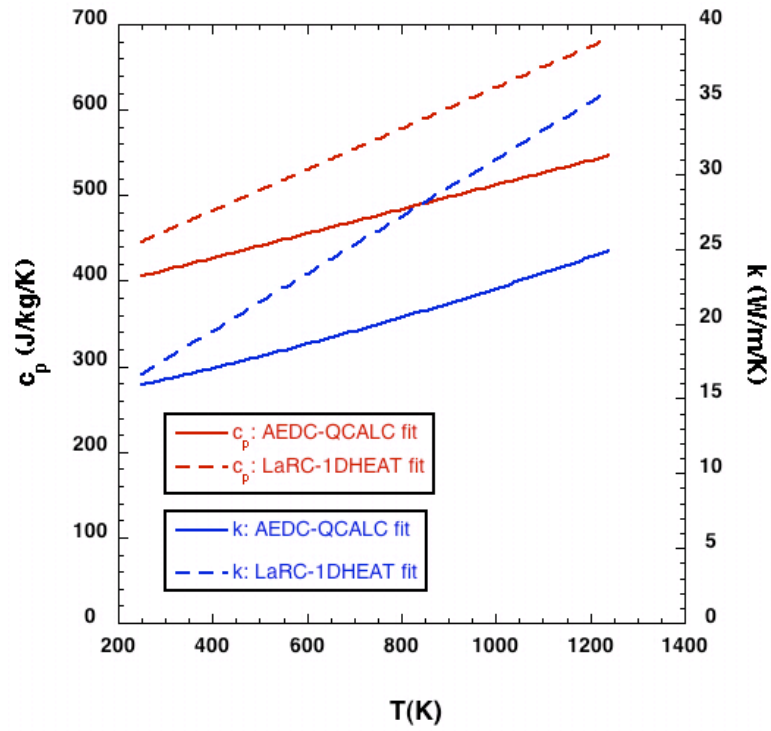


Figure 44. Chromel thermal properties

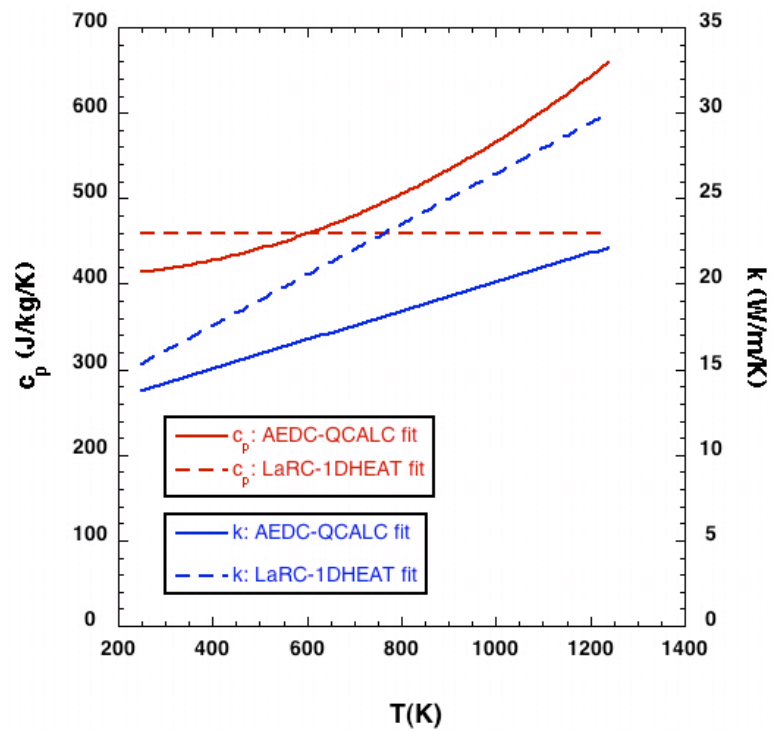


Figure 45. Stainless steel (17-4) thermal properties

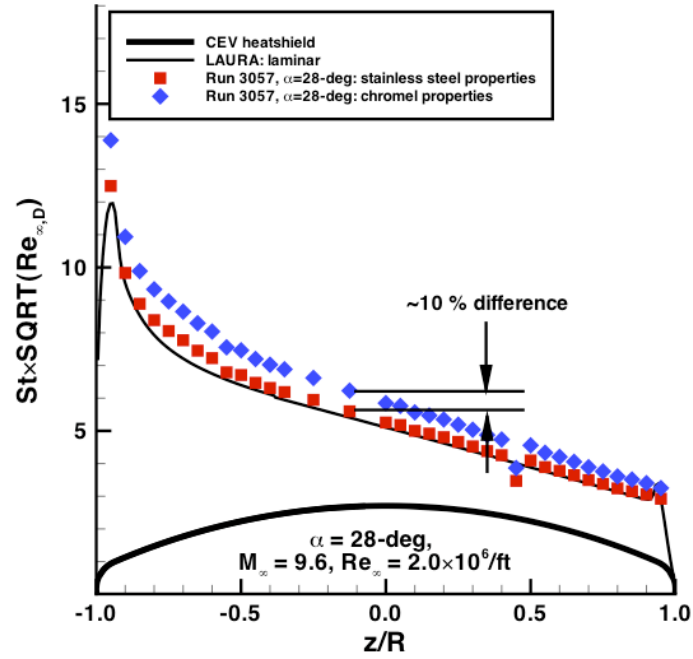


Figure 46. Effects of material thermal properties on CEV experimental heating distribution in AEDC Tunnel 9

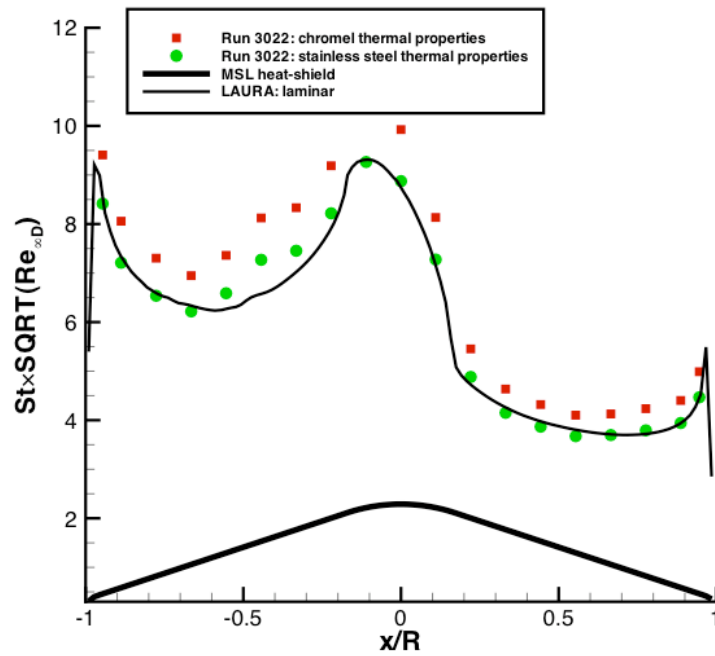


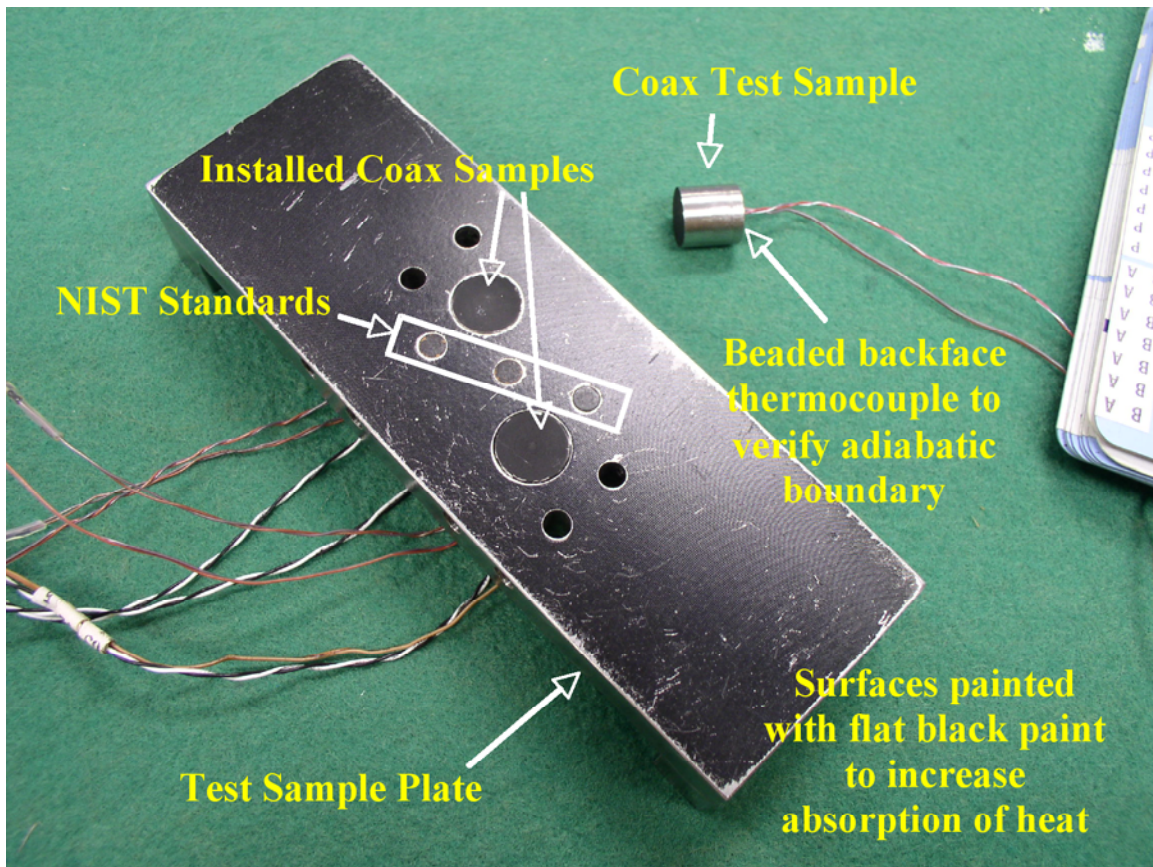
Figure 47. Effects of material thermal properties on MSL experimental heating distribution in AEDC Tunnel 9



Calibration Assembly



Installed Sample Plate (shutter and lamp removed)



Sample Plate with Thermocouples and NIST Standards

Figure 48. Thermocouple Calibration Experiment Set-up

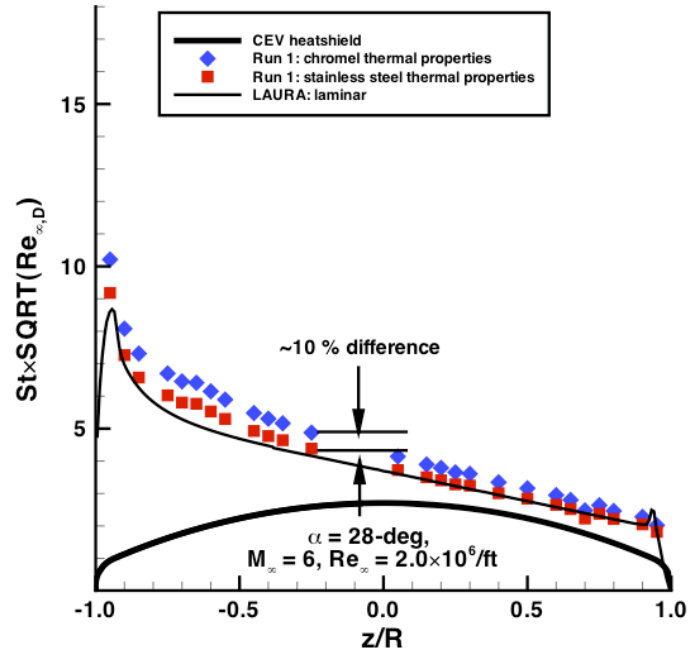


Figure 49. Effects of material thermal properties on CEV experimental heating distribution in LaRC 20-Inch Mach 6 Air Tunnel

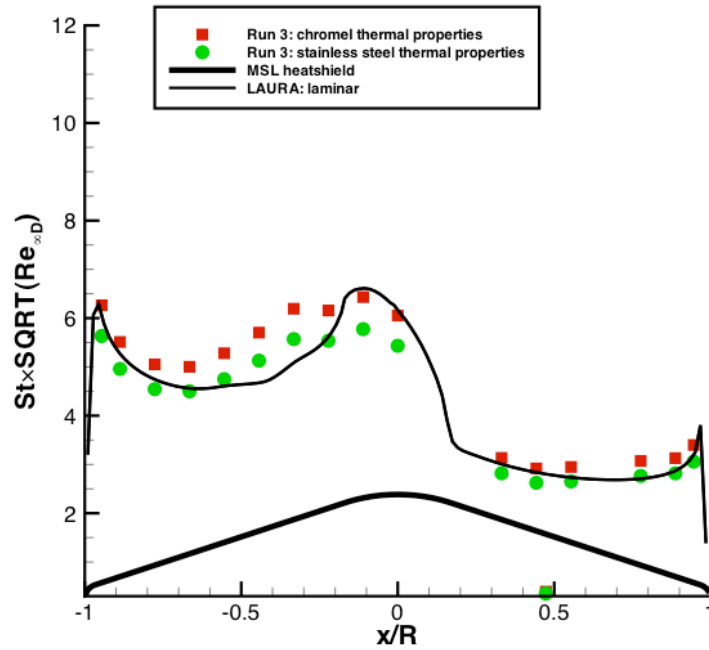


Figure 50. Effects of material thermal properties on MSL experimental heating distribution in LaRC 20-Inch Mach 6 Air Tunnel

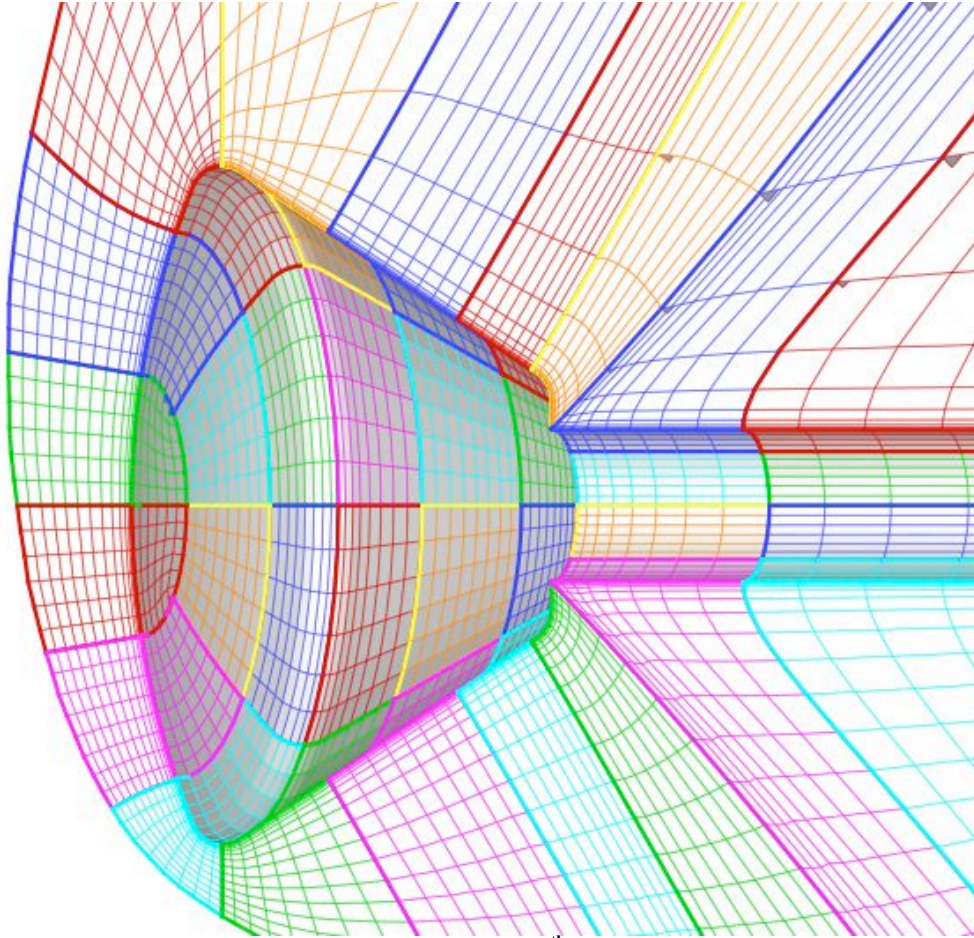
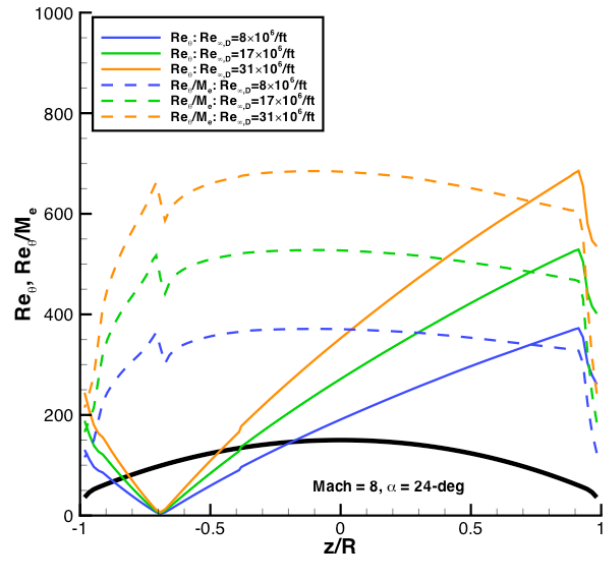
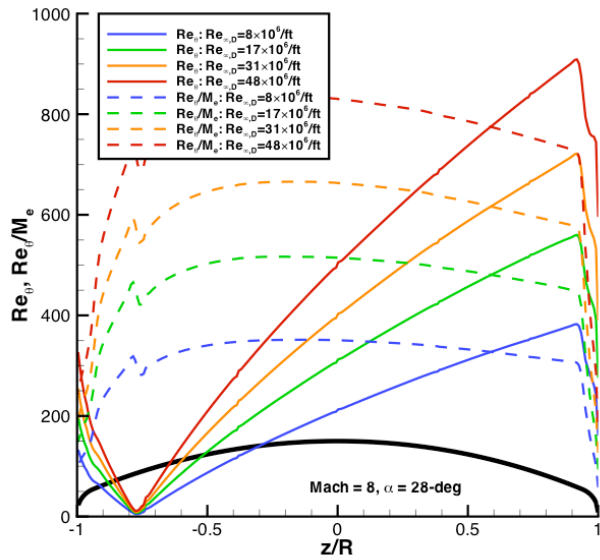


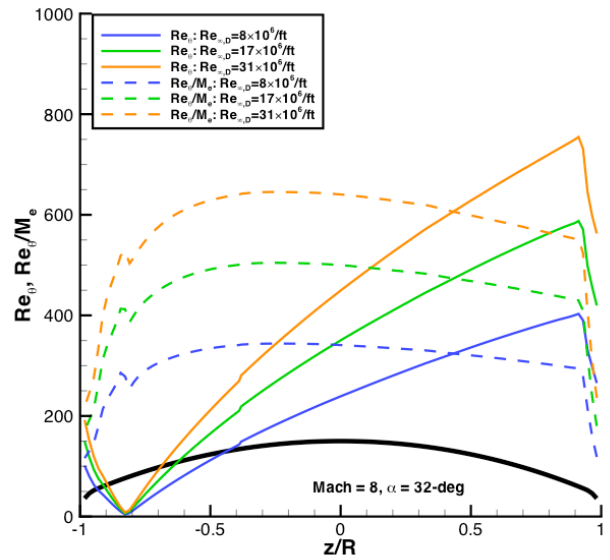
Figure 51. CEV grid (every 4th point shown)



Values at $\alpha = 24$ -deg



Values at $\alpha = 28$ -deg



Values at $\alpha = 32$ -deg

Figure 52. Predicted boundary-layer transition parameters at Mach 8

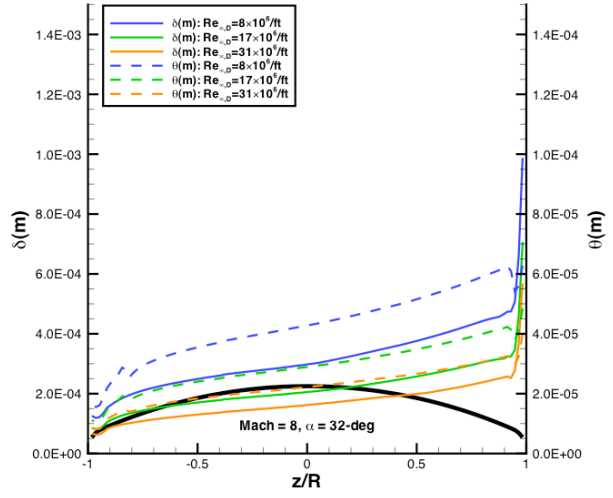
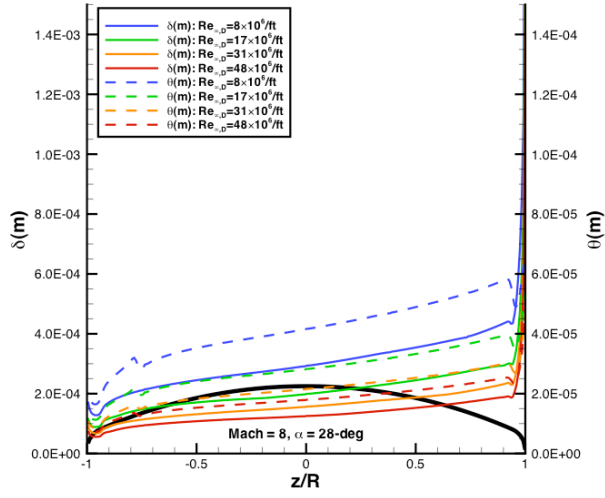
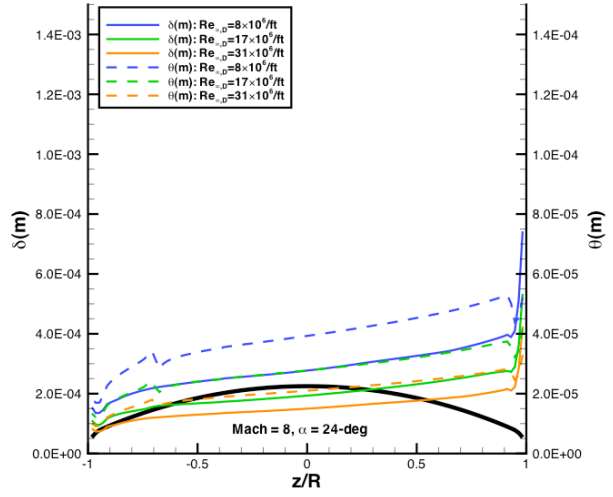


Figure 53. Predicted boundary-layer height parameters at Mach 8

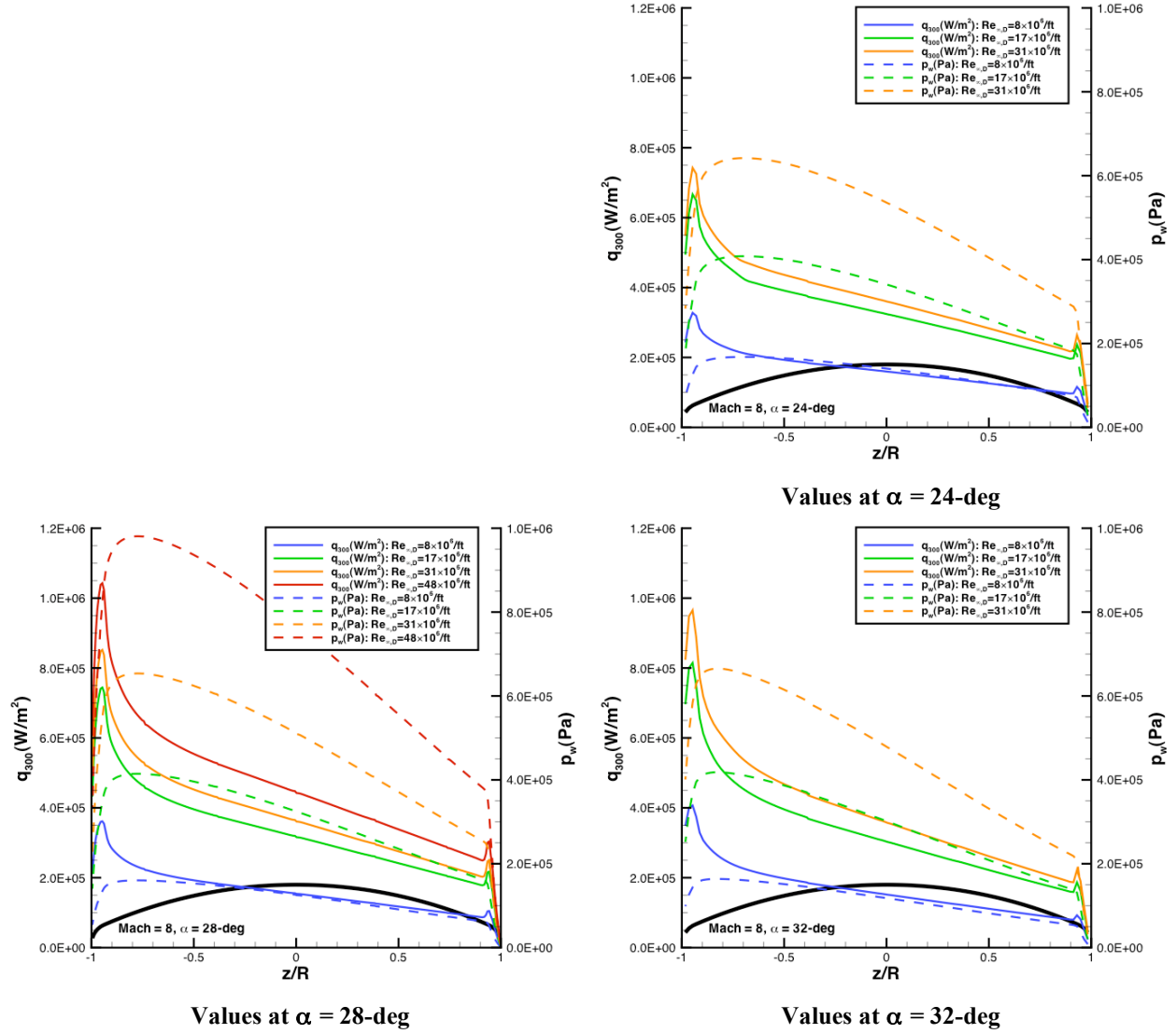


Figure 54. Predicted surface heating and pressure at Mach 8

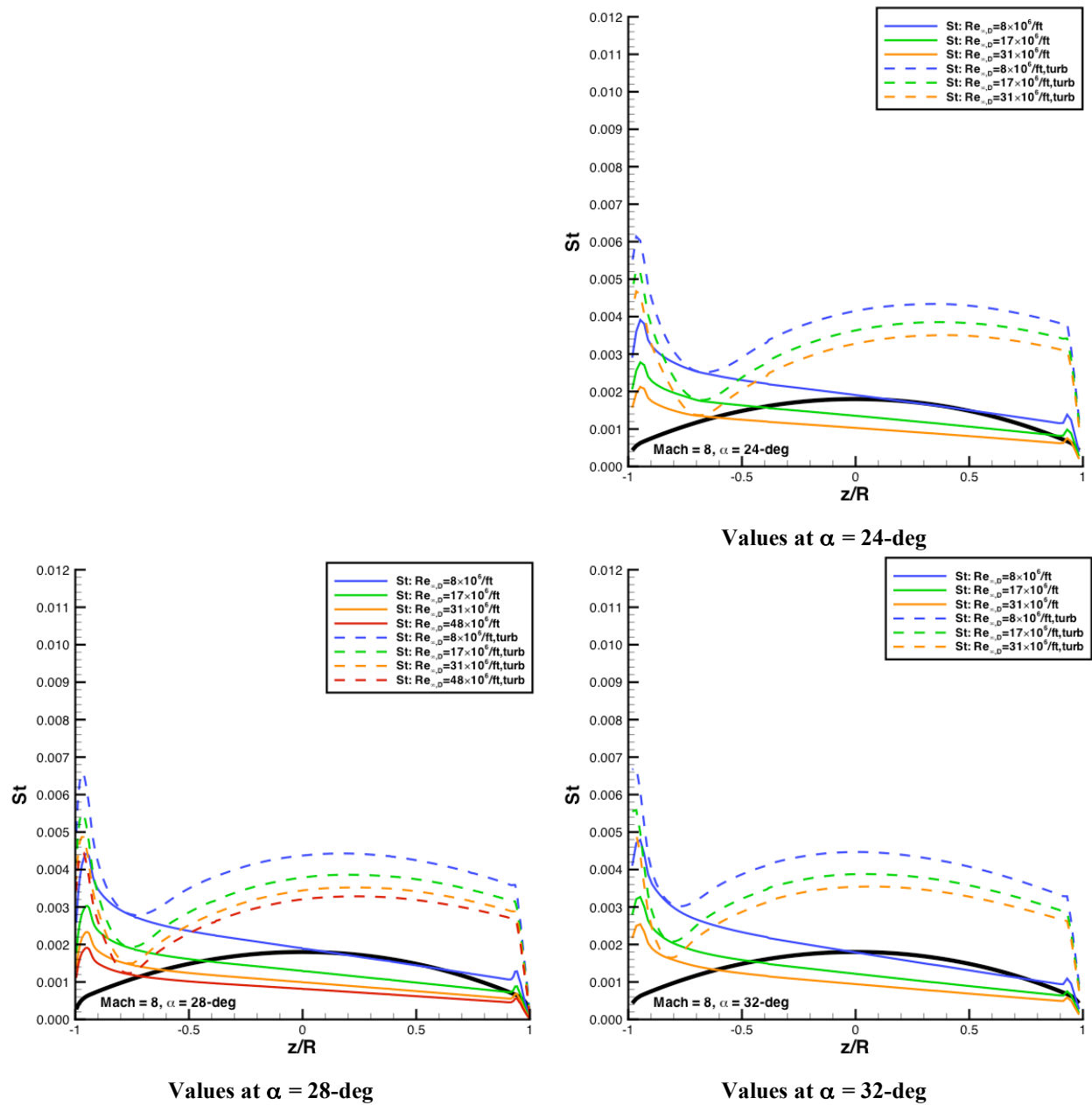


Figure 55. Predicted Stanton numbers at Mach 8

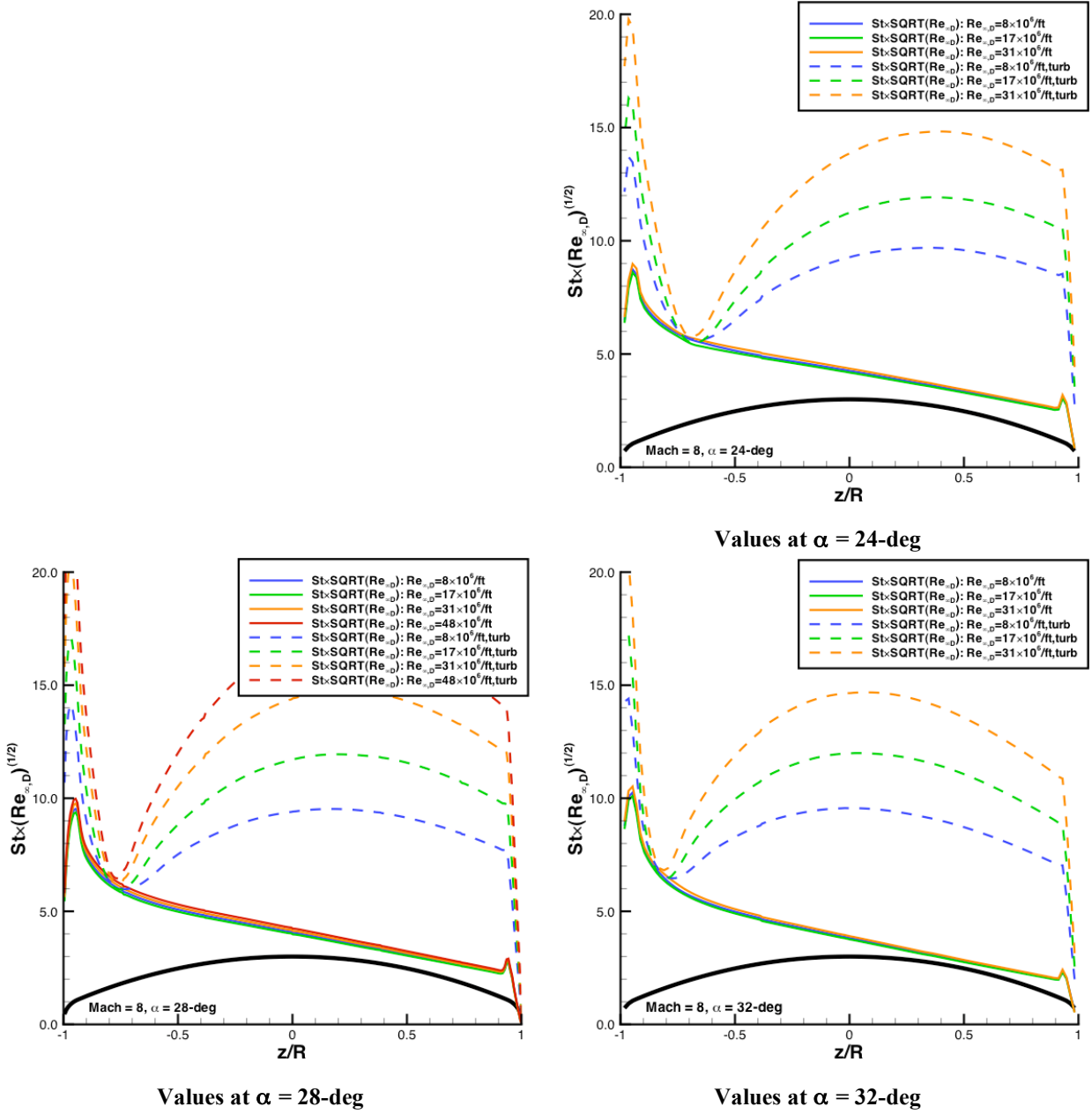


Figure 56. Laminar correlation parameter for predicted heating at Mach 8

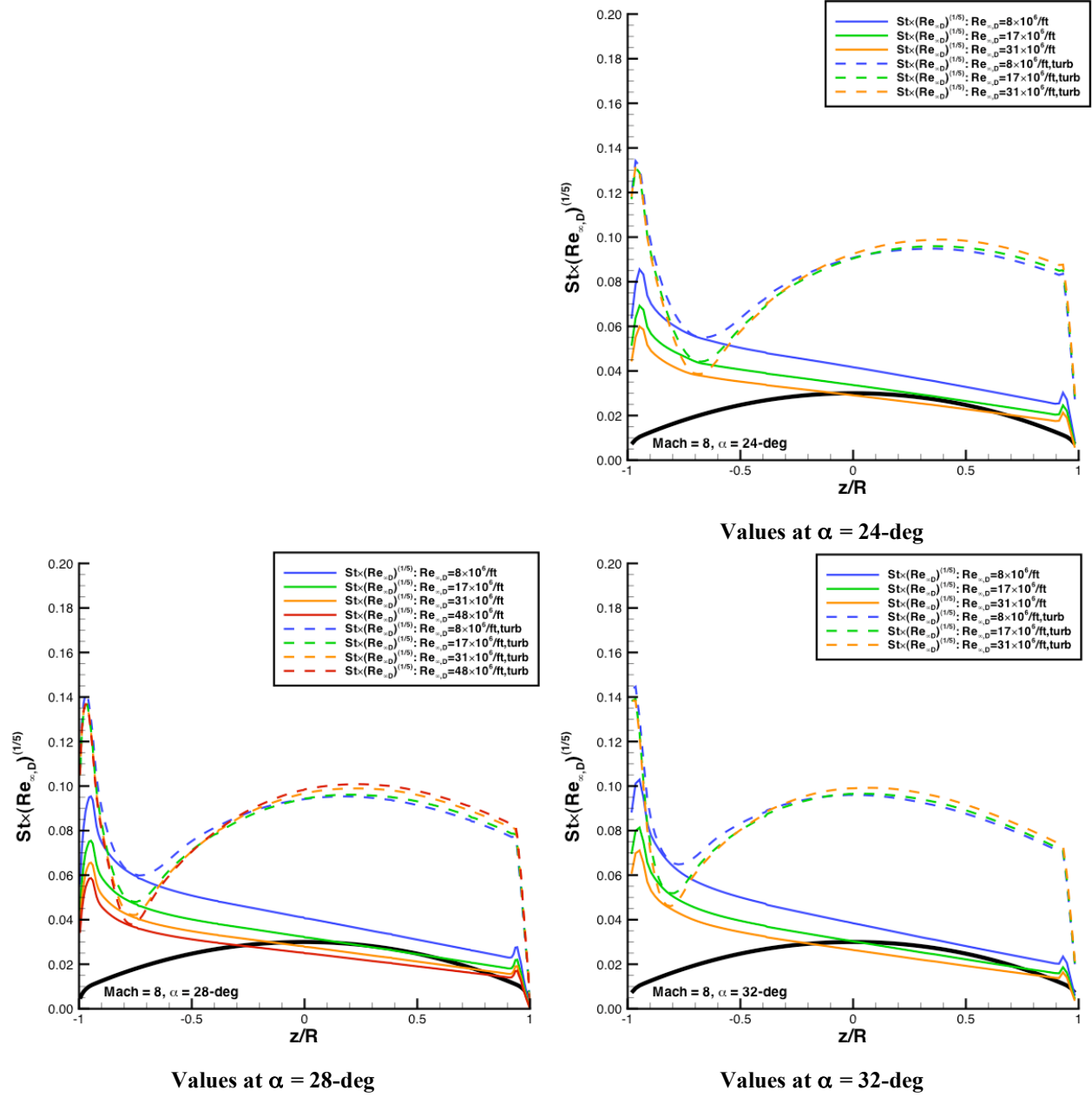
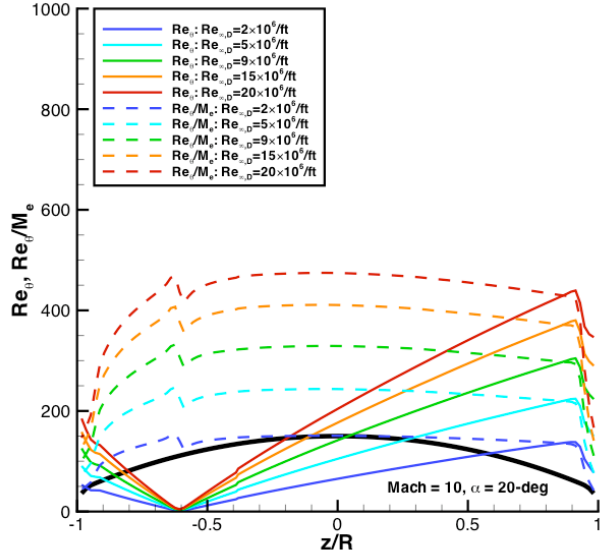
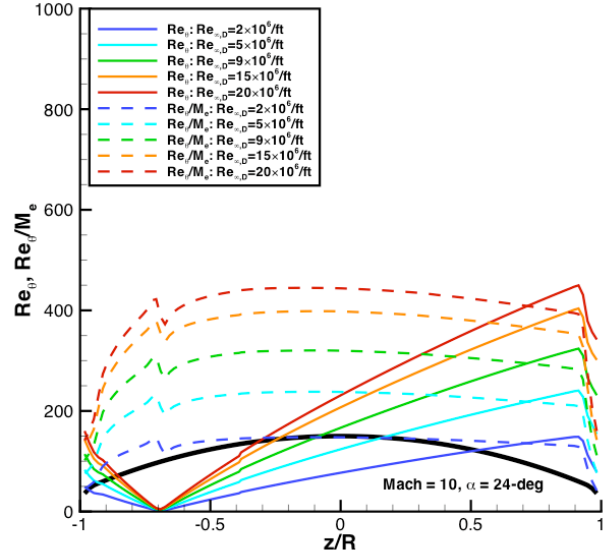


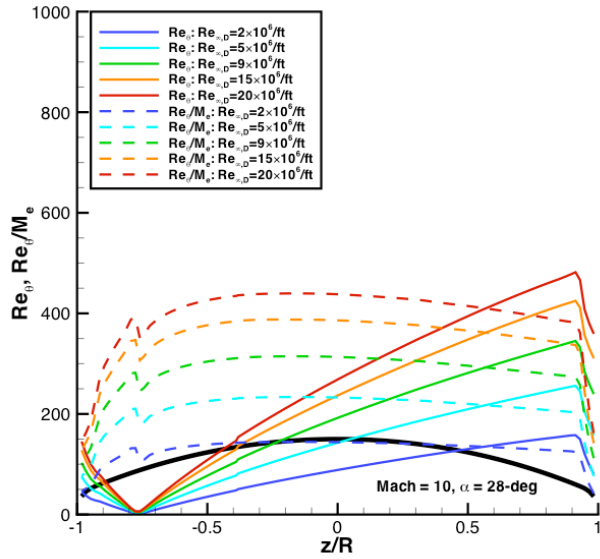
Figure 57. Turbulent correlation parameter for predicted heating at Mach 8



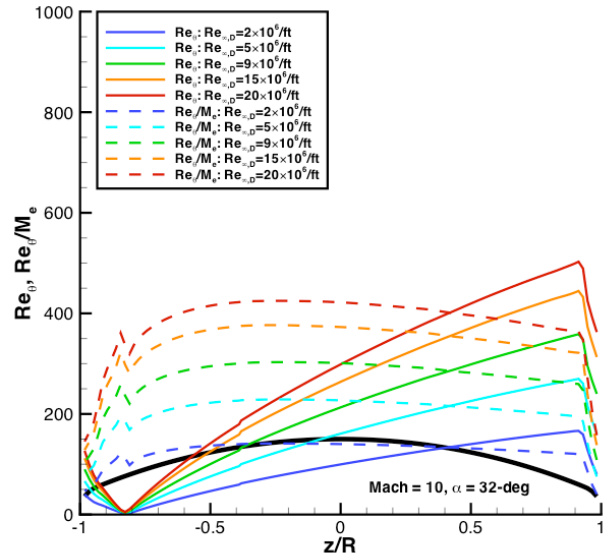
Values at $\alpha = 20$ -deg



Values at $\alpha = 24$ -deg

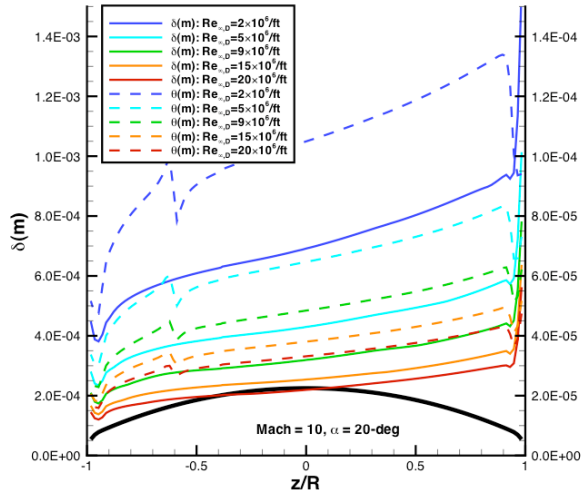


Values at $\alpha = 28$ -deg

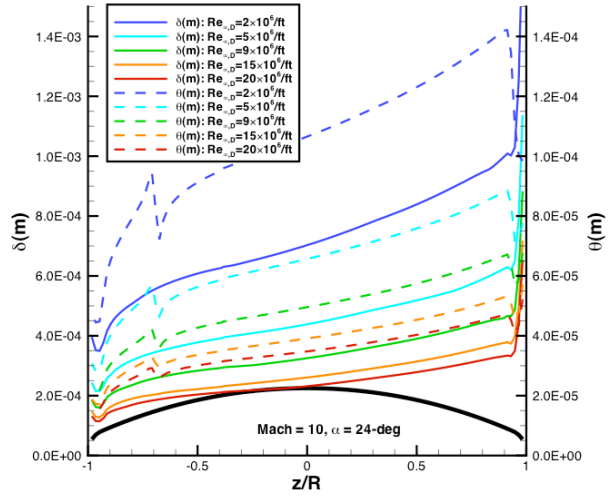


Values at $\alpha = 32$ -deg

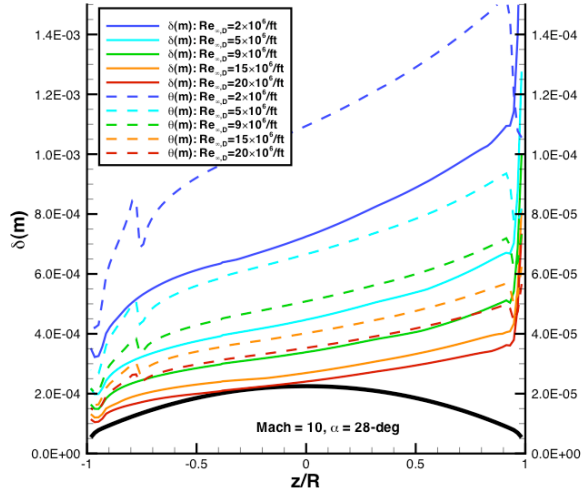
Figure 58. Predicted boundary-layer transition parameters at Mach 10



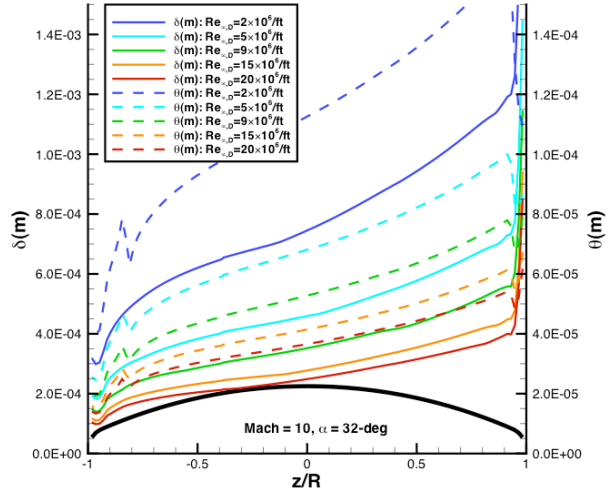
Values at $\alpha = 20\text{-deg}$



Values at $\alpha = 24\text{-deg}$



Values at $\alpha = 28\text{-deg}$



Values at $\alpha = 32\text{-deg}$

Figure 59. Predicted boundary-layer height parameters at Mach 10

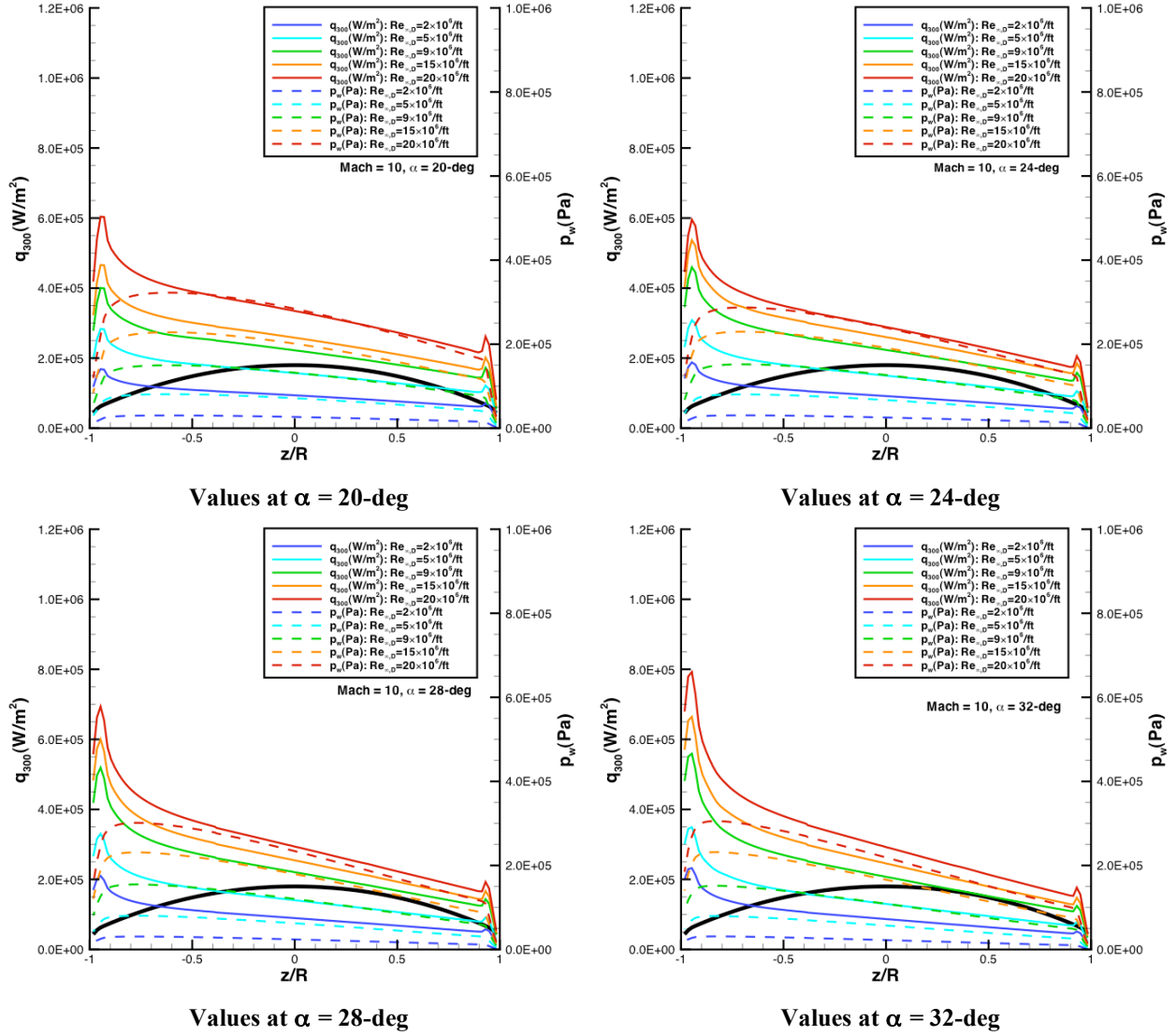
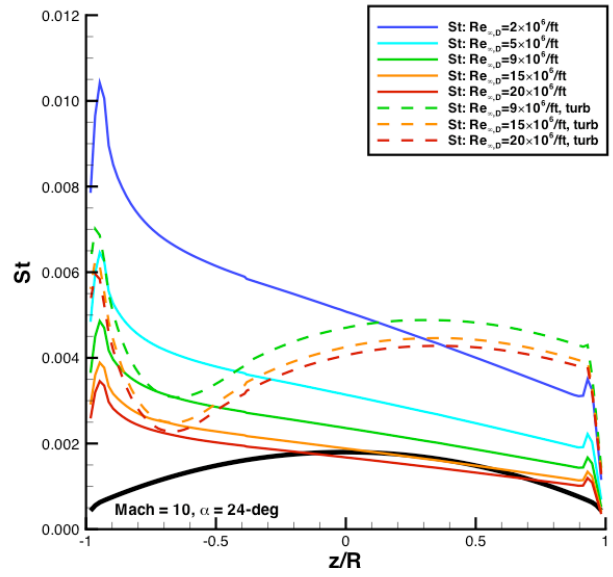
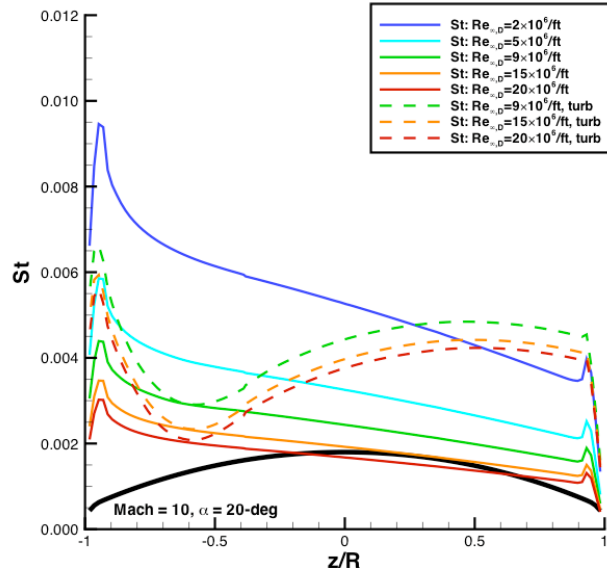
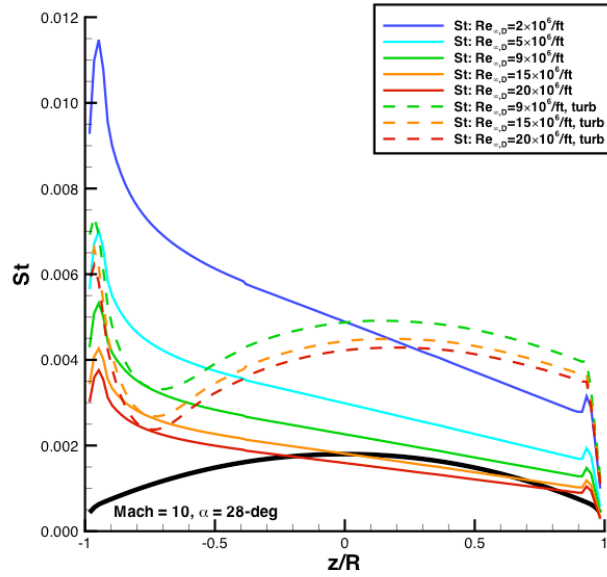


Figure 60. Predicted surface heating and pressure at Mach 10

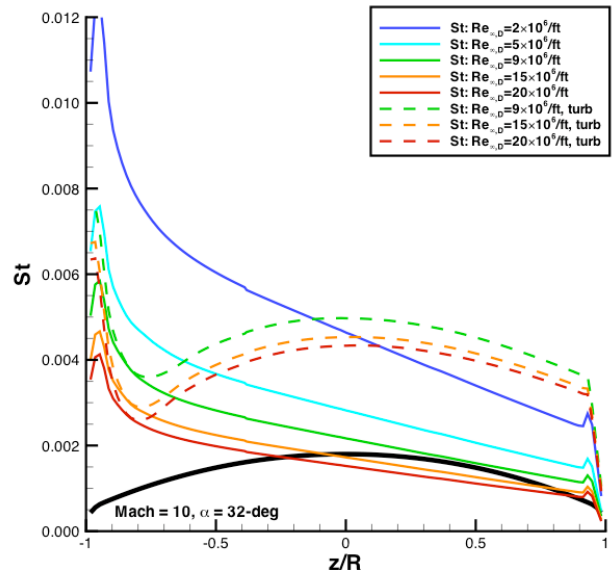


Values at $\alpha = 20\text{-deg}$



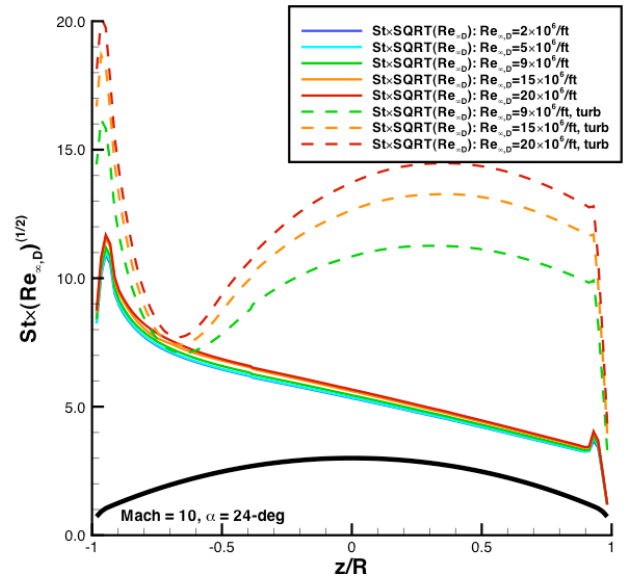
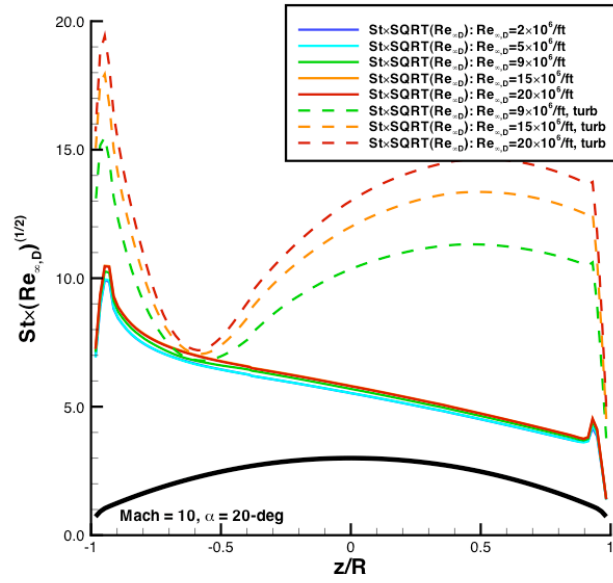
Values at $\alpha = 28\text{-deg}$

Values at $\alpha = 24\text{-deg}$



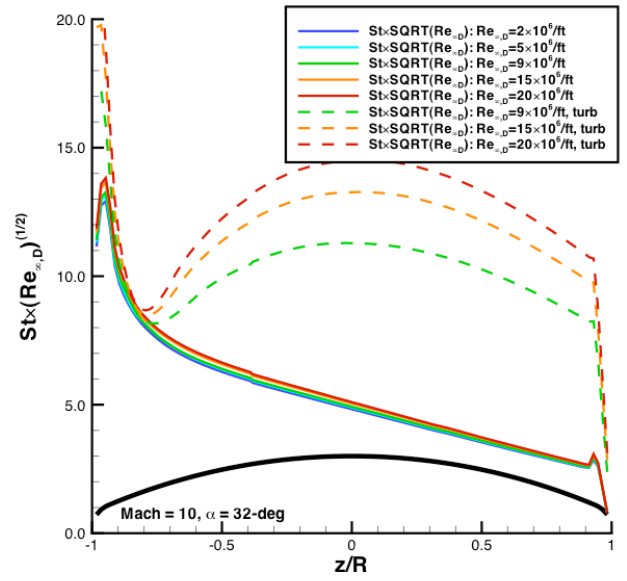
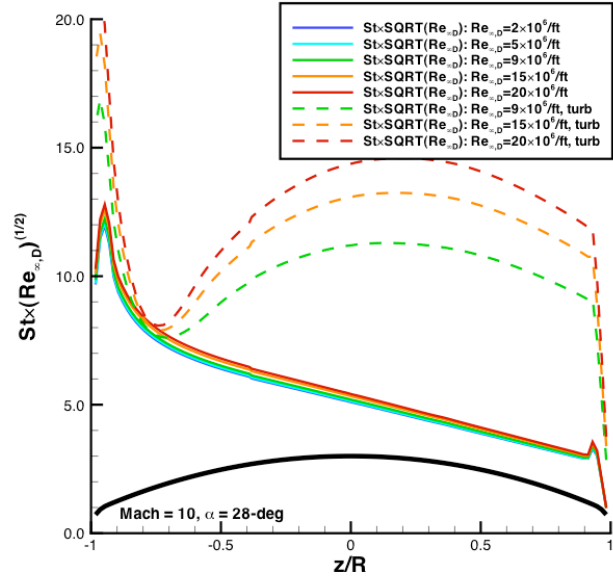
Values at $\alpha = 32\text{-deg}$

Figure 61. Predicted Stanton numbers at Mach 10



Values at α = 20-deg

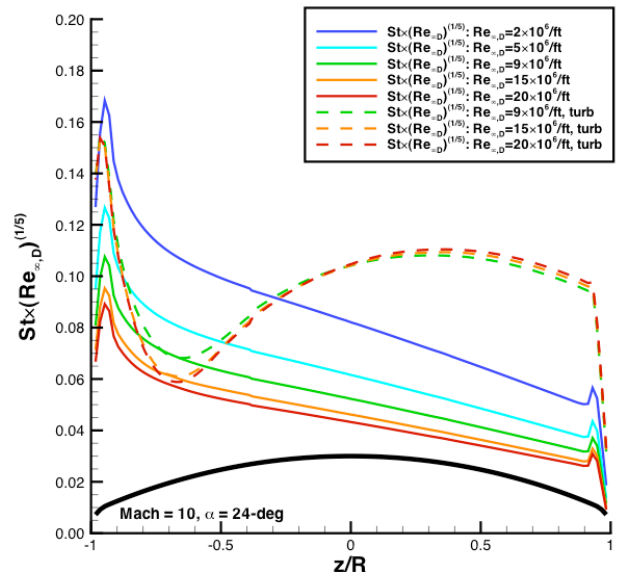
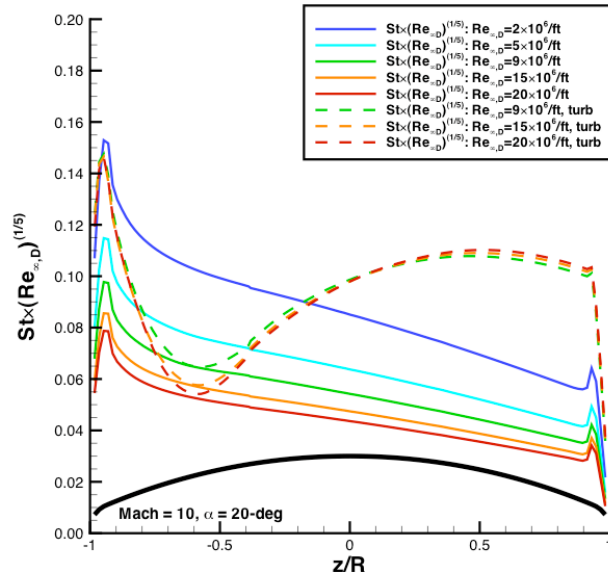
Values at α = 24-deg



Values at α = 28-deg

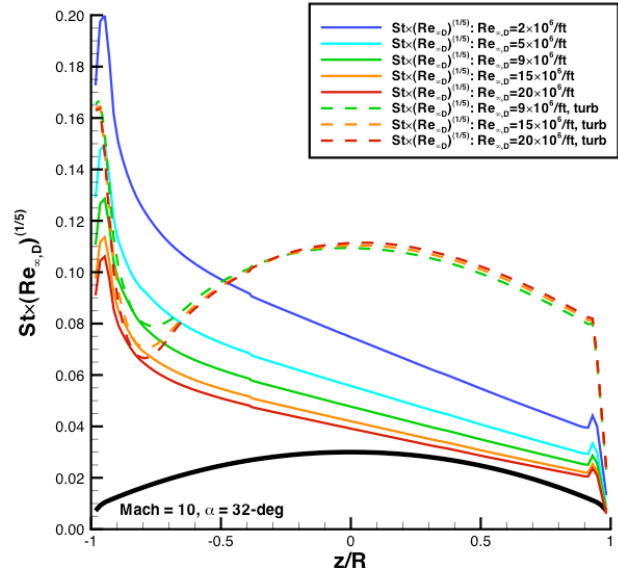
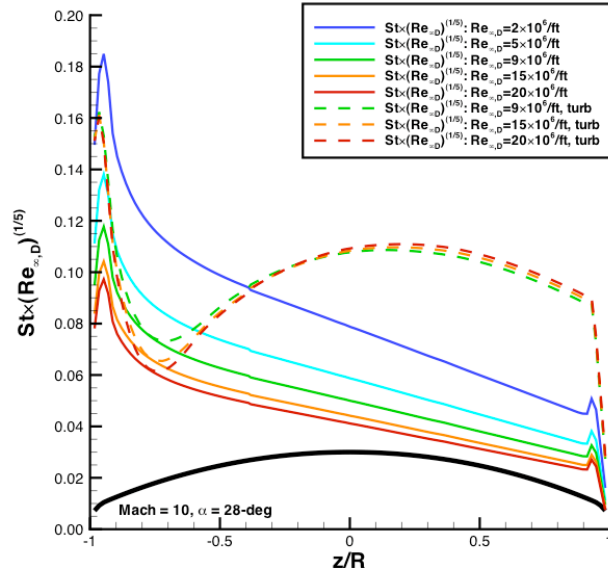
Values at α = 32-deg

Figure 62. Laminar correlation parameter for predicted heating at Mach 10



Values at α = 20-deg

Values at α = 24-deg



Values at α = 28-deg

Values at α = 32-deg

Figure 63. Turbulent correlation parameter for predicted heating at Mach 10

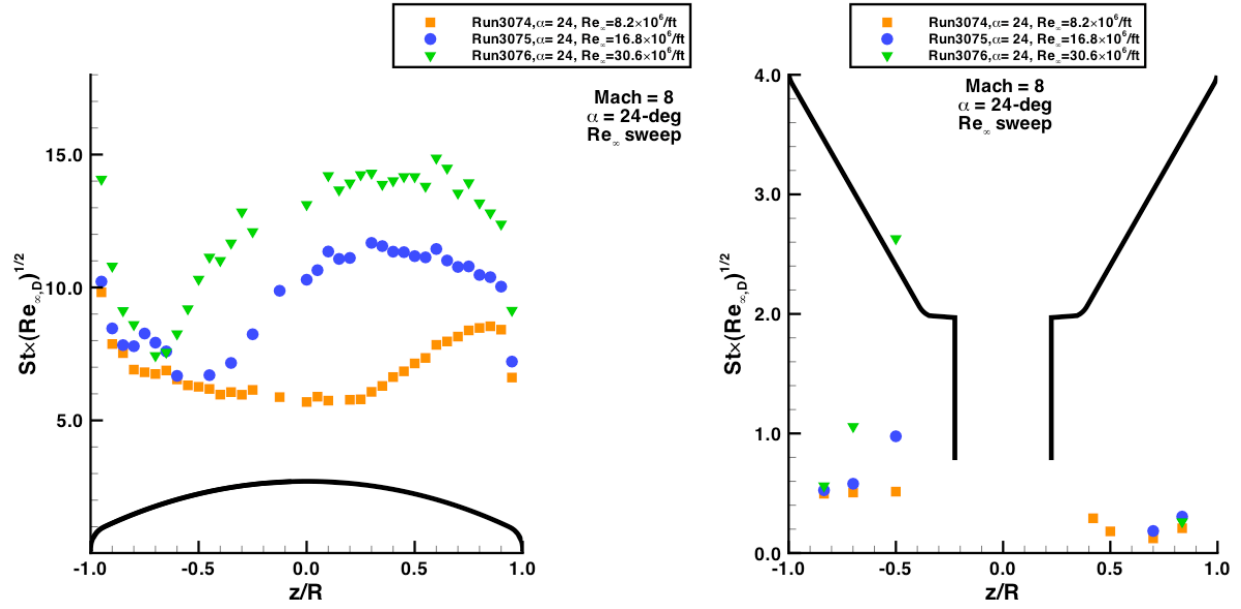


Figure 64. Reynolds numbers effects, Mach = 8, $\alpha = 24$ -deg

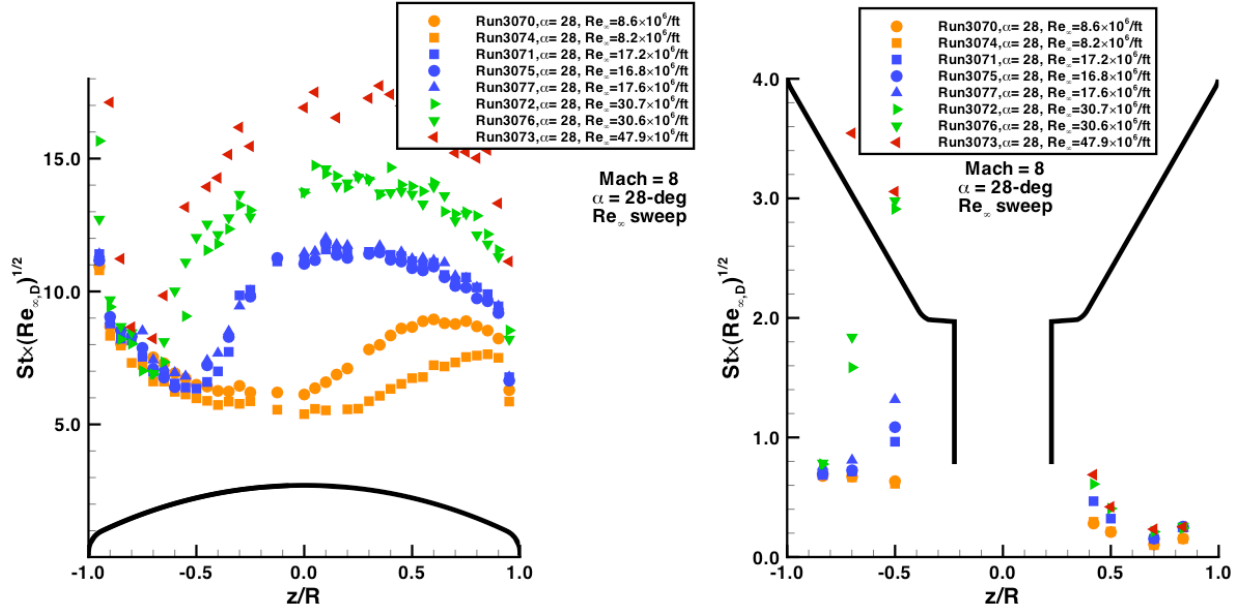


Figure 65. Reynolds numbers effects, Mach = 8, $\alpha = 28$ -deg

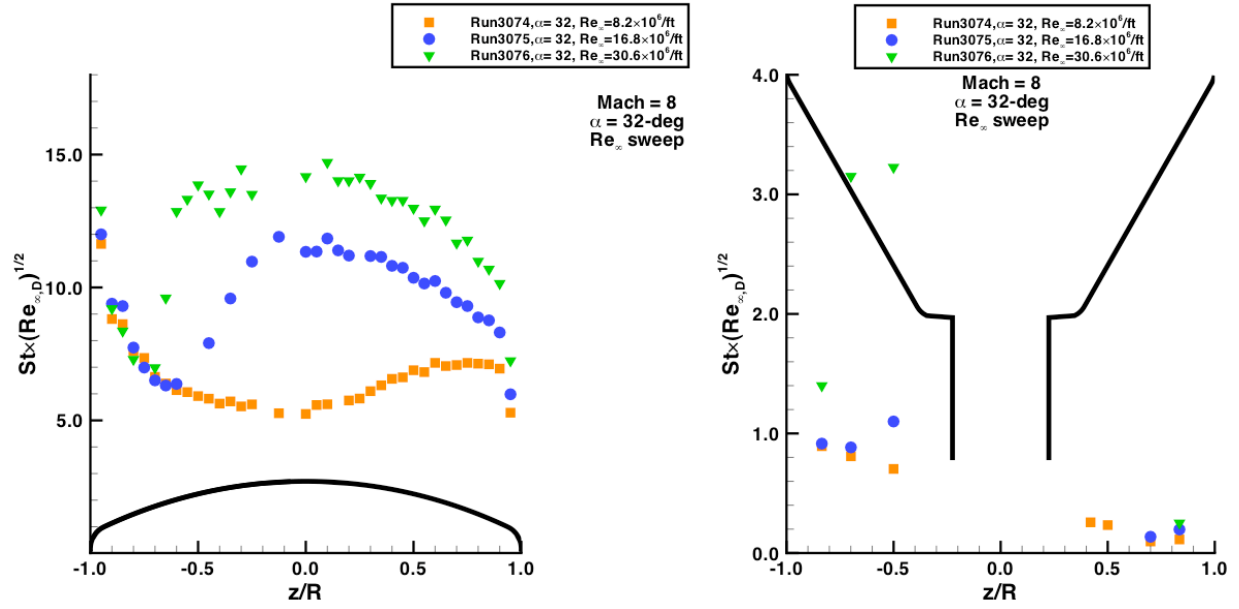


Figure 66. Reynolds numbers effects, Mach = 8, $\alpha = 32$ -deg

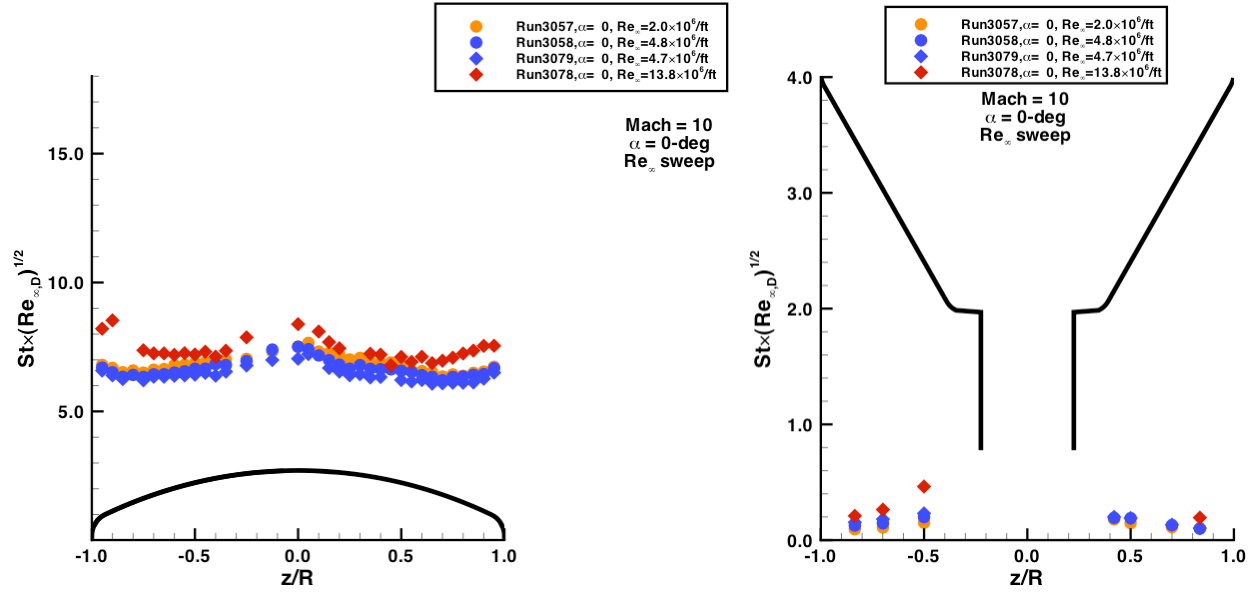


Figure 67. Reynolds numbers effects, Mach = 10, $\alpha = 0$ -deg

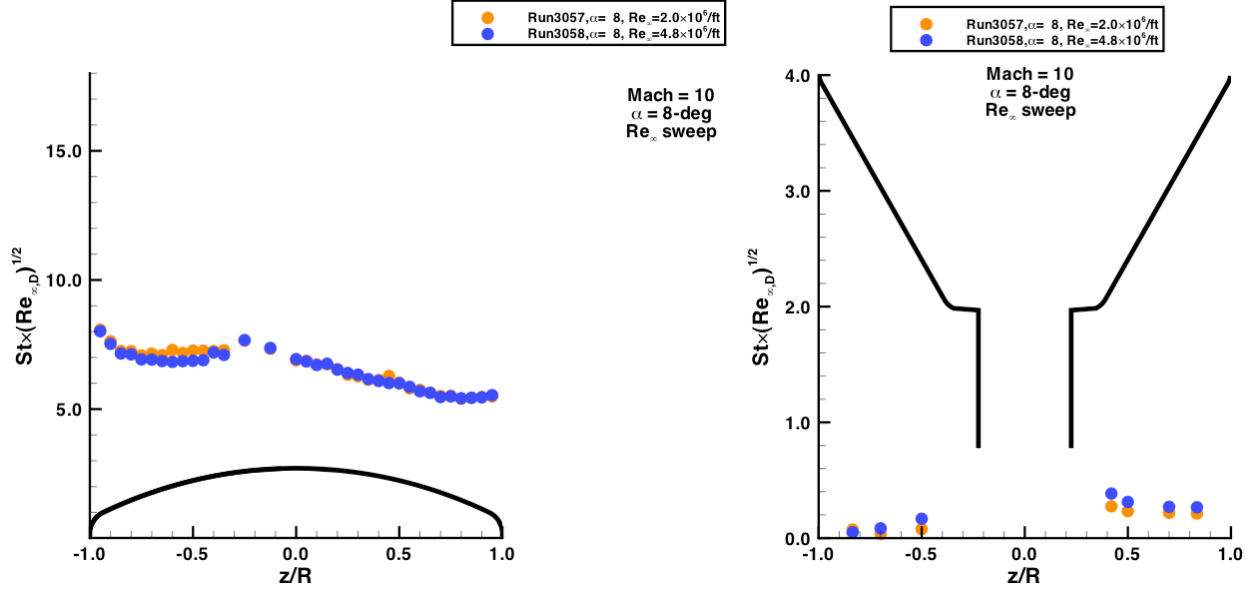


Figure 68. Reynolds numbers effects, Mach = 10, $\alpha = 8$ -deg

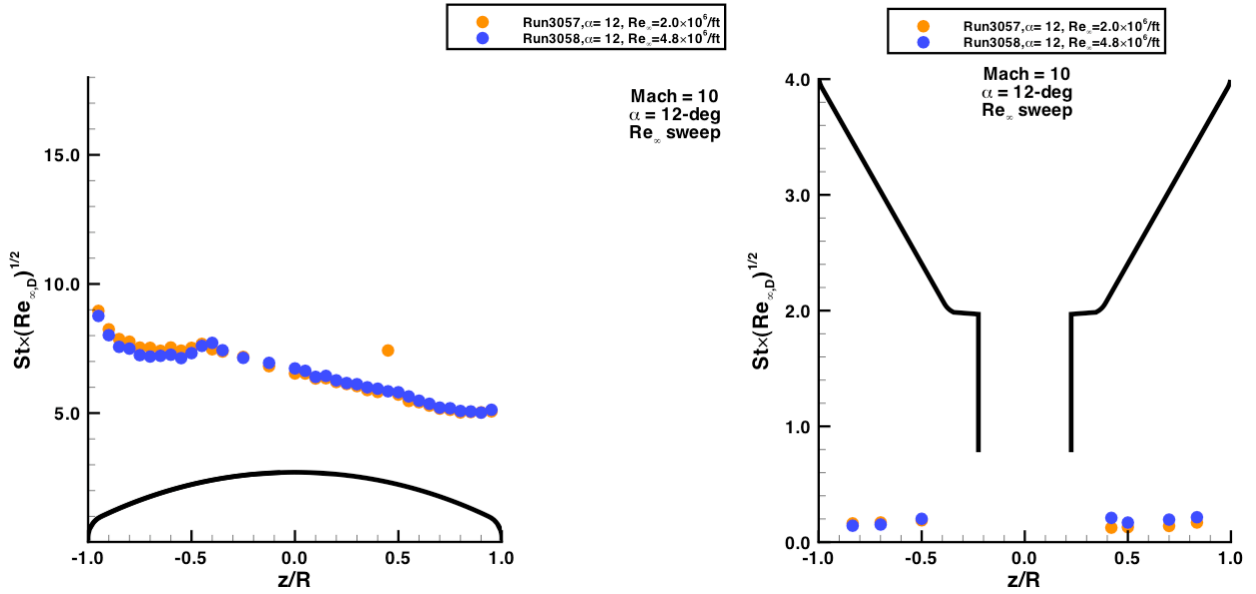


Figure 69. Reynolds numbers effects, Mach = 10, $\alpha = 12$ -deg

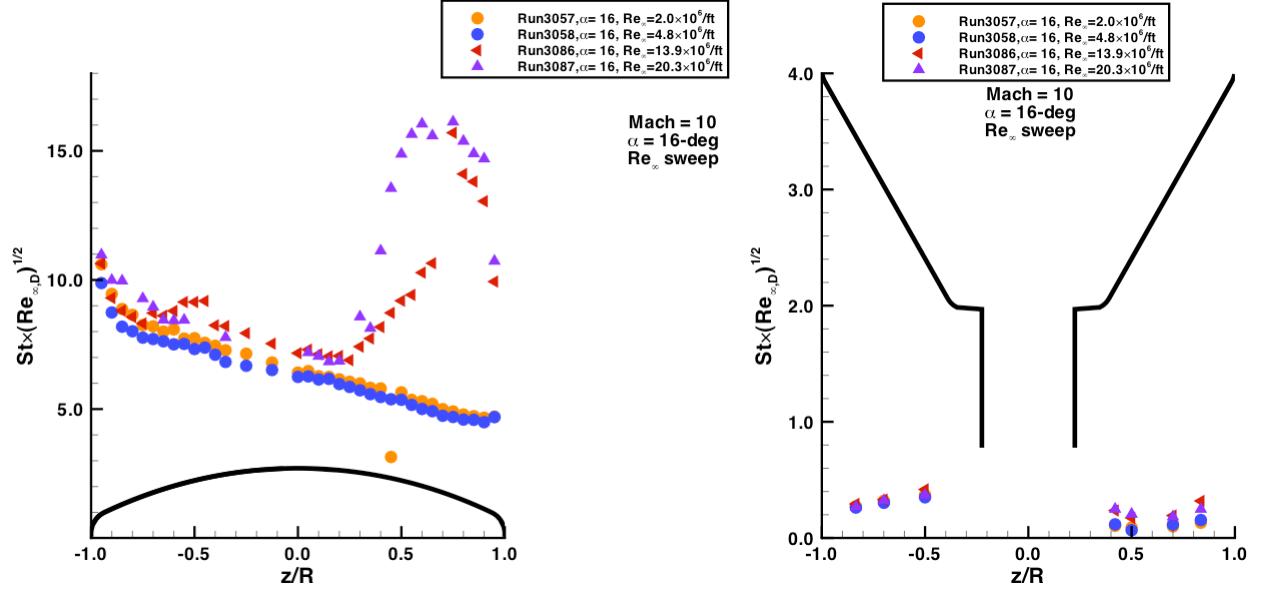


Figure 70. Reynolds numbers effects, Mach = 10, $\alpha = 16$ -deg

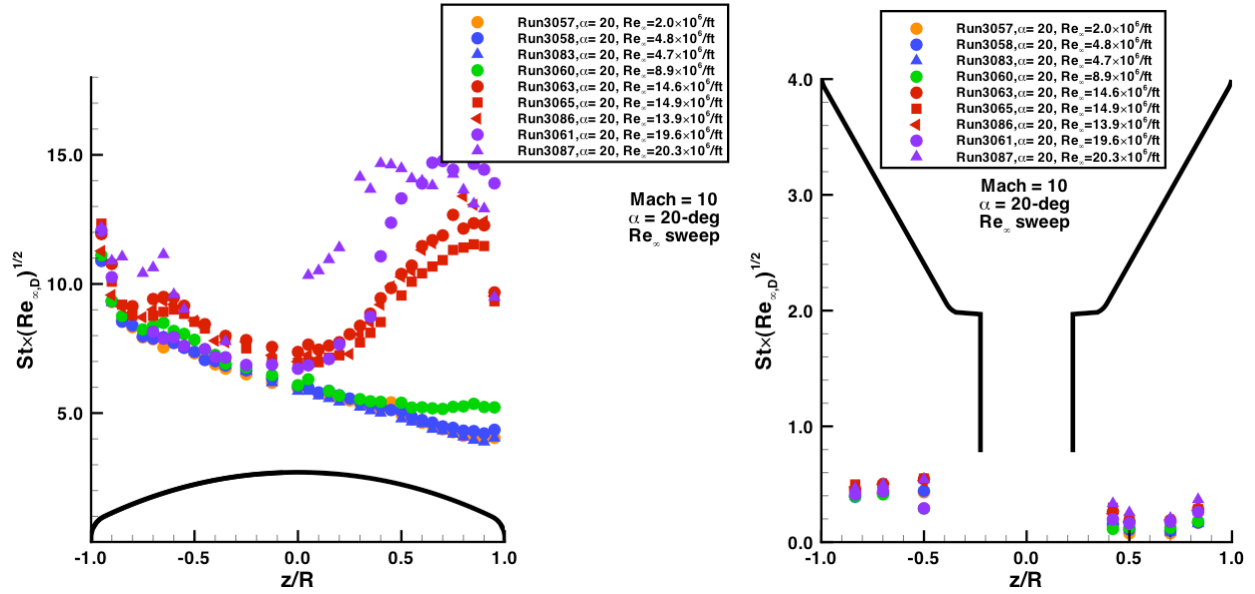


Figure 71. Reynolds numbers effects, Mach = 10, $\alpha = 20$ -deg

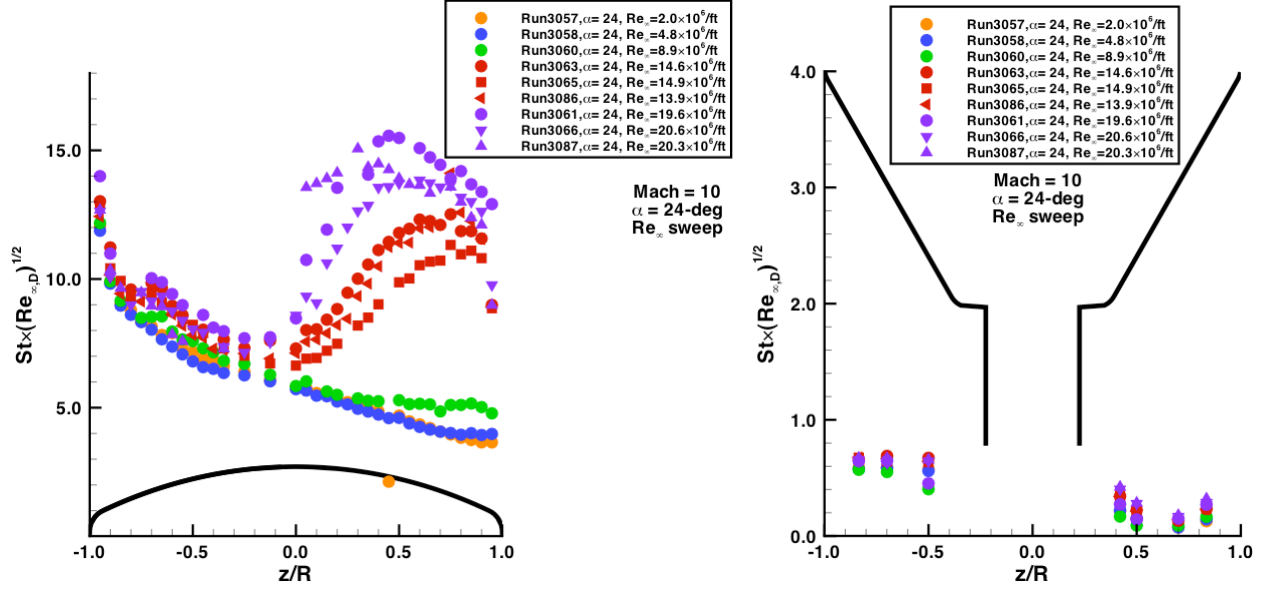


Figure 72. Reynolds numbers effects, $Mach = 10$, $\alpha = 24$ -deg

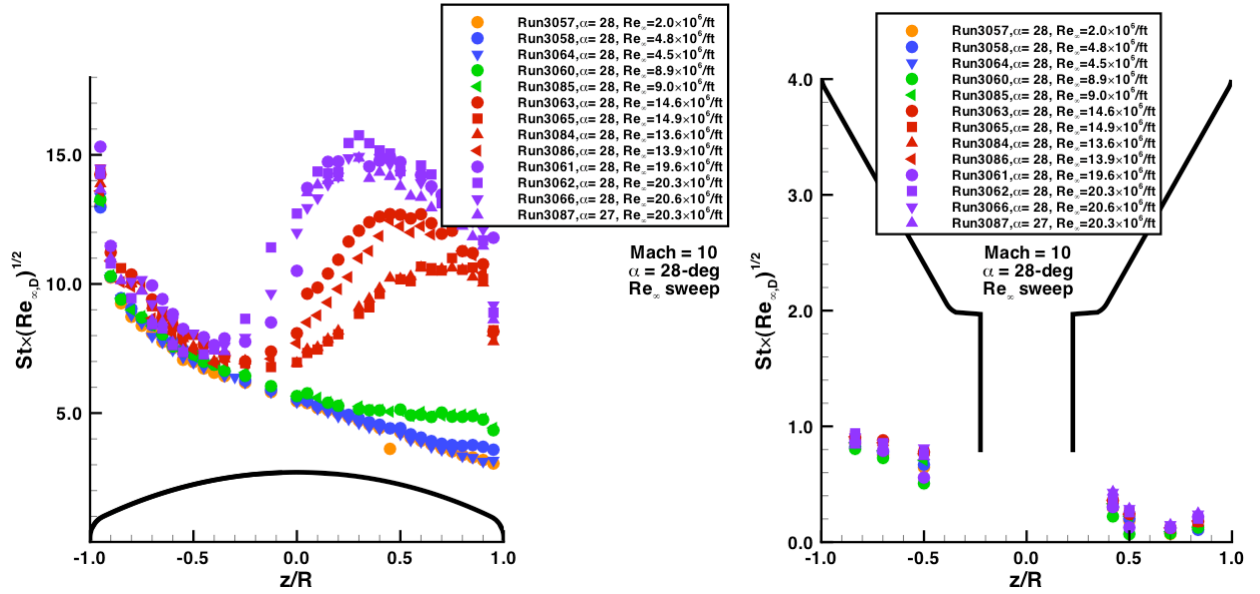


Figure 73. Reynolds numbers effects, $Mach = 10$, $\alpha = 28$ -deg

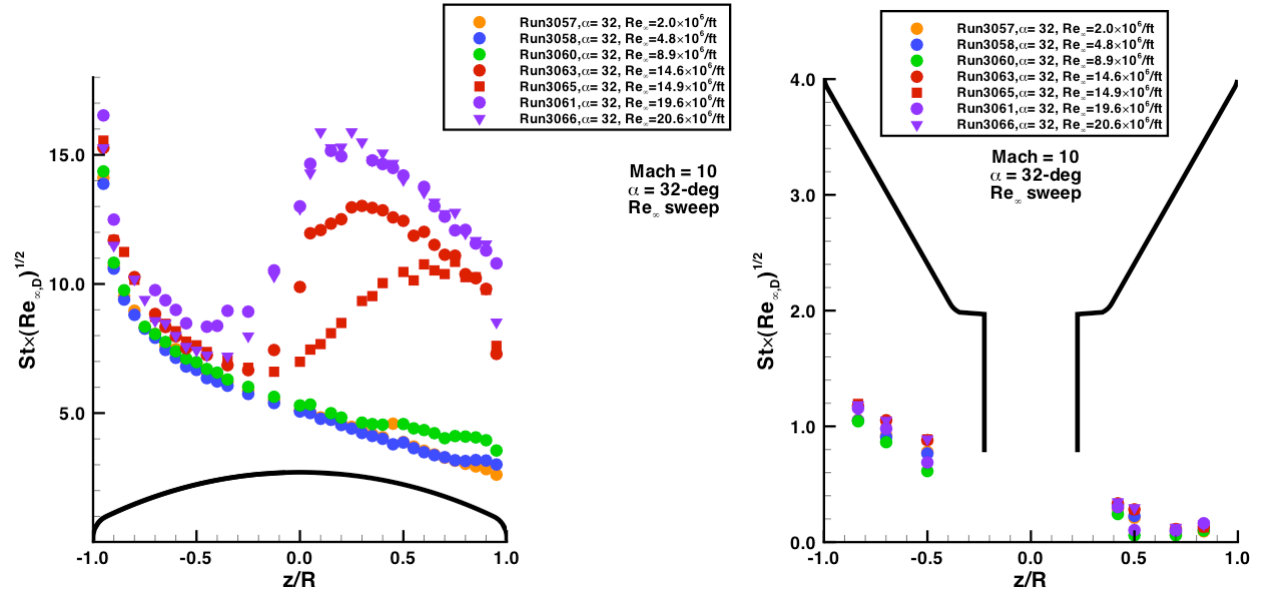


Figure 74. Reynolds numbers effects, Mach = 10, $\alpha = 32$ -deg

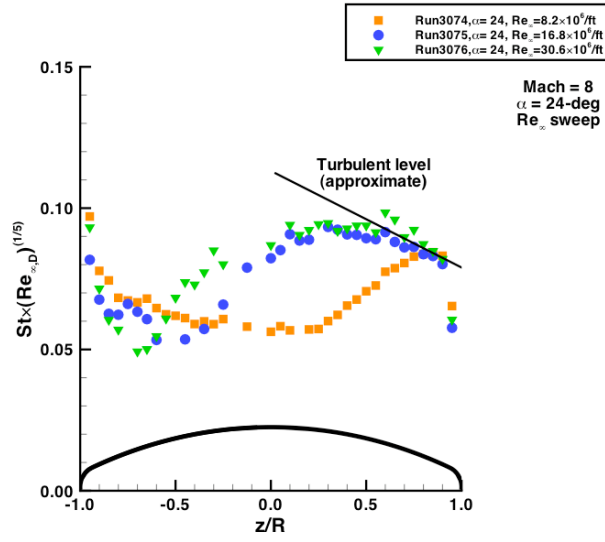


Figure 75. Turbulent heating correlation with Reynolds number, Mach = 8, $\alpha = 24\text{-deg}$

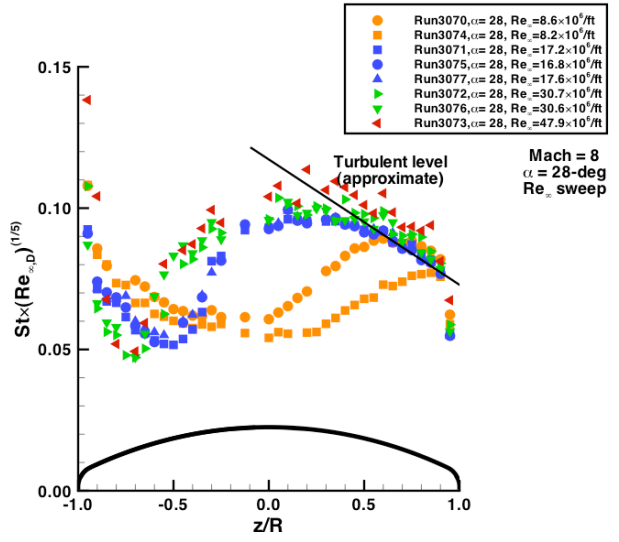


Figure 76. Turbulent heating correlation with Reynolds number, Mach = 8, $\alpha = 28\text{-deg}$

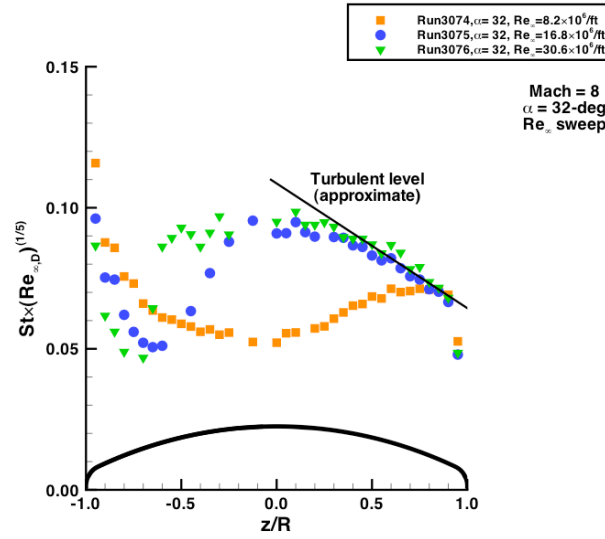


Figure 77. Turbulent heating correlation with Reynolds number, Mach = 8, $\alpha = 32\text{-deg}$

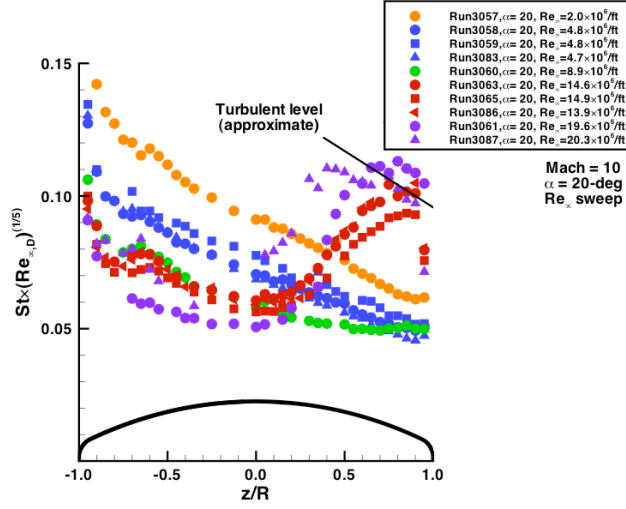


Figure 78. Turbulent heating correlation with Reynolds number, Mach = 10, $\alpha = 20$ -deg

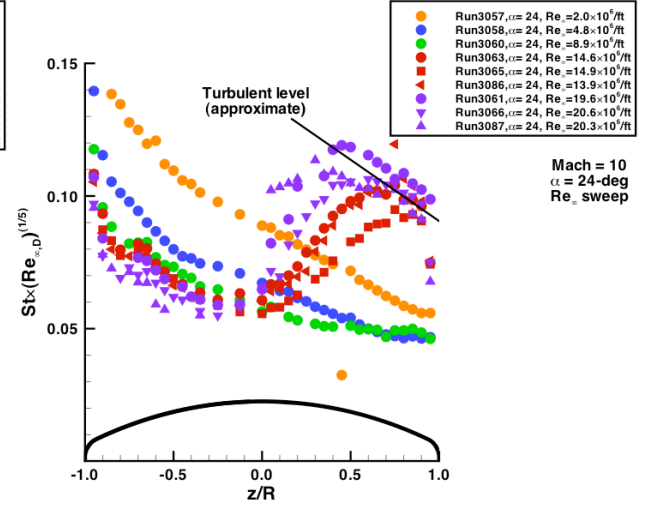


Figure 79. Turbulent heating correlation with Reynolds number, Mach = 10, $\alpha = 24$ -deg

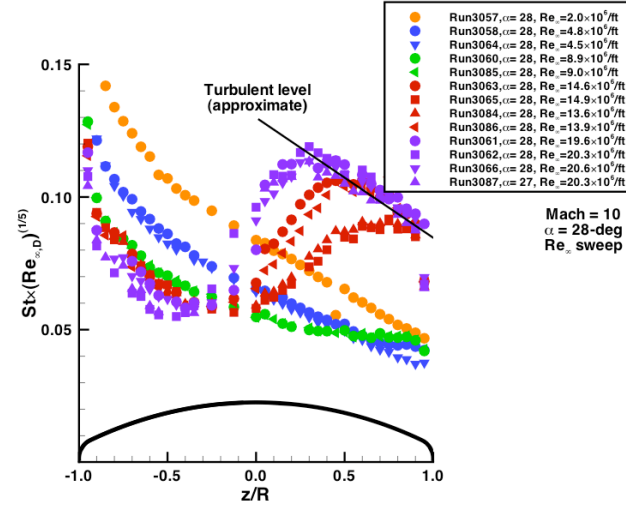


Figure 80. Turbulent heating correlation with Reynolds number, Mach = 10, $\alpha = 28$ -deg

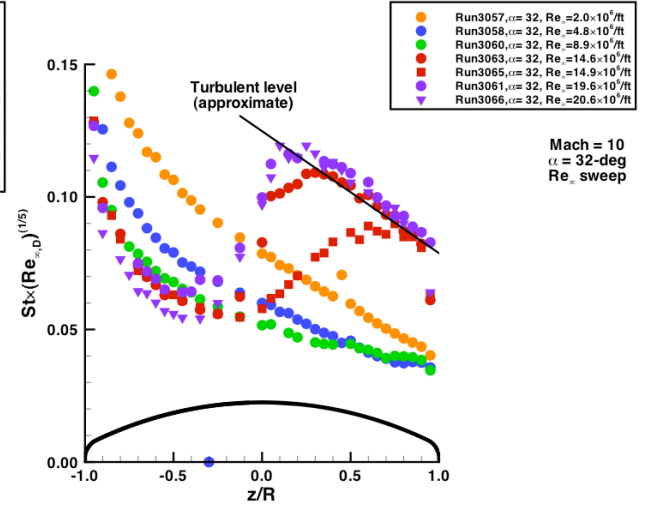


Figure 81. Turbulent heating correlation with Reynolds number, Mach = 10, $\alpha = 32$ -deg

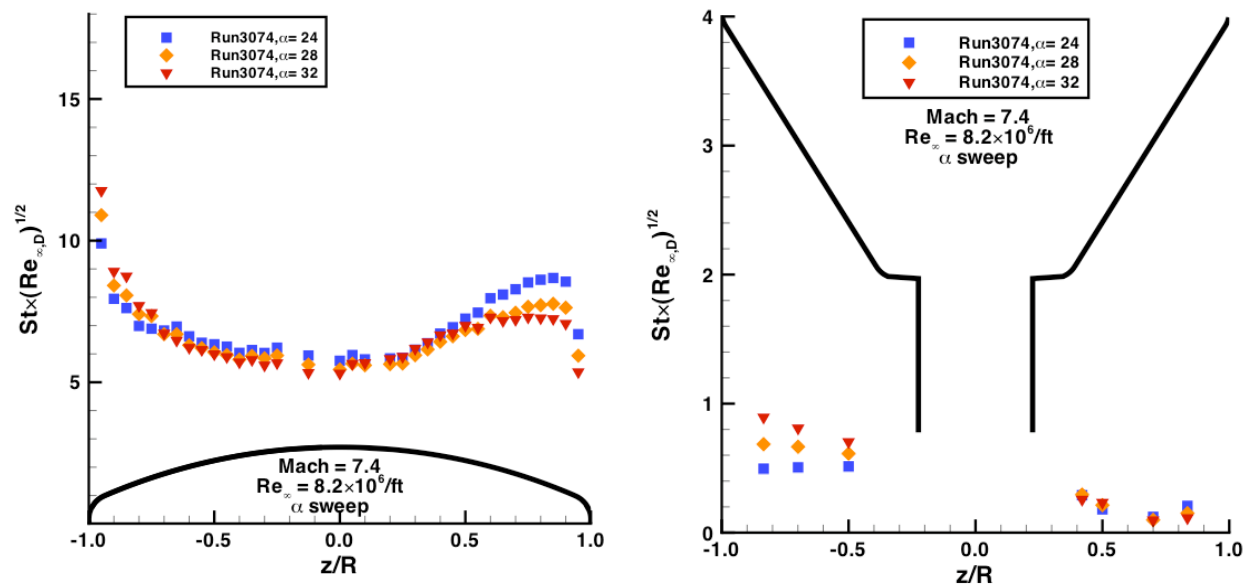


Figure 82. Angle-of-attack effects, Run 3074, Mach = 8, $Re_{\infty} = 8 \times 10^6/ft$

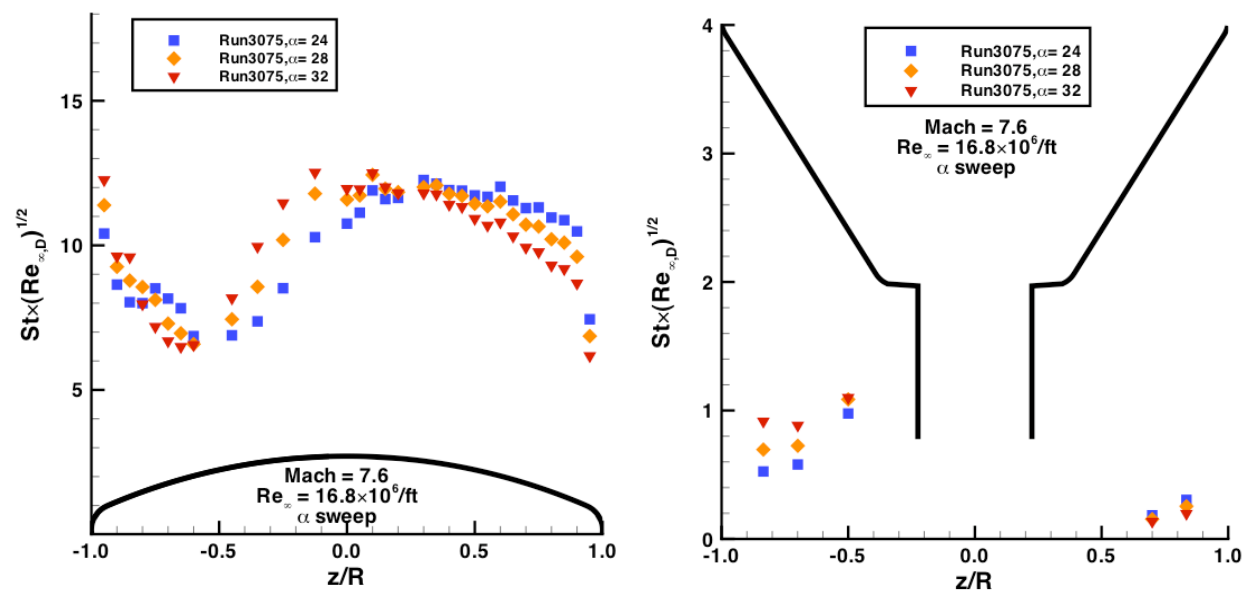


Figure 83. Angle-of-attack effects, Run 3075, Mach = 8, $Re_{\infty} = 17 \times 10^6/ft$

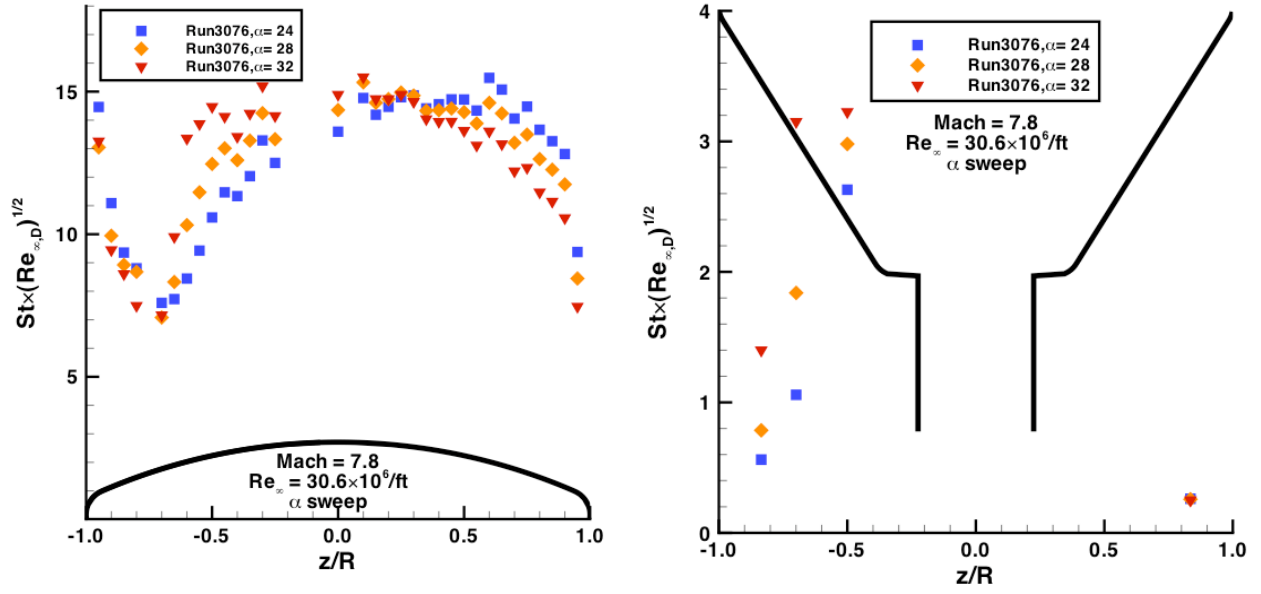


Figure 84. Angle-of-attack effects, Run 3076, Mach = 8, $Re_{\infty} = 31 \times 10^6/ft$

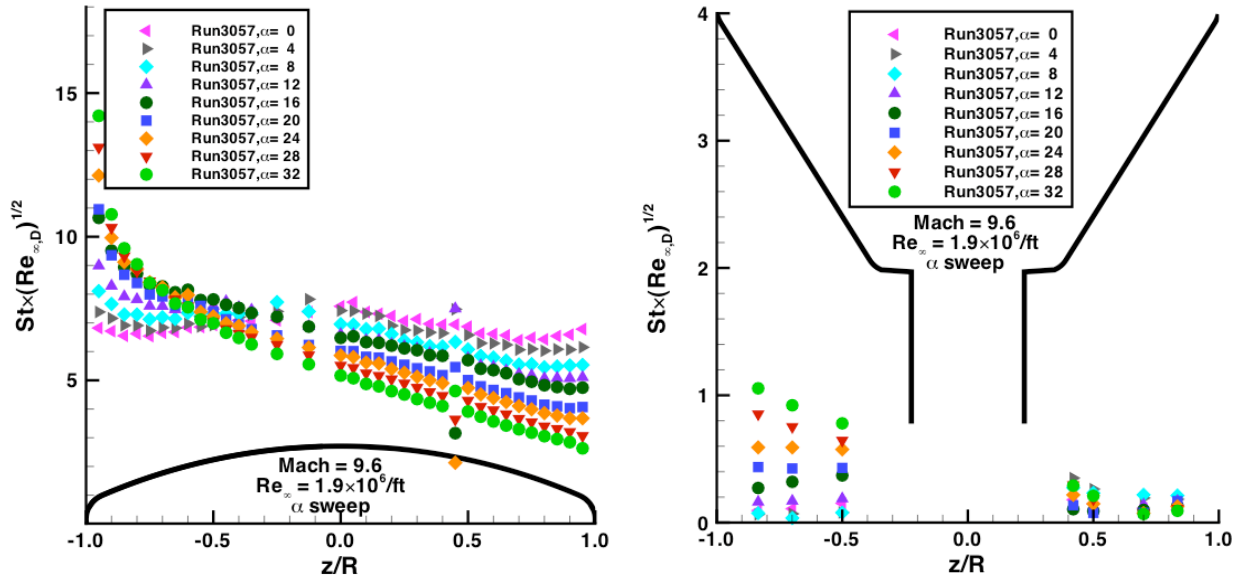


Figure 85. Angle-of-attack effects, Run 3057, Mach = 10, $Re_{\infty} = 2 \times 10^6/ft$

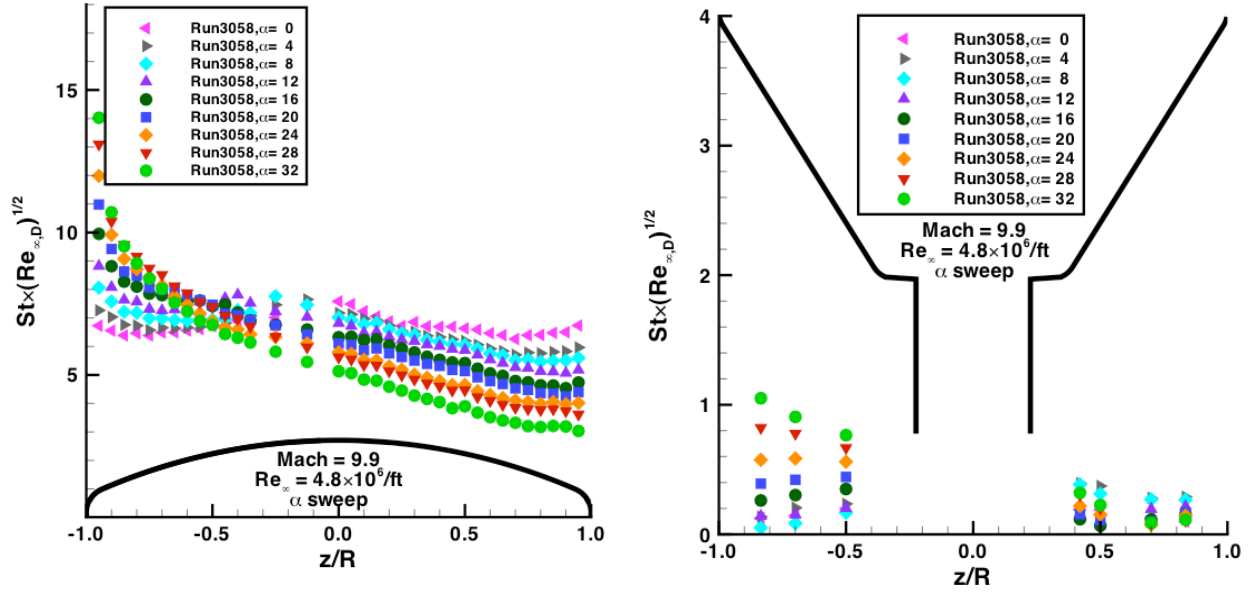


Figure 86. Angle-of-attack effects, Run 3058, Mach = 10, $Re_{\infty} = 5 \times 10^6 / \text{ft}$

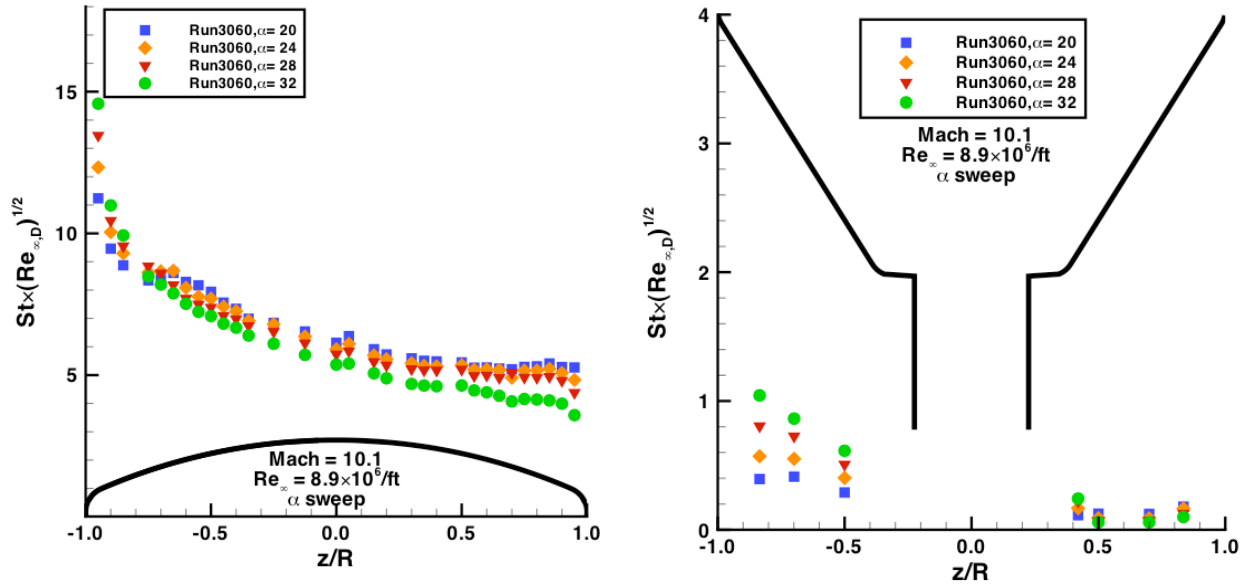


Figure 87. Angle-of-attack effects, Run 3060, Mach = 10, $Re_{\infty} = 9 \times 10^6 / \text{ft}$

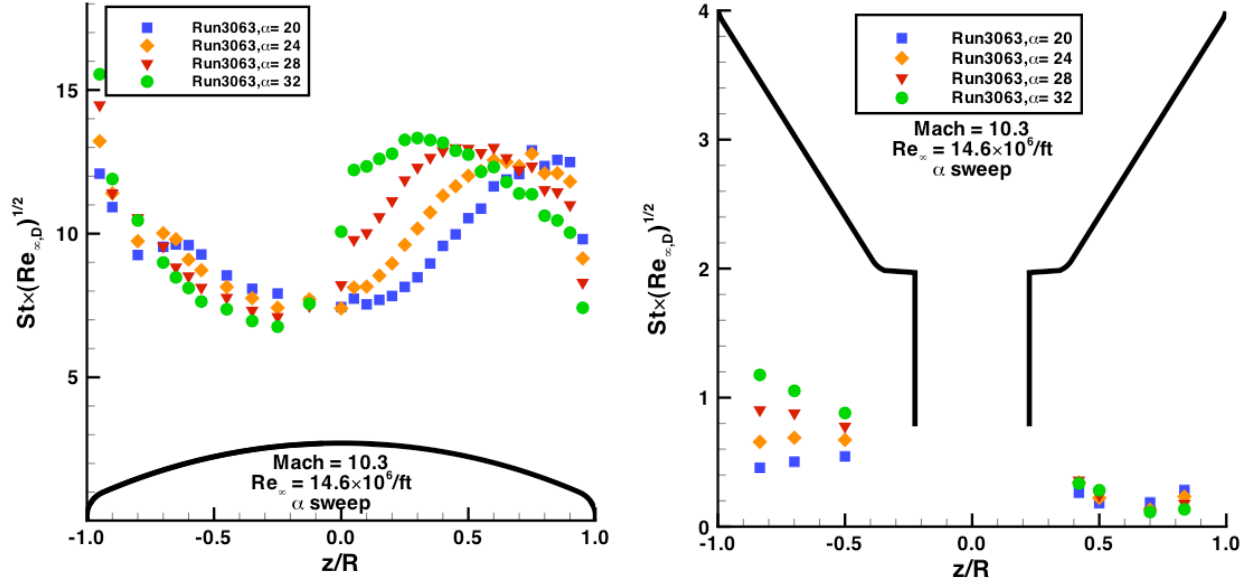


Figure 88. Angle-of-attack effects, Run 3063, Mach = 10, $Re_{\infty} = 15 \times 10^6/\text{ft}$

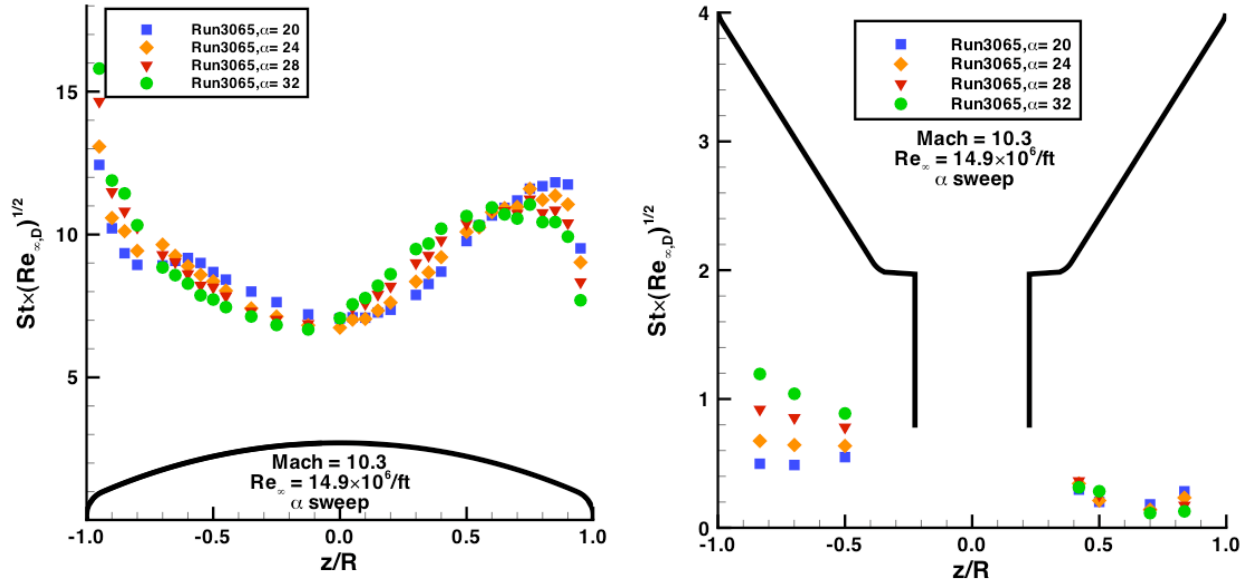


Figure 89. Angle-of-attack effects, Run 3065, Mach = 10, $Re_{\infty} = 15 \times 10^6/\text{ft}$

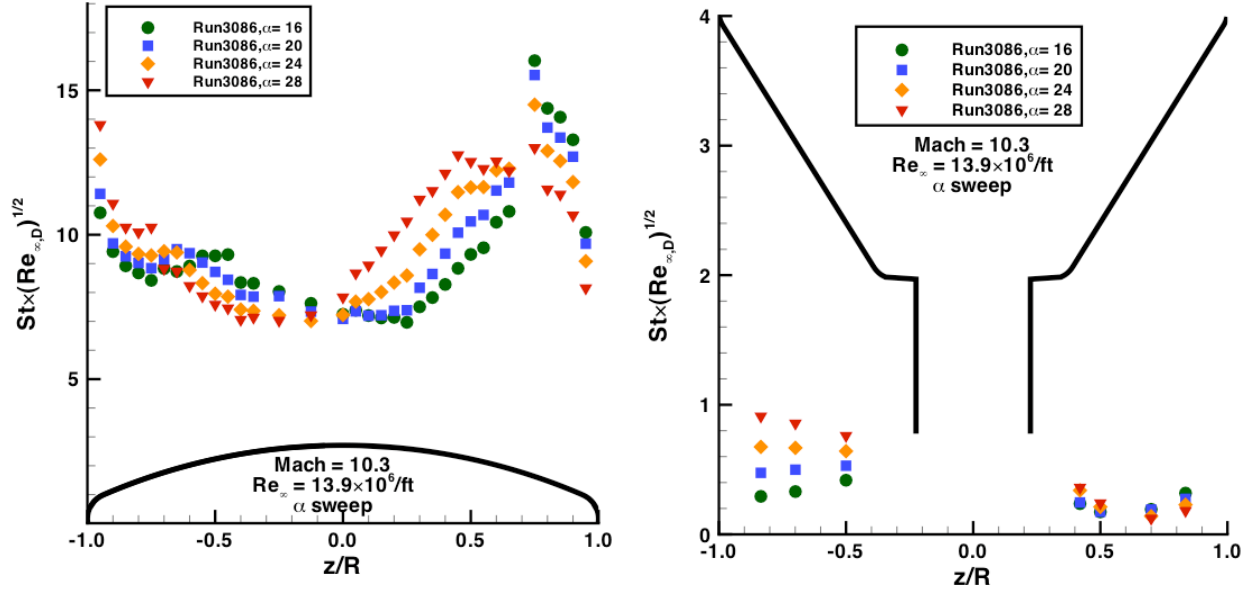


Figure 90. Angle-of-attack effects, Run 3086, Mach = 10, $Re_\infty = 20 \times 10^6/\text{ft}$

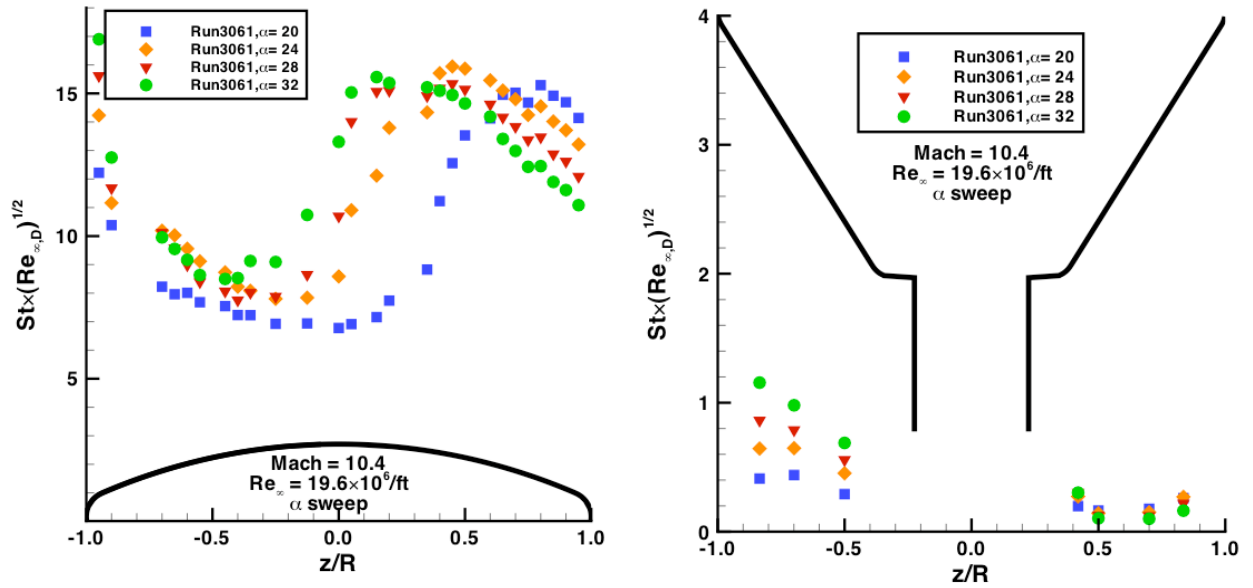


Figure 91. Angle-of-attack effects, Run 3061, Mach = 10, $Re_\infty = 20 \times 10^6/\text{ft}$

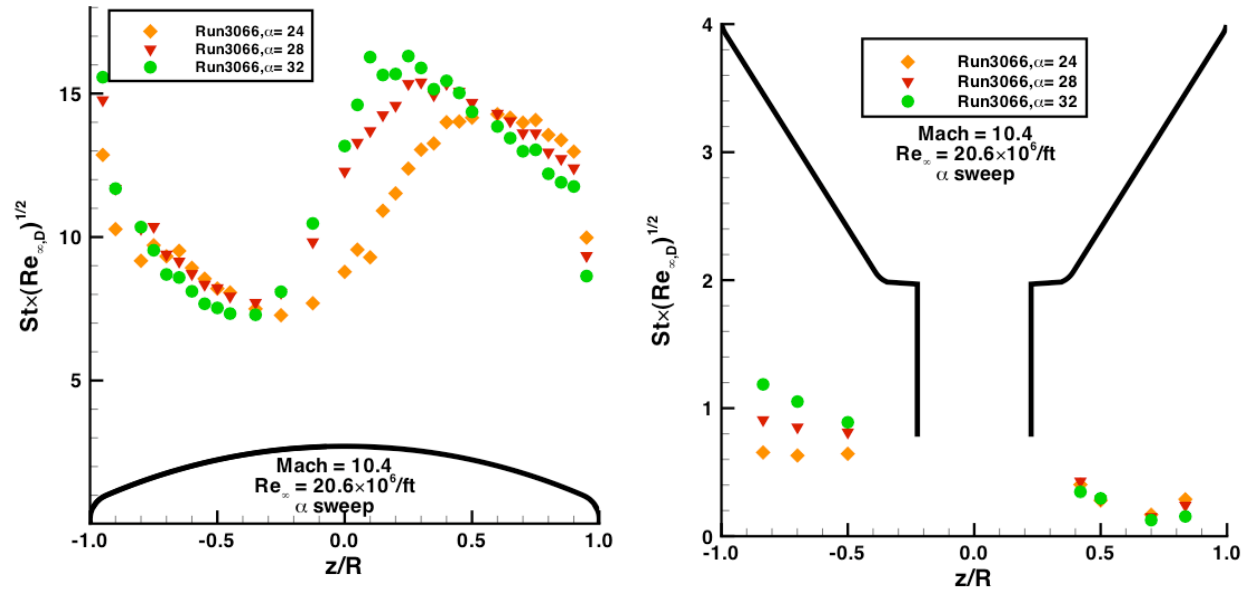


Figure 92. Angle-of-attack effects, Run 3066, Mach = 10, $Re_{\infty} = 20 \times 10^6/ft$

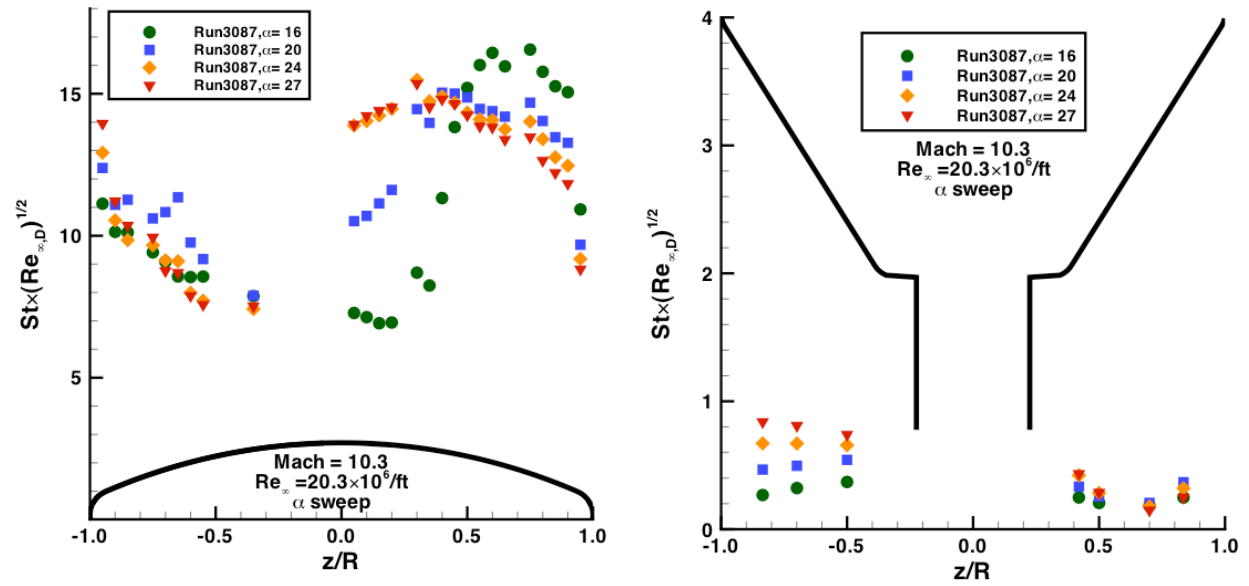
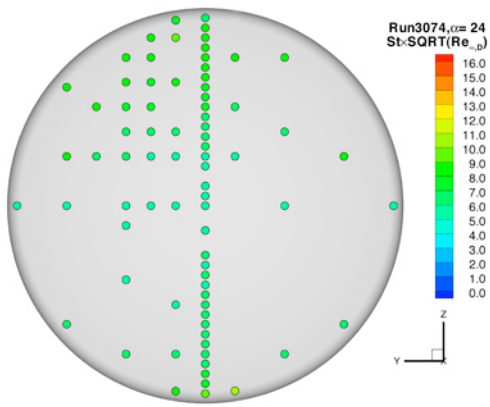
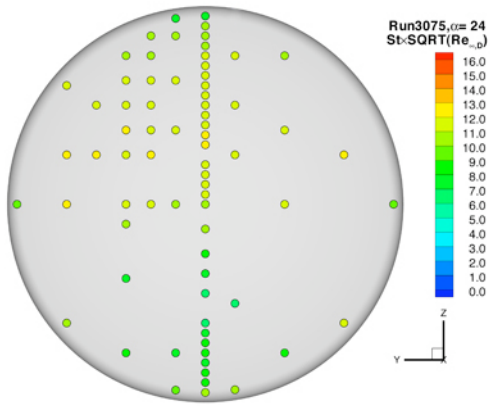


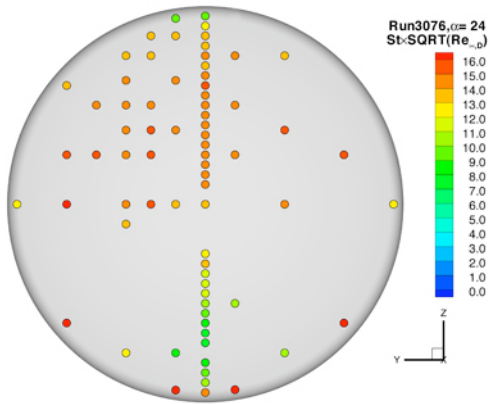
Figure 93. Angle-of-attack effects, Run 3087, Mach = 10, $Re_{\infty} = 20 \times 10^6/ft$



Run 3074, Mach 8, $Re_{\infty} = 8 \times 10^6/\text{ft}$

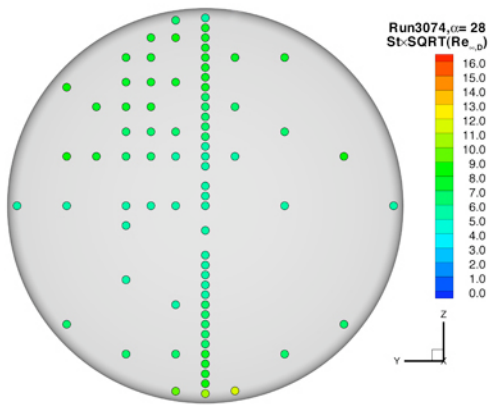


Run 3075, Mach 8, $Re_{\infty} = 17 \times 10^6/\text{ft}$

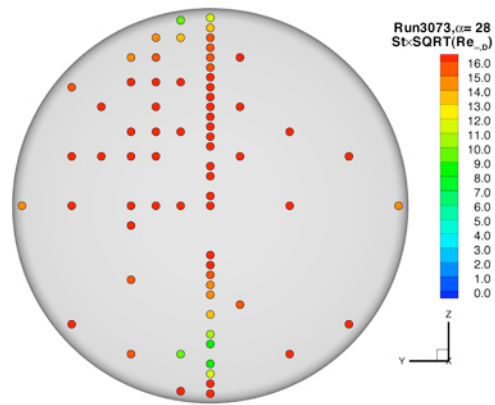


Run 3076, Mach 8, $Re_{\infty} = 31 \times 10^6/\text{ft}$

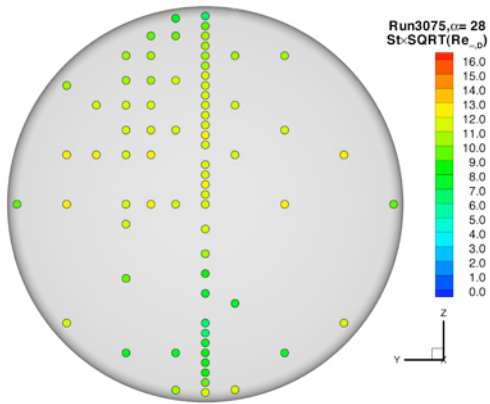
Figure 94. Reynolds numbers effects, Mach = 8, $\alpha=24$ -deg



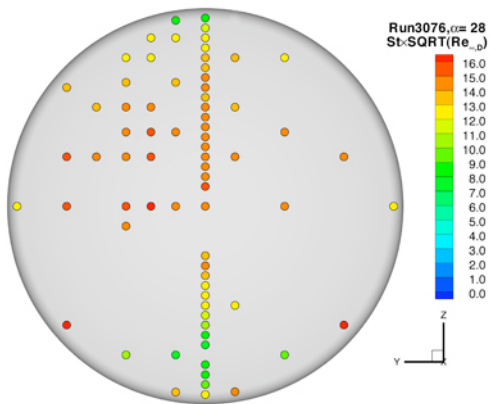
Run 3074, Mach 8, $Re_{\infty} = 8 \times 10^6/\text{ft}$



Run 3073, Mach 8, $Re_{\infty} = 49 \times 10^6/\text{ft}$

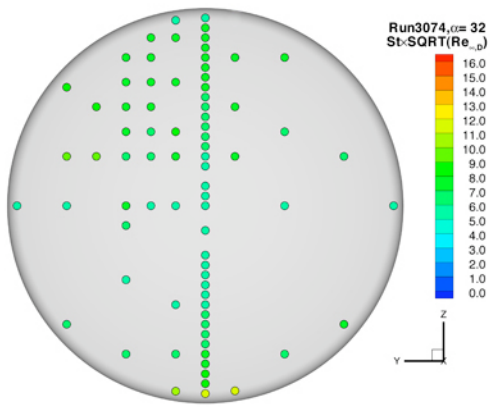


Run 3075, Mach 8, $Re_{\infty} = 17 \times 10^6/\text{ft}$

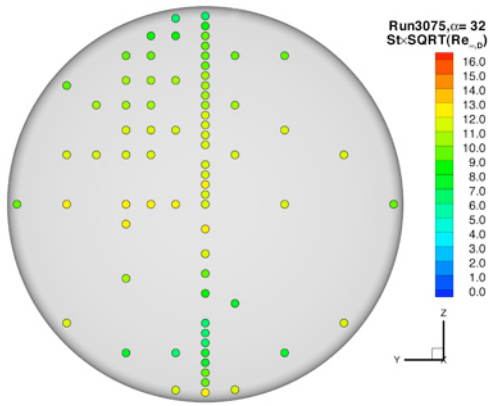


Run 3076, Mach 8, $Re_{\infty} = 31 \times 10^6/\text{ft}$

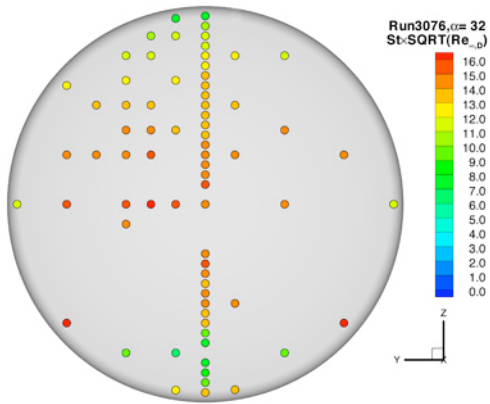
Figure 95. Reynolds numbers effects, Mach = 8, $\alpha=28$ -deg



Run 3074, Mach 8, $Re_{\infty} = 8 \times 10^6/\text{ft}$

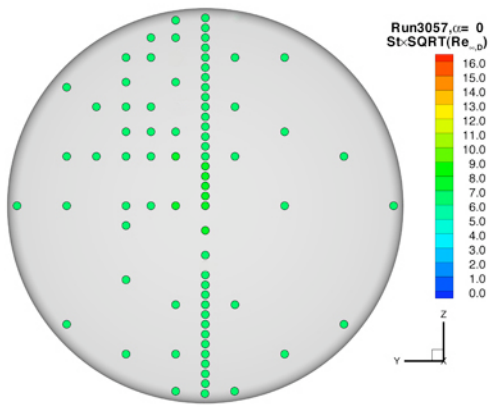


Run 3075, Mach 8, $Re_{\infty} = 17 \times 10^6/\text{ft}$

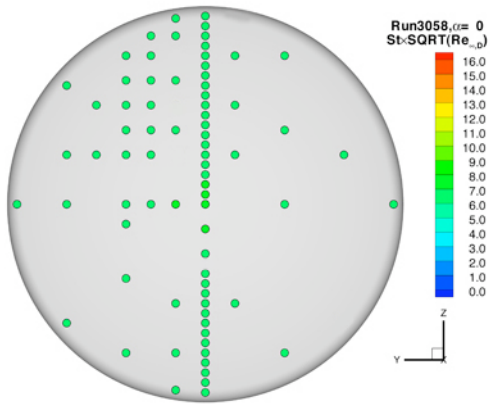


Run 3076, Mach 8, $Re_{\infty} = 31 \times 10^6/\text{ft}$

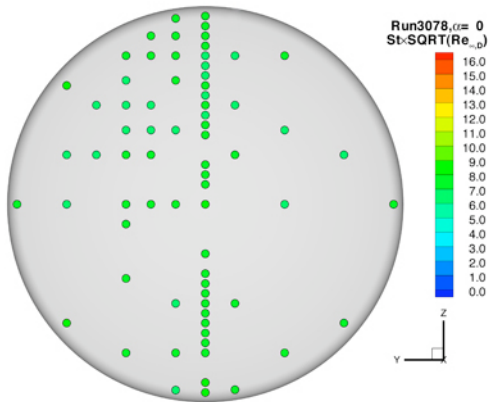
Figure 96. Reynolds numbers effects, Mach = 8, $\alpha=32$ -deg



Run 3057, Mach 10, $Re_{\infty} = 2 \times 10^6/\text{ft}$

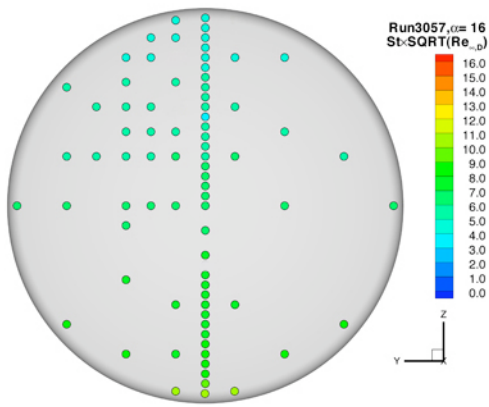


Run 3058, Mach 10, $Re_{\infty} = 5 \times 10^6/\text{ft}$

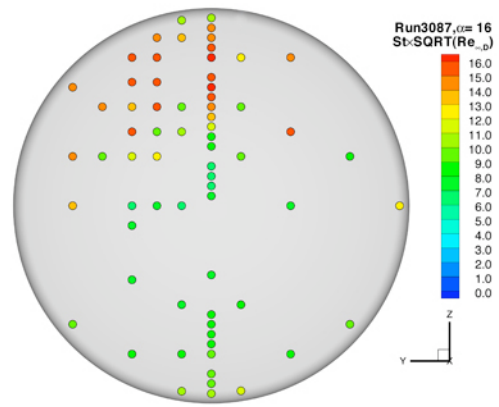


Run 3078, Mach 10, $Re_{\infty} = 14 \times 10^6/\text{ft}$

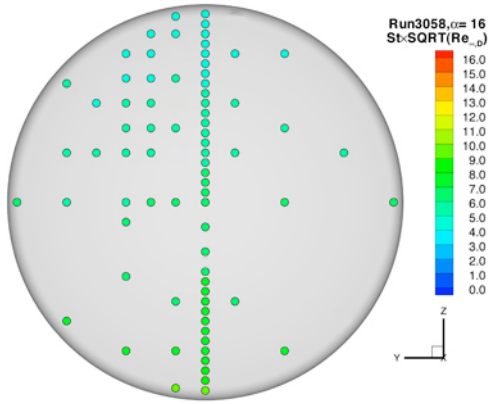
Figure 97. Reynolds numbers effects, Mach = 10, $\alpha = 0$ -deg



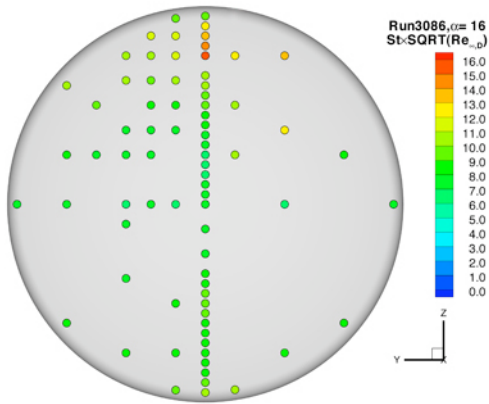
Run 3057, Mach 10, $Re_{\infty} = 2 \times 10^6/\text{ft}$



Run 3087, Mach 10, $Re_{\infty} = 20 \times 10^6/\text{ft}$

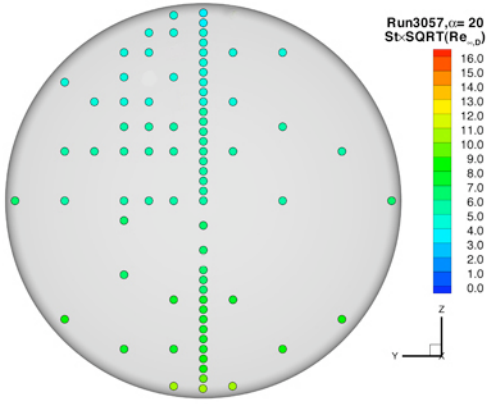


Run 3058, Mach 10, $Re_{\infty} = 5 \times 10^6/\text{ft}$

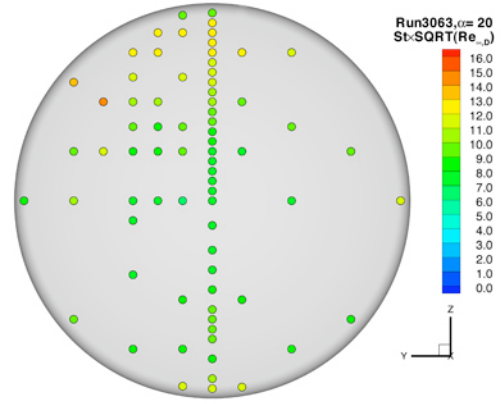


Run 3086, Mach 10, $Re_{\infty} = 14 \times 10^6/\text{ft}$

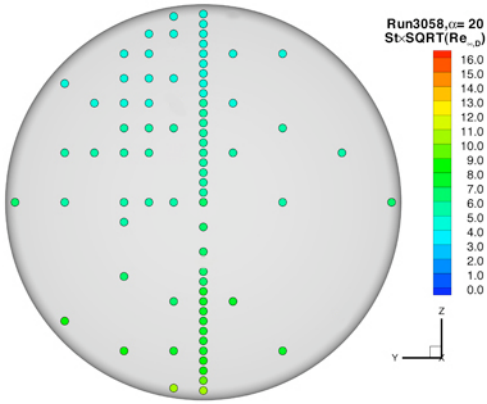
Figure 98. Reynolds numbers effects, Mach = 10, $\alpha = 16\text{-deg}$



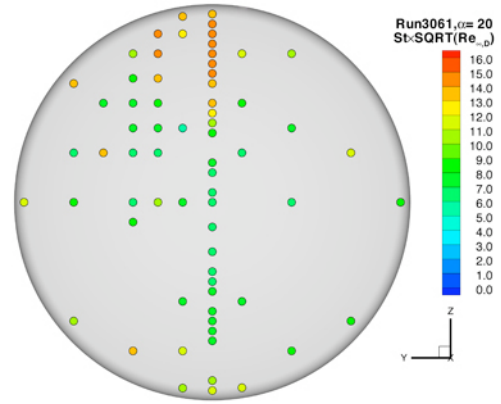
Run 3057, Mach 10, $Re_{\infty} = 2 \times 10^6/\text{ft}$



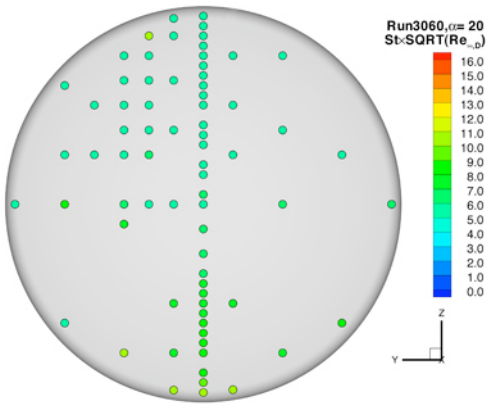
Run 3063, Mach 10, $Re_{\infty} = 15 \times 10^6/\text{ft}$



Run 3058, Mach 10, $Re_{\infty} = 5 \times 10^6/\text{ft}$

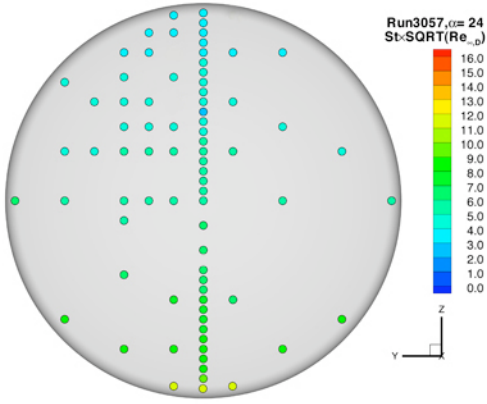


Run 3061, Mach 10, $Re_{\infty} = 20 \times 10^6/\text{ft}$

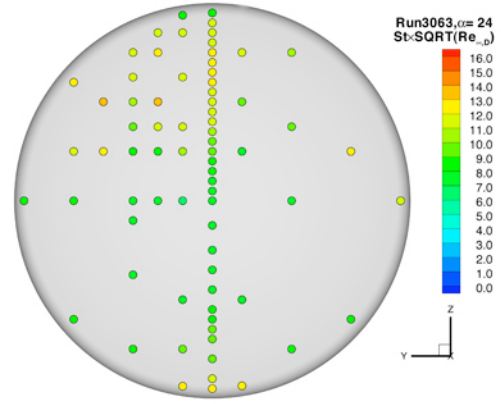


Run 3060, Mach 10, $Re_{\infty} = 9 \times 10^6/\text{ft}$

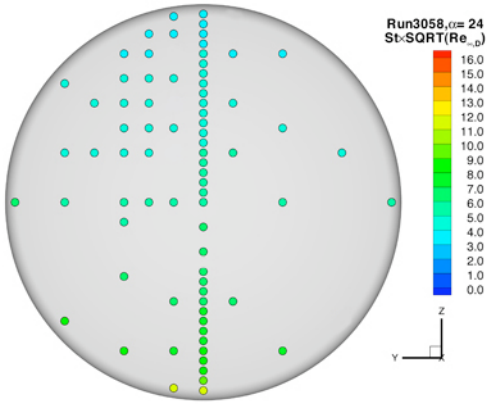
Figure 99. Reynolds numbers effects, Mach = 10, $\alpha = 20\text{-deg}$



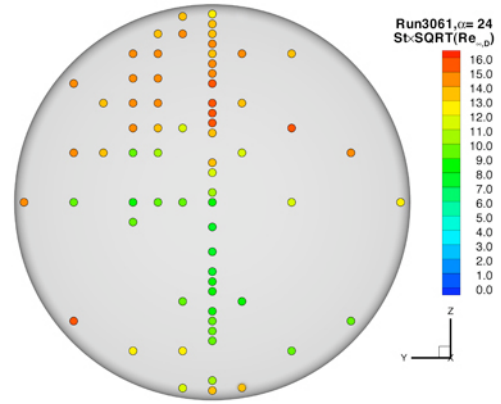
Run 3057, Mach 10, $Re_{\infty} = 2 \times 10^6/\text{ft}$



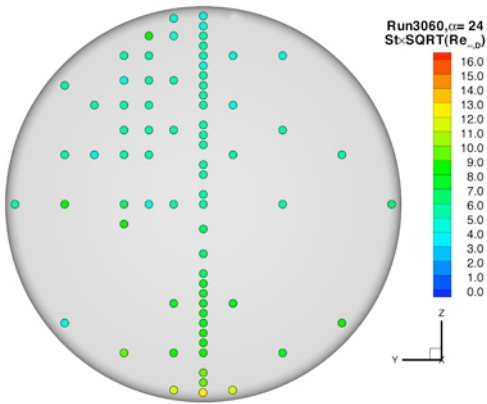
Run 3063, Mach 10, $Re_{\infty} = 15 \times 10^6/\text{ft}$



Run 3058, Mach 10, $Re_{\infty} = 5 \times 10^6/\text{ft}$

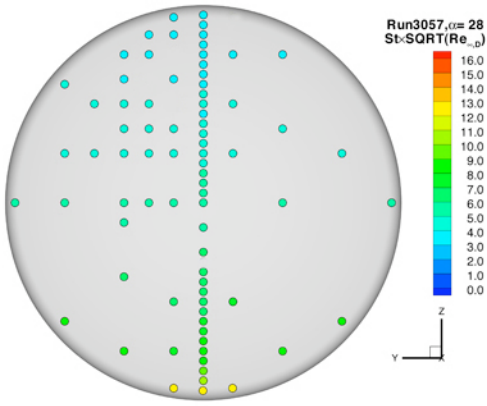


Run 3061, Mach 10, $Re_{\infty} = 20 \times 10^6/\text{ft}$

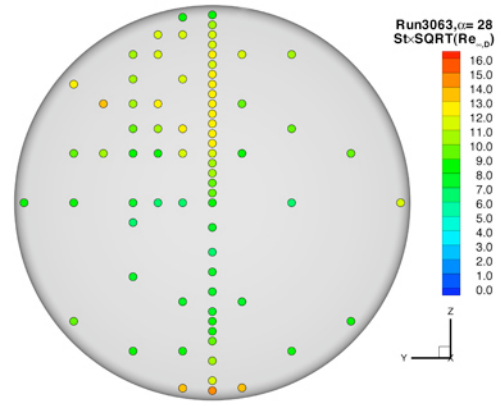


Run 3060, Mach 10, $Re_{\infty} = 9 \times 10^6/\text{ft}$

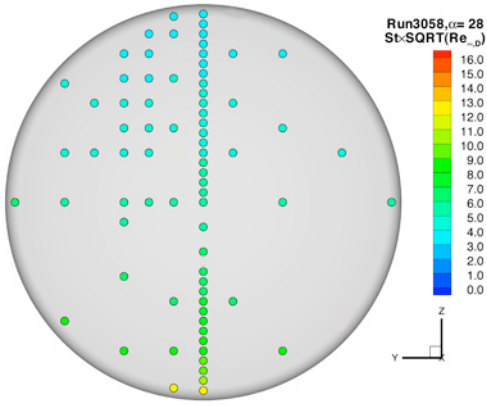
Figure 100. Reynolds numbers effects, Mach = 10, $\alpha=24$ -deg



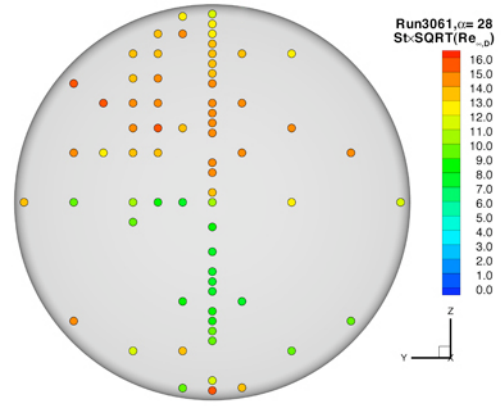
Run 3057, Mach 10, $Re_{\infty} = 2 \times 10^6/\text{ft}$



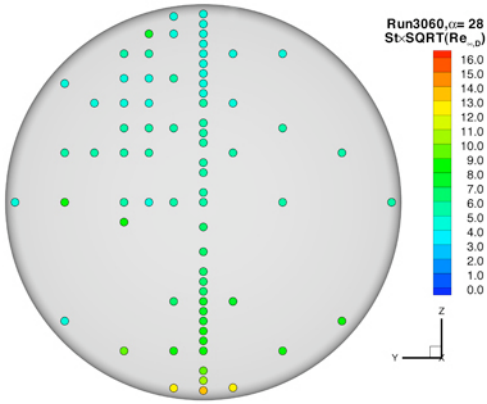
Run 3063, Mach 10, $Re_{\infty} = 15 \times 10^6/\text{ft}$



Run 3058, Mach 10, $Re_{\infty} = 5 \times 10^6/\text{ft}$

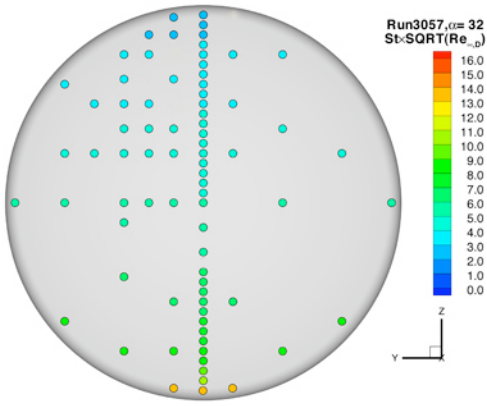


Run 3061, Mach 10, $Re_{\infty} = 20 \times 10^6/\text{ft}$

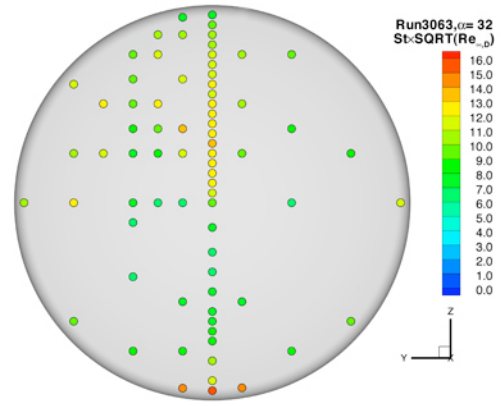


Run 3060, Mach 10, $Re_{\infty} = 9 \times 10^6/\text{ft}$

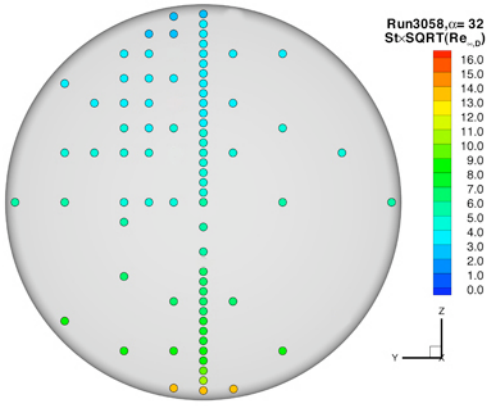
Figure 101. Reynolds numbers effects, Mach = 10, $\alpha=28$ -deg



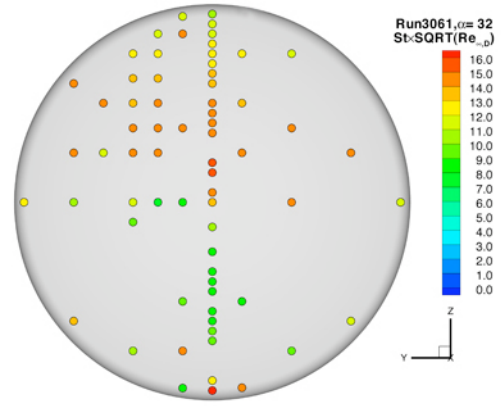
Run 3057, Mach 10, $Re_{\infty} = 2 \times 10^6/\text{ft}$



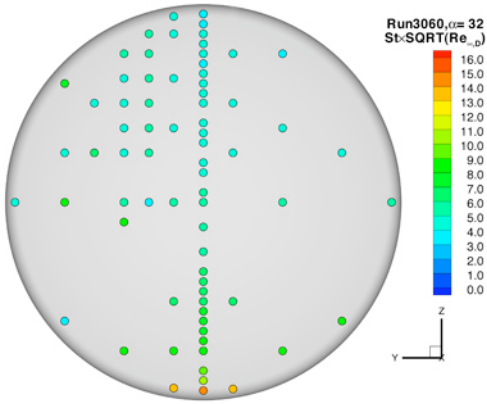
Run 3063, Mach 10, $Re_{\infty} = 15 \times 10^6/\text{ft}$



Run 3058, Mach 10, $Re_{\infty} = 5 \times 10^6/\text{ft}$



Run 3061, Mach 10, $Re_{\infty} = 20 \times 10^6/\text{ft}$



Run 3060, Mach 10, $Re_{\infty} = 9 \times 10^6/\text{ft}$

Figure 102. Reynolds numbers effects, Mach = 10, $\alpha=32$ -deg

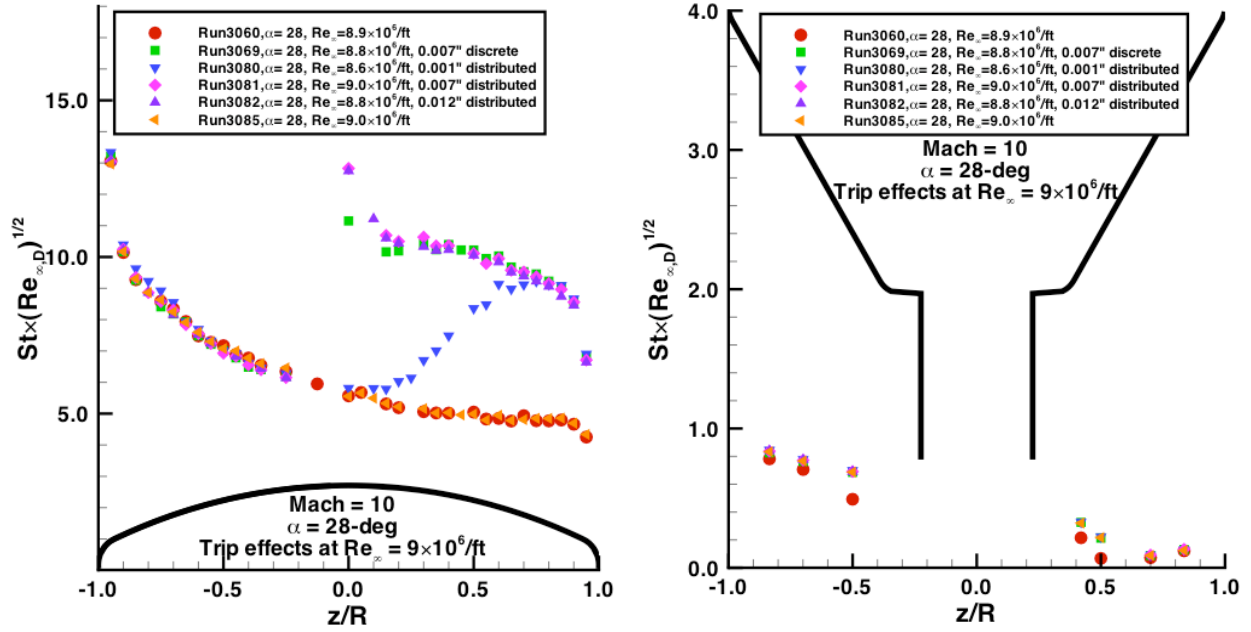


Figure 103. Trip effects on heating, $\alpha = 28\text{-deg}$, $Re_\infty = 9 \times 10^6/\text{ft}$

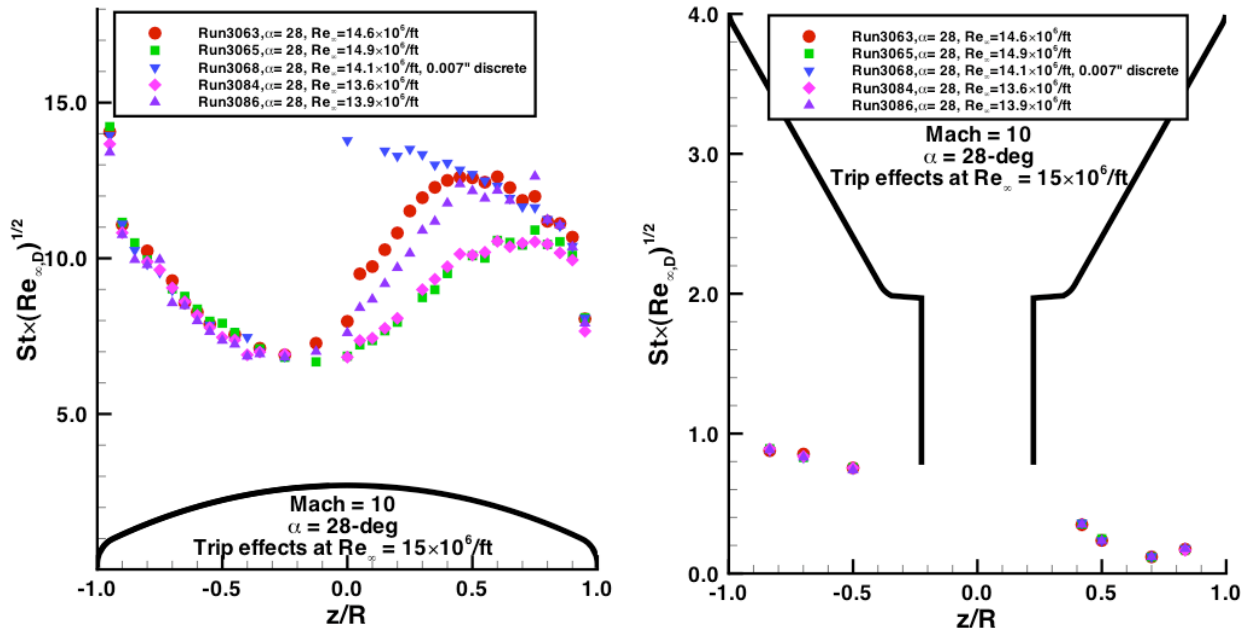


Figure 104. Trip effects on heating, $\alpha = 28\text{-deg}$, $Re_\infty = 15 \times 10^6/\text{ft}$

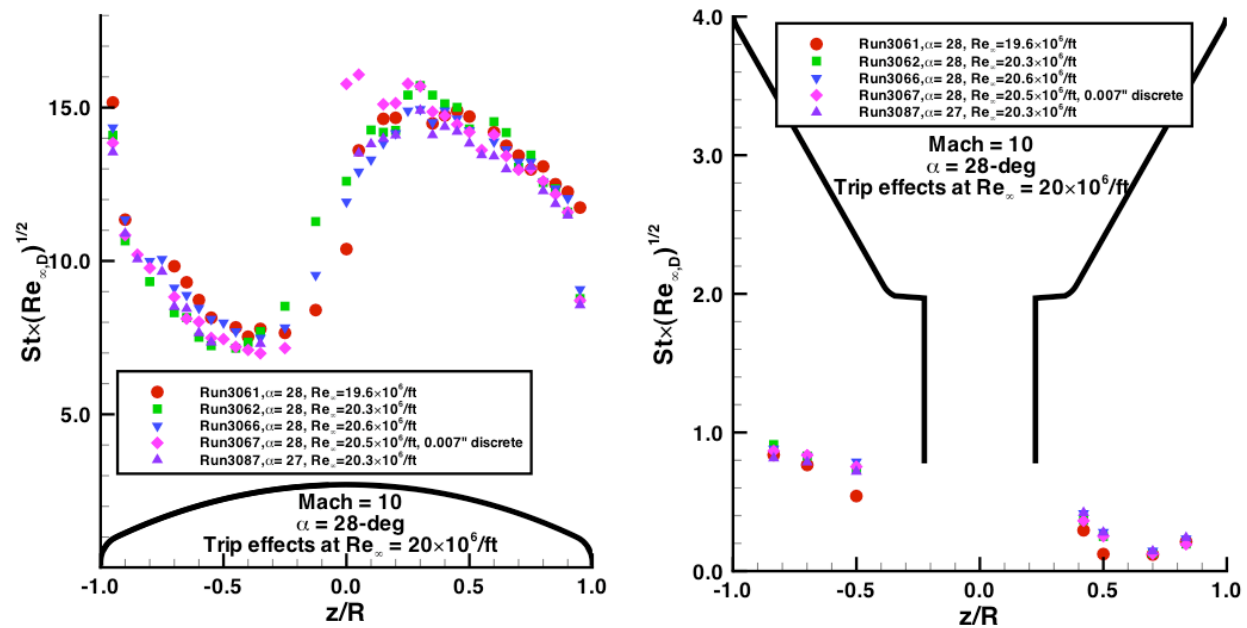


Figure 105. Trip effects on heating, $\alpha = 28$ -deg, $Re_{\infty} = 20 \times 10^6/ft$

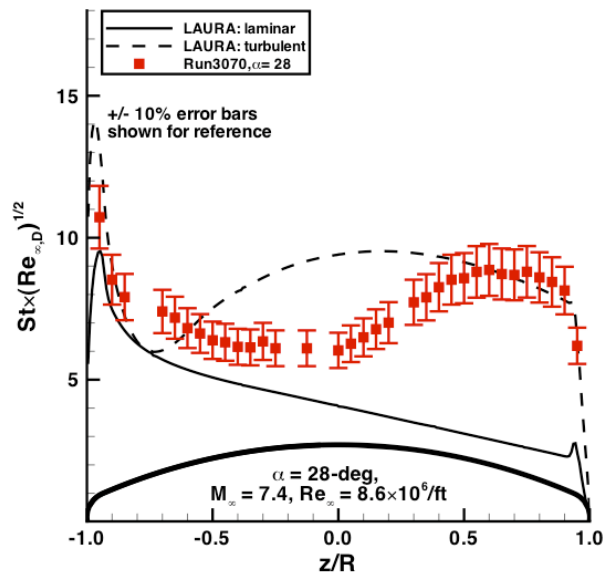


Figure 106. Run 3070 data and comparison with predictions, Mach = 8, $Re_{\infty} = 9 \times 10^6 / \text{ft}$, $\alpha = 28\text{-deg}$

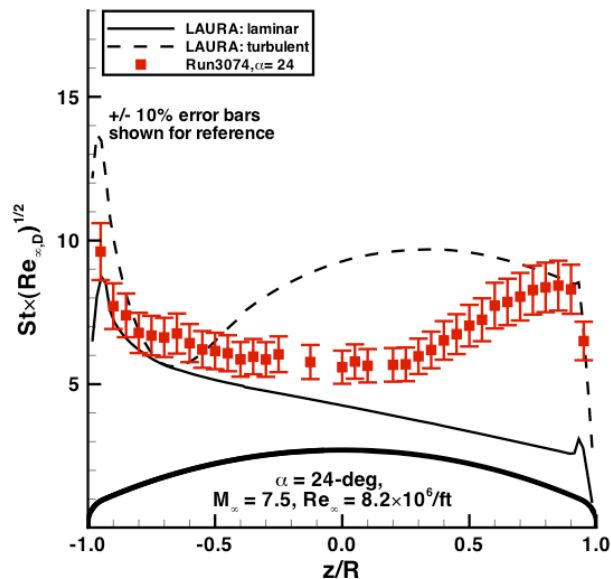


Figure 107. Run 3074 data and comparison with predictions, Mach = 8, $Re_{\infty} = 8 \times 10^6/\text{ft}$, $\alpha = 24$ -deg

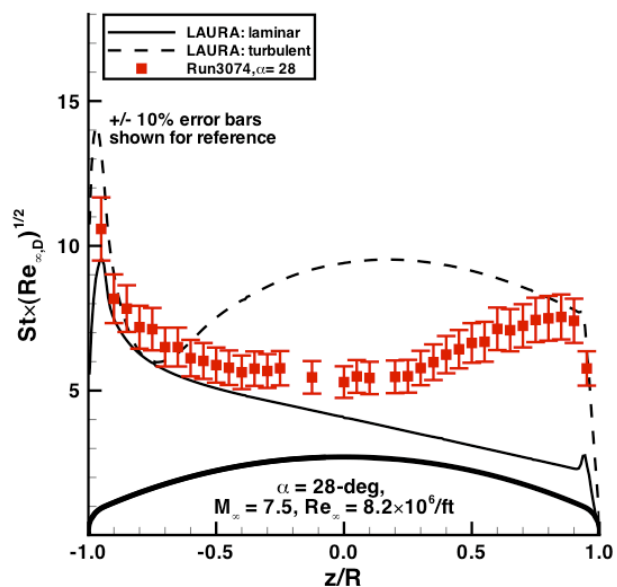


Figure 108. Run 3074 data and comparison with predictions, Mach = 8, $Re_{\infty} = 8 \times 10^6/\text{ft}$, $\alpha = 28$ -deg

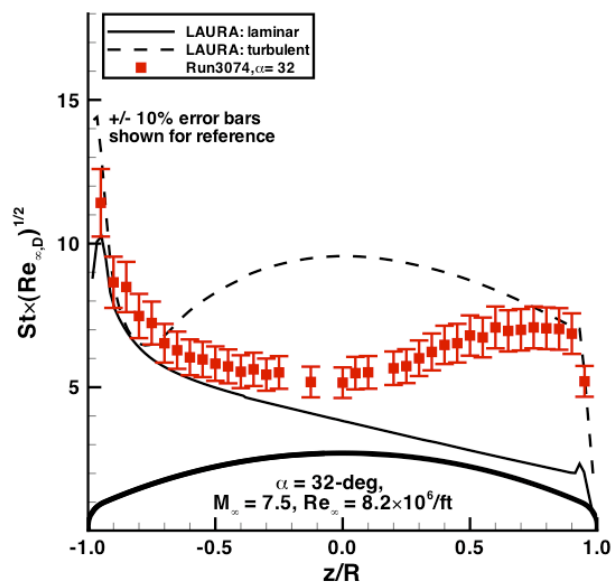


Figure 109. Run 3074 data and comparison with predictions, Mach = 8, $Re_{\infty} = 8 \times 10^6/\text{ft}$, $\alpha = 32$ -deg

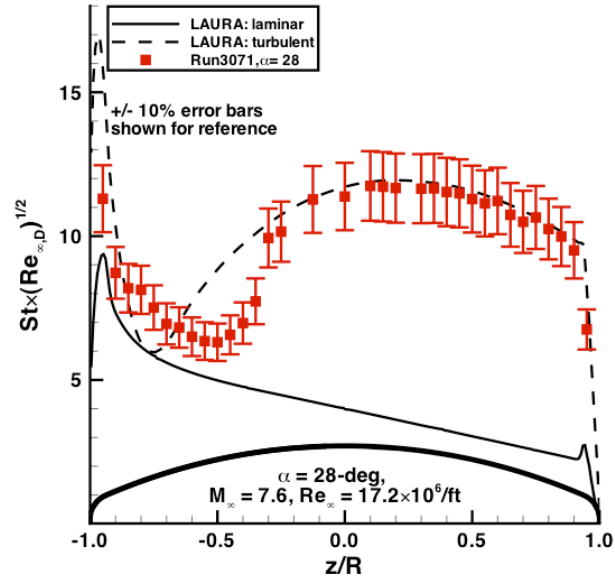


Figure 110. Run 3071 data and comparison with predictions, Mach = 8, $Re_\infty = 17 \times 10^6/\text{ft}$, $\alpha = 28\text{-deg}$

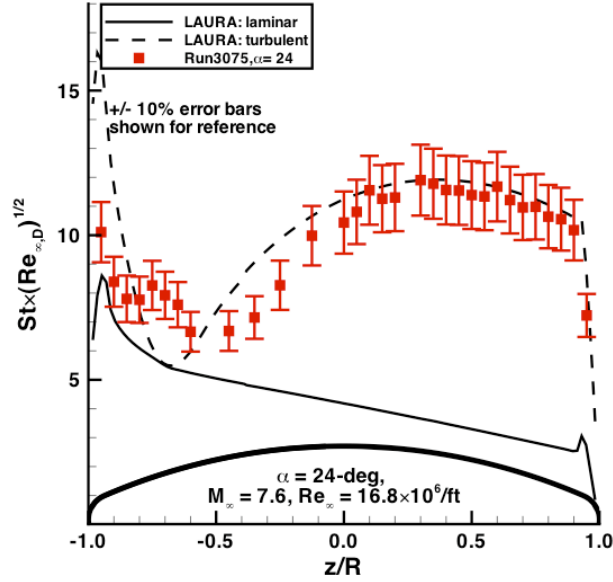


Figure 111. Run 3075 data and comparison with predictions, Mach = 8, $Re_{\infty} = 17 \times 10^6/ft$, $\alpha = 24$ -deg

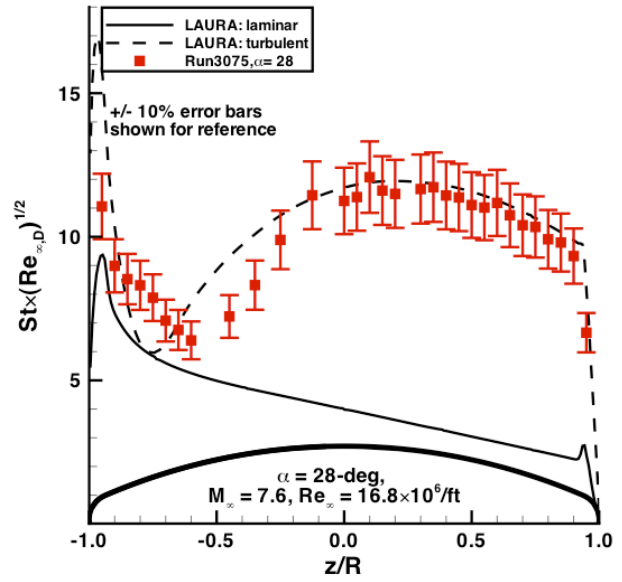


Figure 112. Run 3075 data and comparison with predictions, Mach = 8, $Re_{\infty} = 17 \times 10^6/ft$, $\alpha = 28$ -deg

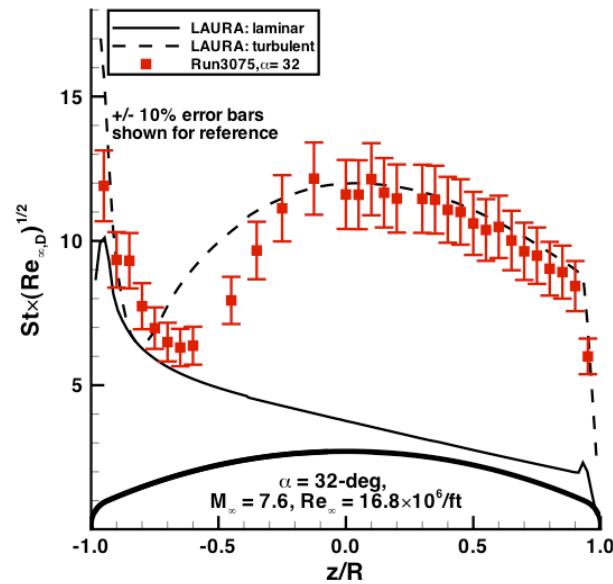


Figure 113. Run 3075 data and comparison with predictions, Mach = 8, $Re_{\infty} = 17 \times 10^6/ft$, $\alpha = 32$ -deg

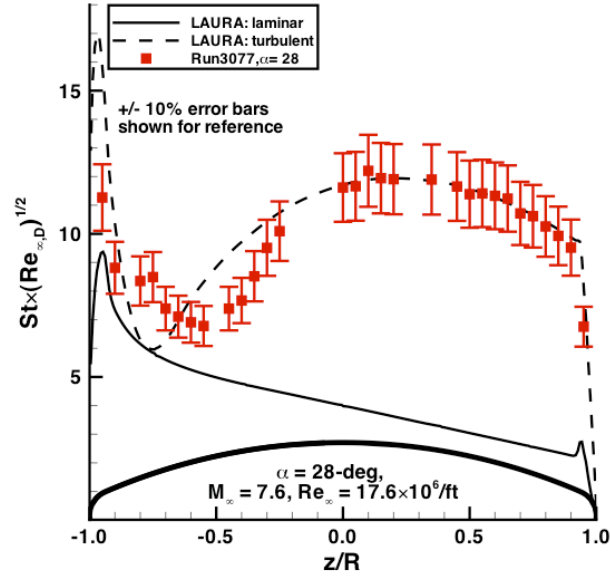


Figure 114. Run 3077 data and comparison with predictions, Mach = 8, $Re_{\infty} = 18 \times 10^6/\text{ft}$, $\alpha = 28\text{-deg}$

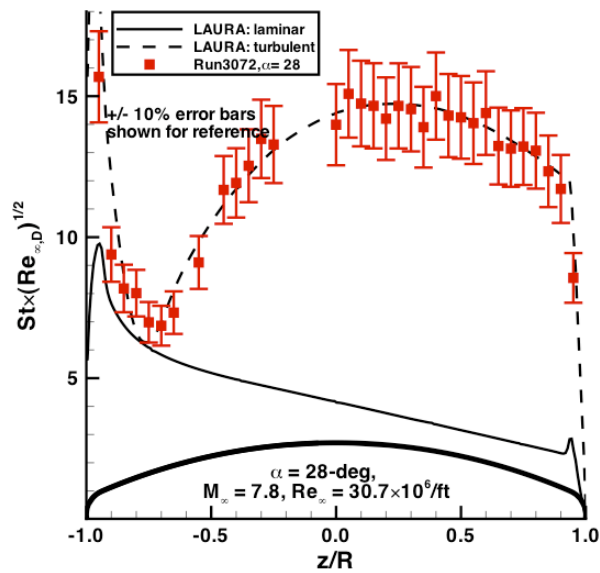


Figure 115. Run 3072 data and comparison with predictions, Mach = 8, $Re_\infty = 31 \times 10^6/\text{ft}$, $\alpha = 28\text{-deg}$

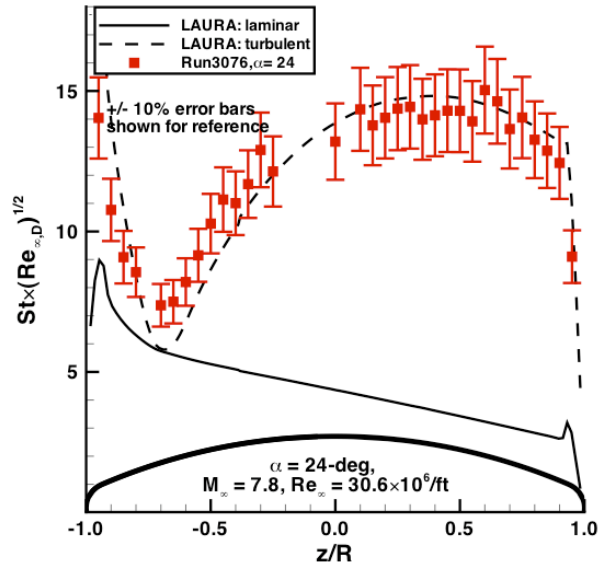


Figure 116. Run 3076 data and comparison with predictions, Mach = 8, $Re_{\infty} = 31 \times 10^6/\text{ft}$, $\alpha = 24$ -deg

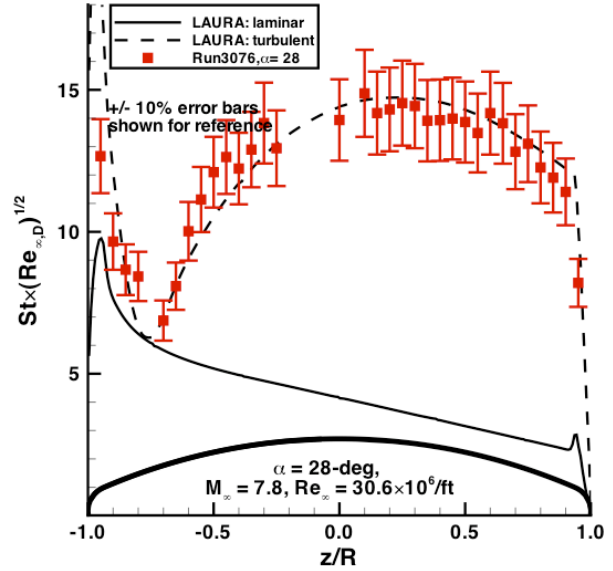


Figure 117. Run 3076 data and comparison with predictions, Mach = 8, $Re_{\infty} = 31 \times 10^6/\text{ft}$, $\alpha = 28$ -deg

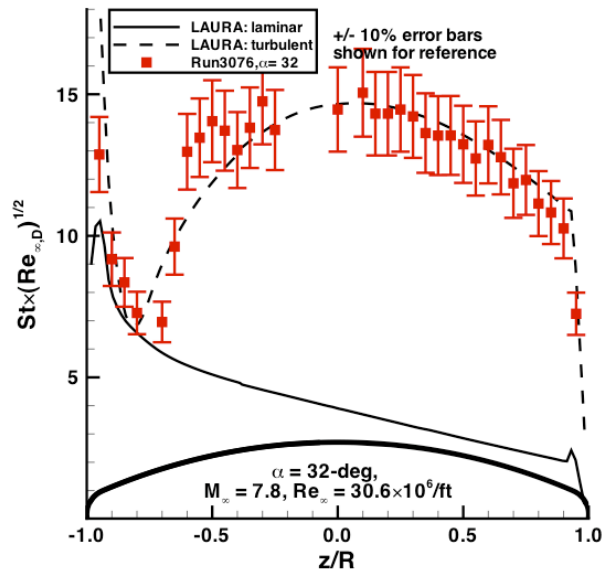


Figure 118. Run 3076 data and comparison with predictions, Mach = 8, $Re_{\infty} = 31 \times 10^6/\text{ft}$, $\alpha = 32$ -deg

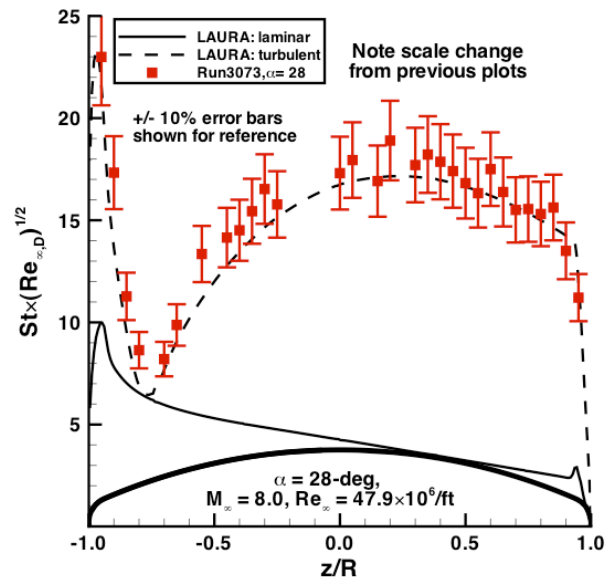


Figure 119. Run 3073 data and comparison with predictions, Mach = 8, $Re_\infty = 48 \times 10^6/\text{ft}$, $\alpha = 28\text{-deg}$

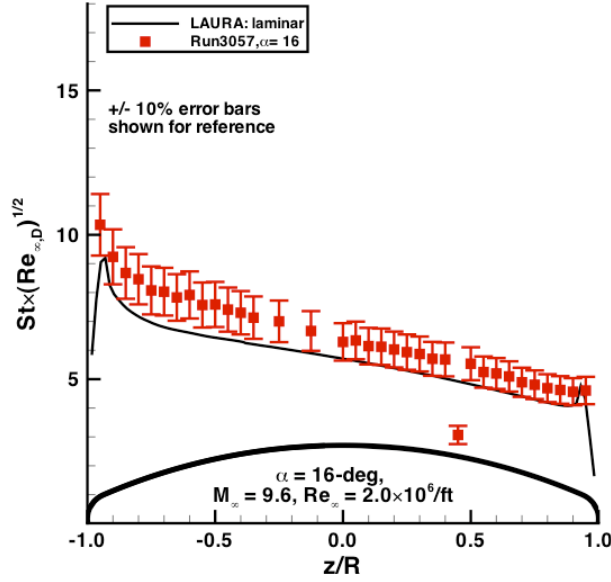


Figure 120. Run 3057 data and comparison with predictions, Mach = 10, $Re_{\infty} = 2 \times 10^6/\text{ft}$, $\alpha = 16\text{-deg}$

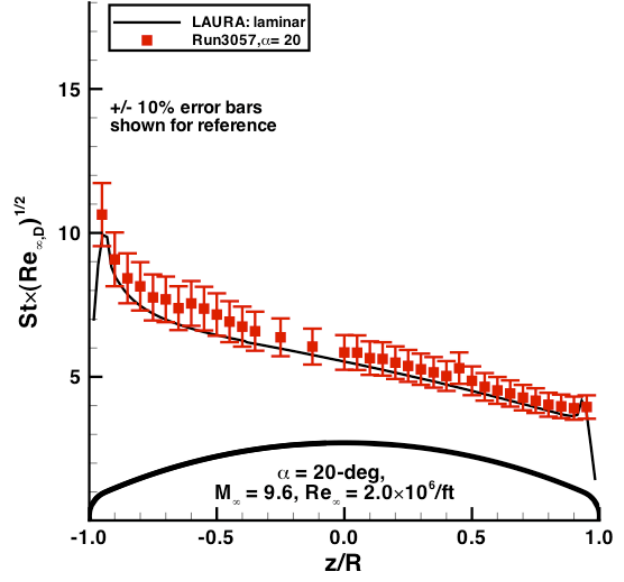


Figure 121. Run 3057 data and comparison with predictions, Mach = 10, $Re_{\infty} = 2 \times 10^6/\text{ft}$, $\alpha = 20\text{-deg}$

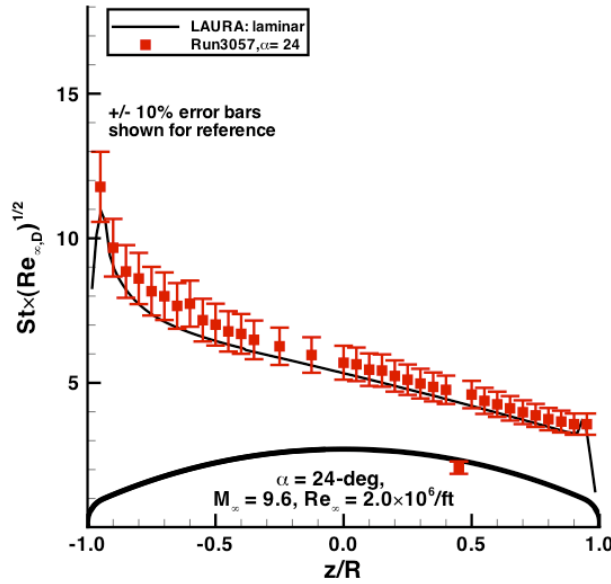


Figure 122. Run 3057 data and comparison with predictions, Mach = 10, $Re_{\infty} = 2 \times 10^6/\text{ft}$, $\alpha = 24\text{-deg}$

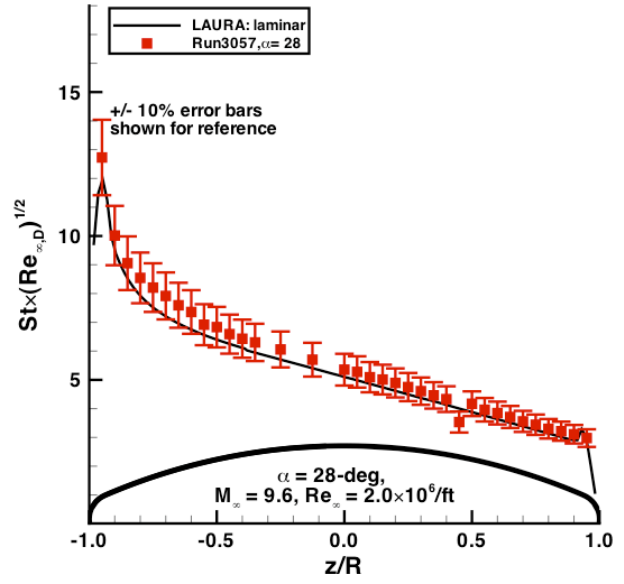


Figure 123. Run 3057 data and comparison with predictions, Mach = 10, $Re_{\infty} = 2 \times 10^6/\text{ft}$, $\alpha = 28\text{-deg}$

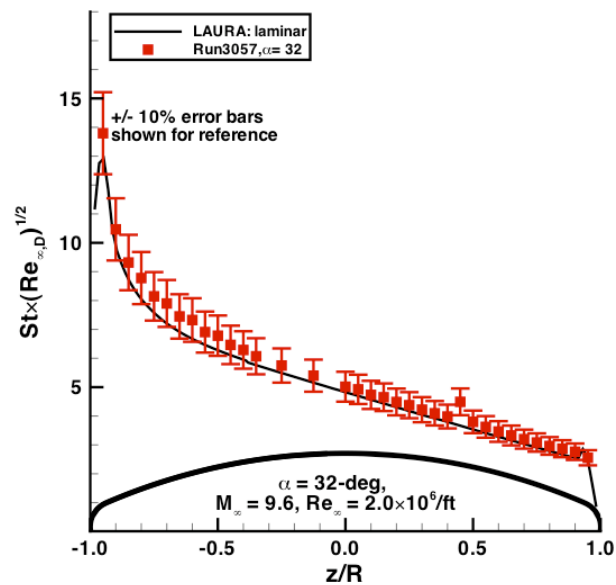


Figure 124. Run 3057 data and comparison with predictions, Mach = 10, $Re_\infty = 2 \times 10^6/\text{ft}$, $\alpha = 32\text{-deg}$

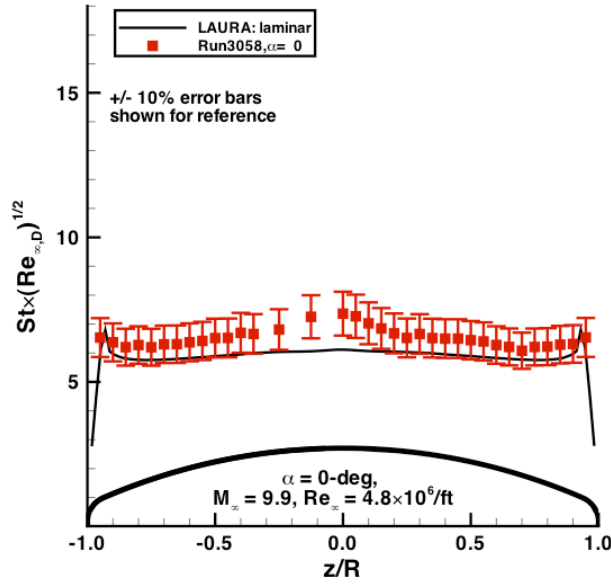


Figure 125. Run 3058 data and comparison with predictions, Mach = 10, $Re_{\infty} = 5 \times 10^6/\text{ft}$, $\alpha = 0\text{-deg}$

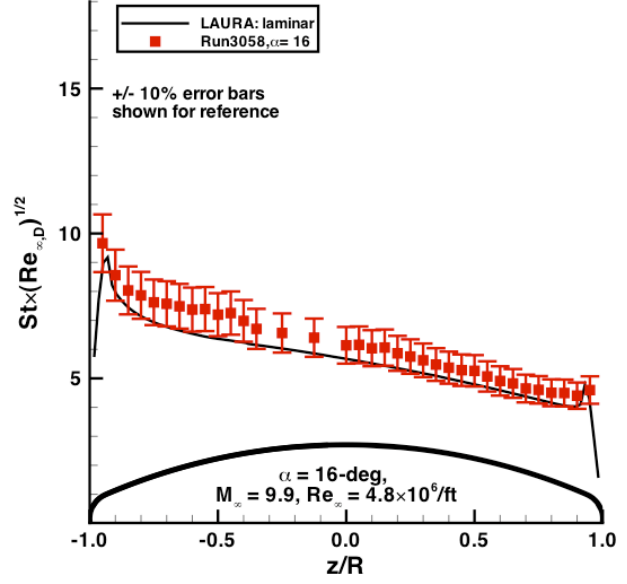


Figure 126. Run 3058 data and comparison with predictions, Mach = 10, $Re_{\infty} = 5 \times 10^6/\text{ft}$, $\alpha = 16\text{-deg}$

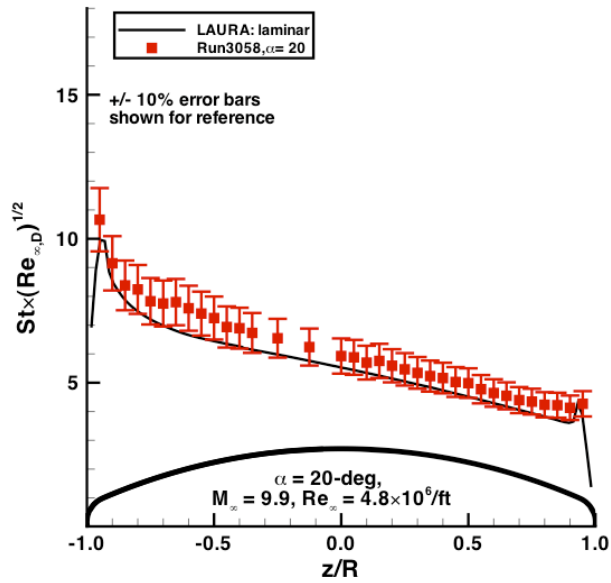


Figure 127. Run 3058 data and comparison with predictions, Mach = 10, $Re_{\infty} = 5 \times 10^6/\text{ft}$, $\alpha = 20\text{-deg}$

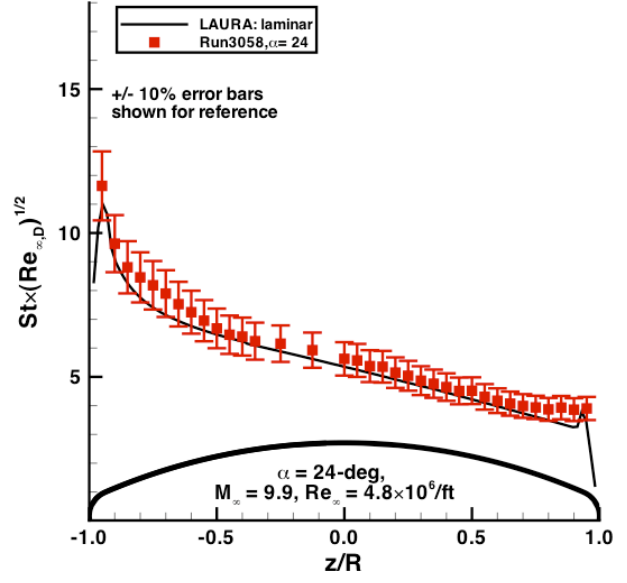


Figure 128. Run 3058 data and comparison with predictions, Mach = 10, $Re_{\infty} = 5 \times 10^6/\text{ft}$, $\alpha = 24\text{-deg}$

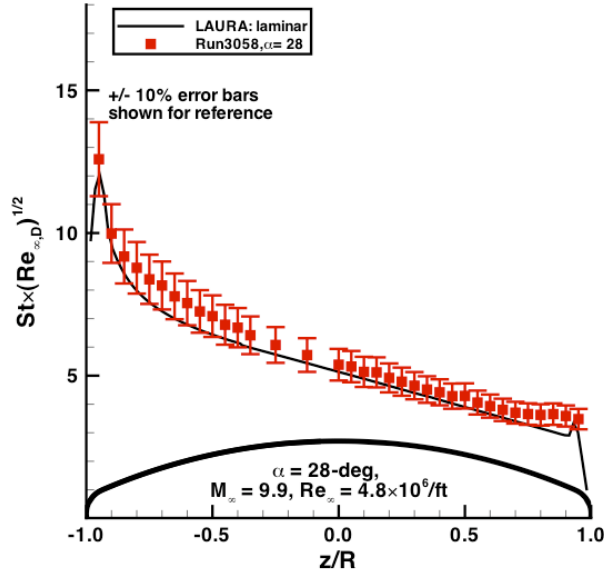


Figure 129. Run 3058 data and comparison with predictions, Mach = 10, $Re_{\infty} = 5 \times 10^6/\text{ft}$, $\alpha = 28\text{-deg}$

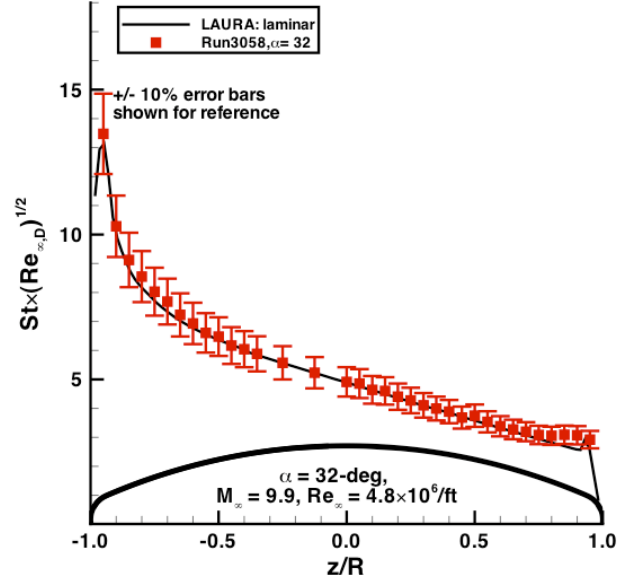


Figure 130. Run 3058 data and comparison with predictions, Mach = 10, $Re_{\infty} = 5 \times 10^6/\text{ft}$, $\alpha = 32\text{-deg}$

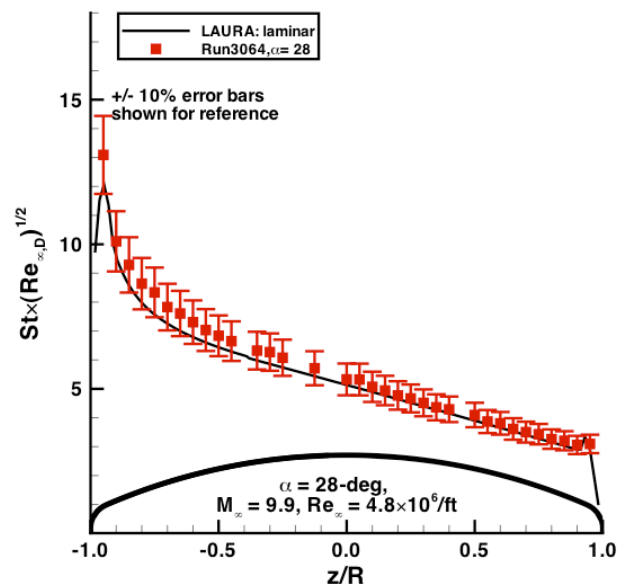


Figure 131. Run 3064 data and comparison with predictions, Mach = 10, $Re_{\infty} = 5 \times 10^6/\text{ft}$, $\alpha = 28\text{-deg}$

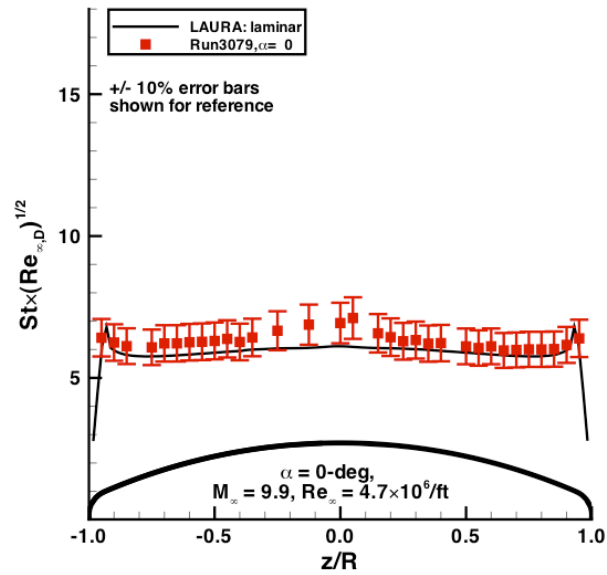


Figure 132. Run 3079 data and comparison with predictions, Mach = 10, $Re_\infty = 5 \times 10^6/\text{ft}$, $\alpha = 0\text{-deg}$

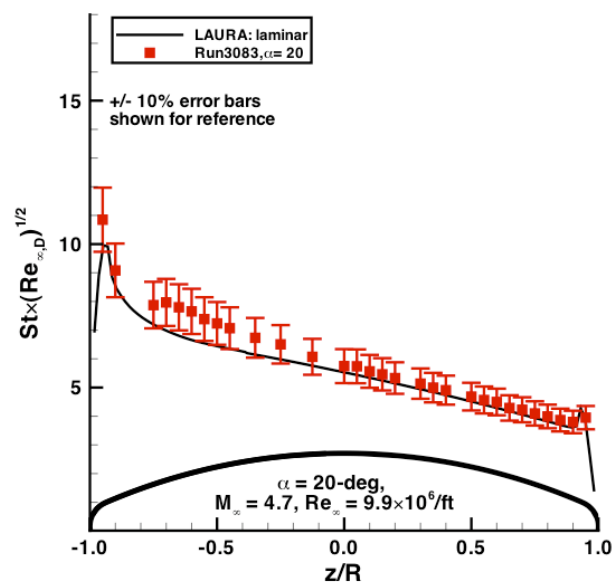


Figure 133. Run 3083 data and comparison with predictions, Mach = 10, $Re_\infty = 10 \times 10^6/\text{ft}$, $\alpha = 20\text{-deg}$

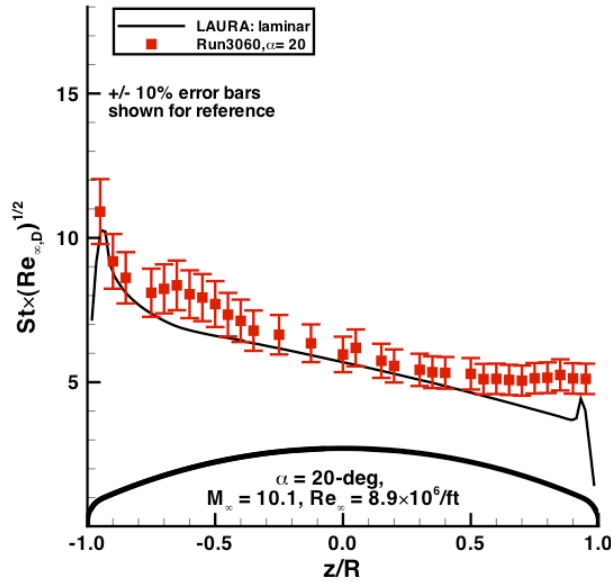


Figure 134. Run 3060 data and comparison with predictions, Mach = 10, $Re_{\infty} = 9 \times 10^6/\text{ft}$, $\alpha = 20\text{-deg}$

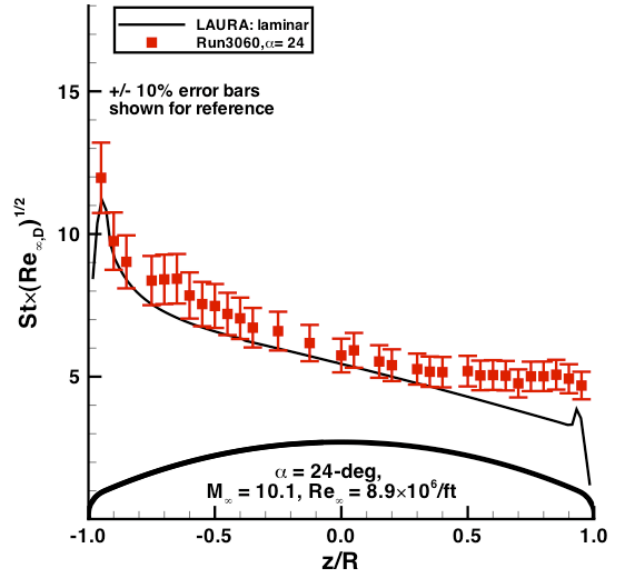


Figure 135. Run 3060 data and comparison with predictions, Mach = 10, $Re_{\infty} = 9 \times 10^6/\text{ft}$, $\alpha = 24\text{-deg}$

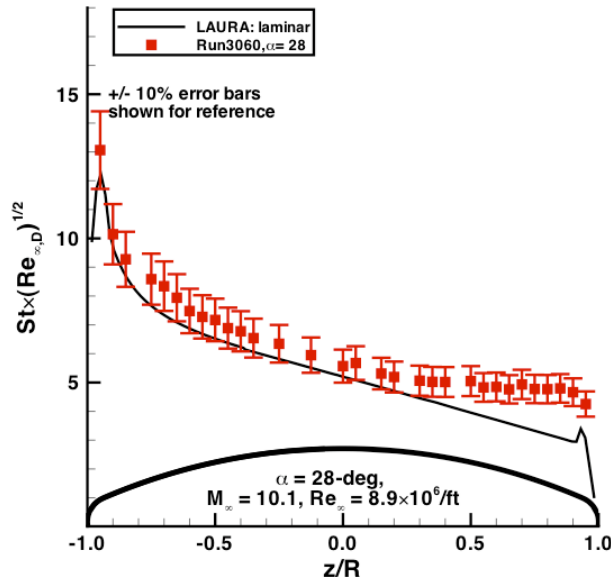


Figure 136. Run 3060 data and comparison with predictions, Mach = 10, $Re_{\infty} = 9 \times 10^6/\text{ft}$, $\alpha = 28\text{-deg}$

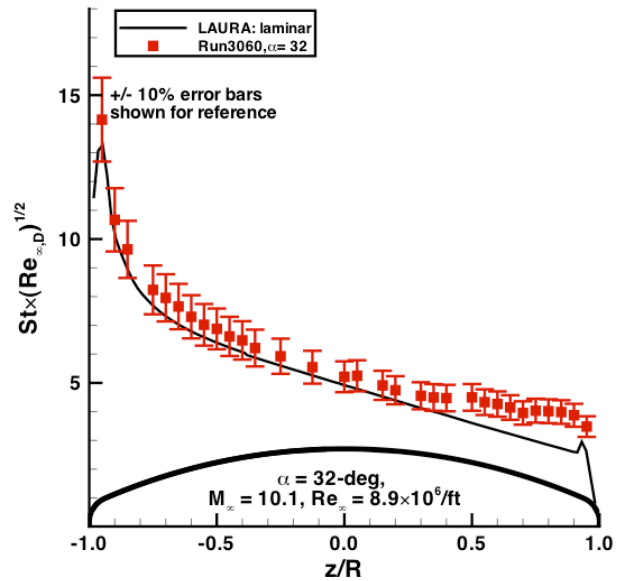


Figure 137. Run 3060 data and comparison with predictions, Mach = 10, $Re_{\infty} = 9 \times 10^6/\text{ft}$, $\alpha = 32\text{-deg}$

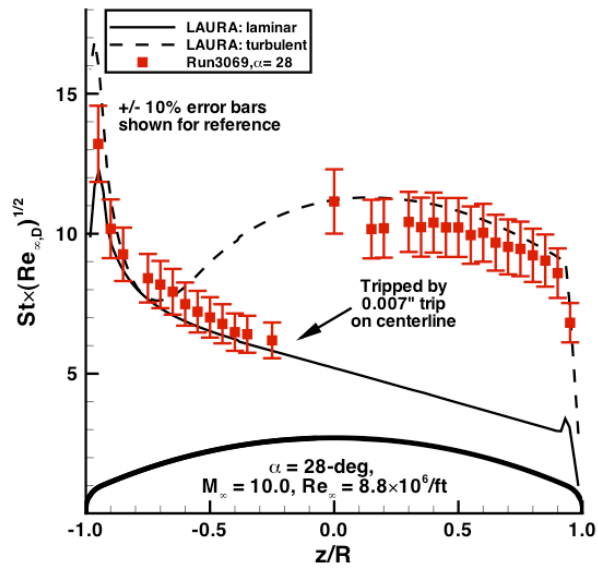


Figure 138. Run 3069 data and comparison with predictions, Mach = 10, $Re_{\infty} = 9 \times 10^6/\text{ft}$, $\alpha = 28\text{-deg}$

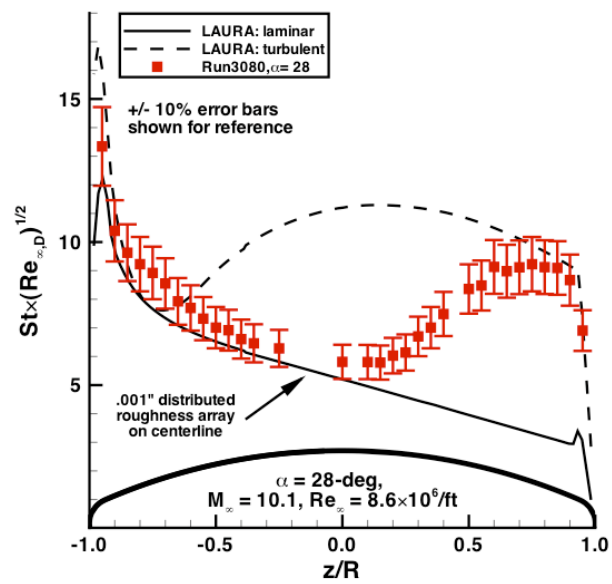


Figure 139. Run 3080 data and comparison with predictions, Mach = 10, $Re_\infty = 9 \times 10^6/\text{ft}$, $\alpha = 28\text{-deg}$

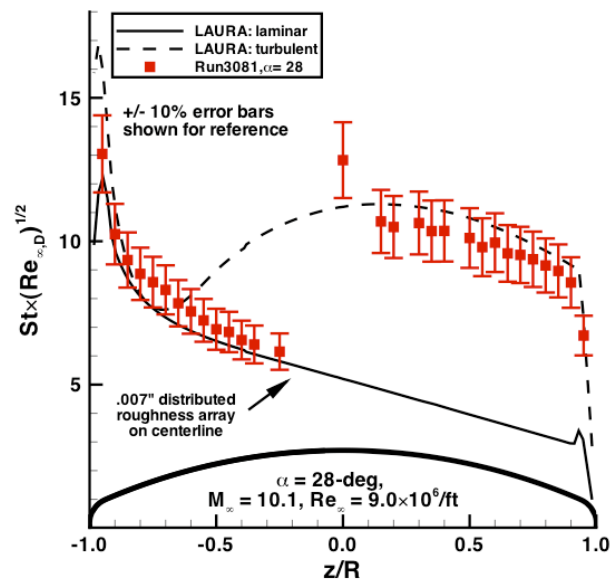


Figure 140. Run 3081 data and comparison with predictions, Mach = 10, $Re_\infty = 9 \times 10^6/\text{ft}$, $\alpha = 28\text{-deg}$

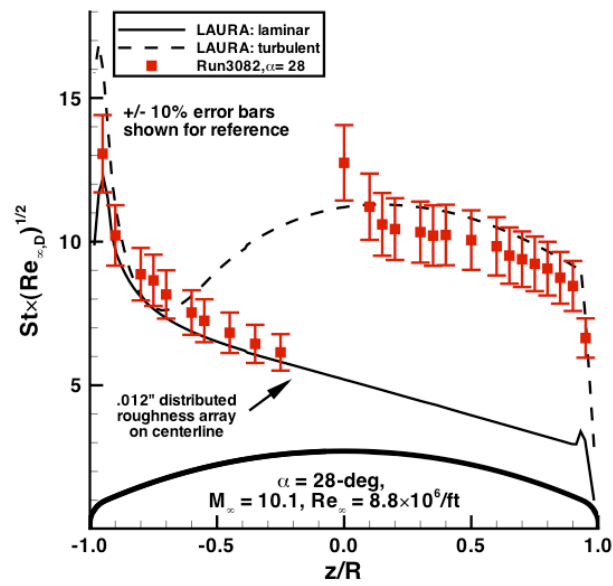


Figure 141. Run 3082 data and comparison with predictions, Mach = 10, $Re_\infty = 9 \times 10^6/\text{ft}$, $\alpha = 28\text{-deg}$

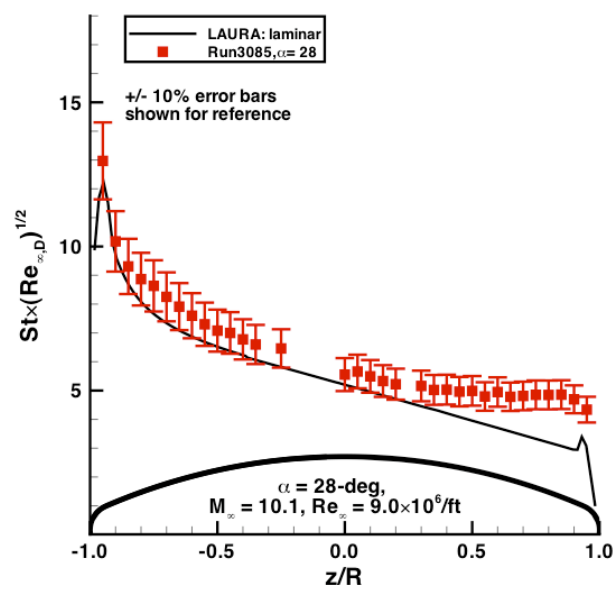


Figure 142. Run 3085 data and comparison with predictions, Mach = 10, $Re_{\infty} = 9 \times 10^6/\text{ft}$, $\alpha = 28\text{-deg}$

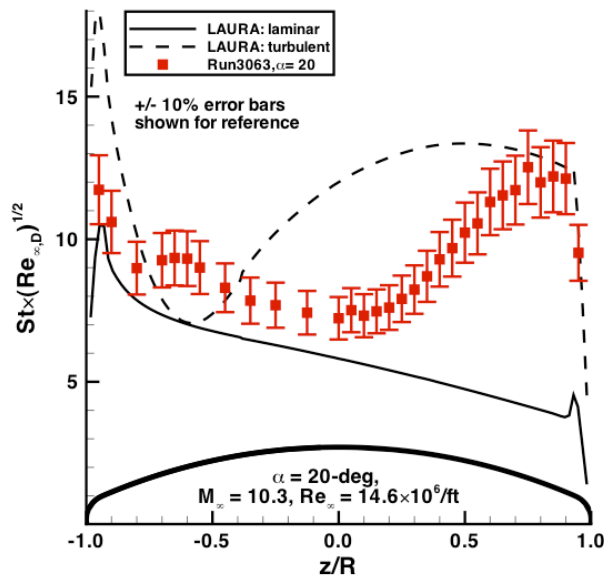


Figure 143. Run 3063 data and comparison with predictions, Mach = 10, $Re_\infty = 15 \times 10^6/\text{ft}$, $\alpha = 20\text{-deg}$

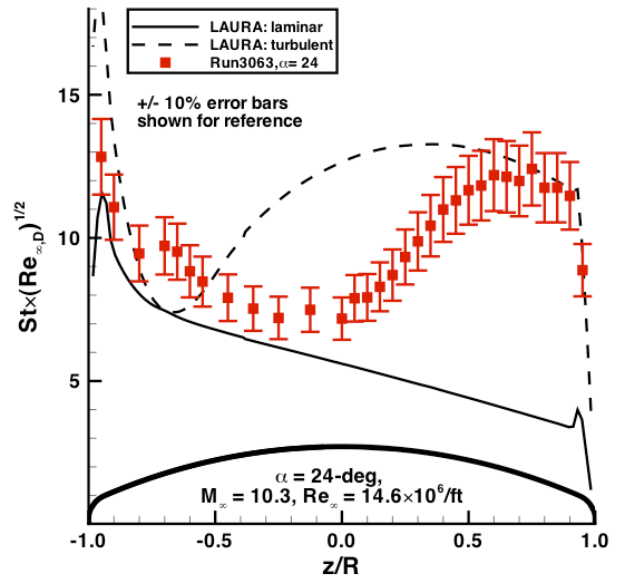


Figure 144. Run 3063 data and comparison with predictions, Mach = 10, $Re_\infty = 15 \times 10^6/\text{ft}$, $\alpha = 24\text{-deg}$

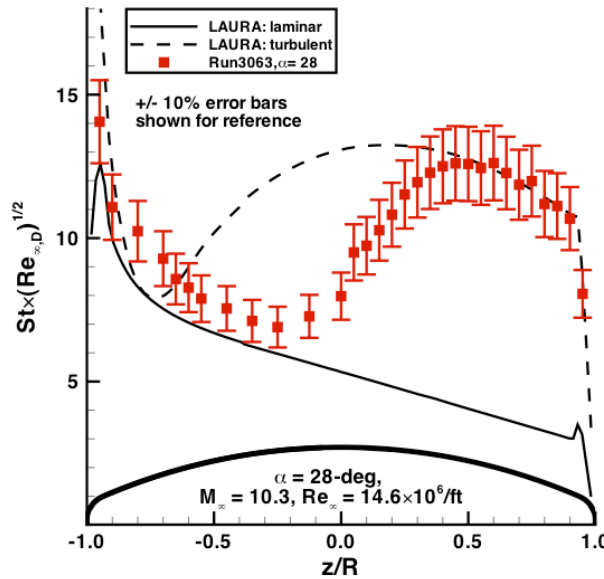


Figure 145. Run 3063 data and comparison with predictions, Mach = 10, $Re_\infty = 15 \times 10^6/\text{ft}$, $\alpha = 28\text{-deg}$

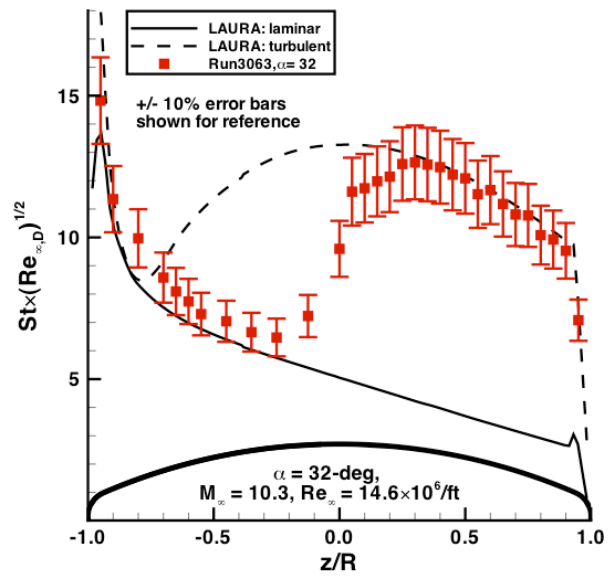


Figure 146. Run 3063 data and comparison with predictions, Mach = 10, $Re_\infty = 15 \times 10^6/\text{ft}$, $\alpha = 32\text{-deg}$

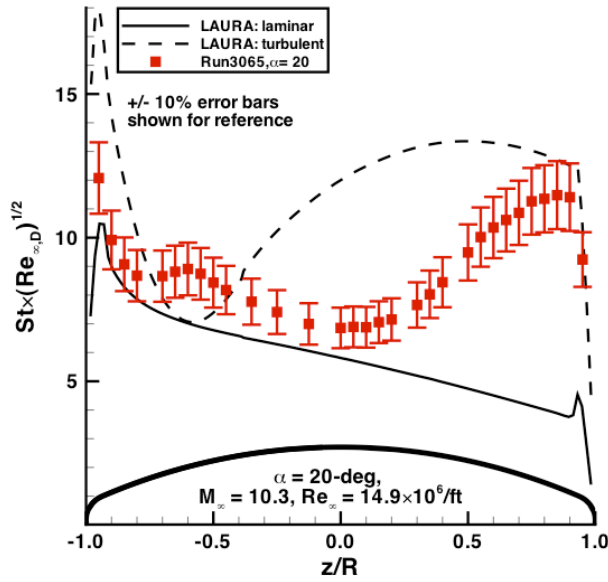


Figure 147. Run 3065 data and comparison with predictions, Mach = 10, $Re_{\infty} = 15 \times 10^6/\text{ft}$, $\alpha = 20\text{-deg}$

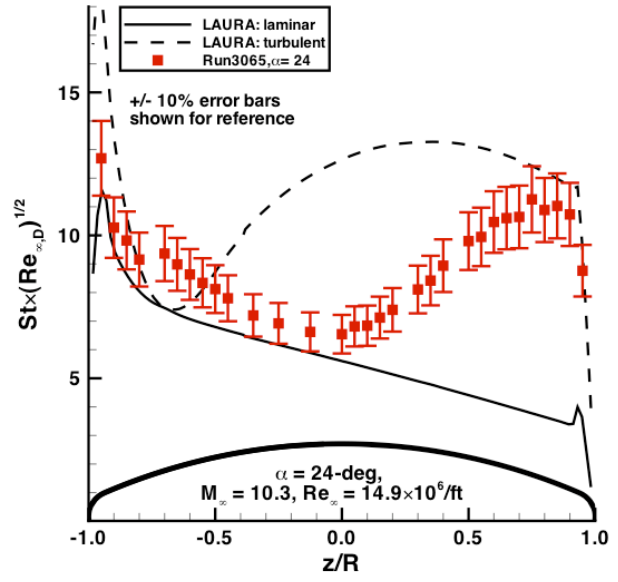


Figure 148. Run 3065 data and comparison with predictions, Mach = 10, $Re_{\infty} = 15 \times 10^6/\text{ft}$, $\alpha = 24\text{-deg}$

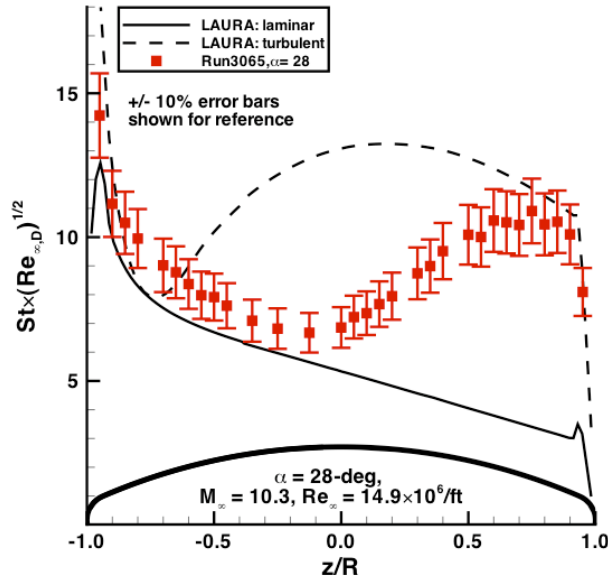


Figure 149. Run 3065 data and comparison with predictions, Mach = 10, $Re_{\infty} = 15 \times 10^6/\text{ft}$, $\alpha = 28\text{-deg}$

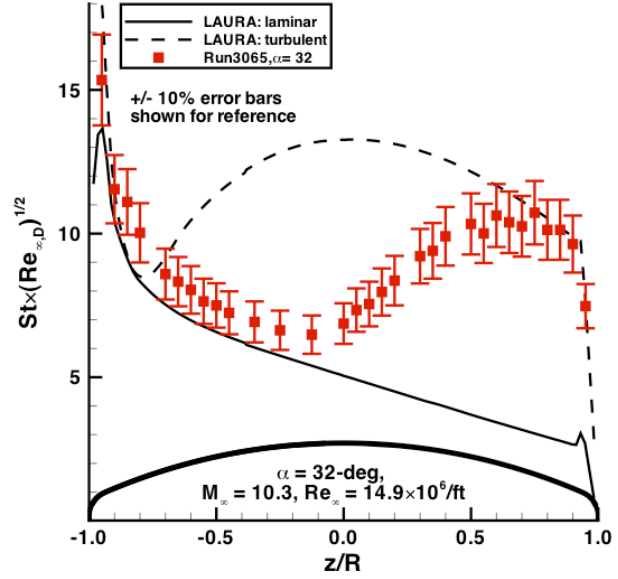


Figure 150. Run 3065 data and comparison with predictions, Mach = 10, $Re_{\infty} = 15 \times 10^6/\text{ft}$, $\alpha = 32\text{-deg}$

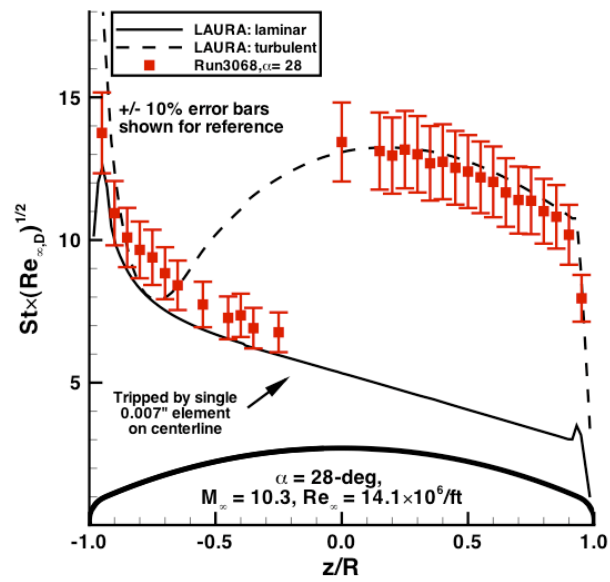


Figure 151. Run 3068 data and comparison with predictions, Mach = 10, $Re_\infty = 14 \times 10^6/\text{ft}$, $\alpha = 28\text{-deg}$

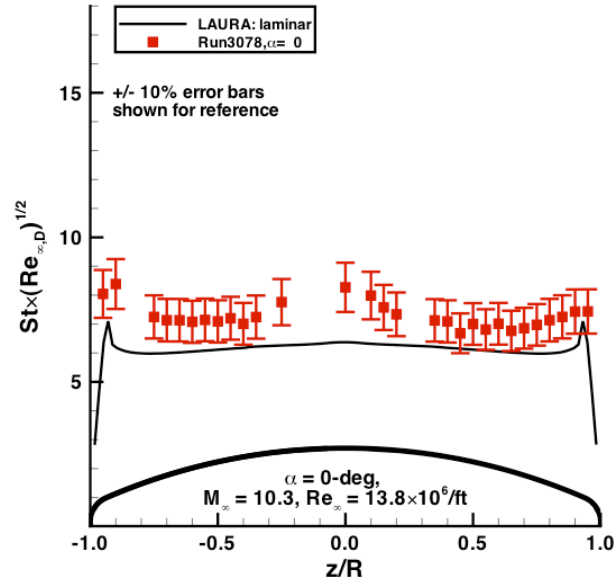


Figure 152. Run 3078 data and comparison with predictions, Mach = 10, $Re_\infty = 14 \times 10^6/\text{ft}$, $\alpha = 0\text{-deg}$

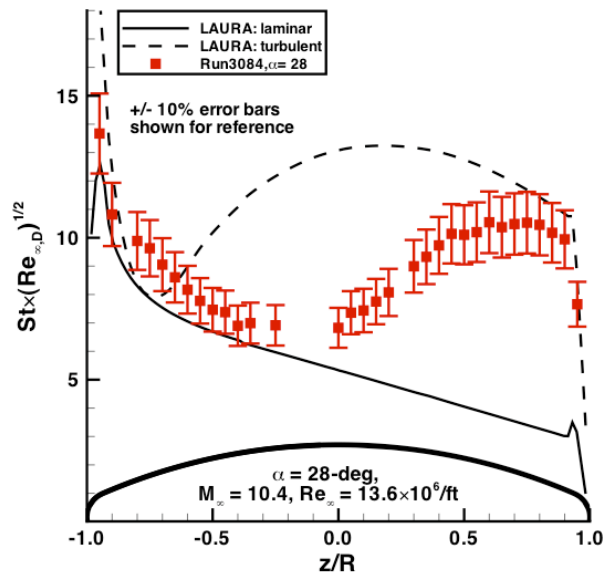


Figure 153. Run 3084 data and comparison with predictions, Mach = 10, $Re_\infty = 14 \times 10^6/\text{ft}$, $\alpha = 28\text{-deg}$

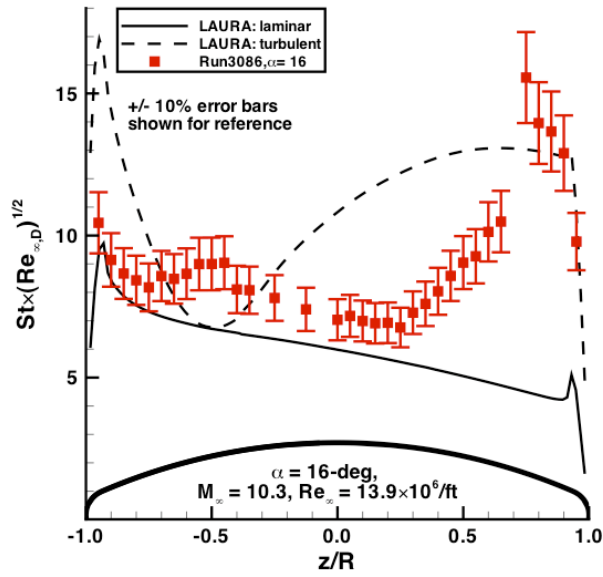


Figure 154. Run 3086 data and comparison with predictions, Mach = 10, $Re_\infty = 14 \times 10^6/\text{ft}$, $\alpha = 16\text{-deg}$

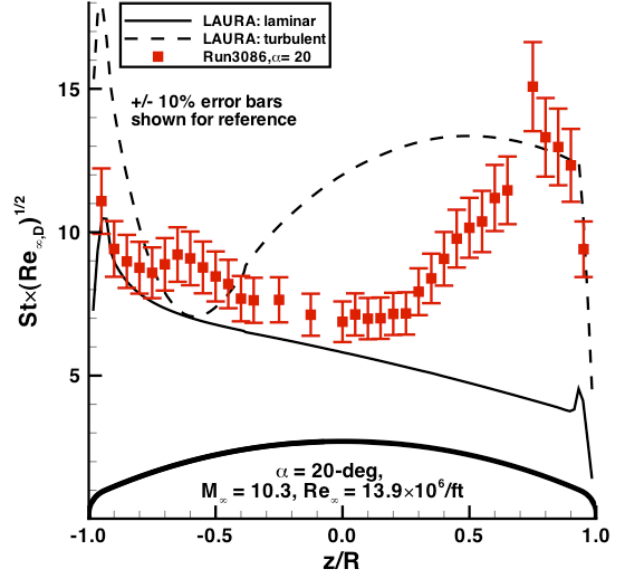


Figure 155. Run 3086 data and comparison with predictions, Mach = 10, $Re_\infty = 14 \times 10^6/\text{ft}$, $\alpha = 20\text{-deg}$

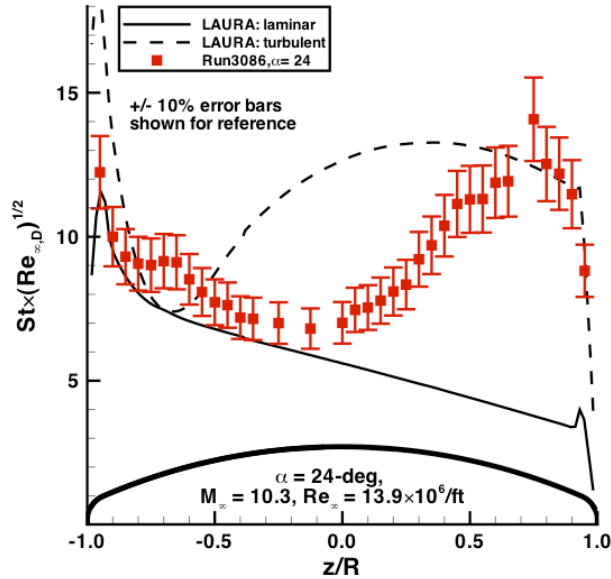


Figure 156. Run 3086 data and comparison with predictions, Mach = 10, $Re_\infty = 14 \times 10^6/\text{ft}$, $\alpha = 24\text{-deg}$

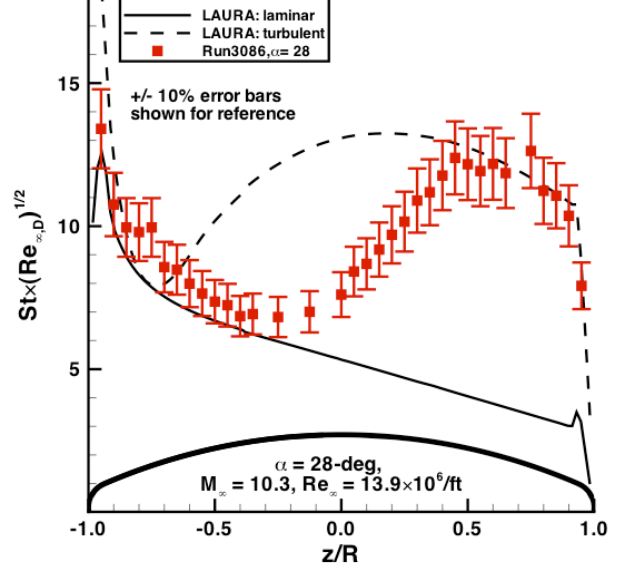


Figure 157. Run 3086 data and comparison with predictions, Mach = 10, $Re_\infty = 14 \times 10^6/\text{ft}$, $\alpha = 28\text{-deg}$

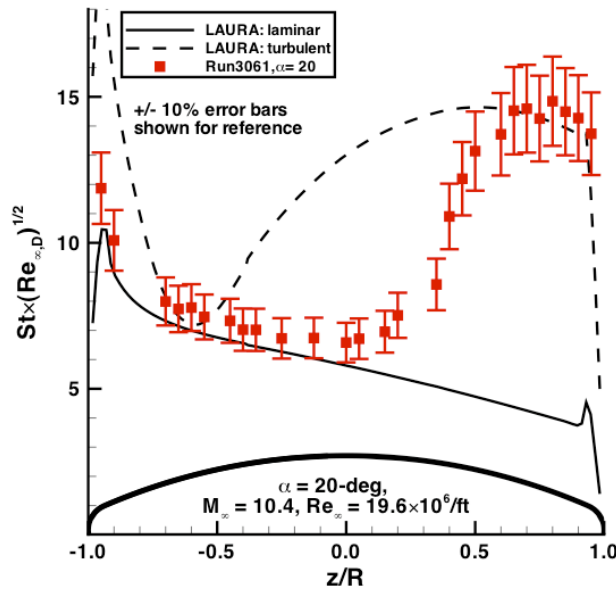


Figure 158. Run 3061 data and comparison with predictions, Mach = 10, $Re_{\infty} = 20 \times 10^6/\text{ft}$, $\alpha = 20\text{-deg}$

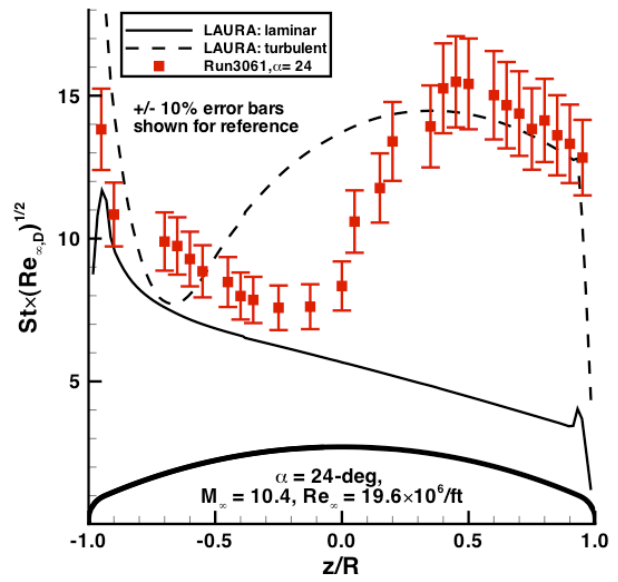


Figure 159. Run 3061 data and comparison with predictions, Mach = 10, $Re_{\infty} = 20 \times 10^6/\text{ft}$, $\alpha = 24\text{-deg}$

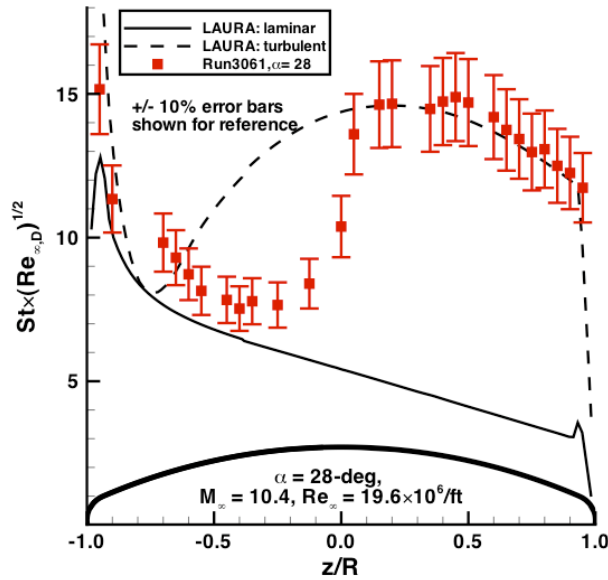


Figure 160. Run 3061 data and comparison with predictions, Mach = 10, $Re_{\infty} = 20 \times 10^6/\text{ft}$, $\alpha = 28\text{-deg}$

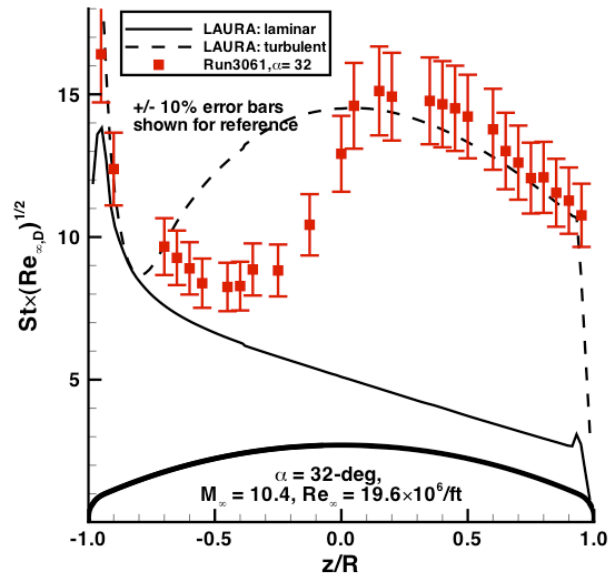


Figure 161. Run 3061 data and comparison with predictions, Mach = 10, $Re_{\infty} = 20 \times 10^6/\text{ft}$, $\alpha = 32\text{-deg}$

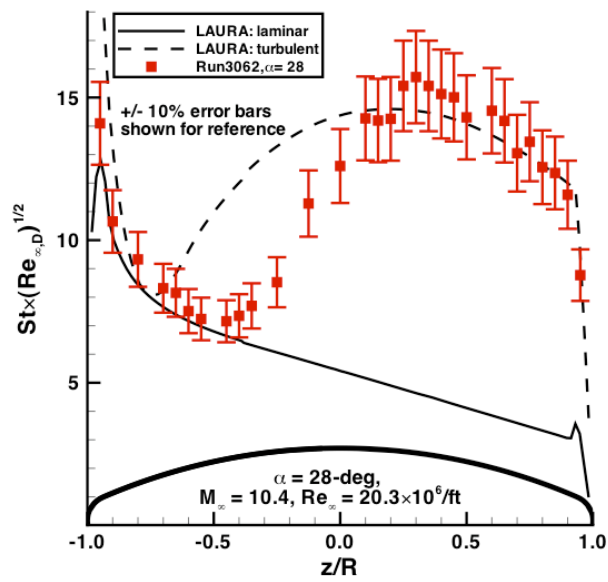


Figure 162. Run 3062 data and comparison with predictions, Mach = 10, $Re_{\infty} = 20 \times 10^6/\text{ft}$, $\alpha = 28\text{-deg}$

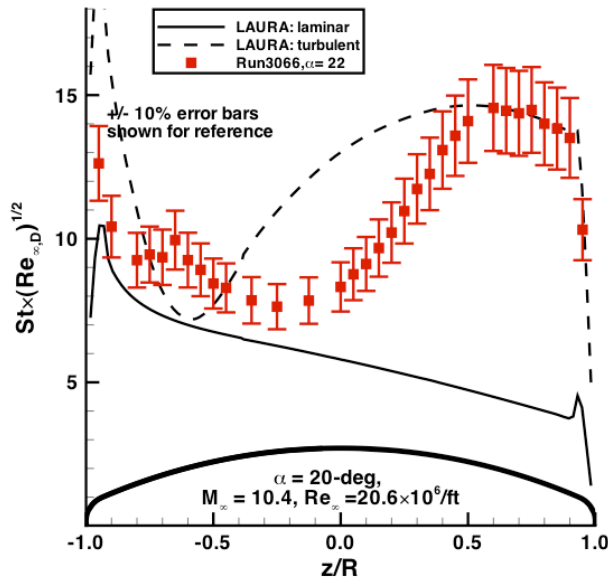


Figure 163. Run 3066 data and comparison with predictions, Mach = 10, $Re_\infty = 21 \times 10^6/ft$, $\alpha = 20\text{-deg}$

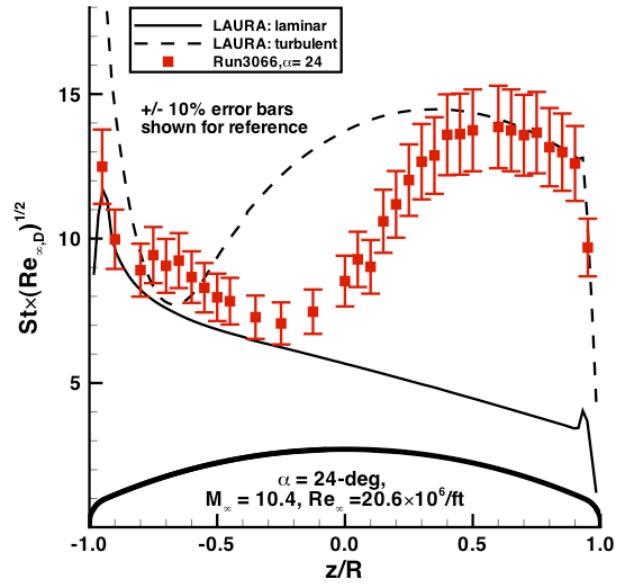


Figure 164. Run 3066 data and comparison with predictions, Mach = 10, $Re_\infty = 21 \times 10^6/ft$, $\alpha = 24\text{-deg}$

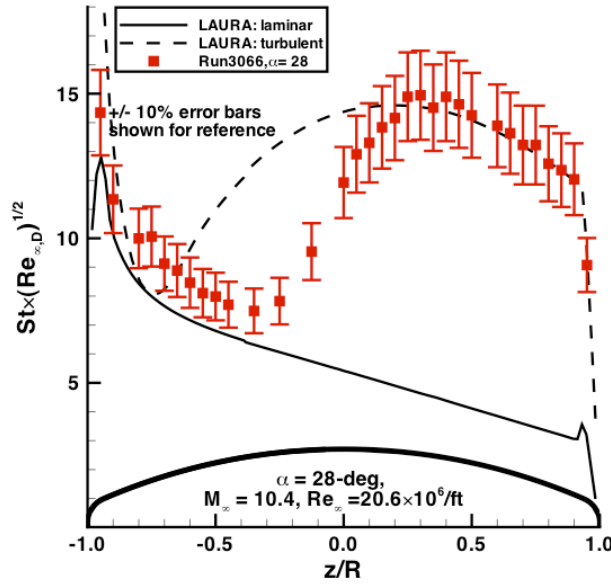


Figure 165. Run 3066 data and comparison with predictions, Mach = 10, $Re_\infty = 21 \times 10^6/ft$, $\alpha = 28\text{-deg}$

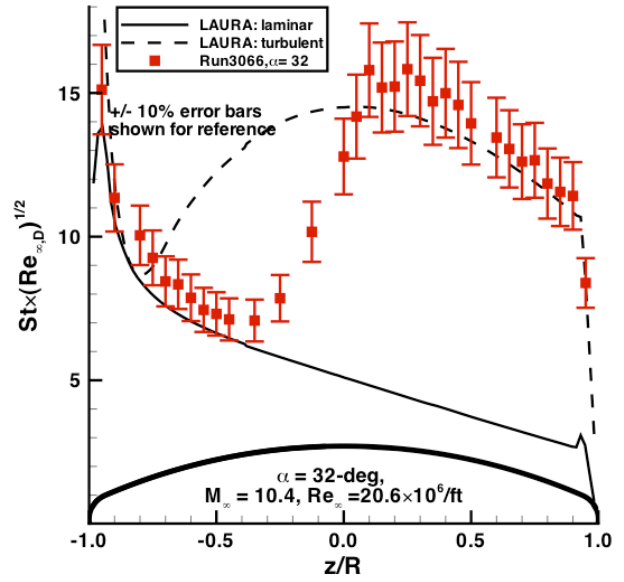


Figure 166. Run 3066 data and comparison with predictions, Mach = 10, $Re_\infty = 21 \times 10^6/ft$, $\alpha = 32\text{-deg}$

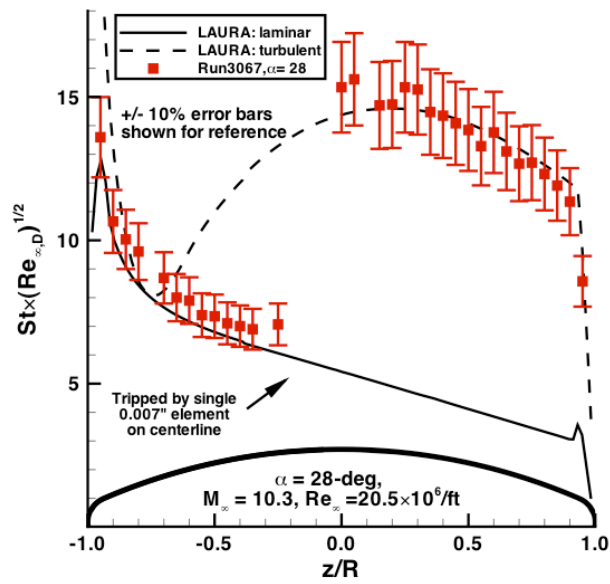


Figure 167. Run 3067 data and comparison with predictions, Mach = 10, $Re_\infty = 21 \times 10^6/\text{ft}$, $\alpha = 28\text{-deg}$

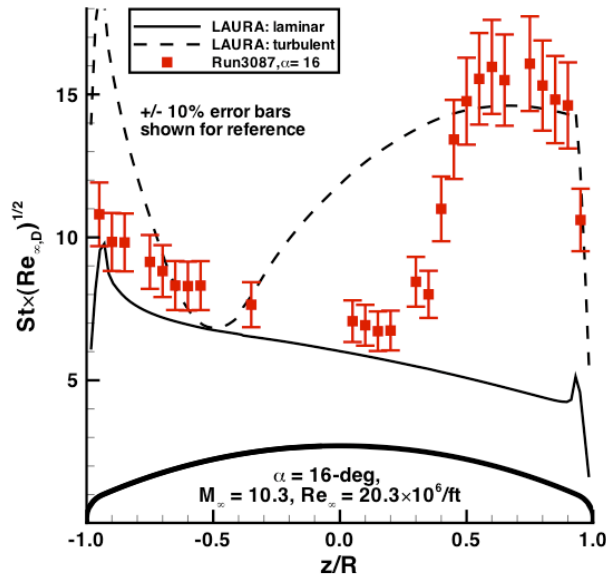


Figure 168. Run 3087 data and comparison with predictions, Mach = 10, $Re_{\infty} = 20 \times 10^6/\text{ft}$, $\alpha = 16\text{-deg}$

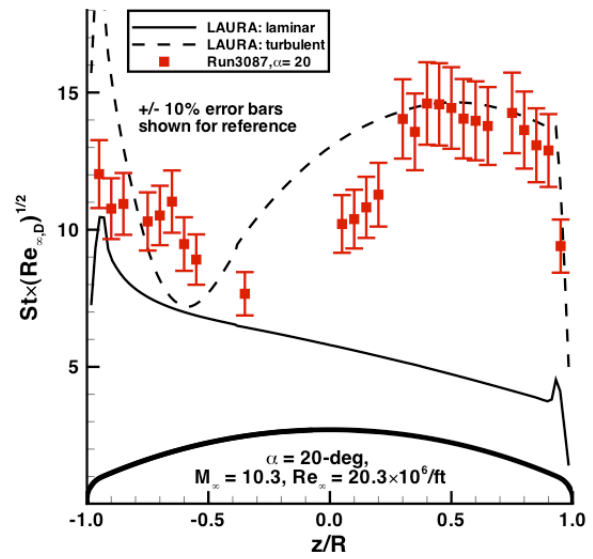


Figure 169. Run 3087 data and comparison with predictions, Mach = 10, $Re_{\infty} = 20 \times 10^6/\text{ft}$, $\alpha = 20\text{-deg}$

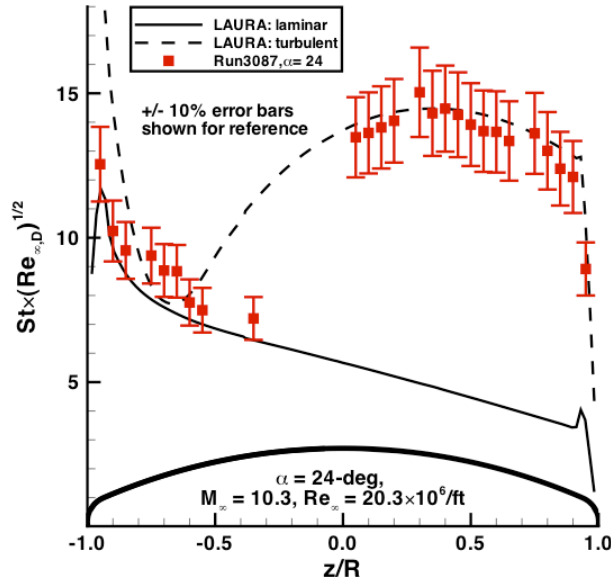


Figure 170. Run 3087 data and comparison with predictions, Mach = 10, $Re_{\infty} = 20 \times 10^6/\text{ft}$, $\alpha = 24\text{-deg}$

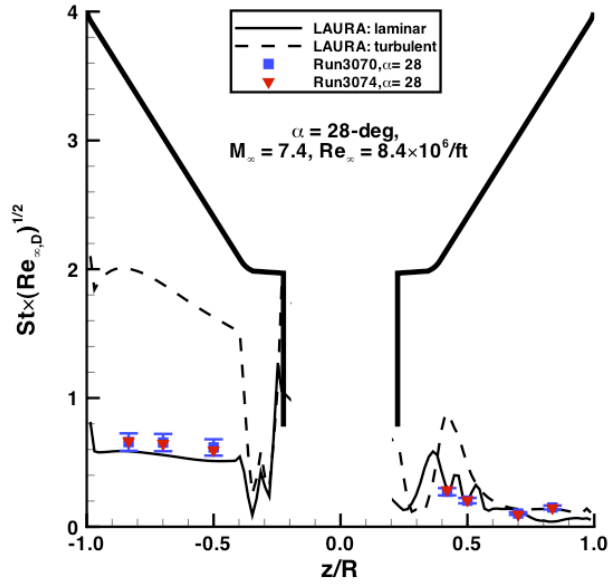


Figure 171. Comparison of wake heating data with predictions, Mach = 8, $Re_\infty = 8 \times 10^6/\text{ft}$, $\alpha = 28\text{-deg}$

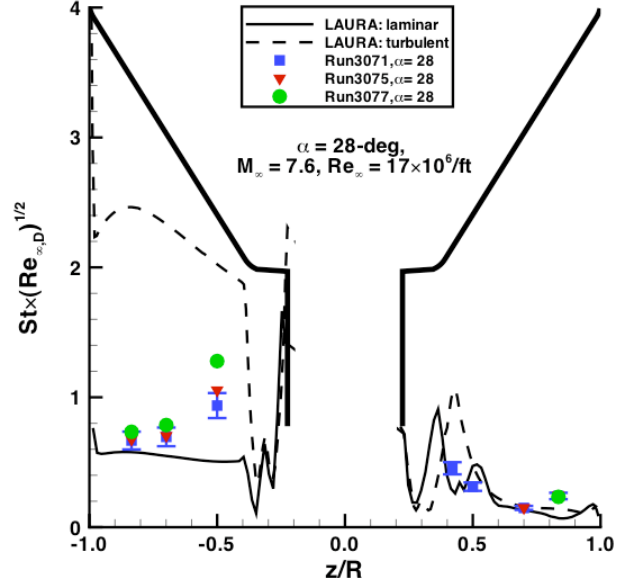


Figure 172. Comparison of wake heating data with predictions, Mach = 8, $Re_\infty = 17 \times 10^6/\text{ft}$, $\alpha = 28\text{-deg}$

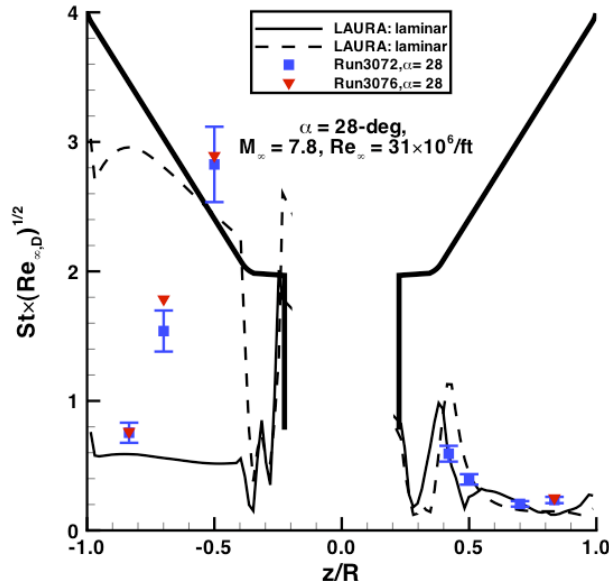


Figure 173. Comparison of wake heating data with predictions, Mach = 8, $Re_\infty = 31 \times 10^6/\text{ft}$, $\alpha = 28\text{-deg}$

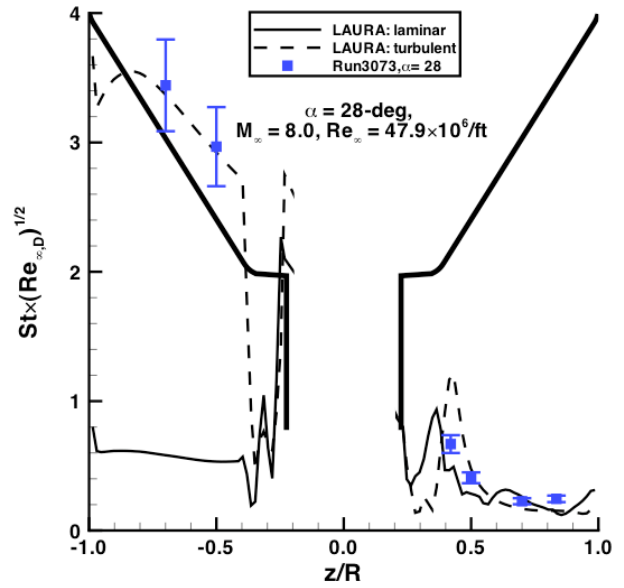


Figure 174. Comparison of wake heating data with predictions, Mach = 8, $Re_\infty = 48 \times 10^6/\text{ft}$, $\alpha = 28\text{-deg}$

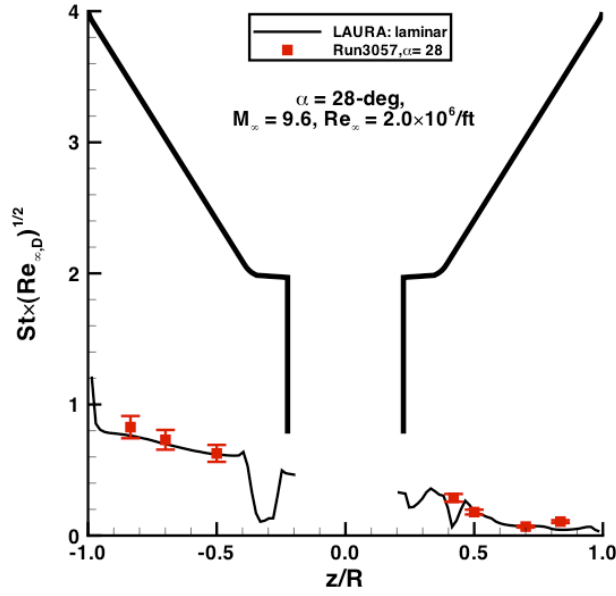


Figure 175. Comparison of wake heating data with predictions, Mach = 10, $Re_\infty = 2 \times 10^6/\text{ft}$, $\alpha = 28\text{-deg}$

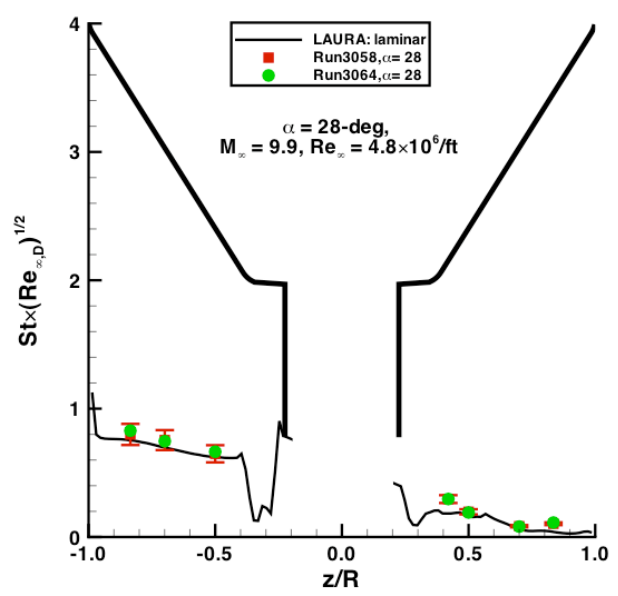


Figure 176. Comparison of wake heating data with predictions, Mach = 10, $Re_\infty = 5 \times 10^6/\text{ft}$, $\alpha = 28\text{-deg}$

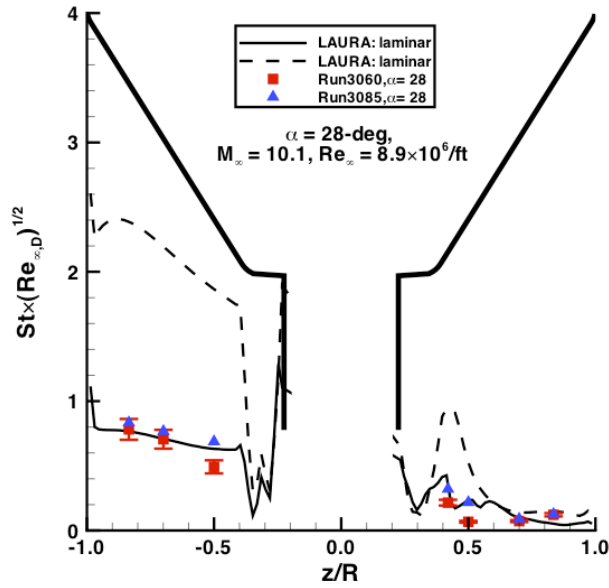


Figure 177. Comparison of wake heating data with predictions, Mach = 10, $Re_\infty = 9 \times 10^6/\text{ft}$, $\alpha = 28\text{-deg}$

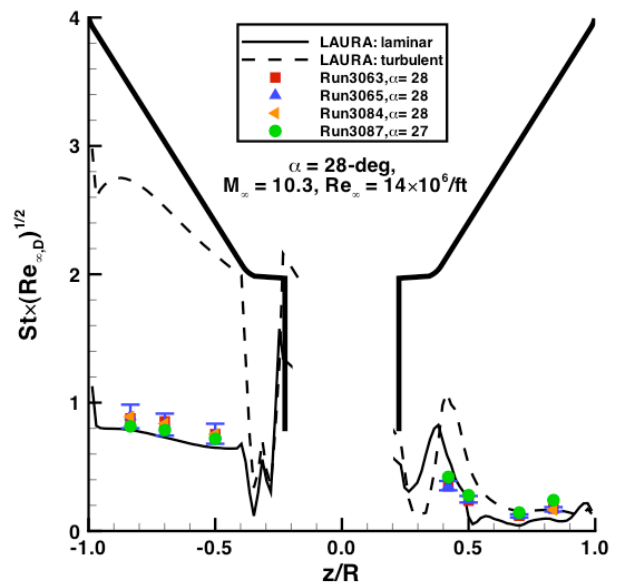


Figure 178. Comparison of wake heating data with predictions, Mach = 10, $Re_\infty = 15 \times 10^6/\text{ft}$, $\alpha = 28\text{-deg}$

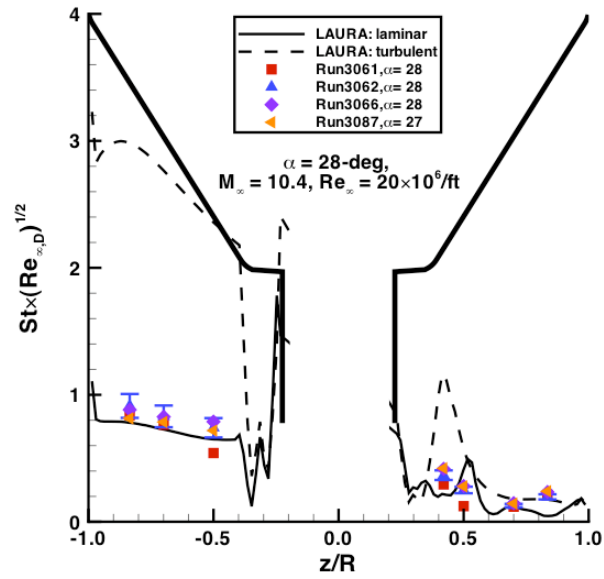


Figure 179. Comparison of wake heating data with predictions, Mach = 10, $Re_{\infty} = 20 \times 10^6/\text{ft}$, $\alpha = 28\text{-deg}$

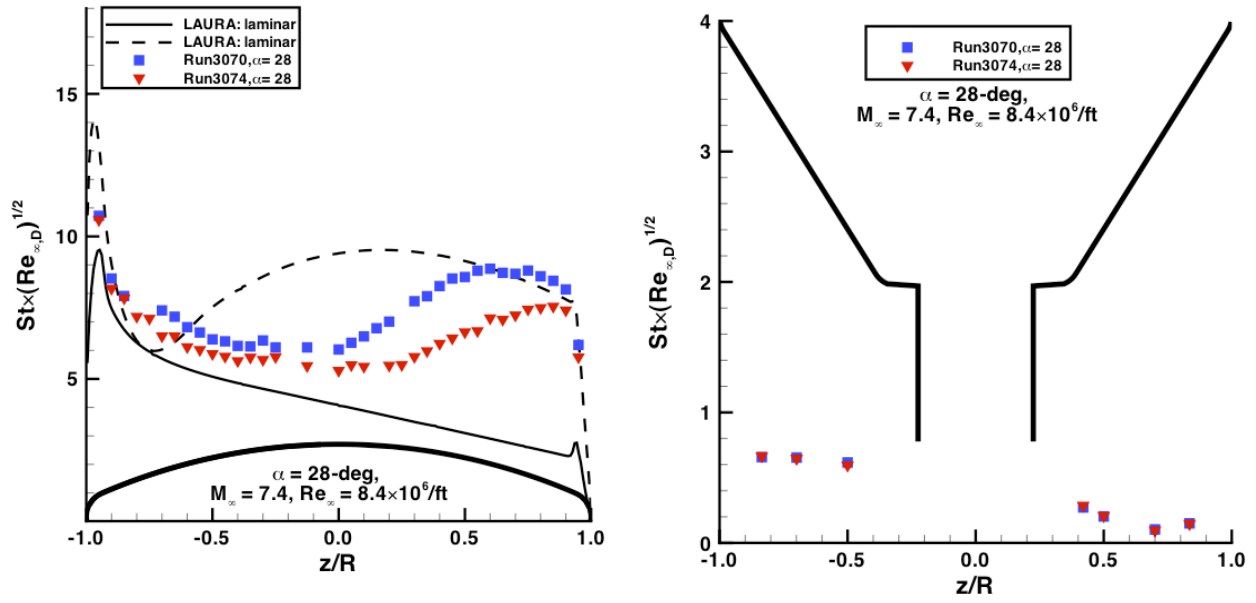


Figure 180. Data repeatability, $\alpha = 28\text{-deg}$, Mach = 8, $Re_\infty = 8 \times 10^6/\text{ft}$

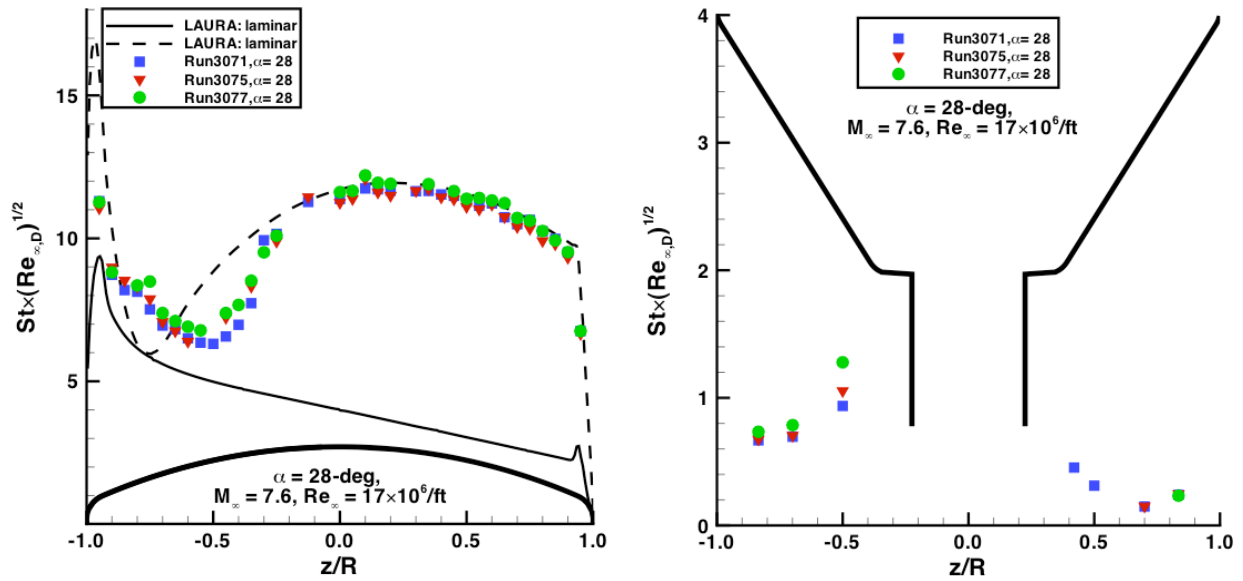


Figure 181. Data repeatability, $\alpha = 28\text{-deg}$, Mach = 8, $Re_\infty = 17 \times 10^6/\text{ft}$

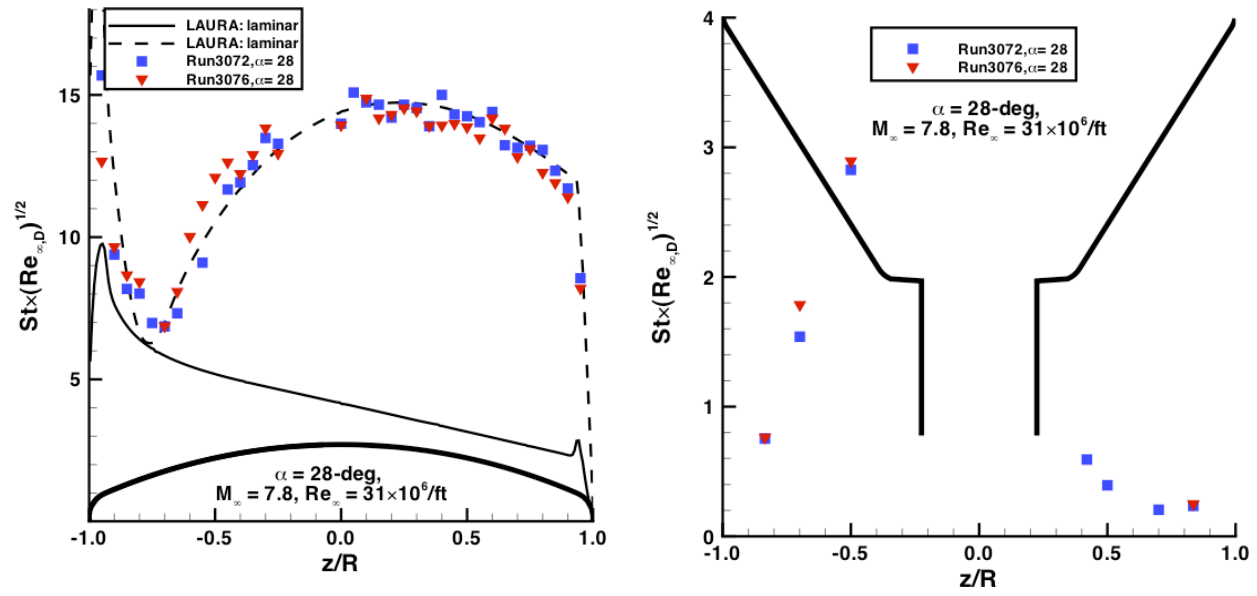


Figure 182. Data repeatability, $\alpha = 28\text{-deg}$, Mach = 8, $Re_\infty = 31 \times 10^6/\text{ft}$

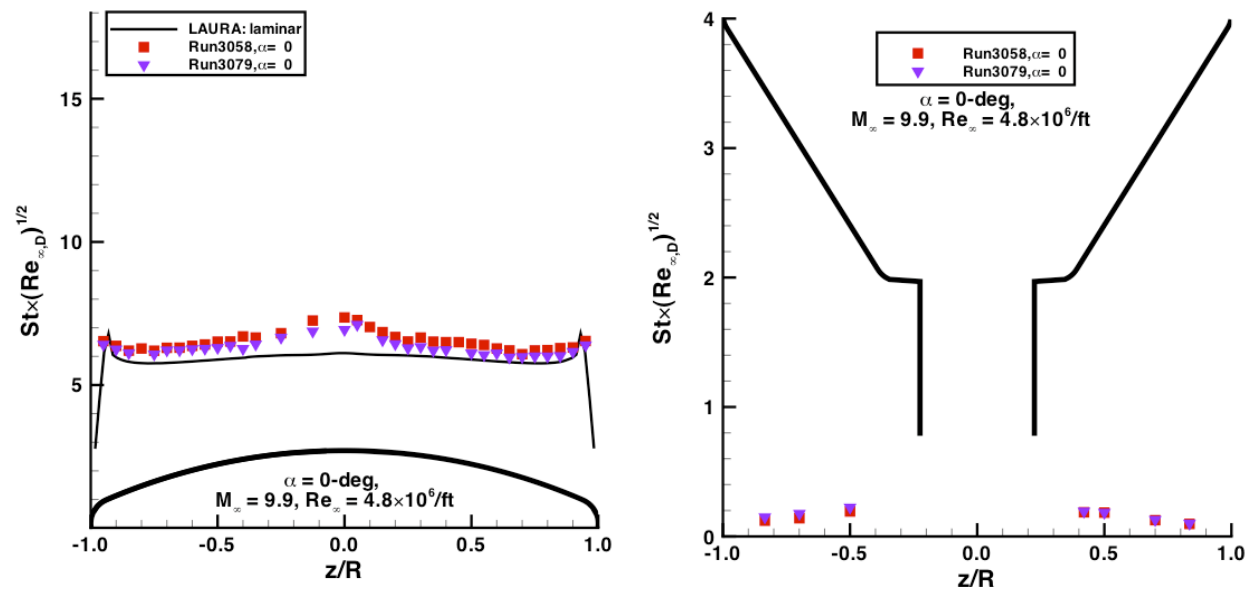


Figure 183. Data repeatability, $\alpha = 0\text{-deg}$, Mach = 10, $Re_\infty = 5 \times 10^6/\text{ft}$

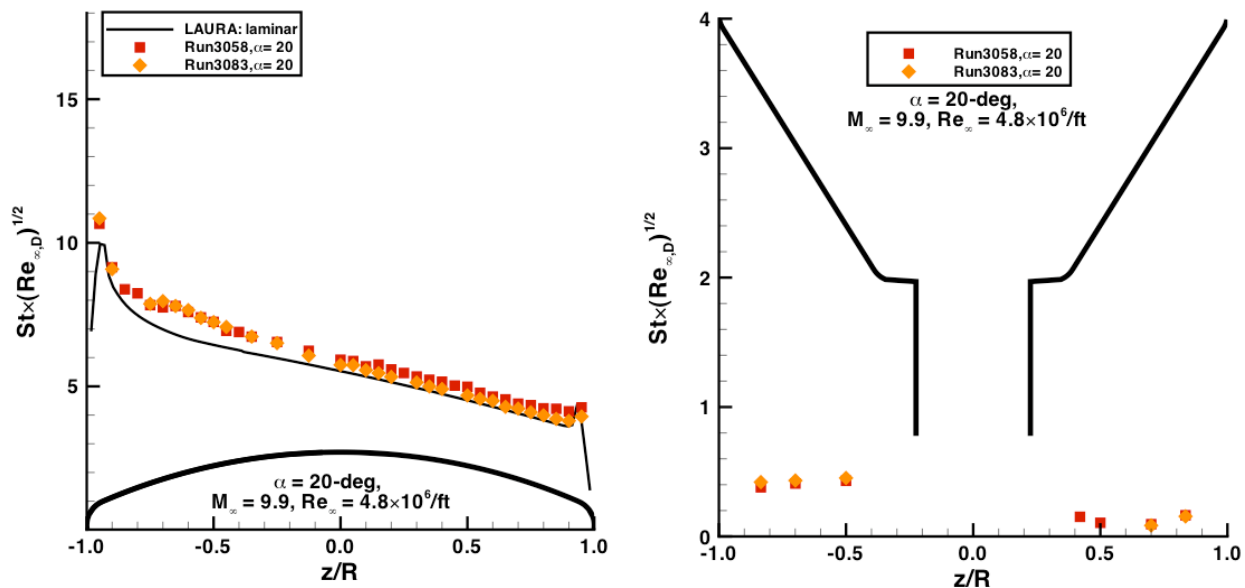


Figure 184. Data repeatability, $\alpha = 20\text{-deg}$, Mach = 10, $Re_\infty = 5 \times 10^6/\text{ft}$

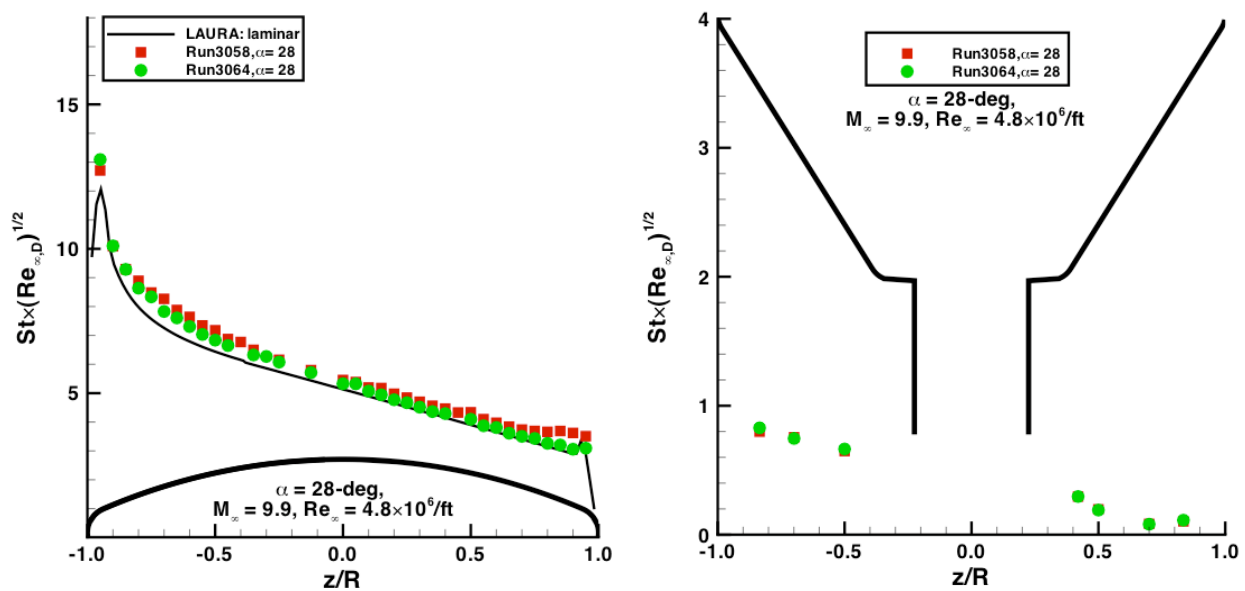


Figure 185. Data repeatability, $\alpha = 28\text{-deg}$, Mach = 10, $Re_\infty = 5 \times 10^6/\text{ft}$

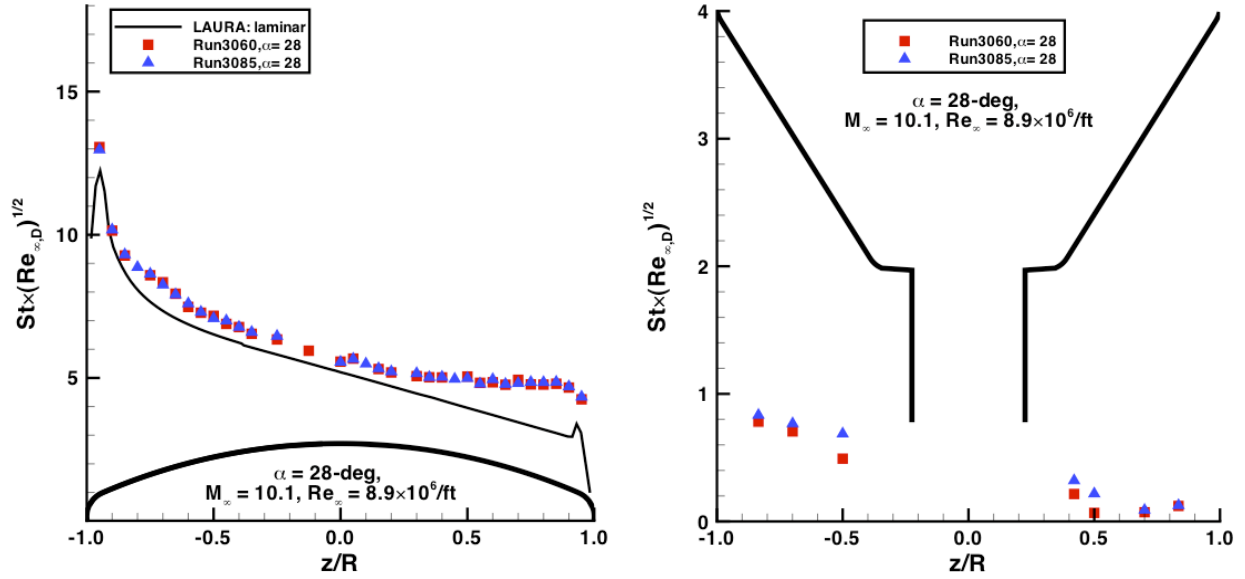


Figure 186. Data repeatability, $\alpha = 28\text{-deg}$, Mach = 10, $Re_\infty = 9 \times 10^6/\text{ft}$

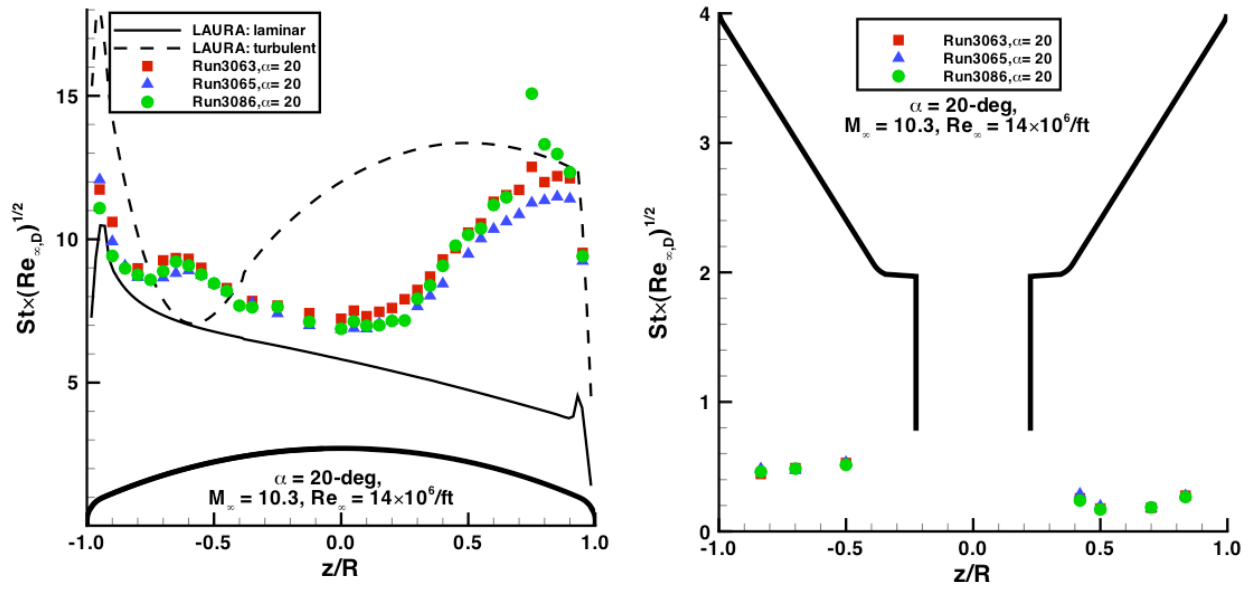


Figure 187. Data repeatability, $\alpha = 20\text{-deg}$, Mach = 10, $Re_\infty = 15 \times 10^6/\text{ft}$

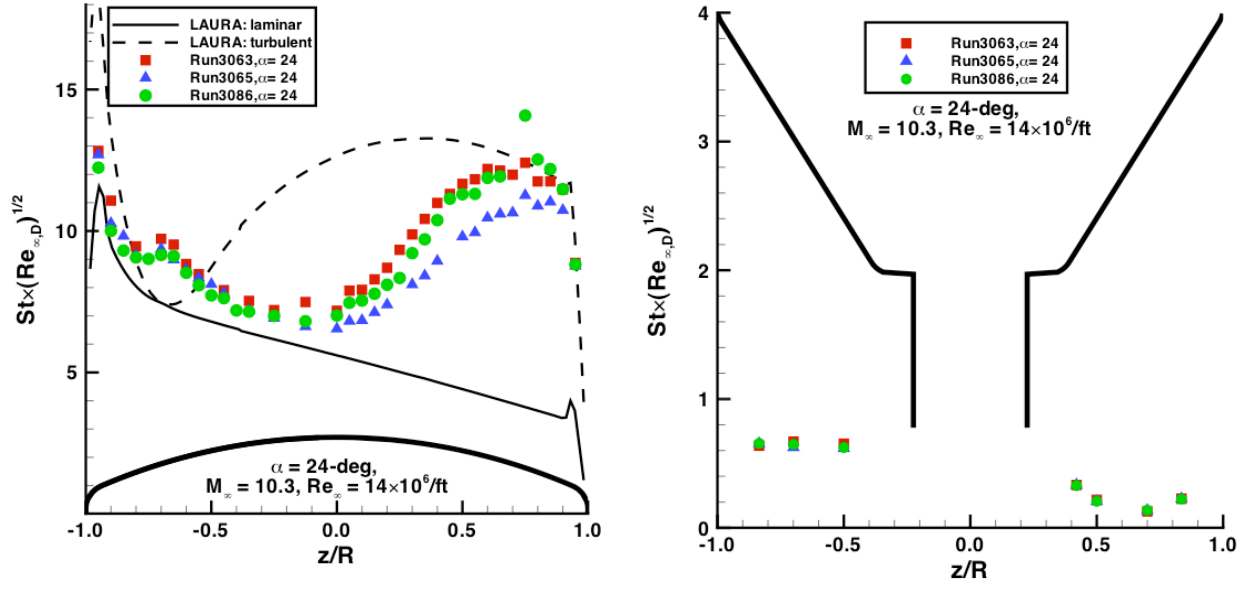


Figure 188. Data repeatability, $\alpha = 24\text{-deg}$, $Mach = 10$, $Re_\infty = 15 \times 10^6/\text{ft}$

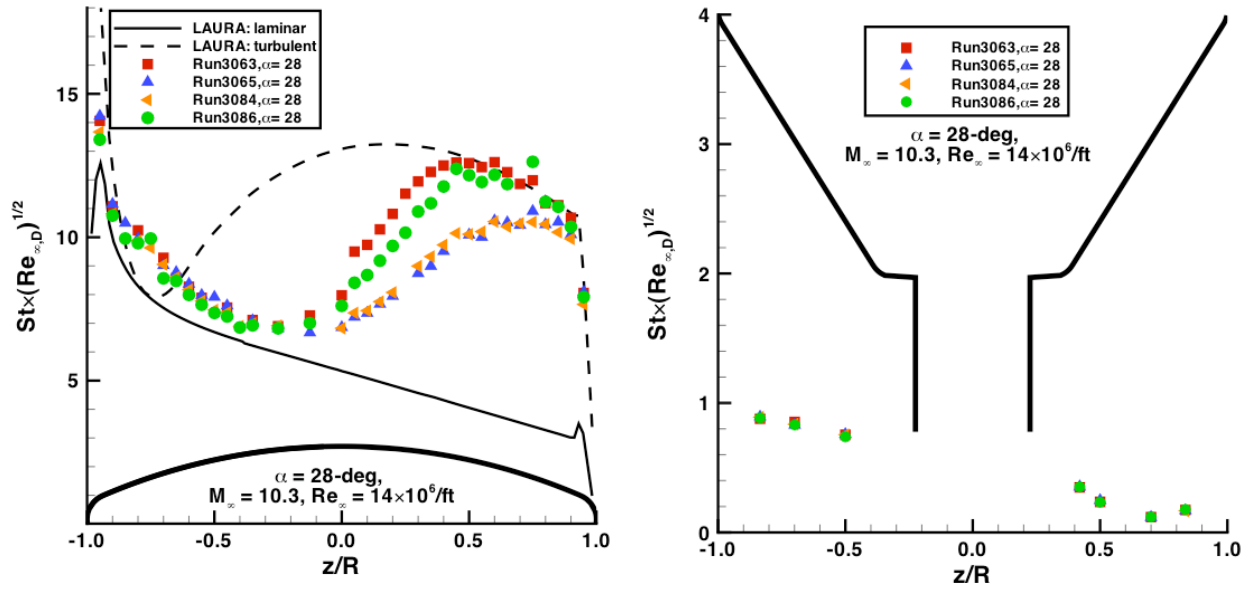


Figure 189. Data repeatability, $\alpha = 28\text{-deg}$, $Mach = 10$, $Re_\infty = 15 \times 10^6/\text{ft}$

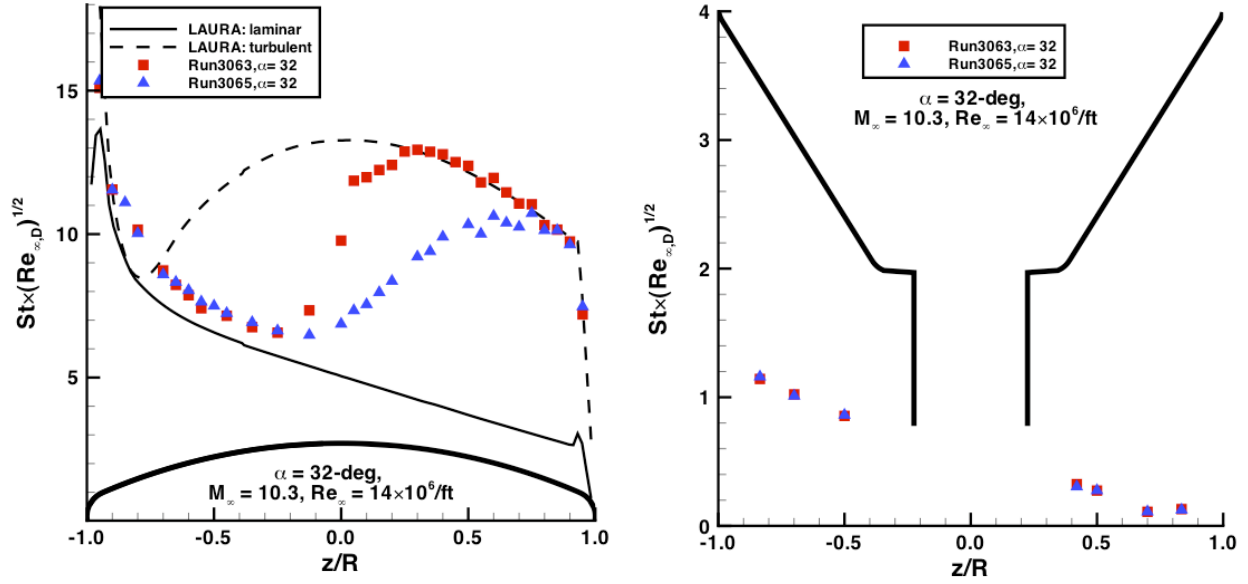


Figure 190. Data repeatability, $\alpha = 32\text{-deg}$, Mach = 10, $Re_\infty = 15 \times 10^6/\text{ft}$

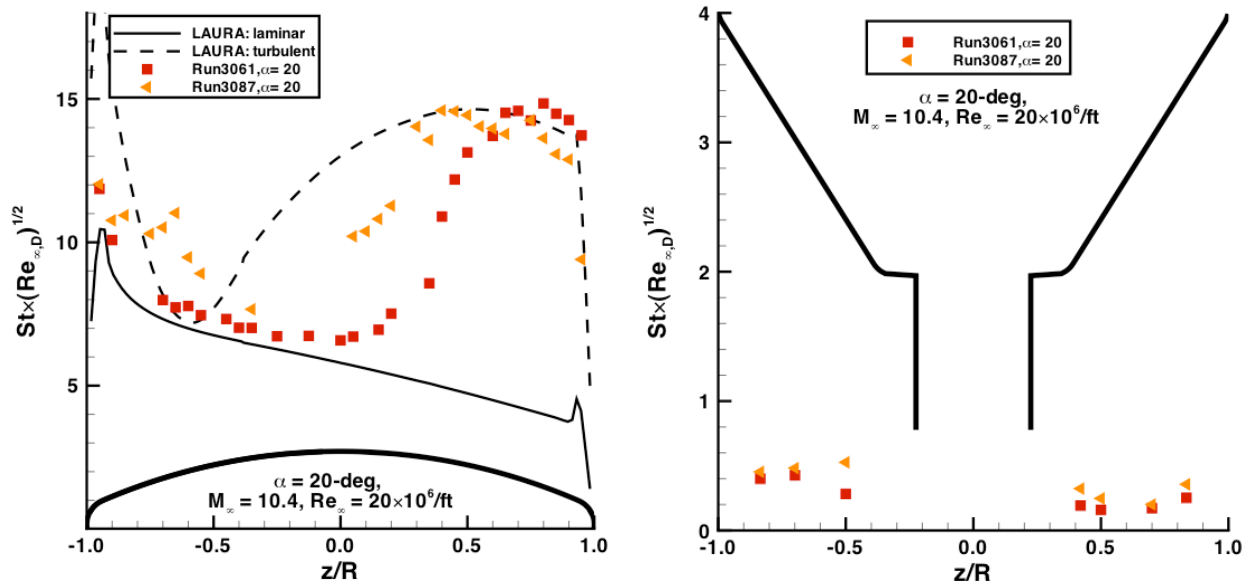


Figure 191. Data repeatability, $\alpha = 20\text{-deg}$, Mach = 10, $Re_\infty = 20 \times 10^6/\text{ft}$

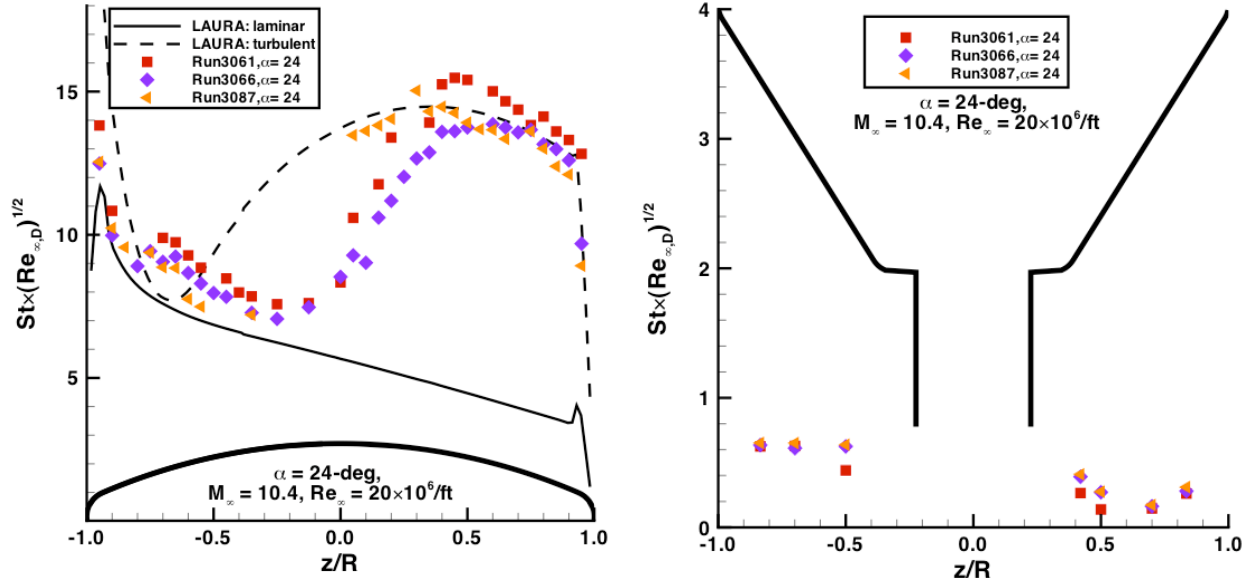


Figure 192. Data repeatability, $\alpha = 24\text{-deg}$, Mach = 10, $Re_\infty = 20 \times 10^6/\text{ft}$

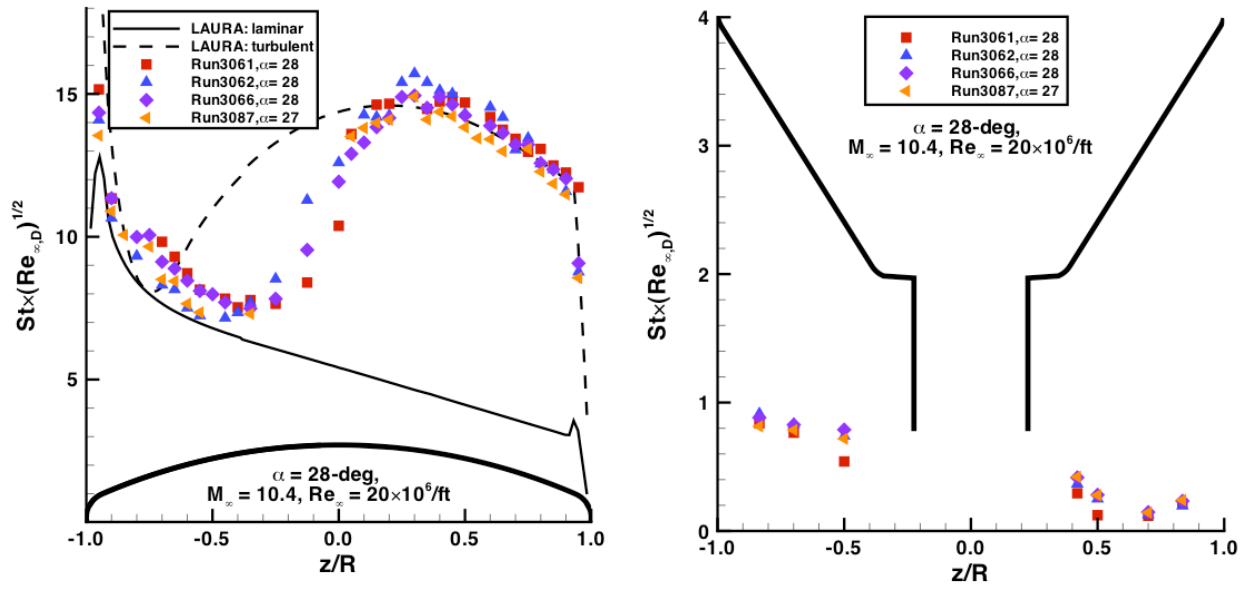


Figure 193. Data repeatability, $\alpha = 28\text{-deg}$, Mach = 10, $Re_\infty = 20 \times 10^6/\text{ft}$

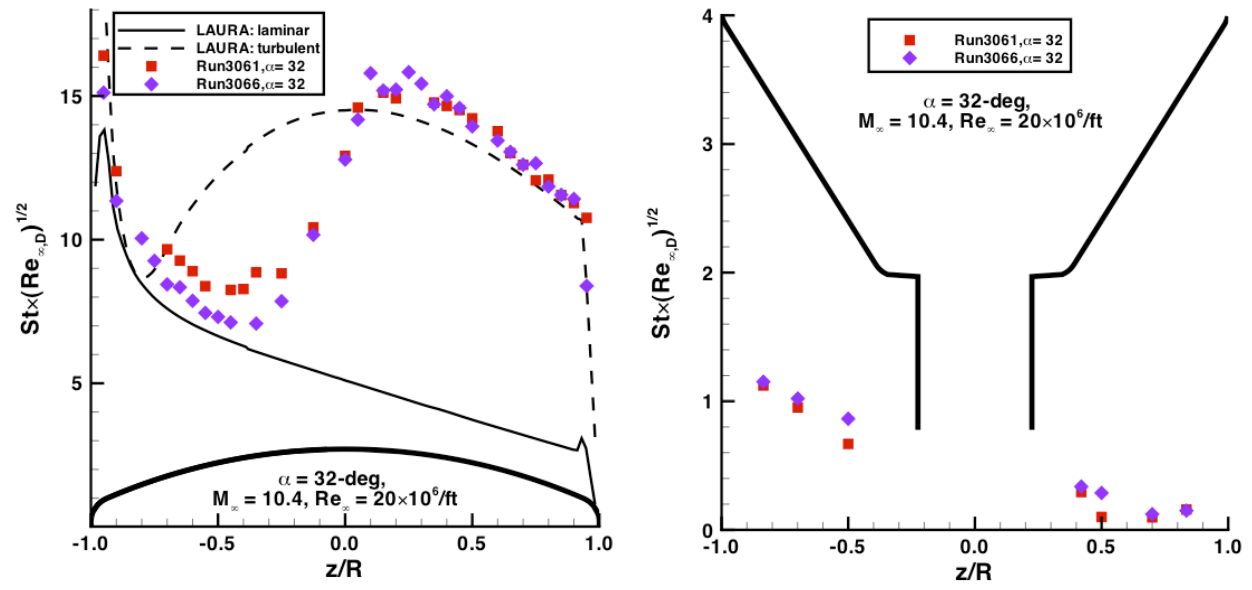


Figure 194. Data repeatability, $\alpha = 32\text{-deg}$, Mach = 10, $Re_\infty = 20 \times 10^6/\text{ft}$

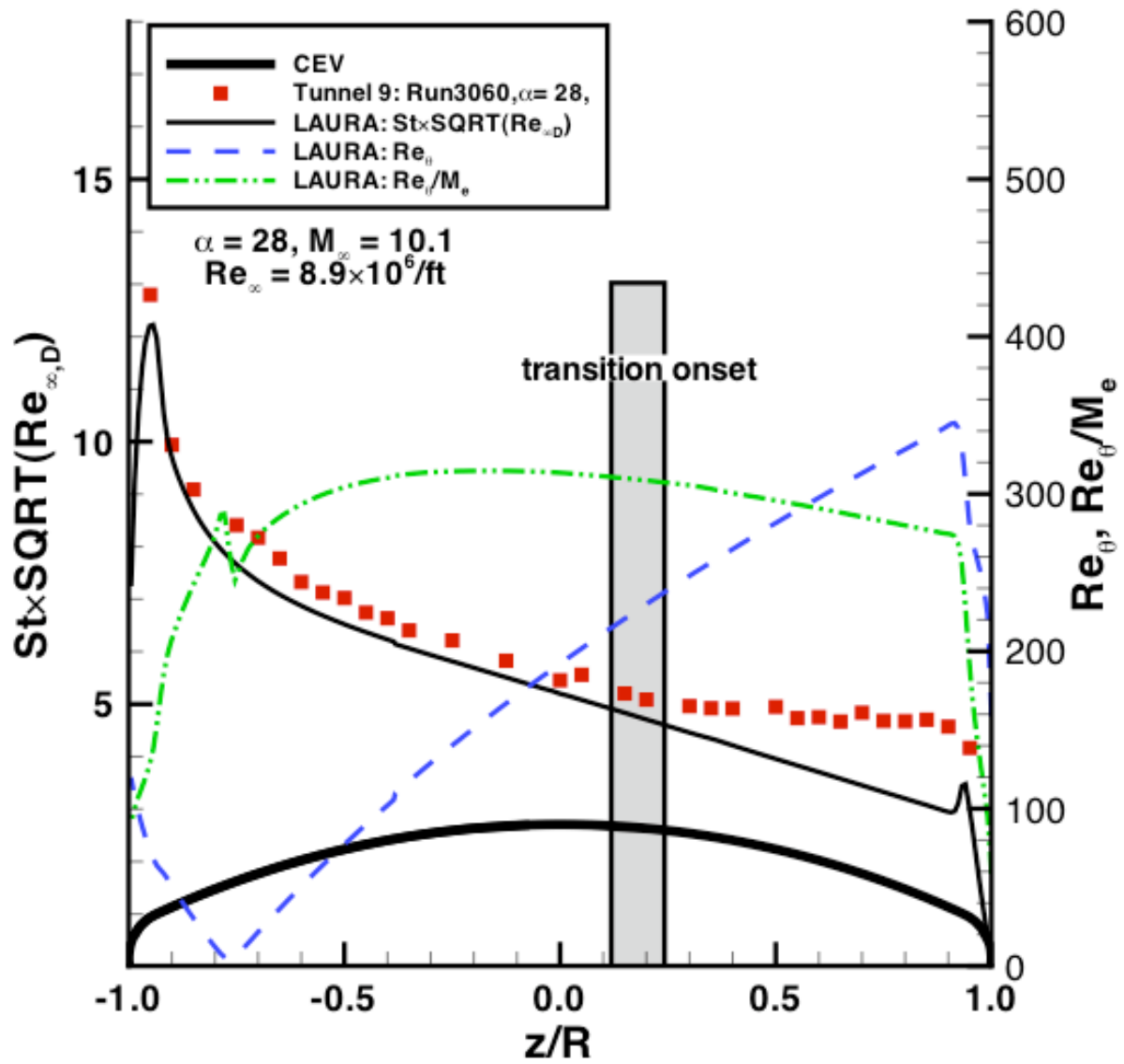


Figure 195. Sample of plot for determination of transition onset location

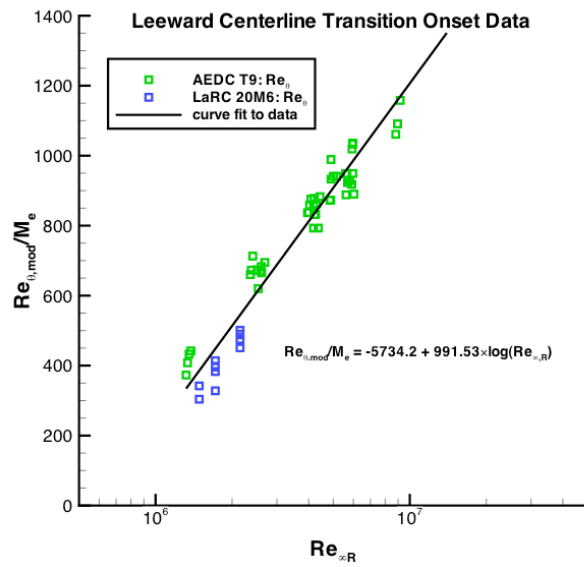
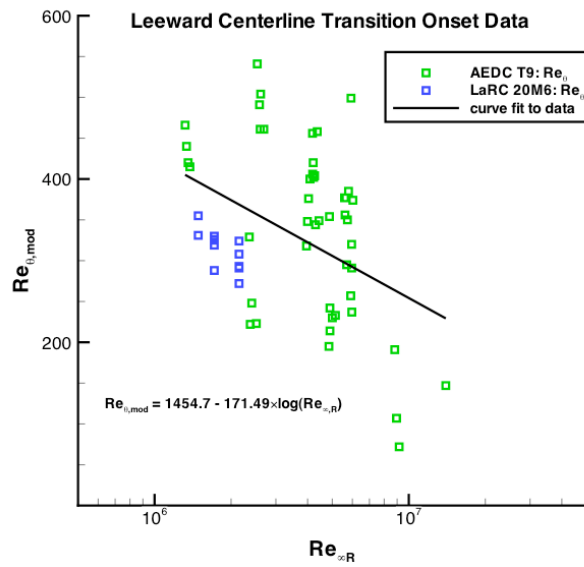
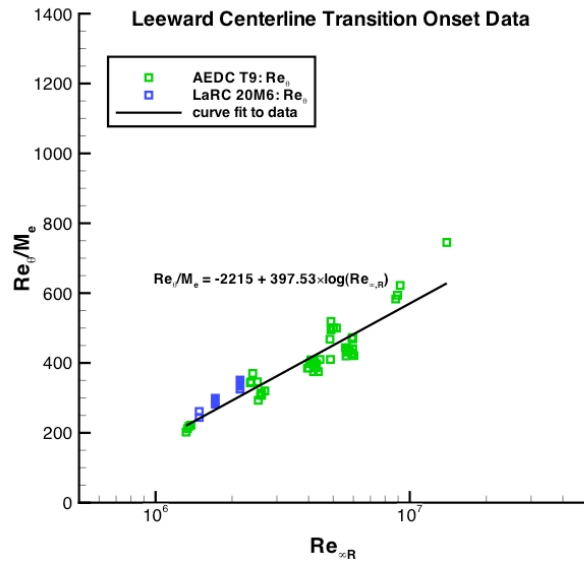
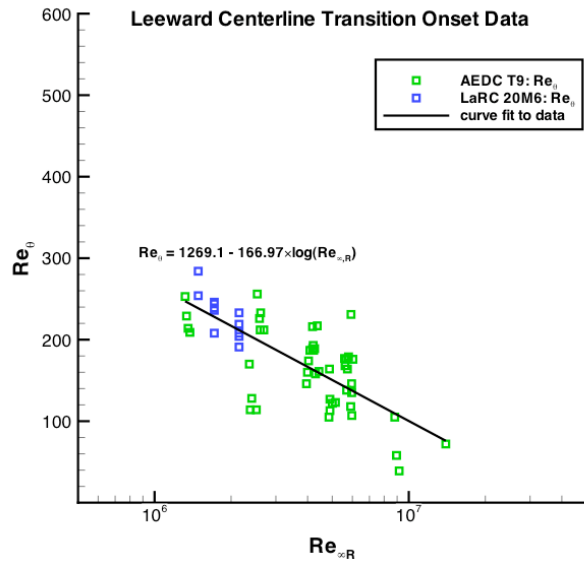


Figure 196. Correlations for forebody leeward centerline transition onset location

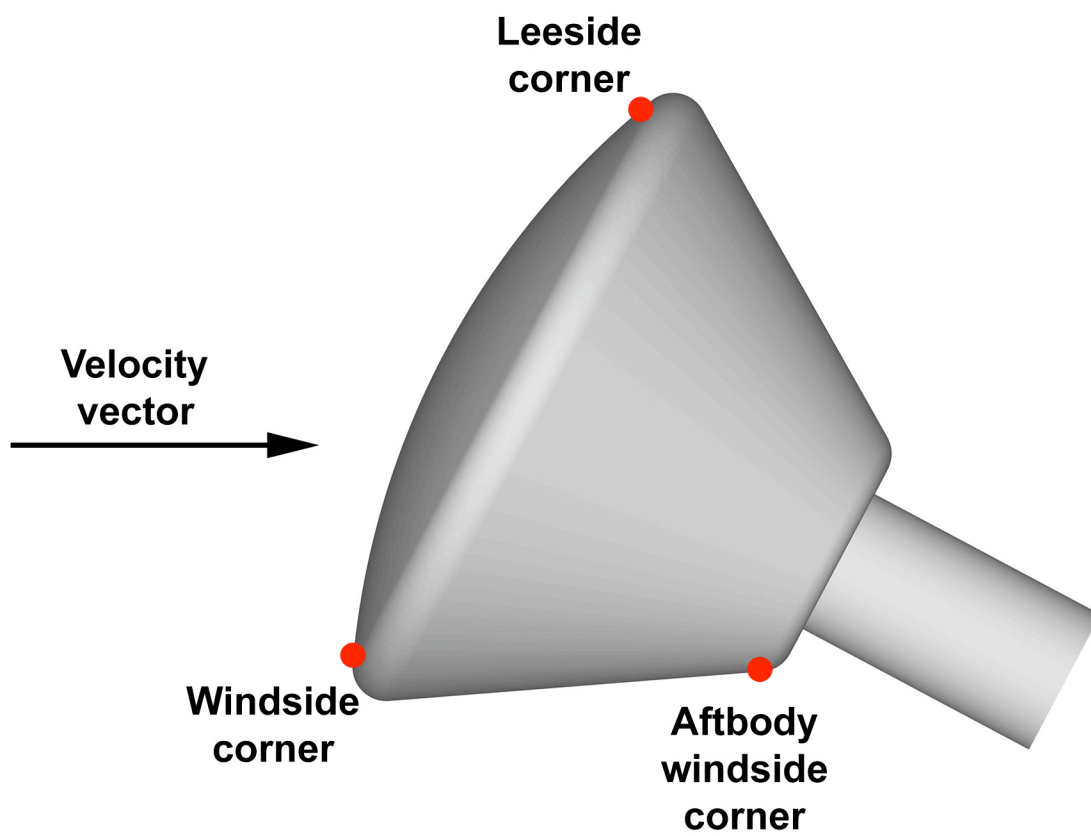


Figure 197. Body points for heating correlations

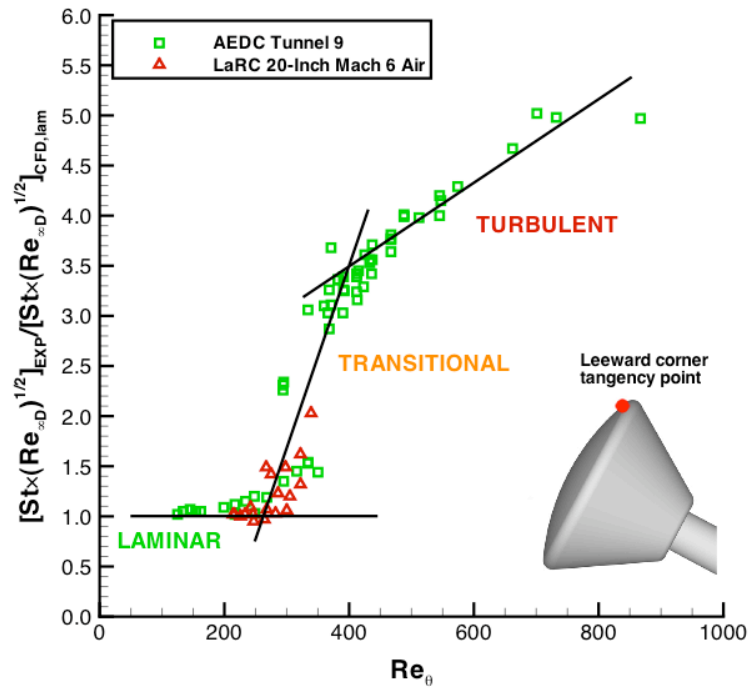


Figure 198. Lee side shoulder heating augmentation ratio

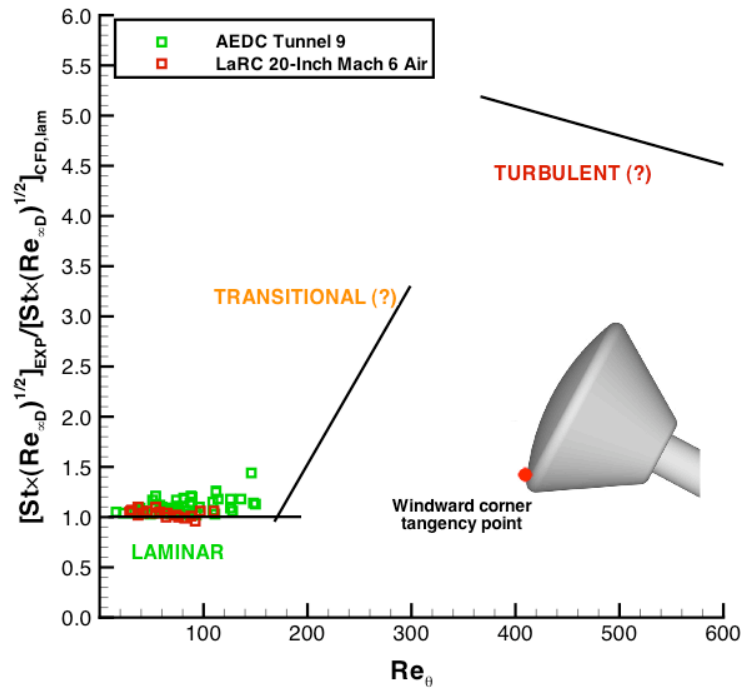


Figure 199. Wind side shoulder heating augmentation ratio

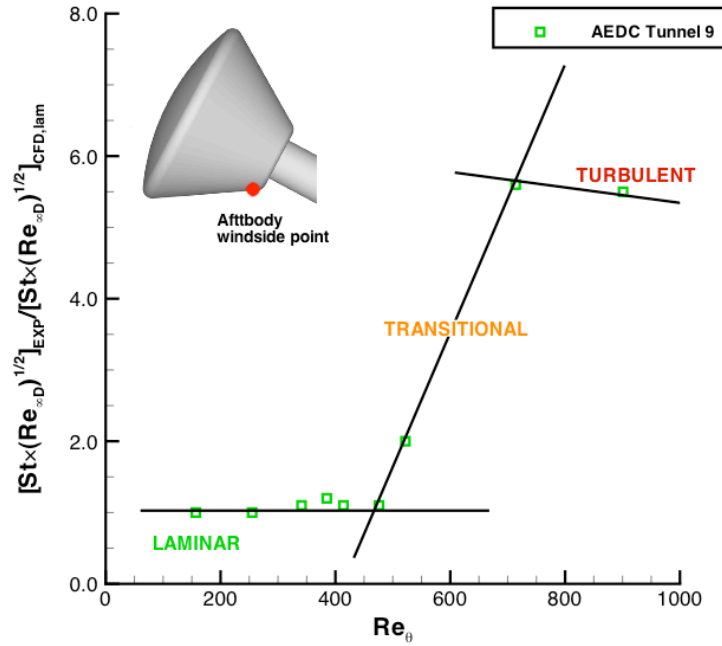


Figure 200. Aftbody corner heating augmentation ratio

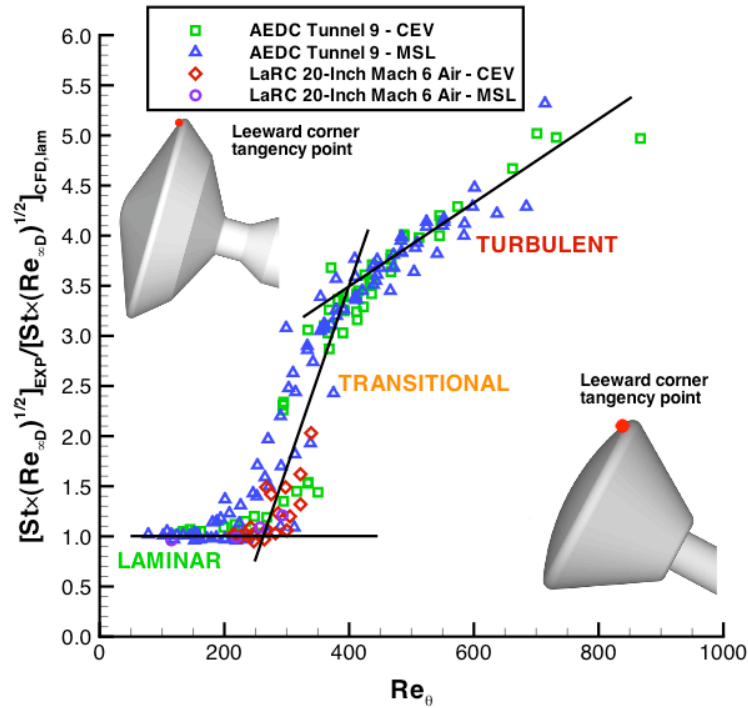


Figure 201. Lee side shoulder heating augmentation ratio with MSL data added

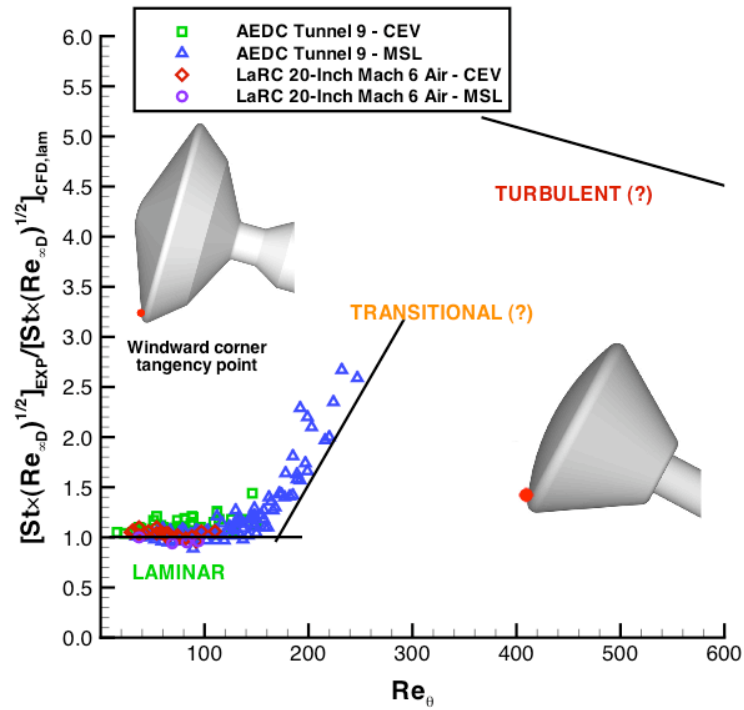


Figure 202. Wind side shoulder heating augmentation ratio with MSL data added

REPORT DOCUMENTATION PAGE					Form Approved OMB No. 0704-0188	
<p>The public reporting burden for this collection of information is estimated to average 1 hour per response, including the time for reviewing instructions, searching existing data sources, gathering and maintaining the data needed, and completing and reviewing the collection of information. Send comments regarding this burden estimate or any other aspect of this collection of information, including suggestions for reducing this burden, to Department of Defense, Washington Headquarters Services, Directorate for Information Operations and Reports (0704-0188), 1215 Jefferson Davis Highway, Suite 1204, Arlington, VA 22202-4302. Respondents should be aware that notwithstanding any other provision of law, no person shall be subject to any penalty for failing to comply with a collection of information if it does not display a currently valid OMB control number.</p> <p>PLEASE DO NOT RETURN YOUR FORM TO THE ABOVE ADDRESS.</p>						
1. REPORT DATE (DD-MM-YYYY)		2. REPORT TYPE		3. DATES COVERED (From - To)		
01- 12 - 2008		Technical Publication				
4. TITLE AND SUBTITLE Experimental Investigation of Project Orion Crew Exploration Vehicle Aeroheating in AEDC Tunnel 9				5a. CONTRACT NUMBER		
				5b. GRANT NUMBER		
				5c. PROGRAM ELEMENT NUMBER		
6. AUTHOR(S) Hollis, Brian R.; Horvath, Thomas J.; Berger, Karen T.; Lillard, Randolph P.; Kirk, Benjamin S.; Coblish, Joseph J.; Norris, Joseph D.				5d. PROJECT NUMBER		
				5e. TASK NUMBER		
				5f. WORK UNIT NUMBER 644423.02.39.04.10.03		
7. PERFORMING ORGANIZATION NAME(S) AND ADDRESS(ES) NASA Langley Research Center Hampton, VA 23681-2199				8. PERFORMING ORGANIZATION REPORT NUMBER L-19359		
9. SPONSORING/MONITORING AGENCY NAME(S) AND ADDRESS(ES) National Aeronautics and Space Administration Washington, DC 20546-0001				10. SPONSOR/MONITOR'S ACRONYM(S) NASA		
				11. SPONSOR/MONITOR'S REPORT NUMBER(S) NASA/TP-2008-215547		
12. DISTRIBUTION/AVAILABILITY STATEMENT Unclassified - Unlimited Subject Category 34 Availability: NASA CASI (301) 621-0390						
13. SUPPLEMENTARY NOTES						
14. ABSTRACT An investigation of the aeroheating environment of the Project Orion Crew Entry Vehicle has been performed in the Arnold Engineering Development Center Tunnel 9. The goals of this test were to measure turbulent heating augmentation levels on the heat shield and to obtain high-fidelity heating data for assessment of computational fluid dynamics methods. Laminar and turbulent predictions were generated for all wind tunnel test conditions and comparisons were performed with the data for the purpose of helping to define uncertainty margins for the computational method. Data from both the wind tunnel test and the computational study are presented herein.						
15. SUBJECT TERMS Aerothermodynamics; CEV; CFD; Turbulence						
16. SECURITY CLASSIFICATION OF:			17. LIMITATION OF ABSTRACT	18. NUMBER OF PAGES	19a. NAME OF RESPONSIBLE PERSON	
a. REPORT	b. ABSTRACT	c. THIS PAGE			STI Help Desk (email: help@sti.nasa.gov)	
U	U	U	UU	168	19b. TELEPHONE NUMBER (Include area code) (301) 621-0390	